

<https://doi.org/10.15388/vu.thesis.343>

<https://orcid.org/0000-0002-3112-4140>

VILNIUS UNIVERSITY

CENTER FOR PHYSICAL SCIENCES AND TECHNOLOGY

Laimonas Deveikis

# Electrically active defects and their transformations in GaN structures

**DOCTORAL DISSERTATION**

Natural Sciences,

Physics (N 002)

VILNIUS 2022

The dissertation was prepared between 2018 and 2022 at Institute of Photonics and Nanotechnology, Vilnius University. The research was supported by Research Council of Lithuania: a scholarship was granted for academic accomplishments.

**Academic supervisor –**

**Prof. Habil. Dr. Eugenijus Gaubas** (Vilnius University, Natural sciences, Physics, N 002).

This doctoral dissertation will be defended in a public meeting of the Dissertation Defence Panel:

**Chairman** – Prof. Dr. Vincas Tamošiūnas (Vilnius University, Natural Sciences, Physics, N 002).

**Members:**

Prof. Habil. Dr. Arturs Medvids (Riga Technical University, Natural Sciences, Physics, N 002),

Assoc. Prof. Dr. Artūras Plūkis (Center for Physical Sciences and Technology, Natural Sciences, Physics, N 002),

Assoc. Prof. Dr. Tomas Šalkus (Vilnius University, Natural Sciences, Technology Sciences, T 008),

Dr. Aldis Šilėnas (Center for Physical Sciences and Technology, Natural Sciences, Physics, N 002).

The dissertation shall be defended at a public meeting of the Dissertation Defence Panel at 14:00 o'clock on 7th October 2022 in “Didžioji Fizikos Auditorija” of the Faculty of Physics, Vilnius University.

Address: Saulėtekio av. 9, Faculty of Physics, Vilnius University, Room “Didžioji Fizikos Auditorija”, Vilnius, Lithuania

Tel. (8 5) 236 6000; email: ff@ff.vu.lt

The text of this dissertation can be accessed at the Vilnius University Library, as well as on the website of Vilnius University: [www.vu.lt/naujienos/ivykiu-kalendorius](http://www.vu.lt/naujienos/ivykiu-kalendorius)

<https://doi.org/10.15388/vu.thesis.343>

<https://orcid.org/0000-0002-3112-4140>

VILNIAUS UNIVERSITETAS  
FIZINIŲ IR TECHNOLOGIJOS MOKSLŲ CENTRAS

Laimonas Deveikis

# Elektriškai aktyvūs defektai ir jų transformacijos GaN dariniuose

**DAKTARO DISERTACIJA**

Gamtos mokslai,  
Fizika (N 002)

VILNIUS 2022

Disertacija rengta 2018–2022 metais Fotonikos ir nanotechnologijų institute, Vilniaus universitete. Mokslinius tyrimus rėmė Lietuvos mokslo taryba: gauta stipendija už akademinis pasiekimus.

**Mokslinis vadovas:**

**Prof. habil. dr. Eugenijus Gaubas** (Vilniaus universitetas, gamtos mokslai, fizika, N 002).

Gynimo taryba:

**Pirmininkas** – prof. dr. Vincas Tamošiūnas (Vilniaus universitetas, gamtos mokslai, fizika, N 002).

**Nariai:**

prof. habil. dr. Arturs Medvids (Rygos technologijų universitetas, gamtos mokslai, fizika, N 002),

doc. dr. Artūras Plūkis (Fizinių ir technologijos mokslų centras, gamtos mokslai, fizika, N 002),

doc. dr. Tomas Šalkus (Vilniaus universitetas, gamtos mokslai, medžiagotyra, T 008),

dr. Aldis Šilėnas (Fizinių ir technologijos mokslų centras, gamtos mokslai, fizika, N 002).

Disertacija ginama viešame Gynimo tarybos posėdyje 2022 m. spalio mėn. 7 d. 14:00 val. Vilniaus universiteto Fizikos fakulteto Didžiojoje fizikos auditorijoje.

Adresas: Saulėtekio al. 9, Vilniaus universiteto Fizikos fakultetas, Didžioji fizikos auditorija, Vilnius, Lietuva.

Tel. (8 5) 236 6000; el. paštas: ff@ff.vu.lt

Disertaciją galima peržiūrėti Vilniaus universiteto bibliotekoje ir VU interneto svetainėje adresu: <https://www.vu.lt/naujienos/ivykiu-kalendorius>



## LIST OF ABBREVIATIONS

AT – ammono-thermal

CERN – European Organization for Nuclear Research (French: *Conseil européen pour la recherche nucléaire*)

ESR – electron spin resonance

FWHM – full width at half maximum

HD – heavy doping

HEP – high-energy physics

HVPE – hydride vapour phase epitaxy

IR – infrared

KTP – potassium titanyl phosphate

LD – low doping

MOCVD – metalorganic chemical vapour deposition

MW-PC – microwave probed photoconductivity

ODS – oriented dosimetry sensor

PAS – positron annihilation spectroscopy

PIL – proton-induced luminescence

PL – photoluminescence

PPIS – pulsed photo-ionization spectroscopy

RT – room temperature

SC – streak camera

SS-PL – steady-state photoluminescence

UV – ultraviolet

## TABLE OF CONTENTS

INTRODUCTION.....	7
LIST OF PUBLICATIONS.....	11
1. GENERAL PROPERTIES OF GaN .....	12
1.1 GaN fabricated using different technologies .....	13
1.2. Intrinsic defects .....	15
1.3. Radiation induced defects .....	16
2. DEFECT SPECTROSCOPY TECHNIQUES .....	17
2.1. Microwave-probed photoconductivity method .....	17
2.2. Technique of the steady-state photoluminescence spectroscopy .....	19
2.3. Technique of pulsed photo-ionization spectroscopy .....	21
2.4. Positron annihilation spectroscopy.....	23
2.5. Electron spin resonance spectroscopy .....	24
3. FINDINGS PRESENTED IN PUBLICATIONS.....	26
3.1. Properties and defects of pristine GaN.....	26
3.2 Defects and transformations of electrical and optical properties of GaN induced by neutron irradiation .....	36
3.3 Radiation sensors and dosimetry instruments created on the basis of the GaN related materials.....	43
CONCLUSIONS .....	54
BIBLIOGRAPHY .....	55
SANTRAUKA .....	60
CURRICULUM VITAE .....	69
COPIES OF PUBLICATIONS .....	70

# INTRODUCTION

## Research problem

Modern microelectronics, nanoelectronics and optoelectronics make widespread use of wide band-gap semiconductors, which, due to their electrical, optical and mechanical properties, are promising materials for production of optoelectronic, high power and high frequency devices addressed to applications in medicine, telecommunication and radiation monitoring equipment [1]. Ionizing radiation (depending on the type and energy) can introduce defects to the material [2], which results in changes of the operational characteristics of the gallium nitride (GaN) based devices. GaN is a wide band-gap semiconductor with a relatively large displacement energy. The displacement energy is an important parameter of material which determines its radiation hardness [3,4,5]. Thereby, GaN is a promising material in production of solar-blind photo-sensors and radiation tolerant, low-leakage current particle detectors. These properties of particle detectors are important, considering the applications in harsh radiation environments such as particle accelerator facilities for high-energy physics (HEP) experiments (e.g. European Center for Nuclear Research (CERN), Fermi National Laboratory (Fermilab), etc.). GaN, being the direct-bandgap semiconductor, exhibits efficient photoluminescence over a wide spectral range. This makes GaN a promising material for fabrication of double response (simultaneous electrical and scintillation) particle detectors.

Suitability of GaN materials for sensor formation depends on their fabrication technology, doping and compensation level. The main obstacle in these applications of GaN remains high density of intrinsic technological defects, such as dislocations with density of about  $10^9 \text{ cm}^{-2}$ . Nevertheless, technologies of GaN growth, such as Chemical Vapour Deposition (CVD), Metal Organic Chemical Vapour Deposition (MOCVD), Hydride Vapour Phase Epitaxy (HVPE), Ammono-Thermal (AT), are developed insufficiently to reliably govern the material and device quality. The high densities of the intrinsic point and extended defects determine a rich spectrum of deep levels by affecting carrier lifetime and by modifying electrical conductivity. To suppress the enhanced unintentional doping, fast recombination centers are commonly introduced by using the transitional metal impurities (such as Fe), to have a semi-insulating GaN material. There, doping of GaN with Mg and Mn can be efficient in formation of compensating, electrically and optically active, impurities. The doping technologies in formation of n-type GaN conductivity are developed to maturity technological level. However,

formation of p-type GaN material is problematic. Doping with carbon seems to be the most relevant way to have p-type GaN material with predictable electrical characteristics. However, this leads to the considerably shorter carrier lifetime, and increasing of the detector thickness to compensate that, for instance, becomes an improper mean for enhancing of an interaction path in particle detectors.

Introduction of the radiation defects during operation of particle sensors in harsh areas of particle accelerators considerably depends on pristine material, exploited for detector fabrication. Integral sensor damage by irradiations varies with thickness of sensors, depending on particle type and energy, due to different interaction cross-sections, and on penetration paths for incident radiations. To reduce radiation damage effect on detectors carrier lifetime, thin sensor structures with internal amplification can be promising for particle tracking. Thus, the high quality MOCVD GaN might be suitable for fabrication of such type sensors. In order to produce rather thick sensors for recording of the penetrative particles with small interaction cross-section, the amonothermally grown GaN with significantly reduced ( $<10^4 \text{ cm}^{-2}$ ) dislocation densities is the most promising material. Therefore, knowledge of the intrinsic and irradiation fluence dependent variations of the optical and electrical characteristics is important. However, production of defects by hadron irradiations, radiation hardness and charge collection efficiency of sensors fabricated on different technology GaN materials are examined insufficiently, as well as spectrum and origin of various species of electrically and optically active defects.

Capacitor-type particle detectors of high sensitivity can be manufactured using a high resistivity ( $\geq 10^6 \text{ }\Omega\text{cm}$ ) GaN [6]. Additionally, high resistivity of GaN is usually achieved by doping with impurities that form acceptor levels. The electrically active defects are also important in modification of polarization effects, inherent for GaN materials and related to piezo- and internal-displacement field properties. Therefore, it is very important to characterize pristine and irradiated materials by identifying defects and impurities as well as estimating their concentrations, in order to produce high-quality reliable devices and to predict the change of detector characteristics after irradiation. Thereby, spectroscopy of various species of defects raises a lot of complicated methodical problems.

The comprehensive study of electrical and optical characteristics, inherent for the pristine and radiation affected GaN, should be performed by combining different measurement techniques. The carrier recombination features can be examined by combining measurements of fluence dependent

variations of carrier lifetime, time integrated and time resolved photoluminescence (PL) spectroscopy. The electron spin resonance (ESR), infrared (IR) and ultraviolet-visible (UV-VIS) light transmission spectroscopy methods have been employed for identification of the grown-in and radiation induced defects. These techniques are valuable non-destructive tools to investigate the material properties. A few techniques have been applied in order to overcome the limitation of the aforementioned techniques, e.g. ESR allows the identification of the spin-active defects, while impurities with ionic character lead to strong IR absorption and bonds with covalent character lead to strong Raman absorption. The characteristics of the non-radiative recombination and trapping of carriers were investigated by the microwave-probed photoconductivity (MW-PC) method. The time integrated and time resolved PL measurements were employed to study the dynamics of different density carriers involved within radiative recombination processes before and after irradiations of GaN samples. The charge collection efficiency (CCE) characteristics were examined by inspection of current transients recorded on sensor structures. The CCE has been estimated from the reduction of the collected charge in sensors irradiated with different fluences. Variations of the ESR, IR and UV-VIS transmission spectra allowed for identification of the dominant intrinsic as well as radiation induced defects and their evolution due to irradiations. Most of the measurements were implemented at room temperature, which is essential for real applications of GaN sensors. It has been proved that AT GaN material is the most suitable for fabrication of rather thick particle detectors. The advanced or modified techniques were also developed to characterize more deeply the electrically and optically active defects in GaN materials, such as: microwave probed photoconductivity method (MW-PC), steady-state and time-resolved photoluminescence spectroscopy (SS-PL and TR-PL, respectively), pulsed photo-ionization spectroscopy (PPIS) and electron spin resonance spectroscopy (ESR). These techniques were employed to characterize the electrical and optical properties of different species of GaN materials (GaN:C, GaN:Fe, GaN:Mg, GaN:Mn) as well as aluminum gallium nitride (AlGaN) alloys with various Al concentrations.

#### Aim and novelty

The aim of this dissertation was to examine the defects, their electrical and optical activity as well as their transformations induced by radiation. Transformations of electrically active defects in GaN were traced in order to

apply this analysis in developing techniques for particle detection and dosimetry. To achieve this aim several objectives were set, as:

- Analysis of the optical and electrical properties of GaN materials before and after irradiation with different high energy particles in order to identify technological and radiation induced defects.
- Identification of technological and radiation induced defects in GaN materials grown using various technologies.
- Tracing of transformations of the electrically active defects after irradiation to acquire knowledge necessary for particle detection and dosimetry purposes using GaN materials.
- Formation of the prototypes of hybrid and triplex sensors, based on GaN materials, and development of techniques suitable for reading of these sensors.

#### Statements to be defended

1. The van Roosbroeck-Shockley approach is applicable to predict the Stokes shift between the absorption and emission spectra in GaN materials.

2. Combining of the photo-ionization, photoluminescence and positron annihilation techniques can be applied for tracing of the evolution of the radiation induced defects in GaN related materials.

3. Hadron introduced non-radiative and radiative recombination centers within GaN structures can be applied for creation of the double-response dosimetry sensors as well as the oriented triplex sensors for the remote identification of the location and dose-rate of harsh radiation sources.

4. The hybrid multi-layer sensor which comprises the scintillator layer made of GaN structure and a photoelectric-response layer made of high purity, large resistivity semiconductor, separated by the visible spectrum filtering, electric insulating and passivating layers, and which operates in pulsed as well as steady-state modes can serve for the contactless discrimination of particle species and particle energy values as well as for measurements of the large fluence dosimetry and fluxmetry.

## Contribution of the author

The majority of experimental measurements and simulations were performed by the author in collaboration with colleagues dr. T. Čeponis, dr. J. Pavlov and dr. V. Rumbauskas. Proton irradiation of the samples was performed in collaboration with dr. V. Kovalevskij. Neutron irradiation of the samples was performed at the Jožef Stefan institute (Ljubljana) TRIGA reactor. Electron and  $\gamma$ -ray irradiation of the samples was performed in collaboration with National Cancer Institute. Interpretation of the results was implemented together with the supervisor Prof. Habil. Dr. E. Gaubas.

## LIST OF PUBLICATIONS

### On the dissertation topic

- [A1] E. Gaubas, T. Čeponis, **L. Deveikis**, D. Meškauskaitė, J. Pavlov, V. Rumbauskas, M. Bockowski, B. Lucznik, Electrical characterization of HVPE GaN containing different concentrations of carbon dopants, *Semicond. Sci. Technol.* **33** (12) (2018) 125024. DOI:10.1088/1361-6641/aecf0
- [A2] E. Gaubas, P. Baronas, T. Čeponis, **L. Deveikis**, D. Dobrovolskas, E. Kuokštis, J. Mickevičius, V. Rumbauskas, M. Bockowski, M. Iwinska, T. Sochacki, Study of spectral and recombination characteristics of HVPE GaN grown on ammono substrates, *Mater. Sci. Semicond. Process* **91** (2019) 341-355. DOI:10.1016/j.mssp.2018.12.010
- [A3] E. Gaubas, T. Čeponis, **L. Deveikis**, D. Dobrovolskas, V. Rumbauskas, M. Viliunas, Room-temperature infrared photoluminescence in GaN doped with various impurities, *Opt. Mater.* **94** (2019) 266-271. DOI:10.1016/j.optmat.2019.05.054
- [A4] J. Pavlov, T. Čeponis, **L. Deveikis**, T. Heikkinen, J. Raisanen, V. Rumbauskas, G. Tamulaitis, F. Tuomisto, E. Gaubas, Spectroscopy of defects in neutron irradiated ammono-thermal GaN by combining photo-ionization, photoluminescence and positron annihilation techniques, *Lith. J. Phys.* **59** (4) (2019) 211-223. DOI:10.3952/physics.v59i4.4137
- [A5] T. Čeponis, K. Badokas, **L. Deveikis**, J. Pavlov, V. Rumbauskas, V. Kovalevskij, S. Stanionytė, G. Tamulaitis, E. Gaubas, Evolution of scintillation and electrical characteristics of AlGaIn double-response sensors during proton irradiation, *Sensors* **19** (15) (2019) 3388. DOI:10.3390/s19153388

- [A6] J. Pavlov, T. Čeponis, **L. Deveikis**, V. Rumbauskas, G. Tamulaitis, E. Gaubas, Modification of characteristics of AlGa<sub>N</sub> photodiodes by 1.6 MeV proton irradiation, *JINST* **15** (2020) C01026. DOI:10.1088/1748-0221/15/01/C01026
- [A7] **L. Deveikis**, J. V. Vaitkus, T. Čeponis, M. Gaspariūnas, V. Kovalevskij, V. Rumbauskas, E. Gaubas, Profiling of proton beams by fluence scanners, *Lith. J. Phys.* **61** (2) (2021) 75-83. DOI:10.3952/physics.v61i2.4436

#### Patents

- [P1] E. Gaubas, T. Čeponis, **L. Deveikis**, J. Pavlov, V. Rumbauskas, Hybrid multi-layer sensor and method for large fluence dosimetry and fluximetry, Application No. 21 165 145.0, submitted: 2021 03 26.
- [P2] E. Gaubas, T. Čeponis, **L. Deveikis**, J. Pavlov, V. Rumbauskas, Oriented triplex sensor and method of identification of the radiation source location and its dosimetry, Application No. EP22171639.2, submitted: 2022 05 04.

#### Conference presentations

- [C1] **L. Deveikis**, T. Čeponis, E. Gaubas, D. Meškauskaitė, J. Pavlov, V. Rumbauskas, Comparative analysis of recombination characteristics and photo-ionization spectra in reactor neutrons irradiated GaN, Open Readings 2018, Vilnius, 2018.
- [C2] **L. Deveikis**, T. Čeponis, E. Gaubas, Spectral characterisation of gallium nitride materials applicable for radiation detectors, Open Readings 2019, Vilnius, 2019.
- [C3] **L. Deveikis**, T. Čeponis, E. Gaubas, Study of electrical and optical characteristics of SiGe and CdZnTe materials applicable to radiation detection, Open Readings 2021, Vilnius, 2021.

## 1. GENERAL PROPERTIES OF GaN

GaN is one of the most promising materials for fabrication of radiation hard particle detectors for future collider facilities. This material exhibit superior electric properties, such as high breakdown field, high electron saturation velocity, high threshold displacement energy, compared to, for example, most widely nowadays used semiconductor - silicon (Si) [7]. The



bandgap of GaN can also be modified by making alloys with other elements, e.g. AlGaN with a wider bandgap which value depends on the concentration of Al. These properties make GaN to be very perspective for fabrication of high power, high frequency and elevated temperature operating devices as well as in harsh radiation environment functioning devices. However, introduction of defects during crystal growth or operation in harsh radiation environment is inevitable, and these defects can play a vital role in predetermination of electrical and optical properties of the material [2]. Some impurities may even be introduced into the crystal lattice intentionally to modify the important properties in favourable ways (e.g.: impurities forming acceptor levels can be added during crystal growth to increase GaN resistivity). Therefore, identification of defects and impurities introduced either during crystal growth or by radiation, and clarification of their impact on material properties is essentially important.

### 1.1 GaN fabricated using different technologies

GaN is a wide direct-bandgap (3.4 eV at room temperature) III-V group semiconductor. It crystallizes in either wurtzite or zinc-blende crystal structures, which are two polytypes of the same material and have similar crystallographic structure (Fig 1.1.1.).

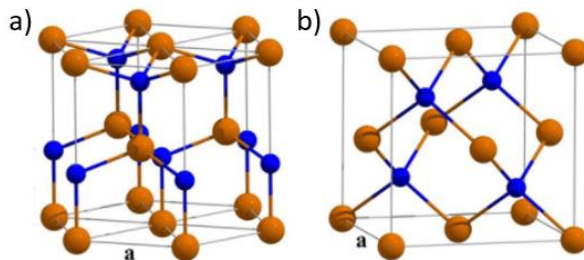


Fig 1.1.1. Crystal lattice structure of wurtzite (a) and zinc-blende (b) GaN configurations [8].

MOCVD is a widely used crystal growth technology in fabrication of III-V group semiconductors. Due to high precision of layer thickness formation, this method is preferable in growth of thin layers of material. The layer thickness is controlled by changing some of the process parameters, such as pressure, temperature, etc. The process starts by injection of the ultrapure precursor gases into a reactor. For an III-V semiconductor, such as GaN, a metalorganic compound can be used as the group III precursor, and a hydride

serves as a group V precursor. As the precursors approach the semiconductor wafer, they undergo pyrolysis and the subspecies are absorbed onto the semiconductor wafer surface. Surface subspecies result the incorporation of the relevant elements into a growing epitaxial layer of the semiconductor crystal lattice [9]. The quality of the crystal highly depends on precursors and substrates that are used within material processing. However, introduction of the impurities from the precursors is unavoidable. Carbon and oxygen are considered as the most important impurities in MOCVD grown GaN. Either sapphire or silicon is often used as the substrate material in growth of GaN epitaxial layers, due to their relatively low cost. However, lattice mismatch is inevitable problem in this case, which causes appearance of defects, such as dislocated regions within a few hundred nanometers near the interface [10]. To minimize the strain of the GaN epi-layers and substrate lattices, a buffer layer of AlN is often fabricated to absorb the strain which appears during crystal growth [11].

In order to form thick GaN crystals, the HVPE technology is used owing to high growth rate (100 - 500  $\mu\text{m}/\text{hour}$ ) [12]. The hydrogen chloride is reacted with the group-III metals during the HVPE process carried out at elevated temperature in order to produce gaseous metal chlorides, which then react with ammonia to produce the group-III nitrides. The predominant impurity introduced to the crystal during HVPE growth is oxygen [13], which often occupies nitrogen sites. HVPE technology can significantly reduce the cost of production compared to the MOCVD technique. The main issue of this technology, similarly to MOCVD, is crystal lattice mismatch with the lattice of the substrate. The HVPE technology can be combined with other crystal growth methods, e.g. using thin initial layer of GaN grown by MOCVD while growth of bulk crystal is proceeded by HVPE technique. The quality of the crystal can also be improved by growing a low-temperature GaN buffer layer, which is addressed to reduce the propagation of dislocations from the interface of GaN crystal and the substrate [14].

AT technique is used to grow multiple GaN crystals at once. The AT growth rate is around 10 times slower than that of the HVPE method, although it is possible to grow hundreds of crystals simultaneously, so AT method is applicable for mass production. During AT growth process, a source of GaN is placed in a lower temperature zone of an autoclave. There, GaN source is melted. Ammonia gas then transports GaN to the higher temperature zone of the autoclave, where GaN crystallizes on the seeds of the crystal. In order to increase GaN solubility in the ammonia, catalysts, such as  $\text{LiNH}_2$ ,  $\text{NaNH}_2$  or  $\text{KNH}_2$  are involved. Parameters of temperature and pressure of the AT process are 500 – 600  $^\circ\text{C}$  and 0.2 – 0.5 GPa respectively [15].

## 1.2. Intrinsic defects

Defects that are introduced into the crystal during the growth process can be classified according to their dimensions:

- Point defects – zero-dimension defects in a crystal structure related to a single atomic site, e.g. vacancies, interstitial or substitutional atoms.
- One-dimensional or line defects – lines along which complete rows of atoms in the crystal are arranged anomalously, e.g. forming dislocations.
- Two-dimensional or planar defects – discontinuities of crystal structure across a plane – normally separate regions of the material that have different crystal structures and/or crystallographic orientations.
- Three-dimensional defects – discontinuities of crystal structure that spans across volume, e.g.: cracks, nanotubes, precipitates.

Point defects are usually introduced into the crystal by either crystal growth or radiation damage. The vibrations of the crystal lattice can cause point defects to migrate within the crystal. Examples of point defects (substitutional impurity atom (1), interstitial impurity atom (2), interstitial host atom (3), vacancy (4)) are illustrated in Fig. 1.2.1.

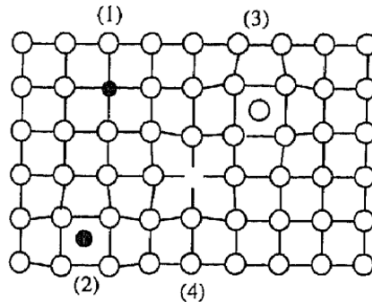


Fig. 1.2.1. Examples of point defects: substitutional impurity atom (1), interstitial impurity atom (2), interstitial host atom (3), vacancy (4).

Bulk defects are formed when the macroscopic areas of different crystal phases or dislocations are introduced to the crystal. Examples of such defects (dislocations (5)-(6), precipitate (7)) are illustrated in Fig. 1.2.2.

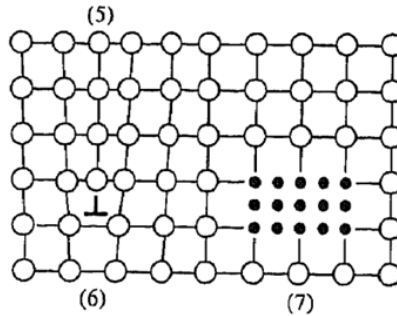


Fig. 1.2.2. Examples of bulk defects: dislocations (5)-(6), precipitate (7).

Types of predominant defects in the crystal strongly depend on the growth process parameters. Most common point defects in GaN crystals are nitrogen and gallium vacancies ( $V_N$  and  $V_{Ga}$  respectively) [16], due to their low formation energy.  $V_N$  vacancies are abundant in *p*-type GaN, while  $V_{Ga}$  prevail in *n*-type GaN. These two types of vacancies together can form a divacancy ( $V_N V_{Ga}$ ) with either donor or acceptor energy level in the bandgap. However, high concentrations of this defect complex in the crystals are rare, due to relatively high formation energy. Large concentrations of Ga and N interstitials ( $Ga_i$ ,  $N_i$ ) and substitutional ( $Ga_N$ ,  $N_{Ga}$ ) atoms are also rarely observed in crystals because of relatively high formation energy, due to small GaN crystal lattice constant and difference in the size of Ga and N atoms [16,17]. However, irradiation by high energy particles might introduce defects to the crystal even of high formation energy.

### 1.3. Radiation induced defects

There are two main types of radiation induced damage of materials:

- Ionization damage takes place through photoelectric effect, Compton effect or formation of charge carrier pairs;
- Radiation damage through kick-out of atoms from their sites resulting in simultaneous formation of vacancies and interstitial atoms (Frenkel-pairs).

Primary radiation induced defects are highly mobile at room-temperature and can migrate over definite distances through the crystal. They can either annihilate by vacancy-interstitial recombination or accumulate at the crystal surfaces. Alternatively, primary defects can cause secondary defects to form. Interstitials can accumulate in the bulk of the material to form extrinsic stacking faults. Accumulation of vacancies leads to a production of voids. However, the impurity atoms commonly trap the migrating vacancies and

interstitials, thereby forming stable defects or defect complexes [18]. Electron and gamma irradiations usually introduce point defects, while proton and neutron irradiations can cause formation of clusters of defects, due to larger interaction cross-section.

One of the most important parameters that describe materials radiation hardness is the threshold energy of atomic displacement. This is the kinetic energy of an incident particle required to remove an atom from its crystal lattice site, forming a stable defect. The threshold displacement energy is not isotropic and can depend on the crystal orientation. The average threshold displacement energies of GaN lattice atoms are determined to be 73.2 and 32.4 eV for gallium and nitrogen atoms, respectively [19].

## 2. DEFECT SPECTROSCOPY TECHNIQUES

### 2.1. Microwave-probed photoconductivity method

One of the most effective methods to consider the recombination processes in the material is the measurement and analysis of charge carrier lifetime [20]. The microwave probed photoconductivity (MW-PC) response, proportional to the concentration of the excess carriers ( $n(t)$ ), is recorded under excitation of excess carriers within bulk of the sample by using pulsed laser ( $\lambda = 1064$  nm) beam. Carrier lifetime is determined by analyzing the slope of the carrier decay transient.

Crystal defects can act as recombination (deep energy levels) or trapping (relatively shallow energy levels) centers. The single exponential decay is observed when a single type recombination centers prevail. Values of carrier lifetime are extracted using a definition of the instantaneous lifetime  $\tau_{inst} = n(t)/(-\partial n(t)/\partial t)$  [20]. However, non-exponential decay appears in the cases either of non-linear recombination processes or competition of multiple recombination and trapping centers. The fast recombination processes are inherent in materials containing high concentration of recombination centers. High concentration of trapping centers acting together with recombination ones determines two-compartmental decay transients with delayed asymptotic component. The surface recombination also leads to non-exponential decay process, and it governs the initial decay component and values of the effective lifetime of the asymptotic process. Surface recombination appears to be the most pronounced for non-passivated samples.

The experimental arrangement employed for recording of the microwave-probed photoconductivity transients in this work is illustrated in Fig. 2.1.1.

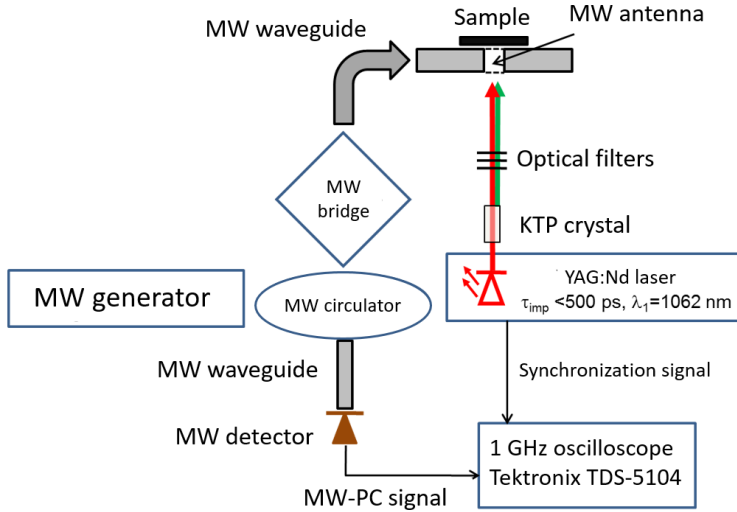


Fig. 2.1.1. Layout of measurement setup for the microwave-probed photoconductivity transients [20].

20-22 GHz microwaves (MW) serve as a photoconductivity probe source. MW are radiated on the sample through the slit or needle-tip resonant antenna. The MW generator and receiver are disjoined by the circulator, while signal coming to the MW detector is controlled by the MW-bridge system. The pulsed radiation of the microchip solid state Nd:YAG laser with discrete wavelength  $\lambda$  of 1062 nm and its second (generated using KTP crystals) or third harmonics are used for excess carrier generation. The MW probe integrates the MW-PC response from the laser excited volume. The photo-generated carrier concentration ( $\Delta n$ ) is evaluated by calibration measurements. The absolute MW-PC signal  $U_{MW}$  values are recorded by a digital oscilloscope where MW response is proportional to the excess carriers concentration. The relaxation curve of the MW reflection modulation by MW-PC process has, as usually, two characteristic parts: a transient non-exponential part and a quasi-exponential asymptotic part, when surface recombination prevails. For irradiated samples, the recombination lifetime is significantly shorter than the characteristic time of the transient component in the surface-recombination-governed carrier decay. The initial component is exponential in radiation-defect containing samples, and it can be definitely attributed to radiation-induced recombination centers. The transient and

asymptotic decay curve components may be significantly modified by carrier trapping effects.

## 2.2. Technique of the steady-state photoluminescence spectroscopy

Photoluminescence (PL) spectroscopy is widely used for qualitative characterization of energy levels in the bandgap ascribed to point defects. The PL spectroscopy is also an efficient technique in analysis of concentration and transformation of electrically active defects induced by irradiation. The PL techniques are most relevant for defect characterization in the direct bandgap materials where radiative recombination is efficient.

The electron transitions from the ground to the excited state are induced by illumination with photons of energy higher than the bandgap of the material - for excitation of PL in GaN an UV laser is commonly used. Various types of radiative recombination occur when electrons relax to the ground state by emitting photons. Such transitions may include inter-band recombination and trap-assisted electron transitions either from the bottom of the conduction band to the neutral acceptor state or via transitions of electrons trapped on donor state to a hole state on the top of the valence band. Also, the donor-acceptor recombination can be observed through transitions of carriers trapped on local centers. Some optical transitions inherent for the defect associated luminescence in GaN are illustrated in Fig. 2.2.1. The transitions involved into radiative recombination of GaN and deep levels within the bandgap attributed to defect levels, sketched in Fig. 2.2.1., had been reviewed in Ref. [16].

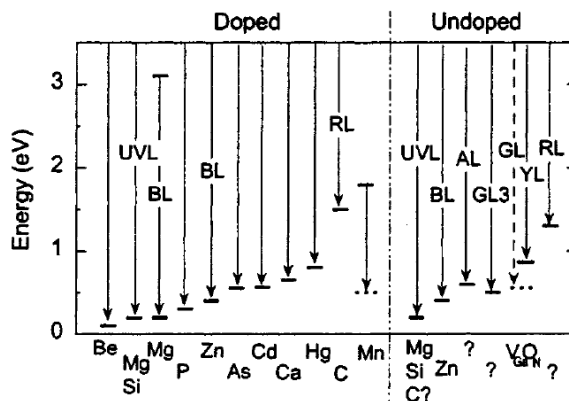


Fig. 2.2.1. Radiative recombination transitions associated with dopant impurities and unintentionally introduced defects in GaN [16].

Arrangement of the PL spectra measurement setup employed in this work is illustrated in Fig. 2.2.2.

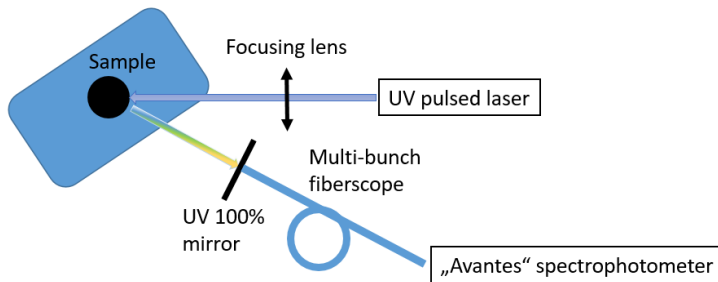


Fig. 2.2.2. A setup of the PL spectra measurement.

The radiative centers are responsible for PL in direct band-gap materials. The non-linearity of radiative recombination caused by band-to-band and through deep levels transitions is usually observed. The rate of radiative recombination through inter-trap transitions depends on carrier densities controlled by non-radiative recombination. The inhomogeneity and non-locality of distributions of different radiative traps and of non-radiative recombination centers require simultaneous measurements of signals collected from the same area of the material. The transient signals of the MW-PC, which displays non-radiative recombination transients and of time-resolved photoluminescence (TR-PL) can be simultaneously measured. The steady-state luminescence spectroscopy is employed in analysis of concentration changes of radiation induced and transformed radiative recombination centers. Both the MW-PC and TR-PL transient signals, generated by the same UV (354 nm) beam spot of a pulsed (400 ps) laser, are displayed by a real-time digital oscilloscope. Variations of the SS-PL intensity ascribed to various spectral bands are registered by spectrophotometer, as illustrated in Fig. 2.2.2. The linearity of the PL response is commonly verified by calibration measurements. The PL light is collected from the area with normal directed towards a bisector between the incident and the reflected UV light beams (Fig. 2.2.2.). The UV filtered PL light is focused to a multi-bunch fiberscope. The PL light is dispersed using a grating monochromator "Avantes".



### 2.3. Technique of pulsed photo-ionization spectroscopy

Pulsed photo-ionization spectroscopy (PPIS) is a contactless technique used to analyze the parameters of deep energy levels related to defects. PPI spectra are recorded by registering variations of the MW-PC amplitudes when the energy of excitation photons is scanned over rather wide spectral range. A spectral step appears in the PPI spectrum when the photon energy ( $\hbar\nu$ ) matches the energy between electron ground state and that of a deep level associated with a defect. Information about activation energy of these resonant levels and photon-electron interaction cross-sections ascribed to these defects is acquired by modelling these spectral steps. A few models had been developed to describe the PPI spectra:

- Lucovsky model [21] describes the spectral characteristic of the electron-photon interaction ignoring an impact of phonons. Thereby, it can be applied for analysis of the photo-ionisation spectra measured at low temperatures. Lucovsky model relates the cross-section of photon-electron interaction to the activation energy  $E_{abs}$  of the defect as:

$$\sigma_{ph-e}(\hbar\nu) \propto AE_{abs}^{1/2} (\hbar\nu - E_{abs})^{3/2} / (\hbar\nu)^3, \quad (2.1)$$

where  $\sigma_{ph-e}$  is the photon-electron interaction cross-section,  $E_{abs}$  is the defect activation energy concerning an optical transition,  $A$  is coefficient specific to the concentration of each level.

- Kopylov-Pikhtin model [22] describes the electron-photon interaction cross-section with electron-phonon interplay taken into account. There, the activation energy of the specific defect is evaluated using the integral relation:

$$\sigma_{ph-e}(\hbar\nu) \propto \int_0^\infty \frac{e^{-(E+E_{abs}-\hbar\nu)^2/\Gamma^2} \sqrt{E} dE}{\hbar\nu(E+E_{abs})^2}. \quad (2.2)$$

The integral is taken over all the states  $E$  in conduction band. The broadening parameter  $\Gamma$  is expressed as:  $\Gamma = \sqrt{2S} \nu_0 \sqrt{2 \coth(\hbar\nu_0/k_B T)}$ . Here  $S$  is the Huang-Rhys factor which quantifies the number of phonons generated during an optical electron transition.

Layout of the PPIS measurement setup is illustrated in Fig. 2.3.1.

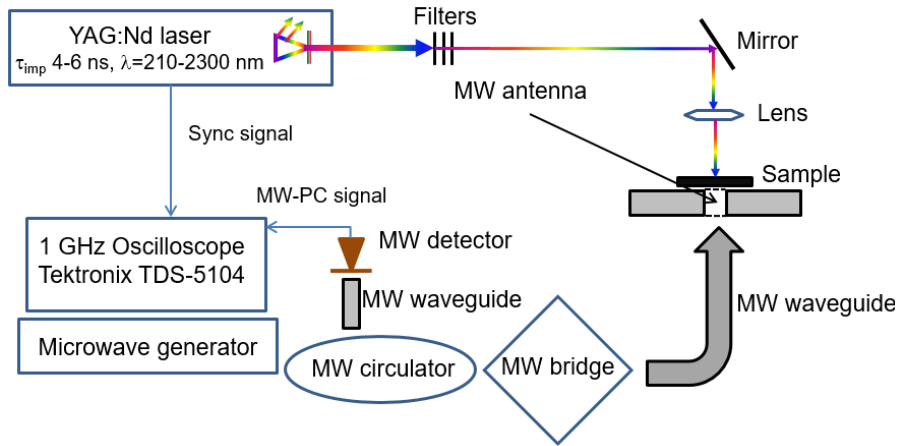


Fig. 2.3.1. Layout of the PPIS measurement setup.

The PPI technique can be efficient for spectroscopy of deep levels when several defect centers are inherent in the material, and it is beneficial relative to the steady-state current measurements, as the recorded MW-PC signal is clearly resolved and synchronized with photo-excitation pulse and needs no subtraction procedure for elimination of the dark current. Additionally, this technique is contactless. Photo-ionization or photo-neutralization of deep levels is characterized by the optical cross-section, and spectroscopy of these cross-sections provides direct information concerning the matrix elements coupling the wave functions of deep levels to the wave functions of band free carriers. Several light sources can be combined to implement a pulsed excitation of photo-response in the range of 0.2 to 2.3  $\mu\text{m}$  wavelength. The excitation pulse durations are fixed to  $\sim 5$  ns by an optical parametric oscillator coupled with differential frequency generators. To estimate the absolute values of the absorption coefficient independently, additional optical transmission measurements are performed. The peak amplitudes and carrier decay transients are simultaneously recorded by a 1 GHz digital oscilloscope TDS-5104. For an excitation pulse with duration  $\tau_L$  significantly shorter than the recombination lifetime  $\tau_R$ , the signal amplitude of a MW-PC ( $U_{MW-PC}$ ) at  $t=0$ , is a direct measure of the intensity of the photo-ionization of the deep levels below the Fermi energy. The PPI spectral steps are observed. A step occurs due to the spectral variation of the cross-section  $\sigma$  of the photon-electron coupling associated with a deep level. The cross-section is estimated by fitting the experimental spectrum. Each step in the PPI spectrum, which is identified by a measured change of  $U_{MW-PC}$ , is simulated by fitting both the shape and the amplitude of the step. The absolute values of the photo-ionization cross-section can also be estimated by correlating the measured

photo-conductivity spectrum with the absorption coefficient variation as available in literature.

## 2.4. Positron annihilation spectroscopy

Positron Annihilation Spectroscopy (PAS) is based on recording of gamma ( $\gamma$ ) rays emerging from the process of annihilation of positrons and electrons. It can be used to examine defects in semiconductors without any special test structures, is independent of sample conductivity and is non-destructive [23]. A positron is a stable particle itself, but when it is combined with an electron, they annihilate each other with the mass of the positron-electron pair converted into energy, i.e.  $\gamma$ -rays (Fig. 2.4.1.).

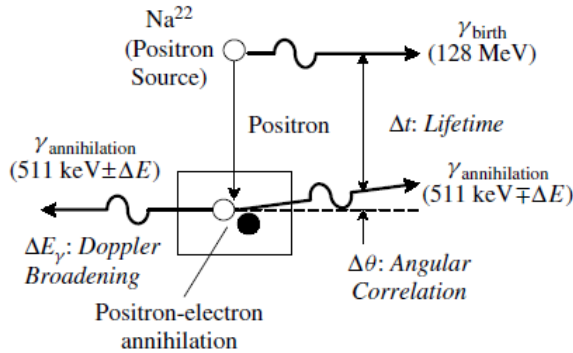


Fig. 2.4.1. Schematic illustration of positron annihilation showing positron creation, positron-electron annihilation,  $\gamma$ -ray emission and the three main experimental techniques for PAS [24].

The energy and momentum conservation during the annihilation of electrons with positrons provides information about the crystal, which is being examined, as the parameters of the annihilation are related to imperfections (mainly due to crystal voids where annihilation is suppressed due to low concentration of electrons) of the lattice. The positron may be trapped in crystal defects, based on the formation of an attractive potential at open-volume defects, such as vacancies, vacancy agglomerates and dislocations. When a positron is trapped in an open-volume defect, the annihilation parameters are changed in a characteristic way. Its lifetime increases due to the lower electron density and momentum conservation leads to a small angular spread of the collinear  $\gamma$ -quanta or a Doppler shift of the annihilation energy [24]. The most probable decay of the positron-electron annihilation decay is by the emission of two  $\gamma$ -rays of opposite directions that slightly deviates from  $180^\circ$ , with the angular deviation  $\Delta\theta$  which depends on the

component of electron momentum that is perpendicular to the emission direction,  $p_{\text{perp}}$ . The difference of energy between each  $\gamma$ -ray,  $\Delta E_\gamma$ , is related to the electron momentum component that is parallel to the emission direction –  $p_{\text{par}}$ . The parameters  $\Delta\theta$  and  $\Delta E_\gamma$  are expressed:

$$\Delta\theta = p_{\text{perp}}/mc \quad (2.3)$$

and

$$\Delta E_\gamma = p_{\text{par}}c/2, \quad (2.4)$$

where  $m$  is the electron mass and  $c$  is the speed of light. These two ( $\Delta\theta$  and  $\Delta E_\gamma$ ) parameters along with the time of emission of aforementioned  $\gamma$ -rays provide the information about the behavior of annihilation and the material where they annihilate [24].

The pristine and neutron irradiated samples were examined at room temperature, using a digital positron lifetime spectrometer with a Gaussian time resolution of 250 ps. Two identical pristine samples were sandwiched together with foiled 1.5  $\mu\text{m}$  thick  $\text{Al}^{22}\text{Na}$   $\mu\text{Ci}$  positron source. To have the PAS spectrum, the positron lifetime records of  $10^6$  positron annihilation (PA) events were collected. The PAS measurements for irradiated samples were made using the same source, but with a different sandwich-structure (the source between the pristine and irradiated sample). The  $2 \times 10^6$  events were accumulated to record a PA spectrum. The spectrum of the positron decay  $P(t)$  (after subtracting the constant background) due to annihilations in the source material (Al foil 210-215 ns, NaCl 400 ns, and positronium 1500 ns), was analysed assuming the sum of the exponential components:

$$P(t) = \sum_i I_i e^{-\frac{t}{\tau_i}}, \quad (2.5)$$

where positrons in state  $i$  annihilate with a lifetime  $\tau_i$  and intensity  $I_i$ . The increase of the average lifetime  $\tau_{\text{ave}} = \sum_i \exp(-t/\tau_i)t_i$  above the bulk lattice lifetime  $\tau_b$  indicates that positrons annihilate as trapped at vacancy defects, and these parameters are extracted using PA spectrum. The  $\tau_b$  parameter is the positron lifetime in the delocalized state in the lattice, while  $\tau_v$  is the lifetime component that gives directly the vacancy-specific lifetime. Because the electron density at a vacancy is lower than that within bulk, the lifetime  $\tau_v$  is always longer than the bulk lifetime  $\tau_b$ .

## 2.5. Electron spin resonance spectroscopy

The ESR spectroscopy is based on Zeeman effect, i.e. on splitting of the unpaired electron energy levels when material is inside of a magnetic field  $B_0$  [25]. Because the electron has a magnetic moment, it will have a state of lowest energy when the moment of the electron is aligned with the magnetic

field and a state of highest energy when the moment is aligned against the magnetic field. The two states are labelled by the projection of the electron spin,  $M_s$ , on the direction of the magnetic field. Because electron is a spin 1/2 particle, the parallel state is designated as  $M_s = -1/2$  and the anti-parallel state is  $M_s = +1/2$ . The energies of these two states are expressed:

$$E = g\mu_B B_0 M_s = \pm \frac{1}{2} g\mu_B B_0, \quad (2.6)$$

Here,  $g$  denotes the g-factor which is a characteristic property of every molecule or paramagnetic center and varies, depending on the electronic configurations of the system;  $\mu_B$  is the Bohr magneton, which is the natural unit of electronic magnetic moment ( $\mu_B = |e\hbar/4\pi m_e = 9.2741 \cdot 10^{-24} \text{ JT}^{-1}$ ). Thus the difference between the two electron energy levels in the magnetic field is expressed, as

$$\Delta E = g\mu_B B_0. \quad (2.7)$$

From this equation it is apparent that the energy of the spin states diverges linearly as the magnetic field increases (Fig. 2.5.1.). A photon of the energy  $\Delta E$  is observed as the electron transfers to the higher energy state.

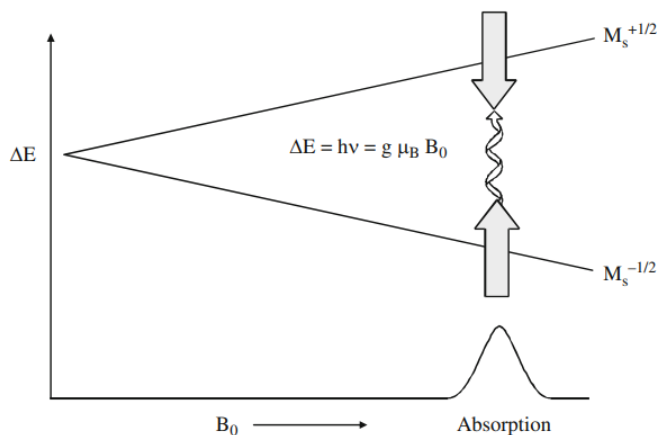


Fig. 2.5.1. The energies of the two spin states of an unpaired electron diverge when the magnetic field is scanned. There the resonance appears in absorption of MW energy by the spins [25], at the magnetic field for which the energy difference between the two electron spin states is equal  $h\nu$ .

In the ESR experiment the magnetic field is scanned and the frequency of MW radiation is kept constant. A peak in the absorption occurs when the magnetic field tunes the two spin states so that their energy difference matches the energy of the radiation. This is called “the field for resonance”.

The value of the field resonance should be supplemented by g-factor values

$$g = h\nu/\mu_B B_0, \quad (2.8)$$

which are independent of the MW frequency, so g-factor is a better way to characterize ESR active centers.

The hyperfine interaction occurs when an unpaired electron resides in the vicinity of nuclei which has the uncompensated spins (i.e.  $I \neq 0$ ). In that case, the magnetic field  $B_0$  must be replaced by the effective magnetic field  $B_{\text{eff}}$ :

$$B_{\text{eff}} = B_0 + B_N, \quad (2.9)$$

where  $B_N$  is an induction of the magnetic field caused by neighbouring nuclei magnetic moments. For an electron interacting with a spin 1/2 nucleus, the ESR absorption signal splits into two signals, related to each  $B_N$ . As the number of nuclei gets larger, the number of resonances increases rapidly. The magnitude of  $B_N$ , and hence the splitting, depends on the type of nucleus, as well as on the electron spin density attributed to those nucleus [25].

### 3. FINDINGS PRESENTED IN PUBLICATIONS

#### 3.1. Properties and defects of pristine GaN

In this chapter, the results of articles [A1-A3], addressed to research of technological defects of GaN, are presented.

Spectral variations of the absorption coefficient ( $\alpha$ ) were extracted from the recorded spectra of optical transmission in HVPE grown and carbon doped GaN:C samples, containing a relatively low (LD) and high (HD) concentration of carbon dopants. The main spectral changes of  $\alpha$  appear in the 370–430 nm spectral range of wavelengths when comparing data for the HD materials relative to LD one (Fig. 3.1.1(a)). To highlight these differences, the spectra of the differential absorption coefficient  $\Delta\alpha = \alpha_{\text{HD}} - \alpha_{\text{LD}}$  were composed for HD1 and HD2 samples (Fig. 3.1.1(b)). The transmission of the rather thick (~400  $\mu\text{m}$ ) samples is drastically decreased with reduction of wavelength of the incident light, when approaching to an UV spectral range. Differential ( $\Delta\alpha$ ) absorption spectra exhibit a peak at  $h\nu = 3.30$  eV photon energy (upper scale in Fig. 3.1.1). The  $\Delta\alpha(h\nu)$  spectral peak at  $h\nu \approx 3.30$  eV is also reported for AT GaN:Mn sample [26]. This indicates that the spectral change of  $\Delta\alpha(h\nu)$  is caused by carbon impurities, while low carbon concentration  $<10^{17}$   $\text{cm}^{-3}$  [26] is inherent for LD sample. Seems, the sample HD1 contains the larger density of absorption active carbon centers, relative to that of HD2.

The absolute of  $\sigma|_{h\nu\approx 3.30\text{eV}} = 1.6\times 10^{-13}\text{ cm}^2$  of the capture cross-section ascribed to the peak of the differential absorption ( $h\nu = 3.3\text{ eV}$ ) was evaluated by calibrating the spectral irradiance of the Perkin-Elmer LAMBDA-1050 light source (halogen lamp). Here, the relations of  $\alpha_{h\nu\approx 3.30\text{eV}} = \sigma|_{h\nu\approx 3.30\text{eV}}\times n_{\text{ex}}|_{h\nu\approx 3.30\text{ eV}}$  with  $n_{\text{ex}}|_{h\nu\approx 3.30\text{eV}} = \alpha F|_{h\nu\approx 3.30\text{eV}}$  were exploited, where  $F|_{h\nu\approx 3.30\text{eV}}$  is the surface density of incident photons. This value of  $\sigma|_{h\nu\approx 3.30\text{eV}}$  was employed as a benchmark for making the absolute scale of values of the cross-sections for the photon-electron coupling.

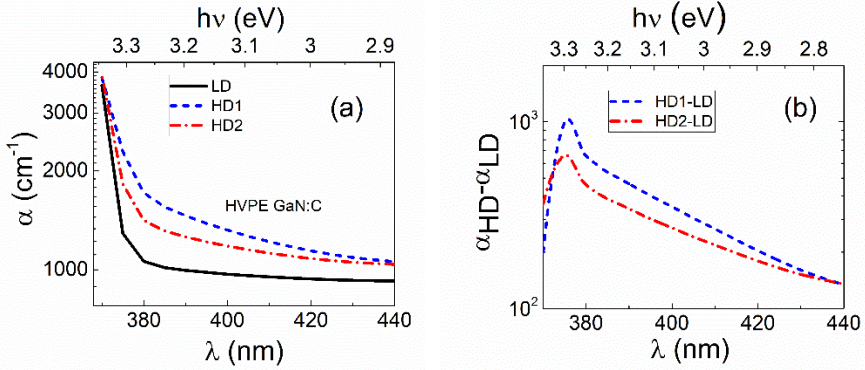


Fig. 3.1.1. (a) - absorption coefficient as a function of wavelength obtained for HVPE GaN:C samples. (b) - differential ( $\alpha_{\text{HD}} - \alpha_{\text{LD}}$ ) spectra of the absorption coefficient composed for the heavily C doped samples relative to that of lightly doped sample.

The efficiency  $\varepsilon = N_{\text{C,A}}/N_{\text{D}}$  of carbon impurities as the compensation centers introduced with large concentrations of  $N_{\text{C}}$  was evaluated from the differential absorption as,  $\Delta\alpha_{h\nu\approx 3.30\text{eV}} = \varepsilon \times \sigma|_{h\nu\approx 3.30\text{eV}} \times (N_{\text{HD}} - N_{\text{LD}})$ . The estimated values of  $\varepsilon \sim 10^{-2}$  show a reduction of compensation efficiency at large concentrations of introduced carbon. This can be caused by clustering of the carbon impurities introduced with high densities of carbon dopants.

The PL spectra recorded using the steady-state UV excitation mode are illustrated in Fig. 3.1.2. These spectra exhibit the prevailing of yellow (Y) PL spectral band, peaked at  $\sim 2.2\text{ eV}$ . The PL intensity is observed to be larger for the LD sample compared to that of HD samples in both the Y and UV spectral bands, exhibiting the small intensity spectral shoulders at 3.3 eV, 3.35 eV and a peak at 3.4 eV (Fig. 3.1.2(a)). However, it has been obtained that the absolute values of PL intensity depend on the wafer side (surface) which is excited by the continuous laser beam, when comparing Figs. 3.1.2(a) and 3.1.2(b). This difference can be caused by carbon doping profile, gradients of other impurity concentration, and asymmetry of the surface recombination velocity.

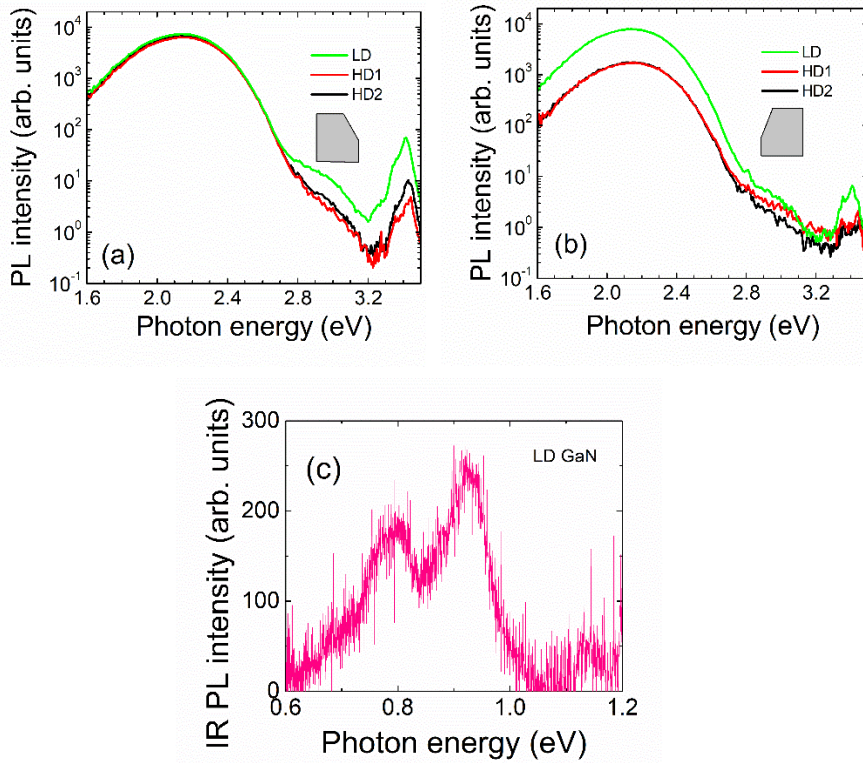


Fig. 3.1.2. SS-PL spectra obtained on HVPE GaN:C samples by exciting the opposite wafer surfaces (Fig. (a) and Fig. (b), which can be resolved using wafer off-cut orientation in figure legends). (c) – SS-PL spectrum obtained for the infrared spectral range of LD sample.

The re-absorption of the PL light, peaked at 3.3 eV (Fig. 3.1.1(b)), could be a reason for the observed reduction of PL intensity within blue (B)-UV PL spectral range. The clear variations of the intensity of B-UV PL, dependent on carbon doping, can be deduced from Fig. 3.1.2(a), where the lowest B-UV PL intensity is obtained for the HD1 sample. The excitation geometry, sketched in Fig. 3.1.2(a), might be ascribed to the surface of the lowest C doping, where Y luminescence intensity has been obtained nearly the same for all the examined samples. On the opposite surface containing the largest C concentration, the PL intensity difference obtained for the LD and HD samples becomes clear. The low intensity SS-PL spectrum (Fig. 3.1.2c) within infrared (IR) range was also recorded to verify the predicted conversion of the PPI spectrum into PL.

The temporal evolution of PL signals was researched by employing the streak-camera (SC) technique, which, however, leads to a necessity of



elevated excitation intensities (with  $n_{ex} \geq 10^{18} \text{ cm}^{-3}$ ). The SC recordable PL signals were only obtained within green-yellow-red (G-Y-R) PL spectral range (Fig. 3.1.3). These PL spectra, obtained at fixed UV energy density per 200 fs pulse, are illustrated in Fig. 3.1.3.

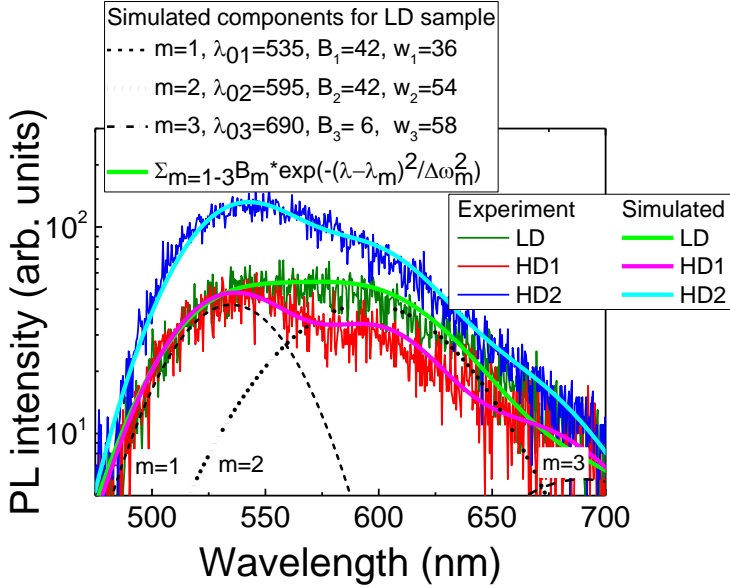


Fig. 3.1.3. The Streak-Camera recorded spectra on the HVPE GaN:C samples: as-recorded (noisy curves) and fitted (solid lines) using an approach of three ( $m=3$ ) Gaussian spectral bands. The simulated components of a PL spectrum (obtained for the LD sample) are illustrated by dotted curves:  $m = 1, 2, 3$ .

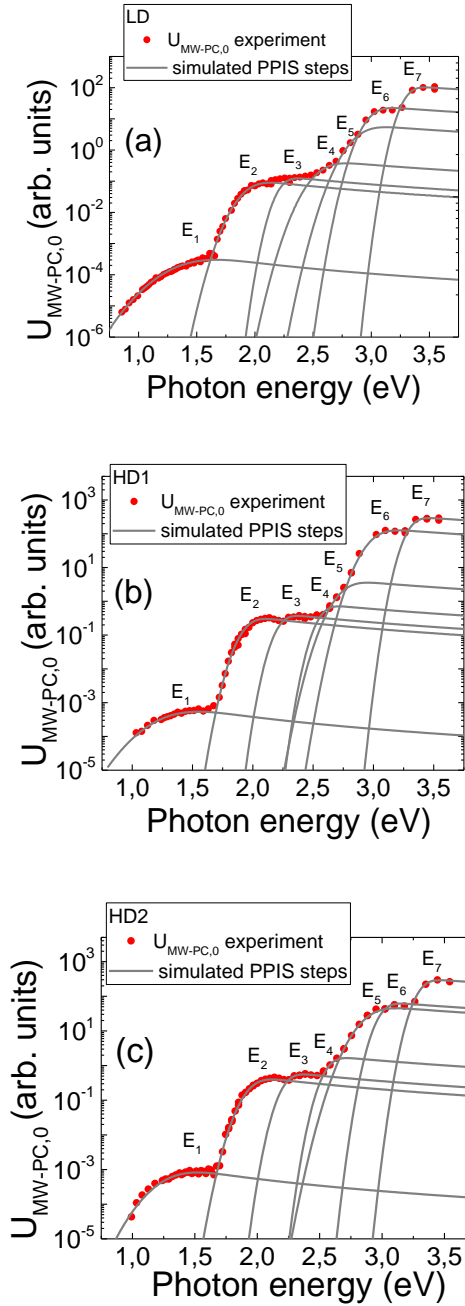
The asymmetric PL spectrum in the range of 450–700 nm wavelengths is observed. The nearly monotonous single-peaked (at 530 nm) band is inherent for the SC spectrum recorded on LD sample, while two-peaks (at 535 and 595 nm) can be resolved for HD samples. Actually, all of the the asymmetric PL spectral bands can be composed of several spectral components. These components, employed in fitting of the experimental (noisy curve) spectrum, are illustrated by thin dot lines in Fig. 3.1.3 for LD sample. There, the Gaussian-shape components, peaked at different wavelengths and having different relative peak-amplitudes ( $B$ ) as well as spectral-band widths ( $w$ ), have been employed to fit the recorded spectrum. The Gaussian line-shape is a rather good approximation, and this shape coincides with the real component of the line-shape approximation function, derived using a configuration

diagram approach [27,28]. To reproduce the asymmetry in simulated spectrum, three Gaussian components were needed. The simulated spectra (Fig. 3.1.3) are represented by thick solid lines. It can be deduced from Fig. 3.1.3, that the amplitude  $B_2$  of the  $m = 2$  spectral component is decreased for HD1 and HD2 samples relative to that for LD sample, while the spectral components peaked at  $\lambda_{01} = 535 \text{ nm}$  ( $\sim 2.3 \text{ eV}$ ) and  $\lambda_{02} = 595 \text{ nm}$  ( $\sim 2.1 \text{ eV}$ ) are of nearly the same intensity in LD sample. The band-width ( $w_1$ ) of the first simulated component  $m = 1$  is always narrower than that for  $m = 2$ , while band-widths of  $m = 2$  and  $m = 3$  components are close.

Variations of the PPI spectra recorded for carbon doped GaN samples are illustrated in Fig. 3.1.4.

The photon-electron coupling for carriers  $n_{f0}$  residing on a definite energy  $E_f$  level determines the values of an absorption coefficient  $\alpha(h\nu) = \sigma(h\nu)n_{f0}$  related to this level. The strength of the coupling is characterized by a spectrally varied cross-section  $\sigma_f(h\nu)$ . The density of photo-emitted carriers  $n_f^* = \alpha(h\nu)F(h\nu)$  determines the peak value ( $U_{\text{MW-PC},0} \sim n_f^* \sim \sigma_f(h\nu)$  (at  $t = 0$ ) of the  $U_{\text{MW-PC}}$  response for a fixed surface density  $F(h\nu) = \text{const.}$  of the incident photons. The surface density of the incident photons  $F(h\nu)$  is evaluated by calibration of the energy per pulse measurements within incident laser beam. The PPIS steps, recorded as  $U_{\text{MW-PC},0}(h\nu)$ , represent the spectral distribution of  $\sigma_f(h\nu)$ . The shape, determined by  $\sigma_f(h\nu)$ , of the spectral steps and spectral position, determined by  $E_f$ , ascribed to several  $f$  centers, serve for evaluation of the photo-activation energy and identification of the definite ( $f$ ) defects. PPI spectrum contains a few spectral steps. The relative concentrations  $N_f$  of different defects  $f$  can be roughly estimated by using a spectrum of an absorption coefficient  $\alpha(h\nu)$ , Fig. 3.1.1(a), independently measured on the same sample, and its correlation with  $\sigma(h\nu) \sim U_{\text{MW-PC},0}$ , as  $N_f(h\nu) = \alpha(h\nu)/\sigma_f(h\nu)$ . The density  $N_f$  of the  $f$  species centers coincides with a partial density of the equilibrium carriers  $n_{f0}$  if  $f$  traps are completely filled.

The Kopylov-Pikhtin [22] approach (Eq. (2.2)) has been applied for simulating of the  $U_{\text{MW-PC},0}(h\nu)$  steps in the experimental spectra implemented by varying  $E_f$  and  $\Gamma_f$  as free parameters, to get the best fit estimated by a non-linear least square method. The activation energies (with fitting uncertainties of about 5%) and  $\Gamma_f$  parameters of the predominant centers have been identified and listed in Table 3.1. The defects have tentatively been identified using the activation energy values taken from literature referenced. Up to seven centers ( $f = 1-7$ ) have been resolved in the examined samples.



3.1.4. PPI spectra recorded for different samples: LD (a), HD1 (b) and HD2 (c), respectively. Solid lines represent spectral steps simulated using Kopylov- Pikhtin (Eq. 2.2) model.

Table 3.1. Activation energy and broadening factor values estimated by fitting PPI spectral steps associated with different defects.

LD		HD1		HD2		Defect type
$E_f$ (eV)	$\Gamma_f$	$E_f$ (eV)	$\Gamma_f$	$E_f$ (eV)	$\Gamma_f$	
$E_1 = 1.4$	0.32	$E_1 = 1.3$	0.3	$E_1 = 1.3$	0.24	C <sub>1</sub> [29, 30]
$E_2 = 1.9$	0.16	$E_2 = 1.9$	0.12	$E_2 = 1.9$	0.13	C related [29]
$E_3 = 2.2$	0.1	$E_3 = 2.2$	0.1	$E_3 = 2.2$	0.1	V <sub>Ga</sub> [31]
$E_4 = 2.6$	0.17	$E_4 = 2.6$	0.1	$E_4 = 2.6$	0.1	V <sub>Ga</sub> [32]
$E_5 = 2.9$	0.17	$E_5 = 2.8$	0.15	$E_5 = 2.9$	0.17	C <sub>N</sub> <sup>-</sup> [33]
$E_6 = 3.0$	0.13	$E_6 = 3.0$	0.15	$E_6 = 3.0$	0.1	C related [29,30]
$E_7 = 3.3$	0.1	$E_7 = 3.3$	0.1	$E_7 = 3.3$	0.1	C <sub>N</sub> O <sub>N</sub> [33] or C <sub>N</sub> [29]

Separation of the PPI spectral steps has been made by controlling whether the same step appears in different samples of nearly the same technology material. For instance, the  $E_4$  PPIS step is doubtful for the HD1 sample while it is more clear for samples LD and HD2. Additionally, the presence of PPIS step has been corroborated by the consequent change of the MW-PC lifetime (Fig. 3.1.4(a)). Separation of the  $E_5$  and  $E_6$  PPIS steps has also been made by comparing the PPI spectra and MW-PC lifetime profiles (as a function of  $h\nu$ ) recorded for all the samples. However, values of the photo-activation energy of  $E_5$  and  $E_6$  PPIS steps are rather close, while this energy differs considerably when comparing simulation parameters for  $E_3$  and  $E_4$  PPIS steps.

The recorded seven deep photo-active centers with activation energies in the range of 1.3 – 3.3 eV are in-line with generally accepted opinion that AT and HVPE GaN materials contain a big nomenclature of point defects regardless of rather perfect crystalline structure relative to extended defects. The big amount of different species of defects complicates the analysis of a definite center. Therefore, the more general approach is necessary to fit spectra of conversion from absorption to light emission and vice versa. Such an approach can be based on van Roosbroeck - Shockley relation [34,35] between absorption and emission, derived using the condition of detail balance:

$$\Delta R_f(h\nu) = \frac{n_{ex,\Delta}(h\nu)}{\tau_{PL,\Delta}(h\nu)} = \rho_{f,PL} \left( \frac{h\nu}{k_B T} \right) \sigma_{f,PL} (h\nu/k_B T) N_d \frac{n_{ex,\Delta}(h\nu) N_d}{n_i^2}. \quad (3.1)$$

Here,  $n_i = 2 \times 10^{-10} \text{ cm}^{-3}$  is the intrinsic carrier concentration for GaN [36],  $k_B$  is the Boltzmann constant,  $h$  is Planck constant,  $\rho_a$  is the surface density of

photons ascribed to a unit frequency  $\nu$  within absorption spectrum for the spectral range  $\Delta(h\nu)$ , inherent to dedicated trap of concentration  $N_d$ ,  $n_{ex,\Delta(h\nu)}$  is the excess carrier density generated through photo-ionization in the definite spectral range  $\Delta(h\nu)$ , and  $\tau_{PL,\Delta(h\nu)}$  is the PL relaxation time. This approach enables simulation of the Stokes shifts between the outspread PPIS steps and the respective PL band peaks.

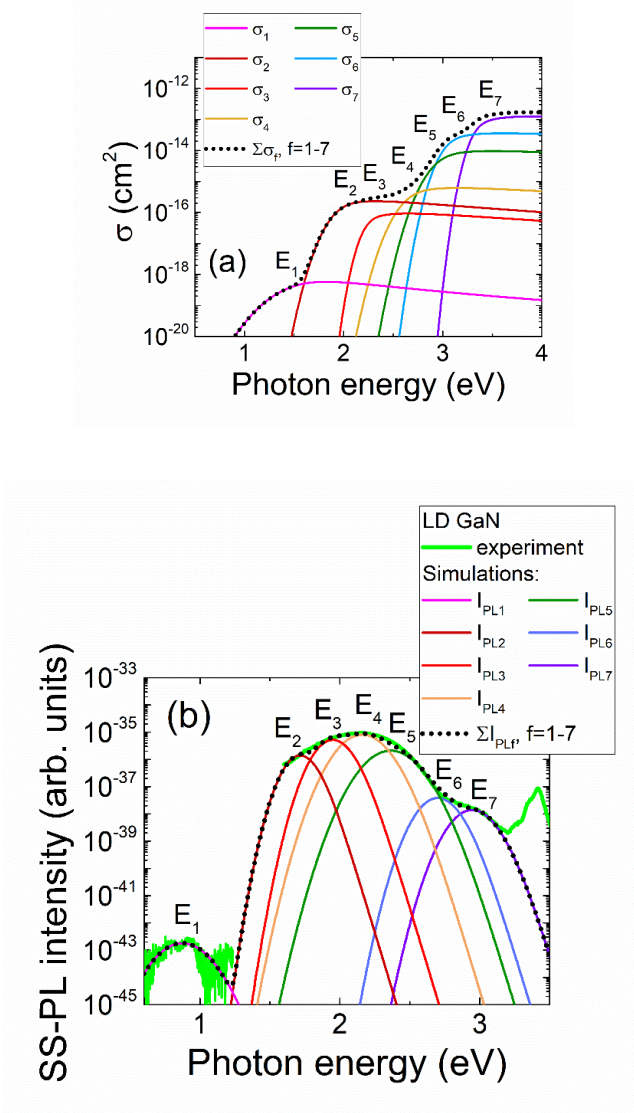


Fig. 3.1.5. Comparison of the simulated PPI (a) and PL (b) spectra using PPIS experimental data (listed in Table 3.1), extracted for the HVPE LD GaN:C material.

The correlation between the PPI and PL spectra can be simulated by using Eqs. (2.2, 3.1). To have the equality in relation of Eq. (2.2), the latter expression should be multiplied by the value of square of the matrix element ( $|M_{fk}|^2$ ) for the transition from level  $f$  to continuum ( $k$ ) [37]. The comparison of the simulated PPI and PL spectra is illustrated in Fig. 3.1.5. The PPI spectrum (Fig. 3.1.5(a)) has been simulated taking the extracted values of the cross-section of photon-electron coupling  $\sigma_f(h\nu)$  and of the photo-ionization energy  $E_f$  as well as broadening factors  $\Gamma_f$  for all ( $f = 1-7$ ) the separated photo-active centers (Table 3.1). As illustrated in Fig. 3.1.5 (for LD sample), a rather good quantitative fit of the simulated (using van Roosbroeck – Shockley relation) and experimental SS-PL spectra has been obtained.

The same approach was used in investigation of GaN samples grown with AT and HVPE techniques, doped with various dopants (magnesium (Mg), manganese (Mn), iron (Fe) and carbon (C)). Here, rather shallow photo-active traps were evaluated from PPI spectra (Table 3.2).

Table 3.2. Parameters of the rather shallow photo-active traps in HVPE and AT GaN processed by different technologies and evaluated by PPI spectroscopy.

HVPE GaN:C			HVPE GaN:Fe		
$E_d$ (eV)	$\Gamma_d$	Defect type	$E_d$ (eV)	$\Gamma_d$	Defect type
$E_{1C} = 1.4$	0.20	C <sub>1</sub> [29,30]	$E_{1Fe} = 0.6$	0.10	V <sub>Ga</sub> <sup>-</sup> [16]
$E_{2C} = 1.9$	0.13	C related [29]	$E_{2Fe} = 1.1$	0.06	N <sub>Ga</sub> [42]
$E_{3C} = 2.2$	0.10	V <sub>Ga</sub> [31]	$E_{3Fe} = 1.6$	0.13	Fe <sup>3+</sup> [43]
AT GaN:Mg			AT GaN:Mn		
$E_d$ (eV)	$\Gamma_d$	Defect type	$E_d$ (eV)	$\Gamma_d$	Defect type
$E_{Mg-1} = 1.3$	0.12	C <sub>1</sub> [29,30]	$E_{Mn-1} = 1.4$	0.15	C <sub>1</sub> [29,30]
$E_{Mg-2} = 1.75$	0.18	Mg related [38,39]			or Mn related [39]
$E_{Mg-3} = 2.07$	0.23	V <sub>Ga</sub> O <sub>N</sub> [40,41]	$E_{Mn-1} = 1.98$	0.23	Mn related [44]

The PPI spectra with simulated energy levels and PL spectra with simulated IR-PL levels are presented in Fig. 3.1.6.

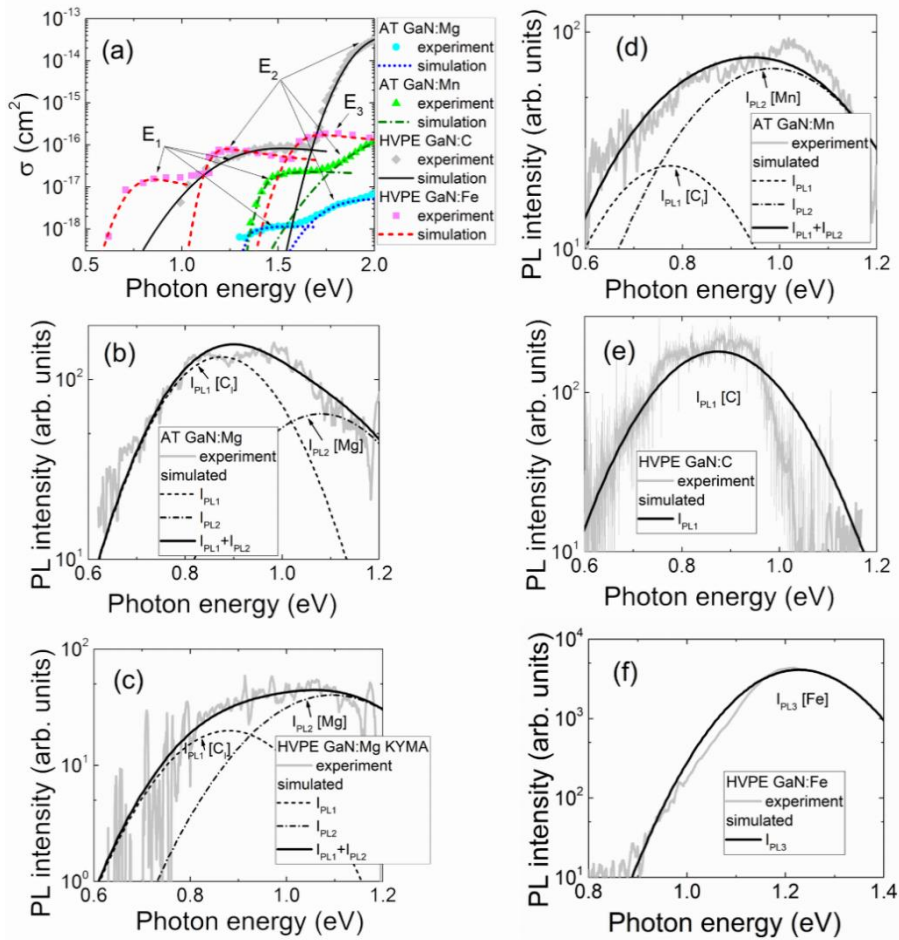


Fig. 3.1.6. (a) – the as-recorded and fitted PPI spectral steps, representing spectral variations of the photon-electron coupling cross-sections responsible for IR-PL in GaN grown using AT and HVPE technologies containing different dopants. (b-f) – Stokes-shifted IR-PL spectral bands relative to the PPI spectral steps (listed in Table 3.2), simulated using either double component (originated from two PPIS steps), for GaN:Fe, GaN:Mg, GaN:Mn materials, or a single component, (for GaN:C and GaN:Fe) IR-PL bands.

### Conclusion for 3.1 chapter

The PPIS and PL spectroscopy techniques were implemented to examine AT and HVPE grown GaN samples doped with C, Mg, Mn and Fe. The energy levels and capture cross-sections of defects were evaluated and defect centers were identified using PPIS technique. The room temperature IR-PL spectra have been correlated with PPI spectra using van Roosbroeck-Schockley

approach for spectrum conversion. Thereby, the extracted PPIS parameters can be employed for prediction of the efficiency and spectrum of RT IR-PL for the UV excited GaN materials.

### 3.2 Defects and transformations of electrical and optical properties of GaN induced by neutron irradiation

In this chapter, the results of the article [A4], addressed to analysis of the radiation induced defects in GaN, are presented.

The PPI spectra have been recorded at room temperature on AT GaN:Mn and AT GaN:Mg samples before and after neutron irradiation with different fluences ( $10^{12} - 5 \times 10^{16} \text{ cm}^{-2}$ ). The evolution of the PPI spectra with neutron fluence is illustrated in Fig. 3.2.1 for AT GaN:Mn (a) and AT GaN:Mg (b), respectively.

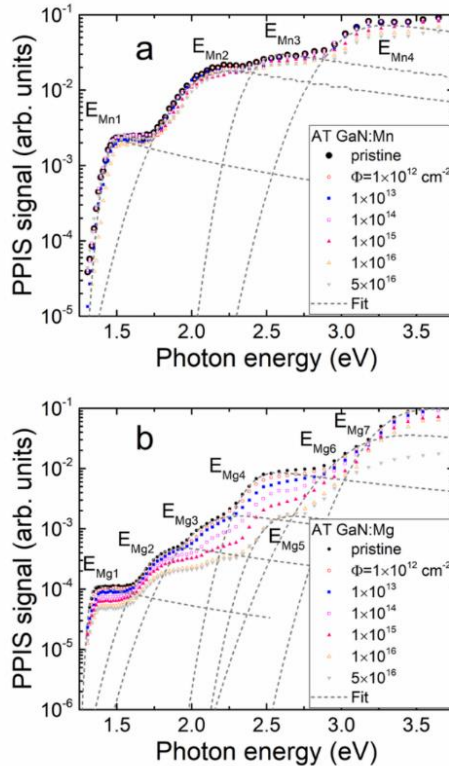


Fig. 3.2.1. Fitting of the PPI spectrum steps, recorded on the pristine and neutron-irradiated samples (AT GaN:Mn (a) and AT GaN:Mg (b)). Thin dash lines show the PPIS steps simulated using Eq. 2.2.



The PPI spectra contained four spectral peaks for AT GaN:Mn (Fig. 3.2.1(a)) and seven peaks for AT GaN:Mg (Fig. 3.2.1(b)) samples. The PPI spectral steps  $E_{Mn1}$  and  $E_{Mn2}$  are nearly independent of neutron irradiation (Fig. 3.2.1(a)). A reduction (relative to that obtained for the pristine sample) of the PPI spectral step height of  $E_{Mn4}$  under fluence enhancement can be deduced from Fig. 3.2.1(a). This implies the decrease of concentration (proportional to the height of the PPIS step) of this  $E_{Mn4}$  definite trap of the same origin (with an invariable cross-section). The insignificant variation of the  $E_{Mn3}$  trap density can also be implied from the fluence-dependent evolution of Mn-doped AT GaN (in Fig. 3.2.1(a)). The decrease of concentration of the initially existing defects formed by crystal growth can be explained by defect transformations. Such a transformation of Mn ascribed defects had also been revealed by ESR spectroscopy in a previous study [45].

In Table 3.3, the identified activation energies and values of the broadening factor are listed for the predominant centers in Mn and Mg doped AT GaN samples.

Table 3.3 The PPIS parameters in the pristine and neutron-irradiated samples extracted by fitting the PPIS steps.

AT GaN:Mn			
	$E_d$ (eV)	$\Gamma_d$	Defect type
$E_{Mn1}$	1.43	0.06	Mn [39]
$E_{Mn2}$	1.99	0.25	Mn [44]
$E_{Mn3}$	2.41	0.15	Ga <sub>I</sub> [38]
$E_{Mn4}$	2.99	0.26	N/A
AT GaN:Mg			
	$E_d$ (eV)	$\Gamma_d$	Defect type
$E_{Mg1}$	1.32	0.03	Donor [46]
$E_{Mg2}$	1.74	0.18	Mg related [47]
$E_{Mg3}$	2.06	0.24	V <sub>Ga</sub> related [31]
$E_{Mg4}$	2.38	0.15	Ga <sub>I</sub> [38]
$E_{Mg5}$	2.48	0.15	V <sub>Ga</sub> related [32]
$E_{Mg6}$	3.10	0.32	Mg related [47]
$E_{Mg7}$	3.31	0.25	V <sub>N</sub> [38]

The amplitudes of different components, which are proportional to the initial filling of the photoactive centers, are plotted in Fig. 3.2.2.

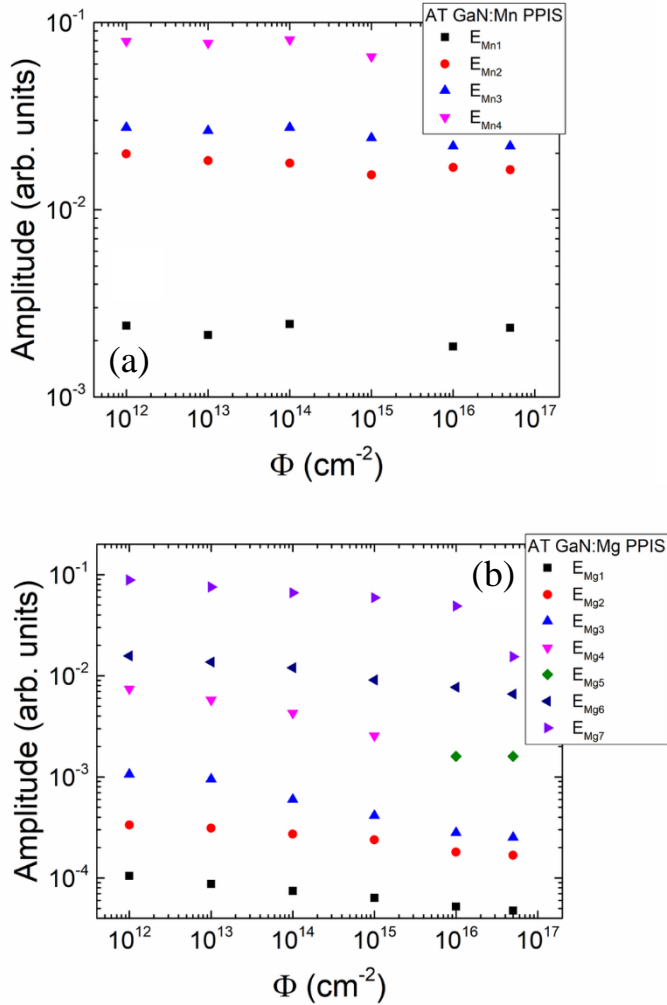


Fig. 3.2.2. Amplitudes of the PPI spectrum components, proportional to the initial filling of different traps, estimated by fitting the PPI spectra for the pristine and neutron-irradiated samples (AT GaN:Mn (a) and AT GaN:Mg (b)), as functions of neutron irradiation fluence.

The density of the Mn associated traps  $E_{\text{Mn1}}$  and  $E_{\text{Mn2}}$  seems to be independent of neutron irradiation fluence. The impact of the carrier lifetime decrease is the same for all the resolved traps  $E_{\text{Mn1}}-E_{\text{Mn4}}$ . This hints that the PPI step height highlights the initial filling state of the definite photoactive trap. Thereby, radiation defects seem to make the biggest impact on the initial filling of the  $E_{\text{Mn4}}$  centers, however, of unknown origin.

A rather different evolution (relative to Mn-doped AT GaN material) of the PPI steps was obtained for Mg-doped AT GaN samples (Fig. 3.2.1(b),

Fig. 3.2.2(b)). The most resolvable changes of the height of PPI  $E_{Mg3}-E_{Mg5}$  spectral steps were obtained. The ESR spectroscopy, performed on these Mg-doped AT GaN samples [45], showed prevailing of the gallium vacancy and substitutional oxygen ( $V_{Ga}-O_N$ ) [45, 48, 49] defects in the pristine material and hinted on the appearance of the nitrogen split interstitial [45, 50, 51] defects under irradiation. A significant decrease (up to an order of magnitude) of the height of the  $E_{Mg3}-E_{Mg4}$  spectral steps has been obtained in this study, while less changes of the PPIS signals have been revealed for  $E_{Mg1}$  and  $E_{Mg2}$  spectral steps. Moreover, nearly invariable height has been observed for the  $E_{Mg7}$  spectral step with enhancement of the neutron fluence. For the Mg-doped samples, appearance of the additional PPIS center  $E_{Mg5}$  in the range of elevated fluences ( $>10^{14}$  n/cm<sup>2</sup>) can be deduced from Figs. 3.2.1(b) and 3.2.2(b). The latter defect can play the role of a fast recombination center. Its impact appears only when the carrier lifetime, linked to this radiation defect, becomes shorter than that inherent for the pristine material. The capture cross-section values for all the mentioned traps are nearly the same. This implies that neutron irradiation governs only the initial filling (density of carriers on the definite type centers) of the technologically induced defects.

The neutron fluence  $\Phi$  dependent evolution of the UV pulse excited PL spectra, recorded *ex situ* in Mn and Mg doped AT GaN, are illustrated in Figs. 3.2.3(a) and 3.2.3(b), respectively. In Mn-doped AT GaN, a rather wide spectral band peaked at 2.5 eV appears in the yellow–green (YG) PL range. A clear decrease of the intensity of the YG-PL band with the enhancement of fluence is clearly observed only for the range of large fluences  $>10^{16}$  n/cm<sup>2</sup>. It is very probable that wide PL bands (especially YG-PL) are composed of several overlapping PL peaks. These peaks can be predicted by correlating PPI and PL spectra in consideration of the conversion from absorption to emission using the van Roosbroeck-Shockley approach (Eq. 3.1). The comparison of the simulated photo-ionization and photoluminescence spectra ascribed to several PPIS steps for GaN:Mn and GaN:Mg samples is illustrated in Figs. 3.2.3(a) and 3.2.3(b), respectively. The evolution of the amplitudes of different PL spectral components with neutron irradiation fluence is illustrated in Fig. 3.2.4. By generalizing the PL data, a significant reduction of the overall PL intensity is quite evident.

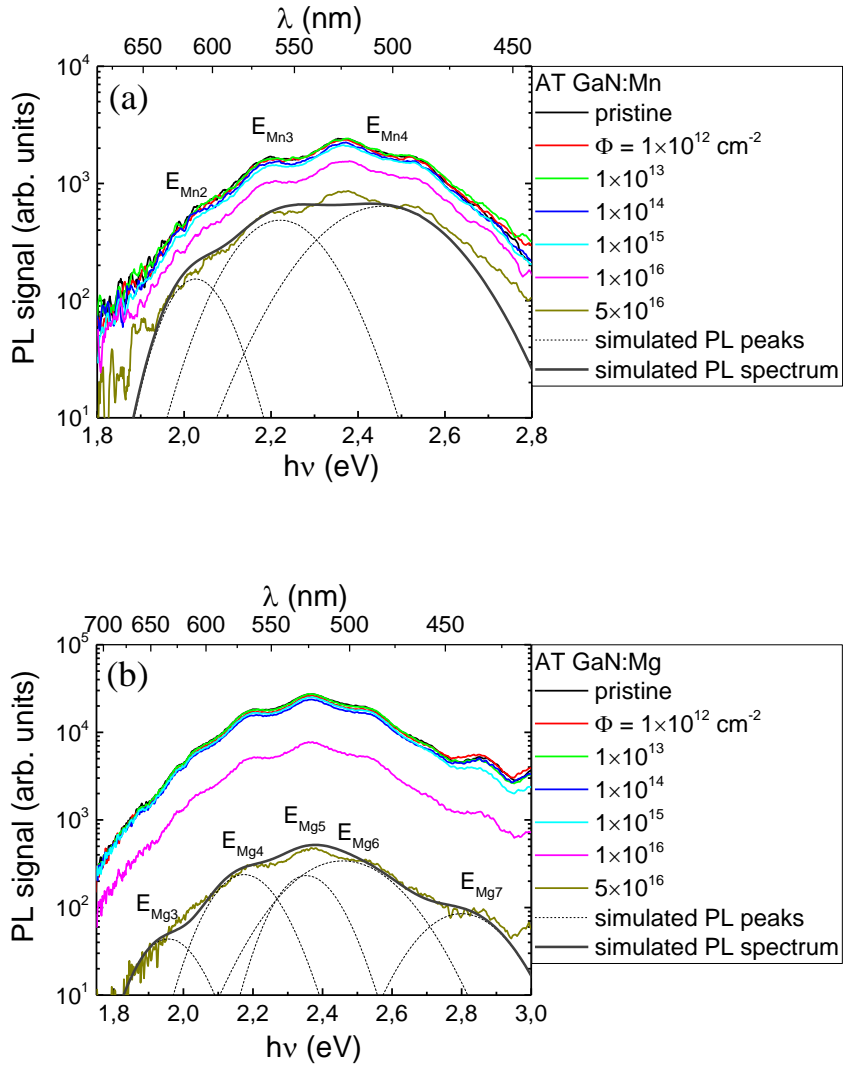


Fig. 3.2.3. The as-recorded and fitted evolution of PL spectra, before and after neutron irradiation by different fluences, using PPIS experimental data (listed in Table 3.3) for AT GaN:Mn (a) and AT GaN:Mg (b) materials. Thin dash lines represent PL peaks simulated using Eqs. (2.2) and (3.1), a thick grey line shows a resultant PL spectrum composed of the simulated PL peaks.

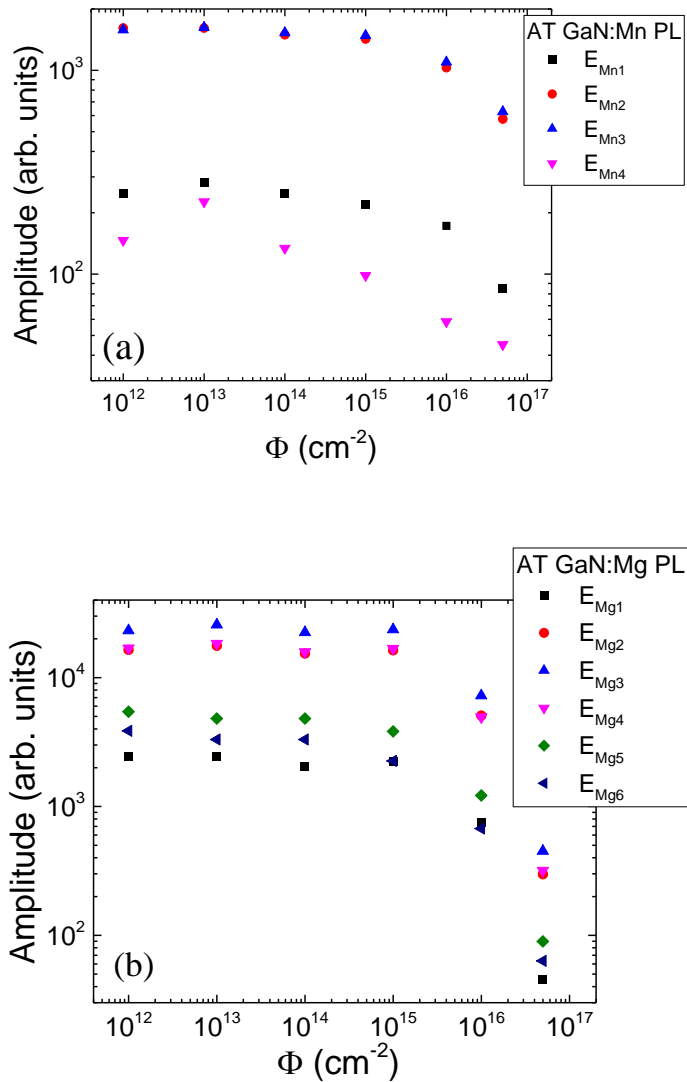


Fig. 3.2.4. The amplitudes of the fitted PL spectral components, extracted for AT GaN:Mn (a) and AT GaN:Mg (b) materials.

Figure 3.2.5 shows the average positron lifetime measured at RT in the pristine and neutron-irradiated AT GaN:Mn and AT GaN:Mg samples.

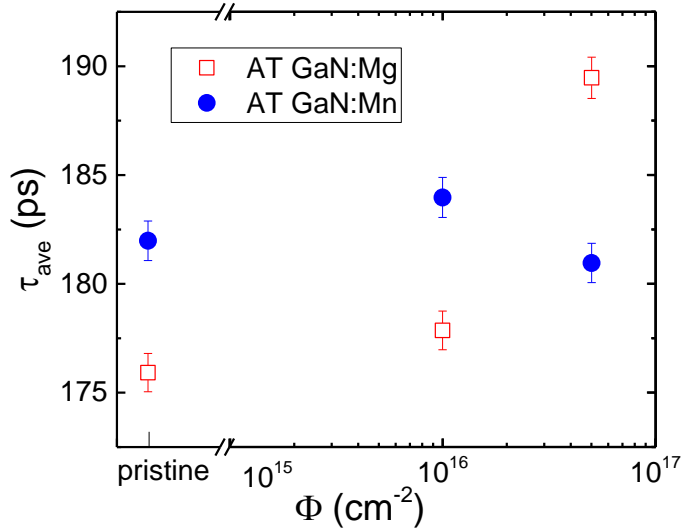


Fig. 3.2.5. Average positron lifetime in pristine and neutron-irradiated AT GaN:Mn and AT GaN:Mg.

The positron annihilation spectroscopy data shows that the pristine AT GaN:Mn material contains higher concentration of vacancy defects than that for AT GaN:Mg. This is seen both as a higher average lifetime of positrons in the pristine material, and also by the neutron irradiation having very little effect on the average lifetime in AT GaN:Mn. In contrast, in AT GaN:Mg, the irradiation (with the highest fluence) causes a strong increase in the vacancy defect concentrations highlighted through the increase of the positron average lifetime. This is equivalent to an increase in the average size of the opening volume around the vacancies. The increase of the positron average lifetime is related to the fact that the ingrown Ga vacancies in AT GaN are present within hydrogen complexes that lead to a shorter lifetimes than values ascribed to the ‘pure’  $V_{\text{Ga}}$  induced by irradiation. It means that the concentration of radiation-induced vacancies is significant compared to that of the ingrown vacancies (Mg-doped) if the average open volume around vacancies increases in material with positron lifetime. Also, it means that the concentration of the ingrown vacancies in Mn-doped AT GaN is significantly larger than that created by irradiation, even at the highest fluence, when no changes of the positron lifetime are observed.

The comparison of the PAS and PL data shows that the Ga vacancies produced by irradiation are non-radiative recombination centers. The significant reduction of the overall PL intensity with the enhancement of

neutron fluence correlates with the PAS data. This effect is stronger in the Mg-doped material, as the ingrown Ga vacancy-hydrogen complexes are probably also detrimental for the PL intensity changes. In general, the Mn-doped material appears to emit less light than the pristine Mg-doped material. Also, the stronger irradiation effect in the Mg-doped materials supports this hypothesis. Moreover, the comparison of the Mg and Mn doped materials evidences the smaller effect in the Mn-doped samples, where the pristine vacancy concentrations seem to be higher, as the irradiation-induced vacancies affect the positron lifetime data so little.

### Conclusion for 3.2 chapter

The combination of photo-ionisation, photoluminescence and positron annihilation spectroscopy techniques was successfully applied to trace the evolution of the radiation induced defects in GaN samples. The decrease of concentration of the initially existing defects, formed by crystal growth, has been observed after neutron irradiation. These observations can be explained by defect transformations. The traps associated with vacancies, interstitials, impurities and dopants have been tentatively identified.

### 3.3 Radiation sensors and dosimetry instruments created on the basis of the GaN related materials.

In this chapter, the results of articles [A5-A7] and patent applications [P1-P2], addressed to creation of the hybrid, double response dosimetry sensors and oriented dosimetry triplex sensors, invented on the basis of investigations of fundamental characteristics of different technology GaN materials, are presented.

Study of the evolution of spectra of the proton-induced luminescence (PIL) and of diode short-circuit current changes during 1.6 MeV proton irradiation in GaN materials has been simultaneously performed in the latter cycle of investigations. Several sets of samples were examined. The first set consists of the commercial photo-detectors (GUVA, GUVB, GUVVC) – planar Schottky diodes, made of AlGa<sub>N</sub> materials with different Al content. The second set of samples was prepared as mesa structures made of top 1 μm thick GaN layer and several AlGa<sub>N</sub> layers underneath, grown on Si substrates.

The fluence ( $\Phi$ )-dependent evolution of the PIL spectra in different layers of the mesa structure samples with various content of Al is illustrated in Fig. 3.3.1. The main feature of this evolution is a decrease of the intensity of the long-wavelength component with enhancement of proton irradiation

fluence. The fluence-dependent variation of peak intensity of the separated PIL spectral bands is illustrated in Fig. 3.3.2. These characteristics imply that the calibrated PIL intensity reduction related to the absolute fluence values can be applied for dosimetry of the penetrative particle irradiation. There, different sensitivity can be reached for various PIL spectral bands and content of Al.

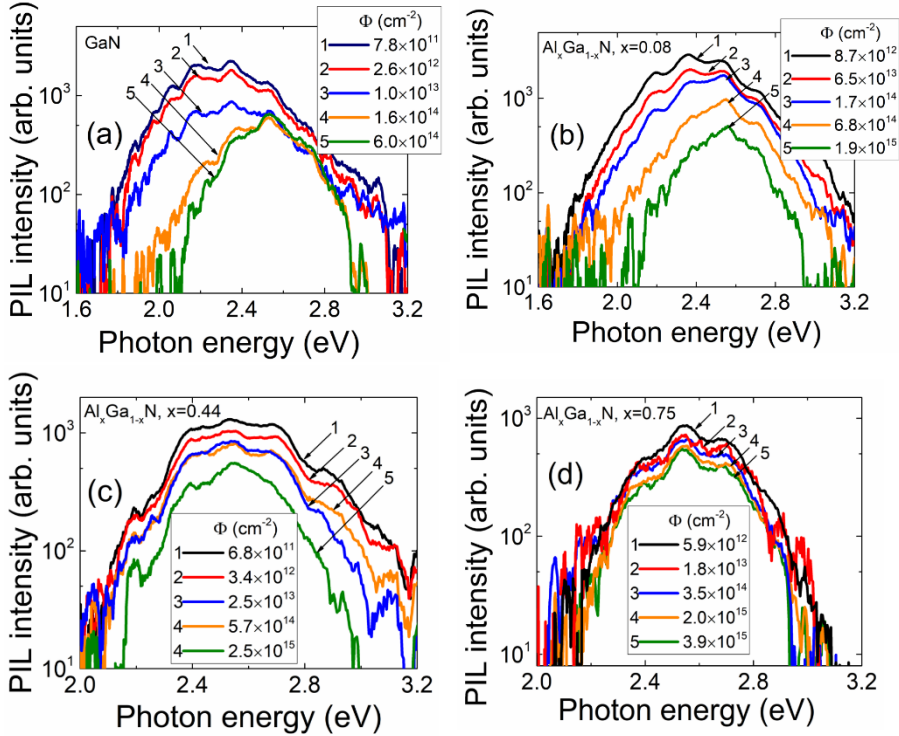


Fig. 3.3.1. Fluence-dependent evolution of PIL spectra recorded on different Al content (0% (a); 8% (b); 44% (c); 75% (d)) GaN mesa structures.

To identify the origin of different PIL components, the predominant spectral components have been correlated with PPI spectra, measured on mesa structures of the same material. Three spectral components peaked at 2.57 eV, 2.31 eV and 2.10 eV in PIL spectra have been ascribed to  $(\text{C}_\text{N}\text{O}_\text{N})^0$ ,  $\text{C}_\text{N}^-$  and  $\text{V}_\text{Ga}$  defects, respectively.



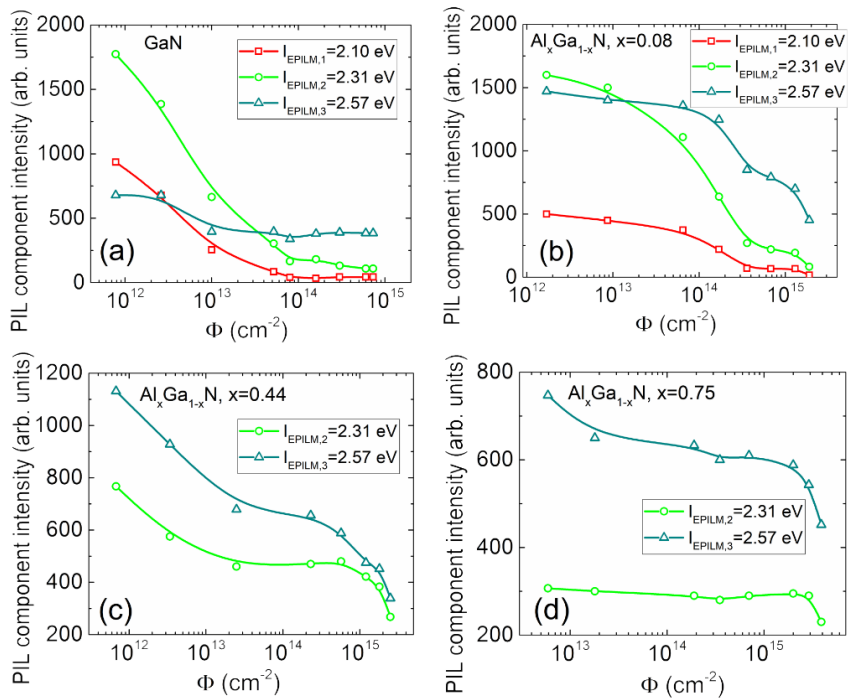


Fig. 3.3.2. Fluence-dependent variations of the intensity of different spectral components within PIL spectra on different Al content (0% (a); 8% (b); 44% (c); 75% (d)) GaN mesa structure samples.

Evolution of PIL spectra recorded on the set of Schottky diode structures during proton irradiation is illustrated in Fig. 3.3.3. The general feature of these spectra variations is a decrease of intensity of the long wavelength PIL with further enhancement of the short wavelength band under increase of proton irradiation fluence.

The fluence-dependent short-circuit current ( $I_{SC}$ ) variations (Fig. 3.3.3(d)), measured simultaneously with PIL spectra, differ significantly when comparing the diodes made of various Al content materials. The largest  $I_{SC}$  values have been observed for pure GaN material (GUYA) diodes. Consequently, the dynamic range of  $I_{SC}$  variations is the widest when using these GUYA diodes. Thereby, sensitivity to fluence changes is also the highest for the GUYA diodes. An increase of bandgap with Al content leads to a reduction of the  $I_{SC}$  current. Therefore, a recordable change of  $I_{SC}$  as a function of fluence is obtained in 32% Al containing material only for the range of moderate fluences of  $\Phi > 3 \times 10^{13}$  p/cm<sup>2</sup>. Even the less absolute values and the related changes of  $I_{SC}$  (for  $\Phi > 10^{14}$  p/cm<sup>2</sup>) were obtained for diodes (GUYC) containing of 50% Al (Fig. 3.3.3(d)).

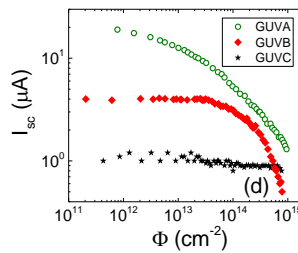
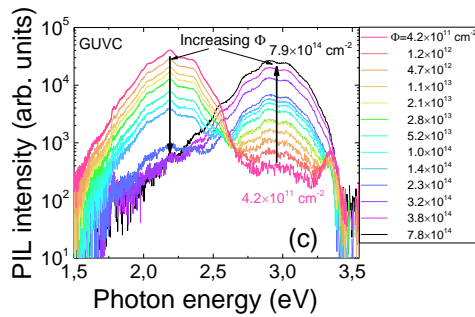
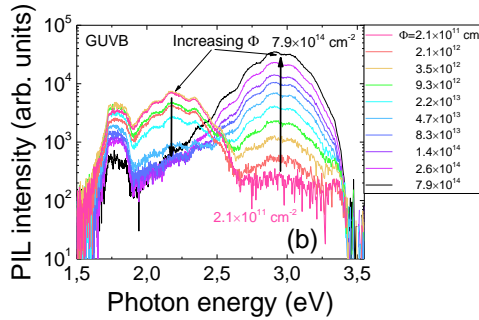
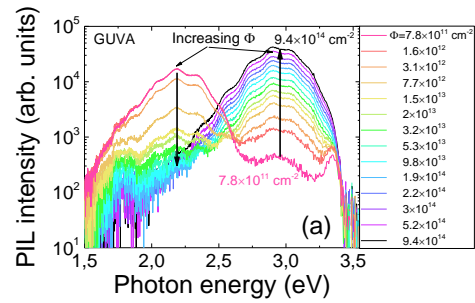


Fig. 3.3.3. Fluence-dependent evolution of PIL spectra recorded on samples made of different Al content (0% (a); 32% (b); 50% (c)) Schottky diode structures (GUVA-GUVc). (d) - evolution of short-circuit current in various GUVA-GUVc diodes.

As can be deduced from Fig. 3.3.3, the spectral and intensity variations of PIL provide reliable characteristics for dosimetry applications.

The rather thin MOCVD GaN layers, that enable detection of  $\leq 2$  MeV protons with  $L_p \sim 26 \mu\text{m}$  stopping range, have been employed for profiling of proton beams. The changes either of the complete scintillation spectrum or of a single spectral peak intensity were scanned before and after irradiation to reproduce a profile of the definite proton beam. The calibrated fluence dependent variation of yellow-green (YG) luminescence intensity (Fig. 3.3.4) of the  $\sim 3 \mu\text{m}$  thick MOCVD grown GaN layer was initially measured to extract fluence values. The recording of the calibration curve was performed by the *in situ* spectroscopy of the GaN luminescence variations under successive accumulation of fluence within a laterally homogeneous irradiation spot. The proton beam of a diameter that exceeds the dimensions of the GaN wafer fragment was applied to have a nearly homogeneously irradiated sensor area. The same GaN sensor material was then exploited for scanning of a rather narrow beam profile (Fig. 3.3.5). The latter procedure was implemented *ex situ* by using UV short pulse (400 ps) laser excitation.

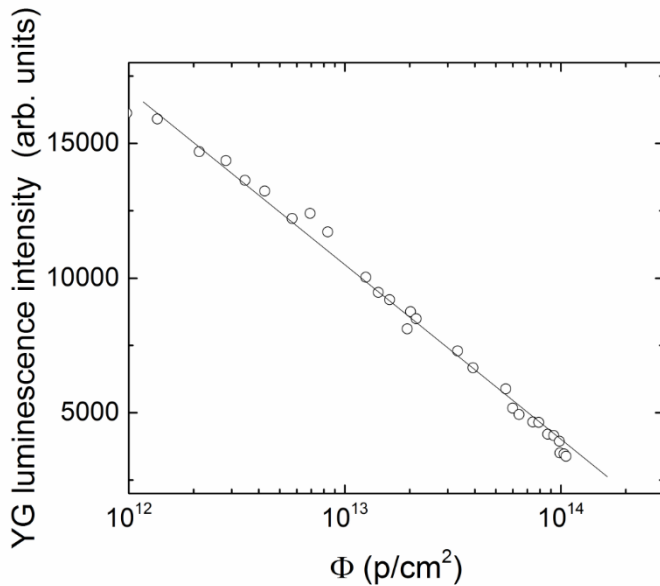


Fig. 3.3.4. The calibration characteristic for the short-range particle beam profiling based on YG luminescence intensity variations dependent on 1.6 MeV proton fluence.

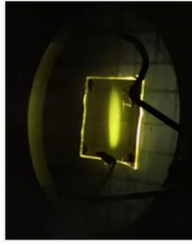


Fig. 3.3.5. The YG luminescence image obtained by narrow 1.6 MeV proton beam. It can be inferred that GaN wafer fragment there exceeds dimensions of the proton beam.

The one-dimensional luminescence intensity profile obtained in the 1.6 MeV proton irradiated  $3\ \mu\text{m}$  thick GaN layer, MOCVD grown on sapphire, is illustrated in Fig. 3.3.6(a).

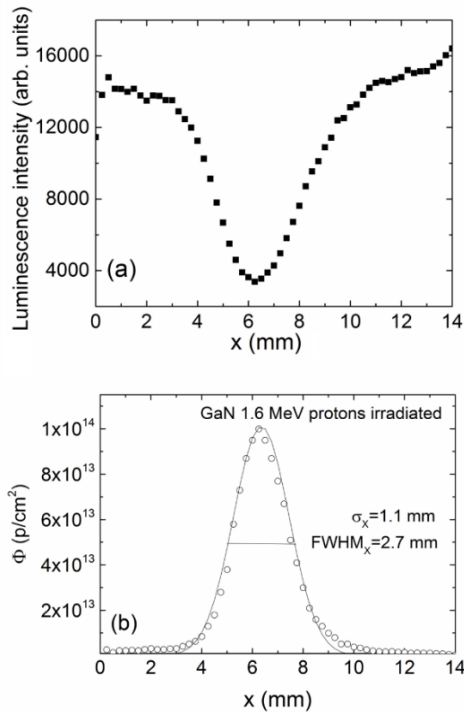


Fig. 3.3.6. The 1D profiles of YG luminescence distribution within a  $3\ \mu\text{m}$  thick MOCVD GaN layer irradiated with 1.6 MeV protons (a) and a reproduced profile of fluence distribution (b) extracted using a calibration curve, illustrated in Fig. 3.3.4. In Fig. 3.3.6(b), the fluence distribution profile (symbols) is represented obtained by using the Gauss function (a solid curve) for the beam shape fit.

The fluence distribution profile can then be restored (Fig.3.3.6(b)) using the calibration curve (Fig. 3.3.4) which relates the YG scintillation intensity of the same GaN material and the accumulated fluence.

An oriented triplex dosimetry sensor was formed for the identification of the radiation source location and its dose-rate characteristics. A single oriented dosimetry sensor contains layered combination of the microwave-probed photo-sensor made of high-purity large-resistivity semiconductor homogeneous bulk-plate pasted to the intermediate organic material (alanine) layer, where free radicals emerge under high energy irradiations, which is agglutinated further with a thin top layer of a GaN scintillator (Fig. 3.3.7). The accumulated dose and its depth distribution (sketched in Fig. 3.3.7) within layers depends on orientation of the triplex sensor.

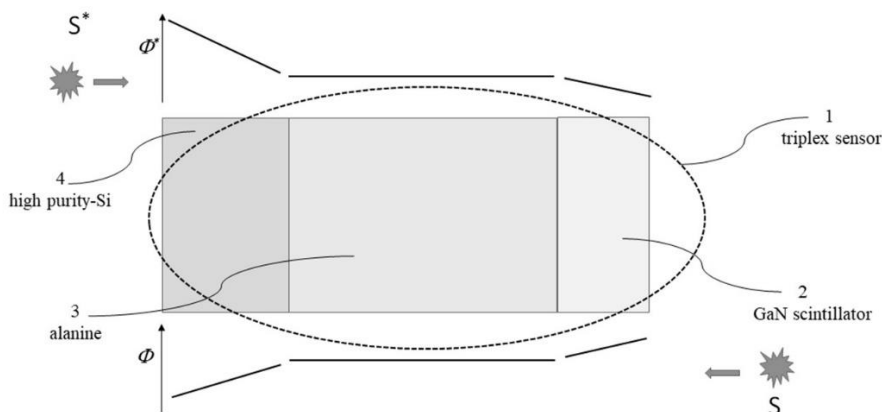


Fig. 3.3.7. Triplex sensor manufactured by sticking different material and thickness pieces and fluence distribution within sensor layers dependent on detector orientation relative to either the irradiation source S or S\*.

The measured dose value also depends on the response type: variation of the MW-PC transients in large-resistivity semiconductor (Fig. 3.3.7(4)), of microwave ESR resonance amplitude in alanine (Fig. 3.3.7(3)), and PL spectral amplitude of GaN scintillator (Fig. 3.3.7(2)), respectively.

The top scintillator layer is designed according to absorption depth in the optical spectral range of the luminescence radiation which is addressed to generate a scintillation spectrum inherent for definite radiation dose. This scintillator layer of the triplex detector also operates as a particle species identification sensor acting as the spectral shape discriminator. It generates a combination of spectral shapes (Fig. 3.3.8), characteristic for different particle

beams. The direction (over layers from 2 to 4) is determined by the oriented triplex sensor (Fig. 3.3.7(1)) using a profile of the recorded doses in different sensor layers.

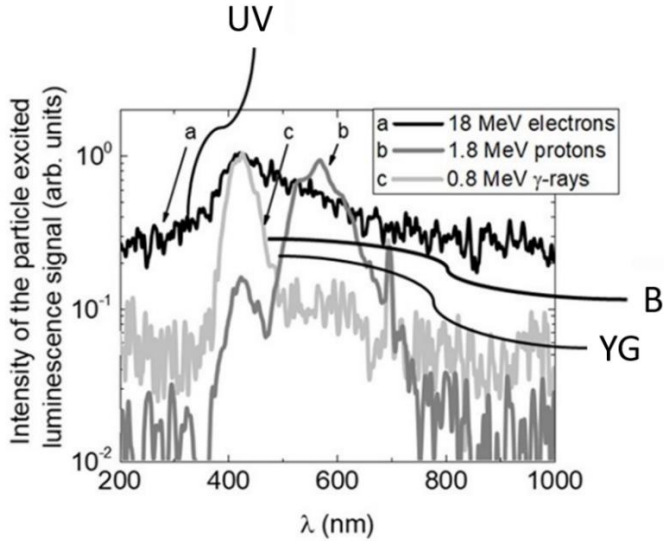


Fig. 3.3.8. Variations of spectrum structure within UV, blue (B) and green-yellow (YG) PL spectral ranges, recorded on the same GaN scintillator dependent on irradiation particle type, as: 18 MeV electrons (a); 1.8 MeV protons (b) and 0.8 MeV  $\gamma$ -rays (c).

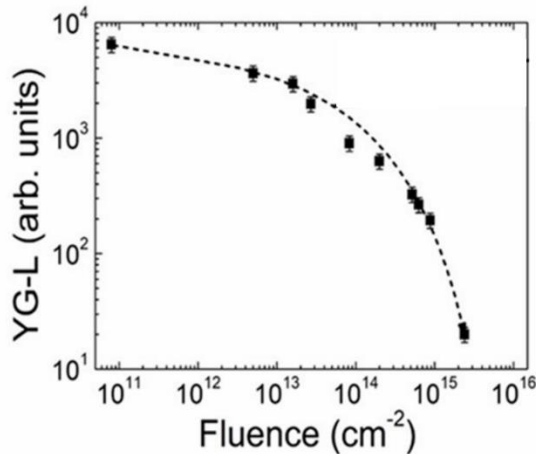


Fig. 3.3.9. Green-yellow luminescence (YG-L) intensity of the proton irradiated GaN scintillator as a function of the irradiation fluence.

The intensity of the UV laser induced luminescence generated by the top scintillator layer is calibrated according to the dose dependent intensity characteristics within different spectral bands, for instance, green-yellow PL (Fig. 3.3.9) intensity dependent on collected fluence of high energy particles (for instance, protons). The integrated spectral band area and spectrum shape serve for comparison of the scintillator signals ascribed to different impinging particles when luminescence responses are exploited for spectral shape discrimination. The GaN scintillator layer of the triplex sensor operates either in particle identification regime or for fast estimation of the radiation source (location, dose range as well as dose-rate). The intermediate organic material (alanine) layer is addressed to evaluate the integral irradiation dose independent of the high energy irradiation type. The irradiation creates free radicals in the alanine material which concentration is proportional to the ESR spectra amplitude. Then the radiation dose can be evaluated by comparing ESR spectral peaks associated with radiation induced free radicals to that of a calibrated reference marker (Fig. 3.3.10). Thickness of this layer is chosen to conform to the ESR reader arrangement, the triplex sensor size, the dose range of recorded particles and penetration of intrusive radiations. Thickness of this layer also serves for reduction of the mutual interplay of the scanner (IR excitation in MW-PC, microwaves of 20 GHz for MW-PC and UV excitation for visible spectrum scintillation) radiations.

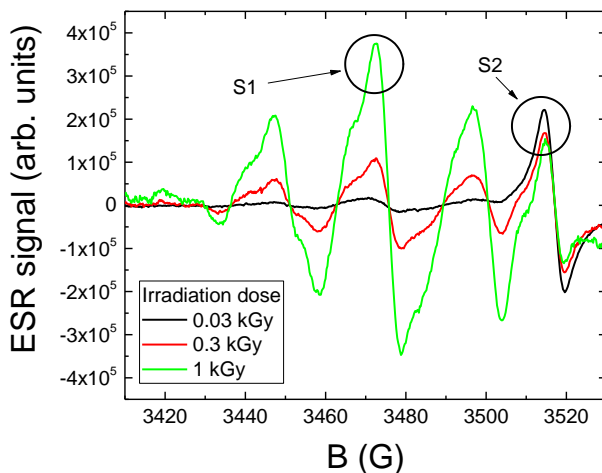


Fig. 3.3.10. ESR spectra dependent on irradiation doses recorded using alanine dosimeters. Dose evaluation is implemented by comparing spectral peaks associated with radiation induced free radicals in alanine (S1) and  $Mn^{++}$  reference (S2).

The third element of the oriented triplex sensor, being the high-purity large-resistivity semiconductor (for instance, Si) homogeneous bulk-plate, serves for scanning of depth-distribution of carrier recombination or trapping lifetime. The carrier lifetime is calibrated to evaluate the irradiation fluence (Fig. 3.3.11). The thickness of the high-purity semiconductor plate is chosen according to the predicted penetration depth of the particles under inspection.

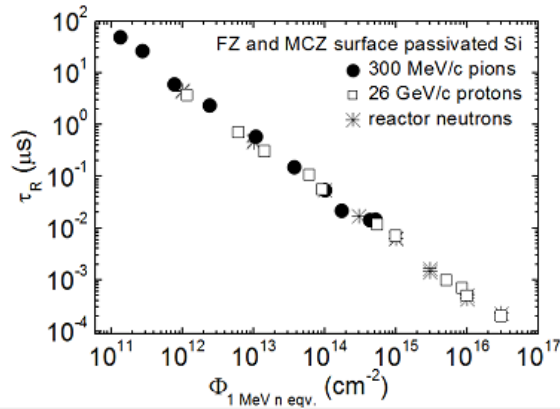


Fig. 3.3.11. Recombination lifetime in the as-irradiated Si wafer fragments as a function of fluence of the reactor neutrons, 26 GeV/c protons and 300 MeV/c pions.

Reading of the oriented dosimetry sensor (ODS) is performed by three-step procedure. The first step is implemented using measurements of the spectral components of the UV laser induced luminescence of the irradiated scintillator layer (collected into spectrophotometer using multi-bundle-fiberscope). The second step of the ODS reading is carried out by the ESR scanner, where triplex ODS sensor is mounted within ESR insert containing a  $\text{Mn}^{++}$  reference. The third step is performed by reading of the triplex ODS dosimetry data using carrier recombination lifetime dependence on irradiation fluence. The carrier recombination lifetime is recorded by MW-PC transient scanner combined with MW-PC  $\tau$ -meter containing additional IR pulsed laser. To enhance precision either of a single ODS or of the monitoring of spatial location of the intensive radiation source, several ODS's can be installed within a tube by stretching them face-to-face or these ODS's can compose a 2D or 3D remote scanner, to measure remotely the space location and activity of radiation source.



### Conclusion for 3.3 chapter

The stability of the fluence-dependent modifications of the spectral and electrical characteristics has been verified by comparing the UV pulsed laser-excited photo-luminescence spectra and electrical signals measured before and after proton irradiations. The radiation induced defects were responsible for the changes of photoluminescence spectra of GaN based mesa structure samples as well as the correlated changes of the photoluminescence spectra and the short-circuit current of double response sensors. By scanning the photoluminescence intensity as a function of a coordinate along the sample, the proton beam profile was evaluated. Triplex oriented dosimetry sensors were formed and techniques as well as equipment for their reading were developed.

## CONCLUSIONS

1. The analysis of pulsed photo-ionization and photoluminescence spectra of GaN materials was performed. The van Roosbroeck-Shockley approach was used to predict the conversion of the defect photo-ionization cross-section and the infrared photoluminescence spectra. Defects and impurities of pristine GaN samples associated with photo-ionization spectral steps and photoluminescence peaks were identified.
2. Combination of the pulsed photo-ionization, photoluminescence and positron annihilation techniques was applied to trace the evolution of neutron irradiation induced defects in GaN materials. These defects were identified. The techniques used in this analysis were proved to be reliable for radiation dosimetry using GaN materials.
3. Changes of the optical and electrical responses of GaN samples were examined before and after proton irradiation. Such analysis of proton irradiation introduced non-radiative and radiative recombination centers within GaN structures can be applied for creation of double-response dosimetry sensors.
4. A hybrid multilayer sensor, comprising of a scintillator layer made of GaN, photoelectric-response layer made of high purity, large resistivity Si and a visible spectrum filtering, electric insulating layer of an alanine dosimeter was formed. The techniques and apparatuses for its reading were developed. The triplex sensor for remote and oriented dosimetry was created and tested in pulsed as well as steady-state modes. It was proved that this triplex sensor can serve for contactless discrimination of particle species as well as for remote estimation of a location of the large dose-rate radiation sources and for measurements of their dosimetry parameters.

## BIBLIOGRAPHY

- [1] K. Takahashi, A. A. Yoshikawa, A. Sandhu, *Wide bandgap semiconductors: fundamental properties and modern photonic and electronic devices*, Berlin, Springer (2007). <https://link.springer.com/book/10.1007/978-3-540-47235-3>
- [2] C. Claeys, E. Simoen, *Basic radiation damage mechanisms in semiconductor materials and devices*, Berlin, Springer (2002). DOI: 10.1007/978-3-662-04974-7\_2
- [3] P. J. Sellin, J. Vaitkus, New materials for radiation hard semiconductor detectors, *Nucl. Instrum. Methods Phys. Res.* **557** (2006) 479-489. DOI:10.1016/j.nima.2005.10.128
- [4] A. Ionascut-Nedelcescu, C. Carlone, A. Houdayer, H. J. von Bardeleben, J. L. Cantin, S. Raymond, Radiation hardness of Gallium Nitride, *IEEE Trans. Nucl. Sci.* **49** (2002) 2733-2738. DOI:10.1109/TNS.2002.805363
- [5] S. Fujita, Wide-bandgap semiconductor materials: For their full bloom, *Jpn. J. Appl. Phys.* **54** (2015) 030101. DOI:10.7567/JJAP.54.030101
- [6] E. Gaubas, T. Ceponis, V. Kalesinskas, J. Pavlov, and J. Vysniauskas, Simulations of operation dynamics of different type GaN particle sensors, *Sensors* **15** (2015) 5429-5473. DOI:10.3390/s150305429
- [7] C. J. H. Wort, R. S. Balmer, Diamond as an electronic material, *Mater. Today* **11** (2008) 22-28. DOI:10.1016/S1369-7021(07)70349-8
- [8] T. Wonglakhon, Interaction potentials for modelling GaN precipitation and solid state polymorphism, *J. Phys. Condens. Matter* **32** (20) (2020) 205401. DOI:10.1088/1361-648X/ab6cbe
- [9] G. B. Stringfellow, *Organometallic Vapor-Phase Epitaxy: Theory and Practice*, London, Academic Press (1989). DOI:10.1016/C2009-0-22261-6
- [10] K. Saarinen, *III-Nitride Semiconductors: Electrical, Structural and Defects Properties*, Editor: Omar Manasreh, Elsevier (2000). DOI:10.1016/B978-0-444-50630-6.X5000-4
- [11] H. Amano, N. Sawaki, I. Akasaki, Y. Toyoda, Metalorganic vapor phase epitaxial growth of a high quality GaN film using an AlN buffer layer, *Appl. Phys. Lett.* **48** (5) (1986) 353. DOI:10.1063/1.96549
- [12] B. Lucznik, B. Pastuszka, I. Grzegory, M. Bockowski, G. Kamler, E. Litwin-Staszewska, and S. Porowski, Deposition of thick GaN layers by HVPE on the pressure grown GaN substrates, *J. Cryst. Growth* **281** (1) (2005) 38–46. DOI:10.1016/j.jcrysgro.2005.03.041

- [13] R. Molnar, K. Nichols, P. Maki, E. Brown, I. Melngailis, The Role of Impurities in Hydride Vapor Phase Epitaxially Grown Gallium Nitride, *MRS Proceedings* (1995) 378 - 479. DOI:10.1557/PROC-378-479
- [14] C. Hemmingsson, G. Pozina, Optimization of low temperature GaN buffer layers for halide vapor phase epitaxy growth of bulk GaN, *J. Cryst. Growth* **366** (2013) 61-66. DOI:10.1016/j.jcrysgro.2012.12.016
- [15] R. Dwilinski, R. Doradzinski, J. Garczynski, L.P. Sierzputowski, A. Puchalski, Y. Kanbara, K. Yagi, H. Minakuchi, H. Hayashi, Bulk ammonothermal GaN, *J. Cryst. Growth* **311** (2009) 3015–3018. DOI:10.1016/j.jcrysgro.2009.01.052
- [16] M. A. Reshchikov, H. Morkoc, Luminescence properties of defects in GaN, *J. Appl. Phys.* **97** (2005) 061301. DOI:10.1063/1.1868059
- [17] J. Neugebauer, C. G. Van de Walle, Atomic geometry and electronic structure of native defects in GaN, *Phys. Rev. B* **50** (1994) 8067 - 8069. DOI:10.1103/PhysRevB.50.8067
- [18] E.Simoen, C. Claeys, *Germanium-based Technologies: from Materials to Devices*, London, Elsevier (2007). <https://www.elsevier.com/books/germanium-based-technologies/claeys/978-0-08-044953-1>
- [19] H. Y. Xiao, F. Gao, X. T. Zu, W. J. Weber, Threshold displacement energy in GaN: *Ab initio* molecular dynamics study, *Int. J. Appl. Phys.* **105** (2009) 123527. DOI:10.1063/1.3153277
- [20] E. Gaubas, A. Kaniava, Determination of recombination parameters in silicon wafers by transient microwave absorption, *Rev. Sci. Instrum.* **67** (1998) 2339. DOI:10.1063/1.1146943
- [21] G. Lucovsky, On the photo-ionization of deep impurity centers in semiconductors, *Solid State Commun.* **3** (1965) 299 – 302. DOI:10.1016/0038-1098(65)90039-6
- [22] A. A. Kopylov, A. N. Pikhtin, Profiles of absorption and luminescence spectra of deep centers in semiconductors (oxygen in gallium-phosphide), *Sov. Phys. Solid State* **16** (1975) 1200.
- [23] R. Krause-Rehberg, H.S. Leipner, *Positron Annihilation in Semiconductors*, Berlin, Springer (1999). <https://link.springer.com/book/9783540643715>
- [24] D. K. Schroder, *Semiconductor Material and Device Characterization*, third edition, Hoboken, New Jersey (2006). DOI:10.1002/0471749095
- [25] G. R. Eaton, S. S. Eaton, D. P. Barr, R. T. Weber, *Quantitative EPR*, Wien, Springer-Werlag (2010). DOI:10.1007/978-3-211-92948-3

- [26] E. Gaubas, T. Čeponis, L. Deveikis, D. Meškauskaitė, S. Miasojedovas, J. Mickevičius, J. Pavlov, K. Pūkas, J. Vaitkus, M. Velička, Study of neutron irradiated structures of ammonothermal GaN, *J. Phys.* **50** (2017) 135102. DOI:10.1088/1361-6463/aa5c6c
- [27] M. A. Reshchikov, J. D. McNamara, M. Toporkov, V. Avrutin, H. Morkoc, A. Usikov, H. Helava, Y. Makarov, Determination of the electron-capture coefficients and the concentration of free electrons in GaN from time-resolved photoluminescence, *Sci. Rep.* **6** (2016) 37511. DOI:10.1038/srep37511
- [28] M. A. Reshchikov, D. O. Demchenko, J. D. McNamara, S. Fernandez-Garrido, R. Calarco, Green luminescence in Mg-doped GaN, *Phys. Rev. B* **90** (2014) 035207. DOI:10.1103/PhysRevB.90.035207
- [29] A. Armstrong, A. R. Arehart, D. Green, U. K. Mishra, J. S. Speck, S. A. Ringel, Impact of deep levels on the electrical conductivity and luminescence of gallium nitride co-doped with carbon and silicon, *J. Appl. Phys.* **98** (2005) 053704. DOI:10.1063/1.2005379
- [30] A. Y. Polyakov, N. B. Smirnov, E. A. Kozhukhova, A. V. Osinsky, S. J. Pearton, Temperature stability of high-resistivity GaN buffer layers grown by metalorganic chemical vapor deposition, *J. Vac. Sc. Technol. B* **31** (2013) 051208. DOI:10.1116/1.4820905
- [31] C. H. Qiu, J. I. Pankove, Deep levels and persistent photoconductivity in GaN thin films, *Appl. Phys. Lett.* **70** (1997) 1983. DOI:10.1063/1.118799
- [32] Z. Zhang, C. A. Hurni, A. R. Arehart, J. Yang, R. C. Myers, J. S. Speck, S. A. Ringel, Deep traps in nonpolar m-plane GaN grown by ammonia-based molecular beam epitaxy, *Appl. Phys. Lett.* **100** (2012) 52114. DOI:10.1063/1.3682528
- [33] M. A. Reshchikov, D. O. Demchenko, A. Usikov, H. Helava, Y. Makarov, Carbon defects as sources of the green and yellow luminescence bands in undoped GaN, *Phys. Rev. B* **90** (2014) 235203. DOI:10.1103/PhysRevB.90.235203
- [34] W. Van Roosbroeck, W. Shockley, Photon-radiative recombination of electrons and holes in germanium, *Phys. Rev.* **94** (1954) 1558-1560. DOI:10.1103/PhysRev.94.1558
- [35] J. I. Pankove, *Optical Processes in Semiconductors*, New Jersey, Prentice-Hall (1971). DOI:10.1149/1.2404256
- [36] E. F. Schubert, *Light-Emitting Diodes*, third edition, London, Cambridge University Press (2018). DOI:10.1017/CBO9780511790546

- [37] A. Chantre, G. Vincent, D. Bois, Deep-level optical spectroscopy in GaAs, *Phys. Rev. B* **23** (1981) 5335. DOI:10.1103/PhysRevB.23.5335
- [38] Z. Zhang, A. R. Arehart, E. C. H. Kyle, J. Chen, E. X. Zhang, D. M. Fleetwod, R. D. Schrimpf, J. S. Speck, S. A. Ringel, Proton irradiation effects on deep level states in Mg-doped p-type GaN grown by ammonia-based molecular beam epitaxy, *Appl. Phys. Lett.* **106** (2015) 022104. DOI: 10.1063/1.4905783
- [39] R. Y. Korotkov, J. M. Gregie, B. W. Wessels, Optical properties of the deep Mn acceptor in GaN:Mn, *Appl. Phys. Lett.* **80** (2002) 1731-1733. DOI:10.1063/1.1456544
- [40] L. -H. Lee, A. Y. Polyakov, N. B. Smirnov, A. V. Govorkov, A. S. Usikov, H. Helava, Y. N. Makarov, S. J. Pearton, Deep hole traps in undoped n-GaN films grown by hydride vapor phase epitaxy, *J. Appl. Phys.* **115** (2014) 223702. DOI:10.1063/1.4882715
- [41] M. A. Reschchikov, Point defects in GaN, defects in semiconductors, Book series: Secimonduct. Semimet. **91** (2015) 315-367. DOI:10.1016/bs.semsem.2014.11.003
- [42] H. Tang, Z. Q. Fang, S. Rolfe, J. A. Bardwell, S. Raymon, Growth kinetics and electronic properties of unintentionally doped semi-insulating GaN on SiC and high-resistivity GaN on sapphire grown by ammonia molecular-beam epitaxy, *J. Appl. Phys.* **107** (2010) 103701. DOI:10.1063/1.3415527
- [43] P. Thurian, A. Hoffmann, L. Eckey, P. Maxim, R. Heitz, I. Broser, K. Pressel, B. K. Meyer, J. Schneider, J. Baur, M. Kunzer, Photoluminescence of Fe-complexes in GaN, *MRS Proc.* **449** (1996) 707-712. DOI:10.1557/PROC-449-707
- [44] A. Wolos, M. Palczewska, M. Zajac, J. Gosk, M. Kaminska, A. Twardowski, M. Bockowski, I Grzegory, S. Porowski, Optical and magnetic properties of Mn in bulk GaN, *Phys. Rev. B* **69** (2004) 115210. DOI:10.1103/PhysRevB.69.115210
- [45] E. Gaubas, T. Čeponis, D. Meškauskaitė, J. Mickevičius, J. Pavlov, V. Rumbauskas, R. Grigonis, M. Zajac, R. Kucharski, Pulsed photo-ionization spectroscopy of traps in as-grown and neutron-irradiated ammonothermally synthesized GaN, *Sci. Rep.* **9** (2019) 1473. DOI:10.1038/s41598-018-38138-6
- [46] S. J. Chung, O. H. Cha, H. K. Cho, M. S. Jeong, C-H. Hong, E.-K. Suh, H. J. Lee, Photocurrent spectroscopy investigations of Mg-related defects levels in p-type GaN, *MRS Proc.* **595** (1999) F99W11.83. DOI:10.1557/PROC-595-F99W11.83

- [47] G. C. Yi, B. W. Wessels, Deep level defects in Mg-doped GaN, MRS Proc. **423** (1996) 525-530. DOI:10.1063/1.116075
- [48] N. T. Son, C. G. Hemmingsson, T. Paskova, K. R. Evans, A. Usui, N. Morishita, T. Ohshima, J. Isoya, B. Monemar, E. Janzen, Identification of the gallium vacancy-oxygen pair defect in GaN, Phys. Rev. B **80** (2009) 153202. DOI:10.1103/PhysRevB.80.153202
- [49] N. T. Son, C. G. Hemmingsson, N. Morishita, T. Ohshima, T. Paskova, K. R. Evans, A. Usui, J. Isoya, B. Monemar, E. Janzen, Radiation induced defects in GaN, Phys. Scr. **T141** (2010) 14015. DOI:10.1088/0031-8949/2010/T141/014015
- [50] H. J. Von Bardeleben, J. L. Cantin, U. Gerstmann, A. Scholle, S. Greulich-Weber, E. Rauls, M. Landmann, W. G. Schmidt, A. Gentils, J. Botsoa, M. F. Barthe, Identification of the nitrogen split interstitial (N-N)N in GaN, Phys. Rev. Lett. **109** (2012) 206402. DOI:10.1103/PhysRevLett.109.206402
- [51] H. J. Von Bardeleben, J. L. Cantin, H. Vrielinck, F. Callens, L. Binet, E. Rauls, U. Gerstmann, Nitrogen split interstitial center (N-N)N in GaN: High frequency EPR and ENDOR study, Phys. Rev. B **90** (2014) 85203. DOI:10.1103/PhysRevB.90.085203

# SANTRAUKA

## Įvadas

Šiuolaikinėje mikroelektronikoje, nanoelektronikoje ir optoelektronikoje plačiai naudojami plataus draustinių energijų tarpo puslaidininkiai, kurie, dėl savo elektrinių, optinių bei mechaninių savybių, yra perspektyvūs optoelektronikos, didelės galios bei dažnio prietaisų gamybai, pritaikomų medicinos, telekomunikacijų ir radiacijos detekcijos bei dozimetrijos srityse [1]. Radiacija (priklausomai nuo dalelių tipo ir energijos) gali sukurti defektus medžiagoje [2], kurie lemia įrenginių funkcinių charakteristikų pokyčius. Galio nitridas (GaN) yra plataus draustinių energijų tarpo puslaidininkis, pasižymintis gana didele atominio poslinkio energija. Tai yra labai svarbi savybė nulemianti medžiagos atsparumą radiacinei pažaidai [3,4,5]. Dėl šių savybių GaN yra perspektyvi medžiaga saulės spektro šviesai nejautrių foto sensorių ir radiacijai atsparių, pasižyminčių nedidele nuotėkio srove bei patikimai funkcionuojančių aukštoje temperatūroje dalelių detektorių gamybai. Šios dalelių detektorių savybės yra itin svarbios jiems veikiant radiacinėje aplinkoje, pavyzdžiui, aukštųjų energijų fizikos eksperimentuose, dalelių greitintuvuose. Dėl liuminescencinių savybių GaN taip pat yra perspektyvi medžiaga dvigubo atsako dalelių detektorių gamybai. Tačiau radiacinė pažaida nulemia dalelių detektorių funkcinių charakteristikų degradaciją. Siekiant pagaminti kokybiškus ir ilgai tarnaujančius dalelių detektorius, yra svarbu prognozuoti jų charakteristikų kaitą po sąveikos su aukštų energijų spinduliuotėmis.

Kondensatorinio tipo didelio jautrio dalelių detektoriai gali būti formuojami naudojant didelės savitosios varžos ( $\geq 10^6 \Omega\text{cm}$ ) ir didelio storio (300-600  $\mu\text{m}$ ) GaN kristalus [6]. Panaudojant šių kristalų liuminescencines savybes bei radiacinės pažaidos nulemtą jų kaitą, GaN yra tinkamas nesąlytinių optinio atsako dozimetrijai gamybai. Santykinai ploni GaN kristalai auginami cheminio nusodinimo iš metalo-organinių medžiagų garų fazės (MOCVD), o didesnio storio kristalams auginami naudojamos hidridų garų fazės epitakcijos (HVPE) bei amono-terminė (AT) technologijos. Tačiau kristalo auginimo metu defektų bei priemaišų susidarymas gardelėje yra neišvengiamas, o jų tipas bei koncentracija priklauso nuo auginimo proceso parametrų. Šie pokyčiai kristalo gardelėje nulemia funkcinių prietaisų charakteristikų pokyčius, pavyzdžiui: išaugusių nuotėkio srovę, sumažėjusį krūvio surinkimo efektyvumą. Taip pat didelė savitoji GaN varža dažniausiai pasiekama tikslingai į kristalą įterpant priemaišas, nulemiančias akceptorinius energijos lygmenis draustinės energijos juostoje. Dėl šių



priežasčių, ieškant tinkamų medžiagų patikimų įrenginių gamybai, yra svarbu charakterizuoti išėties bei apšvitintas medžiagas, identifikuojant defektus bei priemaišas. Įvairių matavimo metodikų vystymas tam įgyvendinti taip pat turi didelę metodologinę reikšmę.

Šiame darbe aprašytos matavimų metodikos, išvystytos subtilesniems eksperimentiniams tyrimams. Esminiai rezultatai gauti kombinuojant mikrobangomis zondojuojamo fotolaidumo kinetikų metodą (angl. *Microwave probed photoconductivity* - MW-PC), fotoluminescencijos spektroskopiją (angl. *Photoluminescence* - PL), impulsinę fotojonizacijos spektroskopiją (angl. *Pulsed photo-ionization spectroscopy* - PPIS), pozitronų anihiliacijos spektroskopiją (PAS) ir elektronų sukinių rezonanso spektroskopiją (ESR). Šios metodikos buvo pasitelktos siekiant charakterizuoti GaN bandinių optines bei elektrines savybes bei identifiukuoti kristalo gardelės defektus bei priemaišas.

Siekiant nustatyti priemaišų įtaką GaN optinėms bei elektrinėms savybėms, buvo ištirti įvairiomis priemaišomis legiruoti (GaN:C, GaN:Fe, GaN:Mg, GaN:Mn) GaN dariniai bei AlGaN junginiai su įvairiomis Al koncentracijoms. Siekiant nustatyti kokią įtaką medžiagų optinėms bei elektrinėms savybėms turi radiacijos sukurti defektai bei juos identifiukuoti, tiriamų medžiagų dariniai buvo apšvitinti įvairių energijų bei įteklių hadronais, elektronais bei gama spinduliuote.

### Darbo tikslas ir naujumas

Šio darbo tikslas buvo ištirti išėties bei apšvitintus GaN bandinius ir įvertinti kokią įtaką apšvitos daro GaN optinėms bei elektrinėms savybėms. Elektriškai aktyvių defektų transformacijos GaN buvo ištirtos, siekiant panaudoti sukauptas žinias vystant dalelių detekcijos bei dozimetrijos technologijas. Šiam tikslui pasiekti, suformuluoti tokie uždaviniai:

- Ištirti optines bei elektrines GaN savybes prieš ir po įvairių dalelių apšvitos.
- Identifiukuoti technologinius bei radiacijos sukurtus defektus GaN.
- Aptiktas elektriškai aktyvių defektų GaN transformacijas po apšvitų skirtingomis dalelėmis pritaikyti dalelių detekcijos bei dozimetrijos metodų vystymui.
- Suformuoti hibridinio bei tripleksinio sensorių prototipus GaN pagrindu ir išvystyti metodikas bei įrangą jų nuskaitymui.

## Ginamieji teiginiai

1. van Roosbroeck-Shockley metodas yra tinkamas Stokso poslinkio tarp GaN sugerties ir emisijos spektrų įvertinimui.
2. Fotojonizacijos, fotoluminescencijos bei pozitronų anihiliacijos spektroskopijos metodų kombinavimas leidžia atskleisti radiacinių defektų GaN transformacijų evoliuciją.
3. Apšvitos hadronais sudarytų spindulinių bei nespindulinių rekombinacijos centrų GaN struktūrose elektrinio ir optinio atsako signalų sinchroniniai matavimai leidžia sukurti dvigubo atsako apšvitos detektorius ir dozimetrus.
4. Hibridinis daugiasluoksnis detektorius, kurį sudaro scintiliatoriaus sluoksnis iš GaN ir fotoelektrinio atsako sluoksnis, pagamintas iš aukštos kokybės, didelės varžos puslaidininkio, atskirti organiniu alanino dozimetru bei matomo spektro filtravimo, elektrinės izoliacijos ir pasyvavimo sluoksniais, veikiantis impulsiniu bei nuostovios veikos režimais, gali būti panaudotas nesąlytinei dalelių tipo bei energijos identifikacijai, taip pat didelių dalelių įtėkių dozimetrijai.

## Autoriaus indėlis

Pagrindinė eksperimentinių matavimų dalis bei modeliavimai buvo atlikti autoriaus, bendradarbiaujant su kolegomis dr. T. Čeponiui, dr. J. Pavlov, dr. V. Rumbauskui. Bandiniai buvo apšvitinti protonais bendradarbiaujant su dr. V. Kovalevskij. Neutronais bandiniai apšvitinti Jožef Stefan institute (Liubliana) TRIGA reaktoriuje. Elektronais bei  $\gamma$ -spinduliuote bandiniai buvo apšvitinti Nacionaliniame vėžio institute. Rezultatų interpretacija parengta kartu su darbo vadovu prof. habil. dr. E. Gaubu.

## Įvairios technologijos GaN optinės savybės ir technologiniai defektai

Darbe buvo ištirti garų fazės epitaksijos (HVPE) būdu užauginti ir skirtingomis anglies koncentracijomis (santykinai nedidele (LD) ir didelėmis (HD1 ir HD2)) legiruoti GaN bandiniai. Išmatavus optinės sugerties koeficientą  $\alpha$ , santykinai didelio storio ( $\sim 400 \mu\text{m}$ ) bandiniuose buvo aptiktas staigus optinio pralaidumo sumažėjimas, bangos ilgiui artėjant link ultravioletinio (UV) spektro ruožo. Didžiausias optinės sugerties pokytis gautas ties  $h\nu = 3.30 \text{ eV}$  fotono energija, kai  $\alpha_{\text{HD1}} > \alpha_{\text{HD2}}$ . Galima daryti išvadą, kad HD serijos bandiniuose ties  $3.30 \text{ eV}$  išaugusi sugertis ( $\alpha$ ) yra sietina su didesne anglies legirantų koncentracija, ir didžiausia anglies koncentracija yra HD1 bandinyje. Nustatyta absoliutinė pagavimo skerspjūvio ties  $h\nu = 3.30 \text{ eV}$  fotono energija vertė  $\sigma|_{h\nu \approx 3.30 \text{ eV}} = 1.6 \times 10^{-13} \text{ cm}^2$ .

Didelės koncentracijos anglies legirantų, kaip kompensacinių centrų, efektyvumas  $\varepsilon = N_{\text{C,A}}/N_{\text{D}}$  įvertintas  $\varepsilon \sim 10^{-2}$ , o jo mažėjimas aptiktas augant legirantų koncentracijai. Tai gali būti susieta su anglies klasterių formavimusi esant didelėms anglies legirantų koncentracijoms.

PL spektruose, užregistruotuose anglimi legiruotuose GaN bandiniuose žadinant UV lazerio spinduliuote, aptikta smailė geltonajame (Y) matomos šviesos spektro ruože ties  $\sim 2.2 \text{ eV}$  fotono energija bei mažesnės amplitudės maksimumas UV ruože ties  $3.4 \text{ eV}$  fotono energija. Didesnė PL signalo amplitudė tiek ties Y, tiek ties UV vertėmis registruota LD bandinio spektre, atžvilgiu registruotų amplitudžių HD1 ir HD2 medžiagoje. Taip pat nustatyta, kad signalo amplitudė priklauso ir nuo bandinio žadinamo šviesa paviršiaus. Ši paviršių asimetrija PL signalo amplitudės kitimuose gali būti nulemta anglies legirantų bei kitų priemaišų koncentracijos pasiskirstymo gradiento bei asimetriškos paviršinės rekombinacijos spartos.

PL intensyvumo sumažėjimas mėlynosios–ultravioletinės (B-UV) liuminescencijos spektro diapazone gali būti nulemtas PL reabsorbcijos, kuri pasiekia didžiausią vertę ties  $3.3 \text{ eV}$ . B-UV ruožo PL intensyvumo skirtumai tarp bandinių siejami su anglies legirantų koncentracijos variacijomis - medžiagoje su didžiausia anglies koncentracija registruojamas mažiausias signalo intensyvumas.

PL spektrai žaliosios-geltonosios-raudonosios (450–700 nm) PL spektriniame ruože buvo užregistruoti žybsninės kameros (angl. *Streak camera* - SC) metodu. Šiuose spektriniuose tyrimuose būtina naudoti didelio intensyvumo sužadimą ( $n_{\text{ex}} \geq 10^{18} \text{ cm}^{-3}$ ) impulsine UV lazerio spinduliuote. Spektrai buvo sumodeliuoti aproksimuojant Gauso formos spektriniais komponentais. Visas spektras modeliuojamas kaip Gausio formos komponentų suma, naudojant skirtingus amplitudės bei pločio parametrus

skirtingiems Gauso formos komponentams. Sumodeliuotų spektrinių smailių pozicijos atitiko 535 nm, 595 nm ir 690 nm bangos ilgių vertes. Spektrinės smailės ties 595 nm amplitudės HD1 bei HD2 medžiagų spektruose yra santykinai mažesnės, lyginant su LD bandinio spektru, o LD bandinio spektre 535 nm ir 595 nm spektrinių smailių amplitudės yra artimų verčių. Smailės ties 535 nm spektrinio komponento plotis visų bandinių spektruose yra siauresnis, lyginant su 595 nm ir 690 nm bangos ilgių vertes atitinkančių smailių Gauso formos spektriniais komponentais.

Anglimi legiruotų bandinių PPI spektrų laipteliai buvo sumodeliuoti naudojant Kopylov-Pikhtin modelį [22]. Visų LD, HD1 bei HD2 medžiagų spektruose, 1.3 – 3.3 eV fotonų energijų spektriniame ruože buvo išskirti septyni spektriniai laipteliai, sietini su giliaisiais foto-aktyviais centrais. Derinant su centrams priskirtinų aktyvacijos energijų literatūros duomenimis, šie centrai buvo identifikuoti kaip anglies įterptinis atomas ( $C_i$ ) [29,30], kaip su anglimi siejami defektai [29,30], kaip galio vakansija ( $V_{Ga}$ ) [31,32], kaip anglies pakaitinis atomas azoto mazge ( $C_N^-$ ) [33], kaip pakaitinių anglies ir deguonies atomų azoto mazguose kompleksai ( $C_N O_N$ ) [33], atitinkamai.

Siekiant susieti sumodeliuotus PPI laiptelius su PL spektro smailėmis, buvo pasitelktas van Roosbroeck-Shockley metodas [34,35], kuris leidžia modeliuoti Stokso poslinkį tarp PPI spektro laiptelių ir atitinkamų PL spektro smailių. Naudojant defektų parametrus, įvertintus iš PPI spektrų HVPE GaN:C bandiniuose, gautas geras modeliųjų bei eksperimentinių PL spektrų formos ir struktūros atitikimas. Analogiškai buvo sumodeliuotos PL ir PPI spektrų sąsajos HVPE būdu užaugintiems GaN:Mg ir GaN:Fe kristalams, bei AT būdu užaugintiems GaN:Mg ir GaN:Mn dariniams 0.6 – 1.2 eV spektriniame ruože.

#### Neutronų apšvitos nulemtų elektrinių bei optinių savybių transformacijos GaN

Darbe buvo palyginti išeities bei įvairiais neutronų įtėkiais ( $\Phi = 1 \times 10^{12} - 5 \times 10^{16} \text{ cm}^{-2}$ ) apšvitintų AT auginimo technologijos GaN:Mn ir GaN:Mg medžiagų PPI eksperimentiniai spektrai bei sumodeliuoti gardelės defektų nulemti spektriniai laipteliai. GaN:Mn bandinyje buvo išskirti keturi PPI spektro laipteliai, sietini su Mn [39,44] ir  $Ga_I$  [38] centrais bei neidentifikuotu defektu. Mg legiruotame GaN buvo išskirti septyni spektriniai laipteliai, sietini su donoriniu centru [46] ir su Mg [47],  $V_{Ga}$  [31],  $Ga_I$  [38] bei  $V_N$  [38] centrais. Pasirodė, kad Mn priemaišoms priskiriamų centrų koncentracija nepriklauso nuo neutronų įtėkio. Krūvininkų gyvavimo trukmės sumažėjimas yra būdingas visiems keturiems centrams. Tai leidžia daryti išvadą, kad PPI

spektras yra nulemtas pradinio fotoaktyvių centrų užpildymo. Remiantis eksperimentiniais rezultatais, galima manyti, kad radiacijos sukurti defektai turi didžiausią įtaką neidentifikuoto defekto ( $E = 2.99$  eV) koncentracijai, kuri sumažėja proporcingai neutronų įtėkiui.

Mg legiruoto GaN PPI spektre didžiausias amplitudės pokytis gautas spektro laipteliuose, siejamuose su  $V_{Ga}$  ir  $Ga_I$ , centrais.  $V_{Ga}$  defekto nulemtas spektrinis laiptelis, asocijuojamas su 2.48 eV energijos lygmeniu, spektre atsiranda tik prie santykinai didelių neutronų įtėkių ( $>10^{14}$  n/cm<sup>2</sup>). Šis defektas veikia, kaip greitos rekombinacijos centras.  $V_{Ga}$  įtaka GaN krūvininkų rekombinacijos trukmei tampa pastebima, kai ji pasidaro trumpesnė už krūvininkų rekombinacijos trukmę išėities medžiagose. Visų identifikuoatų defektų fotojonizacijos skerspjūvių vertės yra artimos. Tai leidžia manyti, kad neutronų apšvita įtakoja tik pradinį technologinių defektų lygmenų užpildymą.

Ryškus PL signalo amplitudės sumažėjimas Mn ir Mg legiruotuose AT GaN medžiagose aptiktas po apšvitų santykinai dideliu neutronų įtėkiu ( $>10^{16}$  n/cm<sup>2</sup>). Labai tikėtina, kad plati geltonos-žalios (YG) PL spektro juosta yra sudaryta iš keleto (trijų GaN:Mn ir penkių GaN:Mg, atitinkamai) persidengiančių liuminescencijos spektro smailių. Šių smailių parametrai buvo įvertinti jau minėtu van Roosbroeck-Shockley metodu, susiejant PPI sugerties ir PL emisijos spektrus.

Remiantis pozitronų anihiliacijos spektrų (PAS) eksperimentiniais duomenimis, nustatyta, kad išėities AT GaN:Mn pasižymi žymiai didesne vakansijų koncentracija, lyginant su AT GaN:Mg. Tai siejama su ilgesne pozitronų gyvavimo trukme. PAS rezultatai pagrindžia ir tai, jog neutronų apšvita turi labai nedidelę įtaką pozitronų gyvavimo trukmei AT GaN:Mn, kai lyginama su PAS spektriniais parametrais, įvertintais AT GaN:Mg medžiagose. Pozitronų gyvavimo trukmės išaugimas GaN:Mg po apšvitos neutronais yra sietinas su Ga vakansijų koncentracijos išaugimu.

Palyginus PAS bei PL eksperimentinius duomenis, daroma išvada, kad neutronų apšvitos sukurtos Ga vakansijos GaN kristale veikia kaip nespindulinės rekombinacijos centrai, kurių koncentracijos išaugimas lemia PL signalo amplitudės mažėjimą bei pozitronų gyvavimo trukmės pailgėjimą. Šis efektas ryškesnis AT GaN:Mg bandinyje dėl mažesnės kristalo augimo metu susidariusių Ga vakansijų koncentracijos.

Radiacijos detektoriai bei dozimetrijos instrumentai sukurti GaN pagrindu

Šiame tyrimų cikle buvo išnagrinėtos keturių sudėčių GaN/AlGaN *mesa* struktūros, sudarytos iš 1  $\mu\text{m}$  storio GaN sluoksnio bei po juo esančių AlGaN sluoksnių, kuriuose kito Al kiekis (0%, 8%, 44%, 75%). Siekiant ištirti protonų apšvitos įtaką bandinių liuminescencijos spektrų struktūrai, spektrai buvo *in situ* registruojami matuojant PL signalus iš skirtingo Al kiekio *mesa* struktūros sluoksnių. Nustatyta, kad pagrindiniai kitimai pasireiškia geltonai žaliosios (YG) liuminescencijos spektro ruože. Šios spektro juostos intensyvumas mažėja didėjant protonų įtėkui. Gauta, kad spektro pokyčiai yra ryškiausi GaN/AlGaN sluoksniuose su nedideliu Al kiekiu (0% ir 8%). Remiantis šiais rezultatais įvertinta, kad AlGaN struktūros yra tinkamos protonų detekcijai, o, sukilibravus liuminescencijos spektro komponentių pokyčius, protonų apšvitos dozimetrijai.

Siekiant identifikuoti atskiras AlGaN liuminescencijos spektrų komponentes, spektrai buvo sumodeliuoti pasitelkiant PPI spektrų parametrus. Buvo identifikuoti trys spektro komponentai: smailės ties 2.57 eV, 2.31 eV ir 2.10 eV buvo priskirtos  $(\text{C}_\text{N}\text{O}_\text{N})^0$ ,  $\text{C}_\text{N}^-$  ir  $\text{V}_\text{Ga}$  defektams, atitinkamai.

Siekiant suformuoti spinduliuočių sensorius taip pat buvo ištirti trys komerciniai foto-detektoriai (GUVA, GUVB, GUVVC), pagaminti kaip planariniai Šotkio diodai sudaryti iš AlGaN sluoksnių su skirtingu Al kiekiu (0%, 32%, 50%). Įvertinus skirtingų spektrinių komponentių liuminescencijos spektruose kitimus, nustatyta, kad 1.5 – 2.5 eV spektro ruožo komponentės amplitudė mažėja, o 2.5 – 3.5 eV spektro ruožo amplitudė auga, didėjant protonų įtėkui. Didžiausias pokytis buvo registruojamas dariniuose su didžiausiu (50%) Al kiekiu.

Trumpojo jungimo srovės  $I_{\text{SC}}$  pokyčiai, sinchroniškai su liuminescencijos spektrais *in situ* išmatuoti AlGaN dariniuose, ženkliai priklauso nuo Al kiekio. Didžiausias  $I_{\text{SC}}$  pokytis, didėjant protonų įtėkui, gautas GaN medžiagoje (GUVA). Didėjantis su Al kiekiu draustinių energijų juostos tarpas nulemia  $I_{\text{SC}}$  sumažėjimą. Todėl registruotinas  $I_{\text{SC}}$  pokytis didesnio Al kiekio medžiagoje matomas tik prie didesnių įtėkių. Todėl AlGaN medžiagoje su 32% Al kiekiu gali būti pamatuotos  $\Phi > 3 \times 10^{13}$  p/cm<sup>2</sup> įtėkių vertės, o AlGaN medžiagoje su 50% Al -  $\Phi > 10^{14}$  p/cm<sup>2</sup> įtėkių vertės. Remiantis gautais rezultatais, galima teigti, kad AlGaN liuminescencijos spektrų bei AlGaN pagrindu suformuotų Šotkio diodų trumpo jungimo srovės pokyčių registravimas yra patikimi didelių įtėkių protonų apšvitos dozimetrijos metodai, kuriuos galima naudoti kuriant dvigubo atsako dalelių detektorius.

Siekiant užregistruoti protonų pluoštelio profilį buvo ištirti santykinai ploni ( $\sim 3 \mu\text{m}$ ) MOCVD GaN bandiniai. Pradžioje, bandinio liuminescencijos spektro pokyčiai buvo registruojami *in situ*, apšvitinant juos homogenišku protonų pluošteliu, kurio matmenys viršijo bandinio matmenis. Tai atlikta siekiant sukalibruoti YG spektro ruožo liuminescencijos amplitudės verčių pokyčius, kaip funkciją nuo protonų įtėkio. Sukalibravus PL intensyvumų kitimų, priklausančių nuo apšvitos įtėkio, dydžius, GaN bandinys buvo apšvitintas santykinai siauru protonų pluošteliu, kurio matmenys buvo mažesni už bandinio plotą. Apšvitinto bandinio PL spektrai buvo registruojami žadinant bandinį UV lazerio spinduliuote. Pasinaudojant prieš tai atlikta liuminescencijos signalo amplitudės, kaip funkcijos nuo protonų įtėkio kalibracija, gautos PL spektro amplitudės vertės buvo perskaičiuotos į protonų įtėkio vertes. Remiantis šiais rezultatais, daroma išvada, kad GaN PL spektrų pokyčių, kaip funkcijos nuo bandinio koordinatės registravimas, yra patikimas metodas dalelių pluoštelių profiliams registruoti.

Šiame darbe buvo sukurtas tripleksinis kryptinis detektorius, skirtas radiacijos šaltinio vietos nustatymui, spinduliuotės tipo identifikavimui, apšvitos dozės kitimo spartos įvertinimui bei nuotolinei dozimetrijai. Ši detektorių sudaro trys sluoksniai: i) mikrobangomis zonduojamas foto-detektorius suformuotas iš santykinai didelio storio, aukštos kokybės, didelės savitosios varžos puslaidininkio; ii) tarpinio alanino sluoksnio; iii) plono GaN sluoksnio scintiliatoriaus. Sukauptos apšvitos dozės pasiskirstymas per visą detektoriaus struktūrą priklauso nuo jo orientacijos spinduliuotės šaltinio atžvilgiu. GaN scintiliatoriaus sluoksnio, jį žadinant UV lazerine spinduliuote, PL atsako amplitudė priklauso nuo surinkto dalelių įtėkio, o liuminescencijos spektro struktūra yra nulemta dalelių tipo, detektoriui veikiant dalelių identifikavimo režimu. Vidurinis alanino sluoksnis skirtas tiksliai įvertinti detektoriaus sukauptą apšvitos dozę, nepriklausančią nuo spinduliuotės tipo. Radiacija alanine sukuria laisvuosius radikalus, kurių koncentracija yra proporcinga registruojamo ESR signalo amplitudei. Tarpinis alanino sluoksnis taip pat veikia, kaip filtras žadinančiajai IR lazerinei bei zonduojančiajai mikrobangų spinduliuotėms, naudojamoms foto-sensoriaus sluoksnio nuskaitymui. Trečiasis aukštos kokybės, didelės savitosios varžos puslaidininkio (pvz.: Si) sluoksnio atsakas nuskaitymas naudojant MW-PC metodiką. Apšvitos sukurti defektai, veikiantys kaip rekombinaciniai centrai, nulemia nepusiausvirųjų krūvininkų gyvavimo trukmės sumažėjimą. Atlikus nepusiausvirųjų krūvininkų gyvavimo trukmės, kaip funkcijos nuo dalelių įtėkio, kalibraciją, galima įvertinti sluoksnio apšvitos įtėkį ir įvertinti apšvitos dalelių stabdymo gylį, tuo būdu nusakant ir apšvitos tipą. Siekiant padidinti

spinduliuotės krypties nustatymo tikslumą, keletas trigubo atsako detektorių gali būti montuojami į dvimates arba trimates struktūras.

### Išvados

1. Atlikta impulsinės fotojonizacijos ir fotoluminescencijos spektrų GaN dariniuose kombinuota analizė. Siekiant susieti defektų fotojonizacijos ir infraraudonosios fotoluminescencijos spektrus, buvo panaudotas van Roosbroeck-Shockley metodas. Buvo identifikuoti defektai, kurių energijos lygmenys siejami su fotojonizacijos spektro struktūros laipteliais bei fotoluminescencijos spektro smailėmis.
2. Siekiant iširti neutronų spinduliuotės įtaką GaN darinių defektams, buvo pasitelktos ir kombinuojamos impulsinės fotojonizacijos, fotoluminescencijos bei pozitronų anihiliacijos spektroskopijos metodikos. Aptikti defektai buvo identifikuoti bei įvertinta radiacijos įtaka jų koncentracijoms. Naudotos metodikos yra patikimos radiacijos dozimetrijai GaN.
3. Parodyta, kad protonų apšvitos sukurtų nespindulinių bei spindulinių rekombinacijos centrų analizė yra patikimas metodas charakterizuojant medžiagas dvigubo (optinio ir elektrinio) atsako detektorių kūrimui.
4. Suformuotas hibridinio daugiasluoksnio detektoriaus prototipas, susidedantis iš scintiliatorinio GaN, fotoelektrinio atsako aukštos kokybės bei didelės savitosios varžos Si ir organinio dozimetrom, taip pat veikiančio, kaip šviesos filtro bei elektrinio izoliatoriaus, sluoksnio. Buvo išvystytos jo nuskaitymo metodikos bei sukurti tam skirti įrenginiai. Detektoriaus prototipas buvo aprobuotas tiek nuolatinės tiek impulsinės veikos režimais. Šis detektorius yra tinkamas apšvitos dalelių tipo identifikavimui ir didelių apšvitos įtėkių matavimams.



## CURRICULUM VITAE

**Name:** Laimonas  
**Surname:** Deveikis  
**Date of birth:** 1993-04-01  
**e-mail:** laimonas.deveikis@gmail.com

### **Education:**

2018 – 2022 Vilnius University, Faculty of Physics  
*PhD studies*

2016 – 2018 Vilnius University, Faculty of Physics  
*Master's degree in Semiconductor Science and Technology*

2012 – 2016 Vilnius University, Faculty of Physics  
*Bachelor's degree in Modern Technology Physics and Management*

2008 – 2012 Panevėžys Vytautas Žemkalnis Gymnasium

### **Work experience:**

2019 – 2022 Vilnius University, Institute of Photonics and Nanotechnology  
*Junior research fellow*

2016 – 2019 Vilnius University, Institute of Applied Science  
*Engineer*

2015 Vilnius University, Institute of Theoretical Physics and Astronomy  
*Technician*

# COPIES OF PUBLICATIONS

A1

Electrical characterization of HVPE GaN  
containing different concentrations of  
carbon dopants

E. Gaubas, T. Čeponis, **L. Deveikis**, D. Meškauskaitė, J. Pavlov, V.  
Rumbauskas, M. Bockowski, B. Lucznik

Semicond. Sci. Technol. **33** (12) (2018) 125024.

DOI:10.1088/1361-6641/aecf0

(Reprinted with permission from IOP Publishing, Ltd)

PAPER

# Electrical characterization of HVPE GaN containing different concentrations of carbon dopants

To cite this article: E Gaubas *et al* 2018 *Semicond. Sci. Technol.* **33** 125024

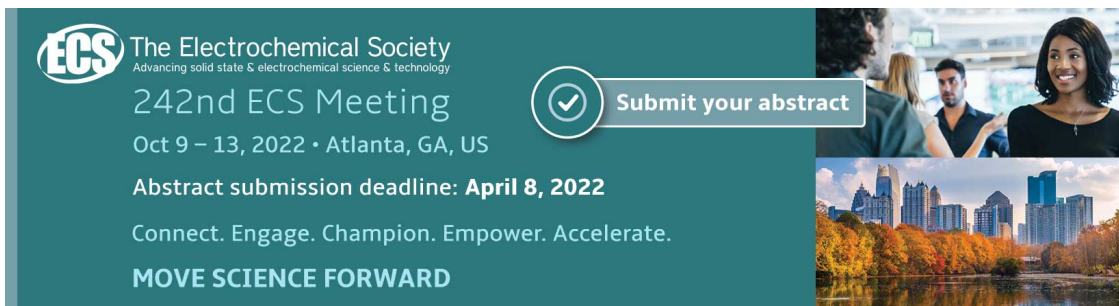
View the [article online](#) for updates and enhancements.

## You may also like

- [Growth of low-threading-dislocation-density GaN on graphene by hydride vapor phase epitaxy](#)  
Shunyu He, Yu Xu, Lin Qi *et al.*
- [The hydride vapor phase epitaxy of GaN on silicon covered by nanostructures](#)  
U Jahn, M Musolino, J Lähnemann *et al.*
- [Micro-Raman studies of strain in bulk GaN crystals grown by hydride vapor phase epitaxy on ammonothermal GaN seeds](#)  
M. Amilusik, D. Włodarczyk, A. Suchocki *et al.*

## Recent citations

- [Plasma and Annealing Treatments to Form Height-Barrier Ni-Based Schottky Contact to \*n\*-GaN](#)  
Tae-Ju Lee *et al*



The Electrochemical Society  
Advancing solid state & electrochemical science & technology

242nd ECS Meeting  
Oct 9 – 13, 2022 • Atlanta, GA, US

Abstract submission deadline: **April 8, 2022**


Connect. Engage. Champion. Empower. Accelerate.

**MOVE SCIENCE FORWARD**

Submit your abstract

This banner features the ECS logo, meeting details, a submission deadline, a slogan, and a 'Submit your abstract' button with a checkmark icon. It also includes two images: one of people in a meeting and another of a city skyline with a lake.

# Electrical characterization of HVPE GaN containing different concentrations of carbon dopants

E Gaubas<sup>1,3</sup> , T Čeponis<sup>1</sup>, L Deveikis<sup>1</sup>, D Meskauskaitė<sup>1</sup>, J Pavlov<sup>1</sup>, V Rumbauskas<sup>1</sup>, M Bockowski<sup>2</sup> and B Lucznik<sup>2</sup>

<sup>1</sup>Institute of Photonics and Nanotechnology, Vilnius University, Sauletekio av. 3, LT-10257 Vilnius, Lithuania

<sup>2</sup>Institute of High Pressure Physics, Sokolowska 29/37, 01-142 Warsaw, Poland

E-mail: [eugenijus.gaubas@ff.vu.lt](mailto:eugenijus.gaubas@ff.vu.lt)

Received 9 July 2018, revised 20 September 2018

Accepted for publication 31 October 2018

Published 20 November 2018



CrossMark

## Abstract

A comprehensive study of the electrical characteristics in Schottky diodes made of GaN:C grown by hydride vapour phase epitaxy (HVPE) technology has been reported. The Schottky junctions were made of an Ni/Au (25/200 nm) metal stack and ohmic contacts were fabricated by Ti/Al/Ni/Au (30/90/20/100 nm) e-beam deposition of the metal thin-films followed by rapid thermal annealing. A good quality of the fabricated Schottky diodes has been proved by considering the transient shape using a pulsed technique of barrier evaluation under linearly increasing voltage (BELIV). The concentrations of equilibrium carriers of  $1 \times 10^{11} \text{ cm}^{-3}$  and of  $2 \times 10^{10} \text{ cm}^{-3}$  have been evaluated for relatively low and high carbon density doped samples, respectively, using photo-capacitance characteristics dependent on excitation intensity. The effective mobility of carriers of  $\mu_{\text{eff}} = 610 \text{ cm}^2/\text{Vs}$  has been estimated by considering the serial resistance variations dependent on excitation density, through analysis of delay times that appeared in the formation of peaks within BELIV transients. Optical deep level transient spectroscopy has shown that thermal emission from the rather shallow centres prevails. The centres, ascribed to vacancies as well as to carbon on Ga sites, have been identified. It has been demonstrated that Schottky junctions made of heavy carbon doped ( $N_C \geq 10^{18} \text{ cm}^{-3}$ ) HVPE GaN material are able to withstand voltages of  $\geq 300 \text{ V}$ .

**Keywords:** carbon doped HVPE GaN grown on Ammono substrates, deep level transient spectroscopy, transient current technique, barrier evaluation by linearly increasing voltage pulsed technique, Schottky diodes

(Some figures may appear in colour only in the online journal)

## 1. Introduction

The III-nitride materials are promising for high-power and high-frequency electronics [1–4] due to their large breakdown voltage and rapid response [5]. GaN devices are also promising as future particle detectors due to radiation hardness [5, 6]. GaN is also a promising material in the production of devices for chemical, gas, biological and pressure sensing [7], for radiation imaging applications [8] and in the fabrication of

high energy particle detectors [6, 9–11] operating in harsh environments. GaN can be employed for the detection and tracking of high-energy particles or dosimetry by recording both electrical and optical signals [11–14]. The suitability of GaN materials for sensor formation depends on the fabrication technology utilised and their doping and compensation levels [15–17]. Doping of GaN with different impurities (e.g., Fe, Mn, Mg) enables governing of the material conductivity and device performance by compensating its natural n-type behaviour via the introduction of acceptors. Several methods to create semi-insulating materials, have been proposed, such as

<sup>3</sup> Author to whom any correspondence should be addressed.

**Table 1.** Concentration of carbon dopants, evaluated by SIMS technique, and of carbon associated traps, estimated by PPIS techniques.

Diode	Diode thickness d ( $\mu\text{m}$ )	Concentration of carbon dopants and carbon associated traps ( $\text{cm}^{-3}$ )					
		C (SIMS)	$C_1$ (PPIS)	$C_{\text{rel},1}$ (PPIS)	$C_{\text{N}}\text{-}(PPIS)$	$C_{\text{rel},2}$ (PPIS)	$(C_N O_N)^0$ (PPIS)
sh-LD	400	$2 \times 10^{17}$	$1.9 \times 10^{17}$	$8 \times 10^{14}$	$1 \times 10^{13}$	$3 \times 10^{12}$	$3 \times 10^{12}$
sh-HD1	390	$1 \times 10^{18}$	$9.9 \times 10^{17}$	$4 \times 10^{15}$	$2 \times 10^{13}$	$2 \times 10^{13}$	$2 \times 10^{13}$
sh-HD2	407	$1 \times 10^{18}$	$1.9 \times 10^{18}$	$4 \times 10^{15}$	$2 \times 10^{13}$	$2 \times 10^{13}$	$2 \times 10^{13}$

the implantation of acceptor dopants [18], the use of nitrogen as a carrier gas [19, 20] or, more commonly, doping with Fe [21] or C impurities [22]. Carbon can be intentionally incorporated into GaN to create a semi-insulating material that improves the performance of GaN based heterojunction field effect transistors [23, 24]. Also, it is important in the fabrication of particle detectors where high resistivity of the diode base region is needed. Doping with carbon also reduces the leakage current and improves the breakdown voltage of GaN power devices [25]. However, carrier trapping effects are enhanced by the presence of C-related deep levels [25, 26]. It has been shown [25, 27–29] that C determines several levels within the GaN bandgap depending on its lattice position. The main obstacle for the wide application of GaN devices remains a high density of the intrinsic technological defects, such as dislocations with densities of about  $10^8 \text{ cm}^{-2}$ . Therefore modern materials, such as ammono-thermally synthesized GaN [30–32] and hydride vapour phase epitaxy (HVPE) grown GaN on Ammono substrates [33], containing sufficiently low dislocation densities ( $<5 \times 10^4 \text{ cm}^{-2}$ ), are promising in the fabrication of fast response devices. It has been well established that various impurities and crystal imperfections of GaN, like e.g. carbon, introduce a rather rich spectrum of deep levels. These defects are able to crucially modify the electrical characteristics of GaN based devices [34–36]. Moreover, the usage of routine techniques (such as C-V's and I-V's) [35, 37–39] for the electrical characterization of devices made of semi-insulating compensated materials is aggravated.

In this work, alternative electrical characterization techniques have been applied for the comprehensive evaluation of parameters of Schottky diodes made of heavily carbon doped GaN. A methodology based on the combined measurements of dark and photo-capacitance characteristics, spectroscopy of emission centres, scanning of current transients, induced due to the injected charge drift and decay have been demonstrated. It has been shown that the rather small densities of free carriers, which are hardly measurable by routine C-V's, are obtained by the introduction of compensating carbon dopants. The semi-insulating state of diode base regions leads to full-depletion of diodes in dark conditions. Therefore, the pulsed photo-capacitance and optical-deep level transient spectroscopy (DLTS) techniques have been employed to evaluate the equilibrium carrier densities and the parameters of the charge emission traps. Several spectral and recombination characteristics have been compared with those measured on the same HVPE GaN (grown on Ammono substrates) material examined by contactless techniques and reported our recent article [36].

## 2. Samples and experimental techniques

### 2.1. Samples

The Schottky and ohmic contacts were deposited on  $\sim 400 \mu\text{m}$  thick samples, described in our previous article [36]. These GaN samples with the crystal  $c$  axis perpendicular to the sample surface were grown by HVPE by using ammonothermal (AT) GaN substrates. Wafers were both side polished to optical smoothness. Also, the wafer edge-boundaries were polished for optical illumination by steady-state or pulsed light of different spectral range.

The surface cleaning procedures, processed by etch in  $\text{H}_2\text{SO}_4\text{:H}_2\text{-3:1}$ , rinsed in de-ionized water and  $\text{N}_2$  dried, were performed before metallization. The Schottky junctions were fabricated on front surfaces that had shown the lowest surface and bulk recombination, estimated by optical techniques [36]. Metallization, to create ohmic and Schottky barriers, was implemented by vacuum evaporation procedures using electron beams (e-beam evaporation). The ohmic contacts were fabricated on the Ga-face side of the free-standing GaN wafer sample using the procedures of the Ti/Al/Ni/Au (30/90/20/100 nm) metal thin-film deposition by e-beam, followed by rapid thermal annealing (RTA), similar to the procedures referenced in [40]. The Schottky contacts were made of Ni/Au (25/200 nm) metal stack on the N-face surface.

Two sets of Schottky diodes, made of HVPE GaN containing different (low-LD and high-HD) densities of intentionally introduced carbon (GaN:C), were investigated. Concentrations  $N_C$  of the introduced carbon (C) dopants and of carrier traps associated with carbon impurities were estimated by secondary ion mass spectroscopy (SIMS) and pulsed photo-ionisation spectroscopy (PPIS) [36], respectively, and listed in table 1. There, C is the overall concentration of carbon impurities evaluated by SIMS,  $C_1$  denotes the interstitial carbon estimated by PPIS, two traps ( $C_{\text{rel},1}$  and  $C_{\text{rel},2}$ ) related to the introduced carbon impurities (which detail structure and origin are non-identified) have been revealed by PPIS,  $C_{\text{N-}}$  stands for the charged acceptors formed by carbon atoms on the N sites, and  $(C_N O_N)^0$  represents the electrically neutral complexes of carbon.

Several contact techniques were combined in characterization of the diodes made of slightly (sh-LD) and considerably (sh-HD1, sh-HD2) carbon doped HVPE GaN.

### 2.2. Techniques for evaluation of Schottky barrier and spectroscopy of carrier traps

The method of barrier evaluation by linearly increasing voltage (BELIV) [41–44] was applied to measure the pulsed

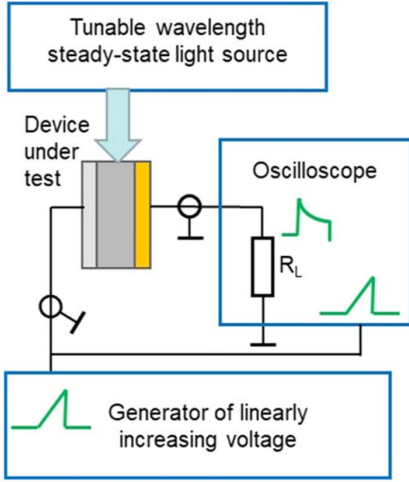


**Figure 1.** Sketch of the arrangement of instruments for implementation of the BELIV technique.

currents (appearing due to charging/recharging of the devices) in the dark and under steady-state or short laser pulse illumination. The setup of instrumentation for implementation of the BELIV technique is illustrated in figure 1.

The BELIV technique for a reverse biased diode is based on analysis of the changes of barrier capacitance ( $C_b$ ) with a linearly increasing voltage pulse,  $U_p(t) = At$ . The variations of the diode  $C_b(t) = C_{b0}(1 + U(t)/U_{bi})^{-1/2}$  with voltage  $U_p(t)$  determine a current pulse, measured on a load resistor, where the barrier capacitance for a non-biased diode of an area  $S$  is  $C_{b0} = \varepsilon\varepsilon_0 S/w_0 = (\varepsilon\varepsilon_0 S^2 e N_D / 2U_{bi})^{1/2}$ . Here,  $\varepsilon_0$  is the vacuum permittivity,  $\varepsilon$  is the material dielectric permittivity,  $e$  is the elementary charge,  $U_{bi}$  the built-in potential barrier,  $w_0 = (2\varepsilon\varepsilon_0 U_{bi} / e N_D)^{1/2}$  is the width of depletion for the non-biased junction with dopant concentration  $N_D$ ,  $A = U_p / \tau_{PL}$  is the ramp of the LIV pulse with  $U_p$  peak amplitude and  $\tau_{PL}$  duration.

The current transient  $i_C(t)$  recorded using a load resistor  $R_L$  in the external circuit is represented (with precision of thermal potential) as:

$$i_C(t) = \frac{dq}{dt} = \begin{cases} \frac{\partial U}{\partial t} \left( C_b + U \frac{\partial C_b}{\partial U} \right) = \frac{\partial U_C}{\partial t} C_{b0} \frac{1 + \frac{U_C(t)}{2U_{bi}}}{\left(1 + \frac{U_C(t)}{U_{bi}}\right)^{3/2}} \approx AC_{b0} \frac{1 + \frac{At}{2U_{bi}}}{\left(1 + \frac{At}{U_{bi}}\right)^{3/2}}, & at \ U < U_{FD} \\ \frac{\partial U}{\partial t} \left( C_{geom} + U \frac{\partial C_{geom}}{\partial U} \right) = \frac{\partial U_C}{\partial t} C_{geom} \approx AC_{geom}, & for \ U \geq U_{FD} \end{cases} \quad (1)$$

This current transient for  $U_p$  voltages below  $U_p < U_{FD}$  the full depletion voltage ( $U_{FD}$ ) contains an initial ( $t = 0$ ) step  $AC_{b0}$  due to displacement current and a descending component governed by the charge extraction. For an insulating material and for  $U_p > U_{FD}$ , this transient contains only a

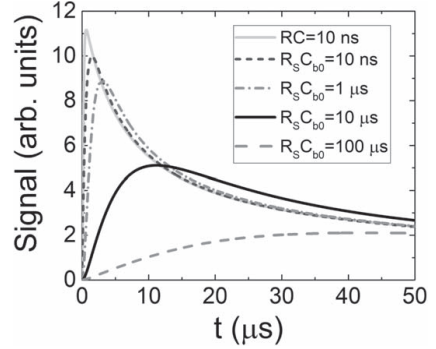


**Figure 2.** The simulated BELIV transients using different delay times appeared due to serial resistance changes ( $R_S C_{b0}$ ) through varied concentration of excess carriers. The delay in the external circuit is included through load resistance  $R_L$ .

displacement current step. For the range of  $0 < U_p \leq U_{FD}$ , the transient contains a displacement current step and a descending charge extraction component (figure 2). Values of  $N_D$  and  $U_{bi}$  can be deduced from the initial current expression  $i_C(0) = AC_{b0}$ , when delay  $R_L C_b$  can be reduced to the time-scale of the LIV pulse initial slope durations. The vertex amplitude within a BELIV transient is proportional to a value of a ramp  $A$  of LIV pulse, which is controlled by differentiating  $(dU_p/dt) = A$  the LIV pulse ( $U_p(t)$ ). The diffusion current may be a reason in formation of a pedestal for  $i_C(t)$  changes.

The generation current  $i_g(t) = en_p S w_0 (1 + U_C(t)/U_{bi})^{1/2} / \tau_g$  might appear due to carrier thermal emission from traps, and it increases with voltage  $U_C(t)$ . This  $i_g(t)$  can exceed the barrier charging current in the rearward phase of the transient. Then,  $N_D$  in expressions for  $w_0$  and  $C_{b0}$  should be replaced by its effective value  $N_{Def} = N \pm N_T^{\pm}$ , due to (compensation) charged traps of density  $N_T$ . The total reverse current is then described by a sum of the currents  $i_{R\Sigma}(t) = i_C(t) + i_{diff}(t) + i_g(t)$ . The descending component of the charge extraction and the ascending component of the generation current imply the existence of a current minimum within a current transient. For traps rich and compensated material, further increments of voltage above  $U_{FD}$  lead to the increase of current component

$i_{emFD}(t) = e(S/2d)n_0\mu_n U_C(t)$ , added to  $i_{CFD}$ . To resolve the prevailing BELIV regime, the external factors (e.g. steady-state light biasing, dc pedestal, temperature, etc) can be varied. These factors modify the occupation of the trap states and highlight the dominant components of current.

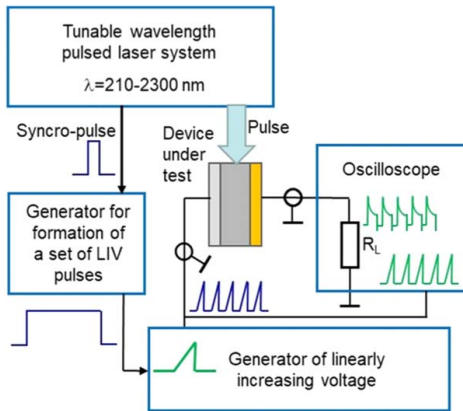


**Figure 3.** Setup of the instruments for spectroscopy of the parameters of recombination and thermal emission using BELIV technique.

At forward biasing of a diode (if the regime of minority carrier injection prevails), the total BELIV current is composed of the barrier ( $i_{CB}(t)$ ) and of the diffusion (storage) capacitance charging ( $i_{Cdiff}(t)$ ) currents and of recombination ( $i_{RC}(t)$ ) and injection/diffusion ( $i_{injC}(t)$ ,  $i_{diff}(t)$ ) ones, with  $U_F(t) = A \cdot R_L i_{\Sigma F}(t)$ .

The parameters of the recombination and thermal emission can be estimated by recording spectral variations of the set of BELIV transients generated by a single short pulse of excess carrier injection. The setup of such experiments is sketched in figure 3. There, a set of LIV pulses scan a relaxation of the concentration of excess carriers. The peak value of  $i_C(t)$  is a reciprocal of the depletion width (formed by the photo-excited free-carriers) and, thereby, it is proportional to the excess carrier concentration at the moment of appearance of a LIV pulse within the scanning sequence of LIV pulses. The spectral changes of the pulsed photo-capacitance characteristics were investigated by scanning the BELIV responses. The nanosecond OPO instrument Ekspla NT342B with pulse duration of 4 ns as well as wavelength tuning range from 210 to 2300 nm was employed for photo-excitation of carriers within a diode base-region. The excitation beam impinges there from a wafer edge boundary. A set of the BELIV transients is recorded after a single excitation pulse. The excess carriers determine an appearance of the diode-inherent BELIV transients, while the changes of the shape and components of these transients indicate manifestation of carrier recombination and thermal emission centres.

### 2.3. Deep level transient spectroscopy of emission centres

The prevailing thermal emission centers were examined by DLTS technique. Direct application of the routine C-DLTS method for the Schottky diodes made of semi-insulating GaN material is impossible, as a diode is initially full-depleted. Therefore, optical-DLTS (O-DLTS) was employed, when steady-state illumination using a blue (380 nm) LED was applied. Deep level transient spectra over a temperature range

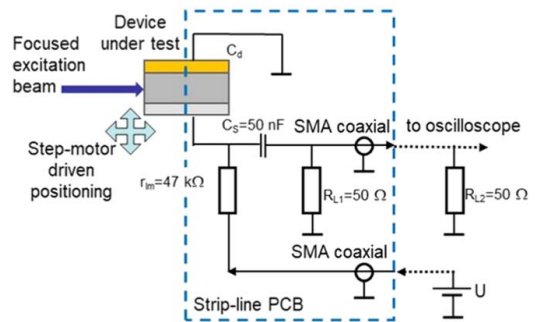


**Figure 4.** A TCT (ICDC) setup for the recording of injected charge current transients and for their profiling.

of 50–400 K were recorded on Schottky diode samples by using a HERA-DLTS System 1030 spectrometer [45]. The HERA-DLTS System 1030 spectrometer covers the scan temperature range from 10 to 450 K. The O-DLTS measurements were performed using the reverse voltage of 10 V. The measurements and data evaluation were controlled using the PhysTech software installed within the HERA-DLTS System 1030 spectrometer [45].

For the rather compensated materials and O-DLTS case, both majority and minority excess carriers determine the amplitude of the transient signal. The O-DLTS regime ( $h\nu \leq E_G$ ) is close to that employed in photo-induced current transient spectroscopy (PICTS,  $h\nu > E_G$ ) technique where transients are mainly governed by carrier density changes due to thermal emission.

As the routine procedures in DLTS methodology, the capacitance-voltage (C-V) and current-voltage (I-V) characteristics are initially measured by the HERA-DLTS System, before temperature scans. However, these characteristics were not sufficiently informative, due to compensation effects in materials with rather high densities of carbon. The dark I-V's and C-V's were more precisely measured by using Vilnius University proprietary made systems, based on a Keithley 6430 femto-ammeter, equipped with an amplifier, and a QuadTech 7600 LRC-meter, equipped with an external-voltage (for the range up to 200 and 600 V) galvanic-source.

### 2.4. Transient current technique for separation of charge transport/decay features

A transient current technique (TCT) is widely applied for the characterization of particle detectors (diode structures) [46–49] and it can also be used for a research of the carrier transport characteristics in capacitor-type devices made of wide band-gap semi-insulating materials [50–54]. This technique (TCT, alternatively, the injected carrier drift currents (ICDC)) is based on recording current transients determined by the carrier drift-diffusion-recombination processes within inter-electrode gaps due to the excess carriers induced by light or impinging ionizing radiations. The GaN Schottky diode structures studied in this work, exhibited the capacitor-like C-V characteristics, recorded in dark.



These capacitor-like devices were mounted on a strip-line PCB with equivalent  $R_L = 25 \Omega$  load resistances. An electrical

of the electron bipolar drift prolonged by the monopolar drift of holes can be represented as

$$i(t) = \begin{cases} i_1 = \frac{qS}{\tau_{r,e}} \left[ \psi_0 \exp\left(-\frac{t}{\tau_{r,e}}\right) + (1 - \psi_0) \right], & \text{for } 0 \leq t \leq \tau_{r,e} = \tau_{bC}; \\ i_2 = \frac{q_h S}{\tau_{Mq,h}} \exp\left(\frac{t}{\tau_{Mq,h}}\right) \left[ \frac{v_0 \Sigma_{bip}}{d} \tau_{Mq,h} + \frac{\tau_{Mq,h}}{\tau_{TOF,h}} - 1 \right], & \text{for } 0 \leq t \leq \tau_{r,h} \equiv \tau_{r,h,mon} \end{cases} \quad (3)$$

circuit (conventional for TCT [47, 51]), figure 4, was employed, and measurements at room temperature were performed. Here, the  $r_{lm} = 47 \text{ k}\Omega$  resistance is used for limitation of the charging current (for a  $C_S = 50 \text{ nF}$  capacitor). For biasing of the GaN capacitor  $C_d$  under test (CUD), the device is connected in series with a direct current (DC) voltage  $U$  source and  $r_{lm}$ . A circuit for a pulsed signal is then comprised of the charged source capacitor  $C_S$ , the sample capacitor  $C_d$  and the load resistor  $R_{L1} = 50 \Omega$  (on input of coaxial cable) connected in series. These elements  $C_d$ ,  $C_S$ , and  $R_{L1}$  are mounted on the strip-line PCB. The  $50 \Omega$  coaxial cable is loaded by  $R_{L2} = 50 \Omega$  on its output and at the input of a 2 GHz band digital oscilloscope LeCroy Wave Runner 620Zi, to get equivalent  $R_L = R_{L1} || R_{L2} = 25 \Omega$ . A closed input of the oscilloscope is discriminated by a few pF capacitor from the DC signals. A 30 ps pulsed PicoQuant laser driven by the PDL 800B current source was used as an excitation source at 405 nm wavelength. The time parameters, evaluated for the electrical and excitation pulse rise, lead then to the overall time-resolution  $\Delta t \cong 500 \text{ ps}$ , in our experiments. The perpendicular experimental geometry (figure 4, when excitation beam impinges perpendicularly to an applied electrical field direction) was employed. The injected charge drift current (ICDC) transients are profiled either by varying the reverse-bias DC voltage or the scanning position of the cylindrical-lens slit-focused laser beam.

Description of the currents induced by the injected carrier capture and drift in capacitor or junction type sensors can be found in [50–54]. This model has been used for the interpretation of current transients. The instantaneous current values depend on the injected charge amount and on transit time which is consequently determined by the characteristic times of dielectric relaxation  $\tau_{Mq\ e,h} = \varepsilon_0 \varepsilon d / q_{e,h} \mu_{e,h}$  and of free flight  $\tau_{TOF,e,h} = d^2 / U \mu_{e,h}$  of the sub-domains of injected carriers with mobilities  $\mu_{e,h}$ . Thereby an instantaneous velocity and the transit time depend on the injected charge ( $q_{e,h}$ ). This current also depends on time variations of the instantaneous positions of sub-domains ( $\psi_{e,h}(t)$ ). The expression for current variations in time, determined by carrier drift and capture processes, can be represented as

$$i(t) = \frac{d\sigma}{dt} S = \left[ -\frac{\partial q_e(t)}{\partial t} (1 - \psi_e(t)) - q_h(t) \frac{d\psi_h(t)}{dt} - \frac{\partial q_h(t)}{\partial t} \psi_h(t) - q_h(t) \frac{\partial \psi_h(t)}{\partial t} \right] S \quad (2)$$

for the mixed drift regime, containing stages of the bipolar and monopolar drift. The generalized expression for current

The duration of the entire pulse ( $t_p$ ) is obtained as a sum of the bipolar drift  $\tau_{bC}$  and the hole domain drift  $\tau_{r,h,mon}$ :  $t_p = \tau_{bC} + \tau_{r,h,mon}$ . The current of the bipolar drift as prolonged by the correlated hole drift (the Ramo's type [55, 56] regime) appears if  $\tau_{TOF,h} = \tau_{Mq,h}$ .

In the case of pure bipolar drift, a drift velocity appears to be invariable due to  $\psi_{e,h}(t) \sim t$ . This leads to a square-wave shape of the current pulse. The real evolution (the rise to peak) of the current should be considered by including the process of the CUD ( $C_d$ ) capacitance charging. Current decreases after the initial peak for the mixed drift regime due to a drag of the late arrived sub-domain by the counter-partner sub-domain. The later phase of the monopolar drift only contains the increasing (if  $\tau_{TOF,h} = \tau_{Mq,h}$ ) or nearly constant (if  $\tau_{TOF,h} < \tau_{Mq,h}$ ) component of velocity. Thereby the double-peak current pulse can be inherent for the mixed (a bipolar changed by a monopolar) drift regime. Duration of the double-peak current pulses significantly varies depending on external voltage. The double-peak current pulse can also appear (the so called extraction from a reservoir regime [57], at rather high excitation levels) when carrier drift-diffusion is governed by the electric field screening in the bulk and charge extraction within regions near electrodes. The current (pulse amplitude) only increases with applied voltage without any clearly observable change of pulse duration in the latter case of enhanced excitation level. A duration of the TCT/ICDC pulse (single-peak shape) is also nearly independent of the applied voltage when carrier capture-recombination processes ( $\partial q_{e,h} / \partial t$  terms in equation (2)) prevail.

### 3. Electrical characteristics of diodes made of different carbon concentration GaN

#### 3.1. C-V and I-V characteristics measured in dark

The I-V's measured in dark on sh-LD and sh-HD diodes are illustrated in figure 5(a). These characteristics were recorded keeping a rather long relaxation time between neighbour voltage changing steps. Fast ramping of voltage in diodes, made of compensated materials, usually leads to a significant shift of current minimum relative to a zero-voltage point, due to random charge emission/trapping and electric field redistribution within diode base. A slim asymmetry can be deduced from figure 5(a) for diodes. This hints at the existence of the Schottky barrier.

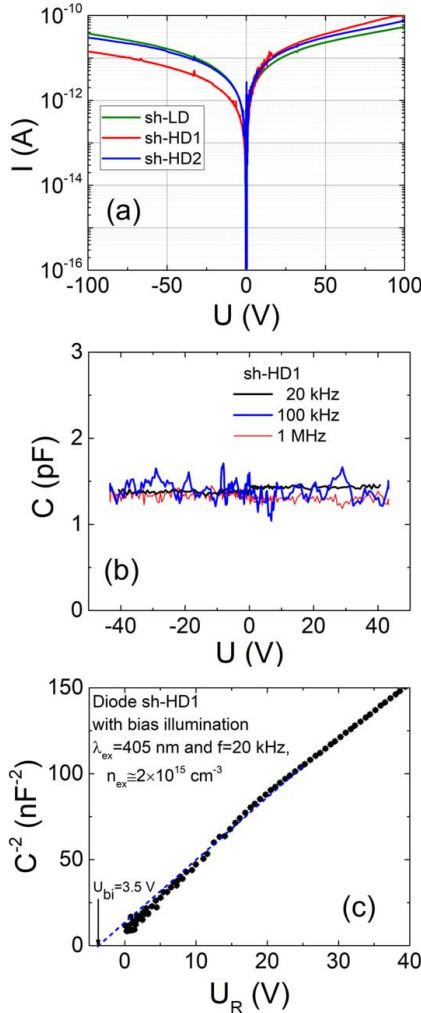


**Figure 5.** The current-voltage (a) and capacitance-voltage (b) characteristics measured in dark using Keithley and QuadTech instruments. I-V's obtained for different Schottky diodes (sh-LD and sh-HD) are illustrated in figure (a). The C-V's measured on sh-HD1 diode at different test signal frequencies are depicted in figure (b). (c) —The  $C^{-2}$  versus  $U_R$  plot deduced from the C-V characteristic measured under steady-state illumination, using 405 nm wavelength light, and 20 kHz test signal frequency.

However, the C-V's measured in dark on all the diodes (figure 5(b)) show the capacitance of a device to be nearly independent of voltage. The noises and average value of capacitance increases reciprocally to a frequency of small test signal. Sometimes these C-V's are measured at extremely low frequency (a few Hz) to reduce the impact of the serial resistance. However, the role of contact quality and the effects of random charge injection/trapping and electric field redistribution increases with the decrease of frequency, especially at the forward biasing ( $U_F$ ) regime. Simultaneously, the

quality factor of the LRC system falls down due to dissipation through carrier trapping/de-trapping from deep centres at low test signal frequencies. Therefore, I-V's and C-V's measured in dark on diodes made of deeply compensated material are not reliable and suitable for the correct evaluation of Schottky barrier and contacts.

The C-V's measured under steady-state illumination, nonetheless, exhibit nearly hyperbolic decrease of capacitance with increase of the reverse voltage ( $U_R$ ). The  $C^{-2}$  versus  $U_R$  plot (figure 5(c)) then enables a routine estimation of the built-in potential  $U_{bi}$  at the intersection point for the derivative to this curve with abscise axis, at  $U_F$ . Actually, these  $C^{-2}$ - $U_R$  characteristics depend on excitation density and test signal frequency. The optimal regime can be found by matching the dielectric relaxation time (being a function of the excess carrier concentration) and the test signal frequency (to avoid an impact of charge trapping/emission effects). Nevertheless, in the range of small voltages, this curve can be faulty (figure 5(c)), as the excess carriers modulate the partial depletion width. The value of the virtual built-in potential for the 20 kHz test signal of 20 mV amplitude has been obtained to be  $U_{bi} \approx 3.5 \pm 0.1$  eV, which is close to the band-gap of GaN at room temperature.

### 3.2. BELIV transients and photo-capacitance characteristics

The role of large serial resistance can be governed (considerably reduced) by the intensity of the photo-injection of excess carriers. A device exhibits the capacitor like BELIV transient (a square-wave pulse) when recorded in dark (inset for figure 6(a)). The steady-state illumination by using properly absorbed light wavelength leads to the diode-inherent BELIV transients (figure 6(a)) for partial depletion regime - this transient for a rather small peak voltage  $U_p$  contains an initial ( $t = 0$ ) current step  $i(t = 0) = AC_{b0}$  ascribed to the displacement current and a descending component governed by the charge extraction. Due to  $\tau_{RL} = R_L C_{b0}$ , an initial delay in the external circuit (with a load resistance  $R_L$ ) or  $\tau_{Rs} = R_s C_{b0}$  caused by a serial resistance  $R_s$  of the material within the electrically neutral region (ENR), this initial step acquires a peak shape (figure 6(a)). The amplitude of the current increases with excitation intensity (power), while a delay time increases with reduction of excess carrier concentration (excitation intensity). The long delay times eventually lead to formation of the square-wave like pulses with a long rise-to-vertex initial component. Further reduction of the intensity of the steady-state illumination intensity determines the approach of the diode-inherent BELIV transients to that of a pure square-wave shape, typical for a capacitor—namely, to the recorded in dark BELIV transients (inset for figure 6(a)).

The observed evolution of the BELIV transients (figure 6) clearly indicates that quality of the Schottky junction and ohmic contact, fabricated on HVPE GaN:C by the described metallization procedures, is good, and these contacts do not limit manifestation of the material electrical characteristics. The excess carriers thus determine variations of barrier capacitance by changing the virtual depletion width  $w$  of a diode when excess carrier density  $n_{ex}$  considerably

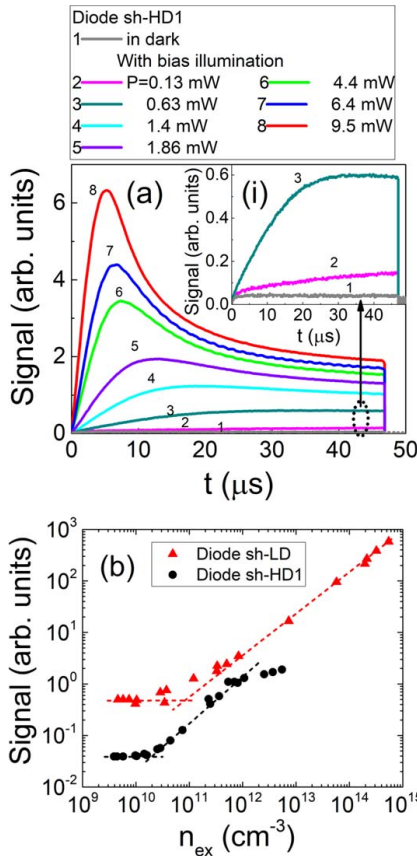


**Figure 6.** (a)—Evolution of BELIV transients with power of the steady-state illumination at  $\lambda_{ex} = 405$  nm wavelength in diodes sh-HD1. In the inset for figure (a), the BELIV transients recorded in the range of dark capacitance are depicted. (b)—BELIV current in diode sh-LD and sh-HD1 at the end of a LIV pulse, with peak-voltage of 12 V and pulse duration of 47  $\mu\text{s}$ , as a function of the excess carrier density  $n_{ex}$ . The latter  $n_{ex}$  is proportional to the power of the steady-state illumination, strip-focused onto the edge of diode boundary (of  $\sim 400$   $\mu\text{m}$  thickness and 2.5 mm length).

prevails over  $n_0$  of equilibrium ones. Actually, the photo-capacitance regime is then present. The features of the photo-diode-type device have also been corroborated by appearance of the storage (diffusion) capacitance component within BELIV transients measured at forward biasing, due to shrinkage of the built-in barrier. Values of the nearly stabilized charge extraction current at the end of the reverse-bias LIV pulse ( $t \approx 47$   $\mu\text{s}$  in figure 6(a)) can be a measure of barrier capacitance obtained for a fixed value of the LIV pulse. These parameters for BELIV transients demonstrated in figure 6(a) are:  $U_{P,LIV} = 12$  V,  $\tau_P = 47$   $\mu\text{s}$ .

The latter values of the nearly stabilized charge extraction current, ascribed to barrier capacitance at a fixed moment of charge extraction, can serve for evaluation of the equilibrium carrier concentration in the compensated (in this case

GaN:C) material. Actually, depletion width  $w$ , for the fixed parameters of a LIV pulse, increases by approaching diode thickness  $d$  with the reduction of the excess carrier concentration  $n_{ex}$ :

$$d \geq w = \left[ \frac{2\epsilon\epsilon_0(U_{bi} + U_{P,LIV})}{e(N_{d,eff} + n_{ex})} \right]^{1/2}. \quad (4)$$

Here,  $N_{d,eff}$  is the effective dopant concentration. The compensation  $\Delta K = n_0 - p_0$  of the prevailing dopants (for instance, donors of the  $N_D$  density at  $n_0 > p_0$ ) can be expressed as [58]:

$$N_{d,eff} \cong \frac{N_D n_0 + \Delta K}{2 n_0}. \quad (5)$$

$N_{d,eff}$  approaches to zero with  $p_0 \rightarrow 2n_0$ . The limit to the depletion width  $w$  changes is equality in equation (4), i.e.  $d = w_{FD}$ , meaning full-depletion condition. This appears as the transition point in the curve of the BELIV signal dependence on steady-state illumination power, where the branch of the decreasing BELIV signal with illumination power hops over the plateau curve branch (figure 6(b)), at  $n_{ex} < N_{d,eff}$ . This condition can be estimated as an intersection point for the derivatives to plateau and descending curve branches in figure 6(b). The excess carrier density is independently evaluated from the calibration measurements of the impinging light beam energy density per single quantum energy at fixed excitation wavelength using the appropriate value of the material absorption coefficient. It can be deduced from figure 6(b) that  $N_{d,eff} \approx 1.8 \times 10^{10} \text{cm}^{-3}$  for sh-HD1 and  $N_{d,eff} \approx 1 \times 10^{11} \text{cm}^{-3}$  for sh-LD diodes, respectively.

The discussed above shape of the BELIV transients, recorded on sh-HD1 diode at steady-state illumination, is also reproduced in the pulsed excitation regime (figures 7(a) and (b)). There a single excitation pulse of 4 ns duration initially injects excess carriers, which density changes in time, are probed by a set of LIV pulses. The descending-shape and the diode-inherent BELIV transients can be clearly observed for the rather short set of BELIV pulses (in figure 7(a)) recorded under reverse bias. The peak amplitude of the BELIV pulses decreases with display time and pulsed excitation intensity. These peak values (figure 7(a)) within a set of LIV pulses represent a reduction of the excess free-carrier concentration due to their recombination. Thus, the evolution of peak values of the BELIV pulses within display scale directly represents the carrier recombination rate in the GaN:C material. The photo-luminescence ascribed decay transients [36] can be scanned by the enlarged scale, i.e. a set of LIV pulses, figure 7(b). The characteristic time-parameters deduced from evolution of the BELIV transients in the sh-HD1 diode are in excellent agreement with that estimated from transients of MW-PC (microwave probed photo-conductivity) and TR-PL (time resolved photo-luminescence) recorded on the same GaN:C samples [36].

However, a spectrum of traps can differ when studying different samples, grown using the same technology. Also, the spectrum of traps can vary due to the lateral in-homogeneity of samples caused by doping and other technological procedures. However, the BELIV transient component,

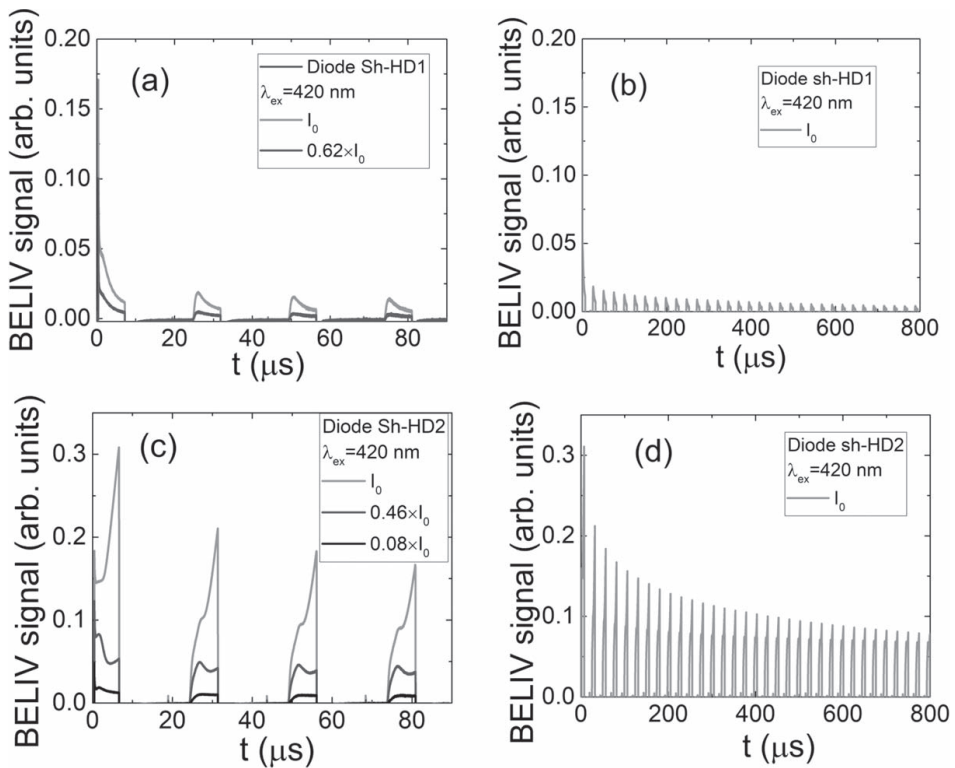


**Figure 7.** Evolution of the sets of BELIV transients recorded at different time scales measured after illumination by a  $\lambda_{\text{ex}} = 420$  nm wavelength laser pulse of 4 ns duration in diodes sh-HD1(a), (b) and sh-HD2 (c), (d) at different light intensity (a) and (c) for excitation laser single pulse.

ascribed to generation current due to emission/trapping from the rather shallow traps, is clearly observable in BELIV transients recorded for the sh-HD2 diode (figure 7(c)). This generation current component appears as the ascending BELIV current after a minimum (the first BELIV transient in the set, figure 7(c)). Certainly, the appearance of this generation current component crucially depends on LIV pulse duration, time-gap between adjacent LIV pulses and on excess carrier (excitation) density (figure 7(c)). Consequently, this also modifies the initial delay within the BELIV transient, as can be noticed in figure 7(c). Nevertheless, the characteristics shown in figure 6 can be obtained by properly chosen measurement regimes. The long scale decays of the BELIV amplitudes exhibit rather different decay parameters for the sh-HD1 and sh-HD2 diodes when comparing figures 7(b) and (d). The observed differences are in line with decay parameters extracted using contactless techniques [36] in characterization of the same samples. However, the fast decay component revealed in the initial stage of the MW-PC and TR-PL transients cannot be separated within BELIV transients due to rather long dielectric relaxation times for equilibrium and excess carrier concentrations less than  $10^{13} \text{ cm}^{-3}$ .

### 3.3. ICDC transients

The injected charge drift current (ICDC) transients with transit times in the time-scale of nanoseconds are very sensitive to the initial-decay stage lifetimes (of a few ns) observed in MW-PC and TR-PL transients [36] recorded on the same samples.

The drift component leads to an increase of the current for strip-focused light beam location approaching the high field contact, due to the shortest distance for carriers to drift (figure 8(a)). However, a final stage of a drift is hidden (not completed) by rapid capture/recombination of drifting carriers. It can thereby be inferred that the recombination term in equation (2) prevails. Therefore, the ICDC (TCT) pulses exhibit the shape of the single-peak with a slightly extended 'tail'. The similar variations of the ICDC transients (figure 8(c)) have been recorded by changing the reverse bias voltage: the stage of the longest transit times at small voltages is cut by the fast recombination of drifting carriers, and no dependence of drift time on voltage is observable for the applied injection pulse durations (of 0.5–4 ns) and voltages  $< 300$  V. Nevertheless, the peak ICDC current values are proportional to the applied reverse voltage (figure 8(d)) over all the examined range of

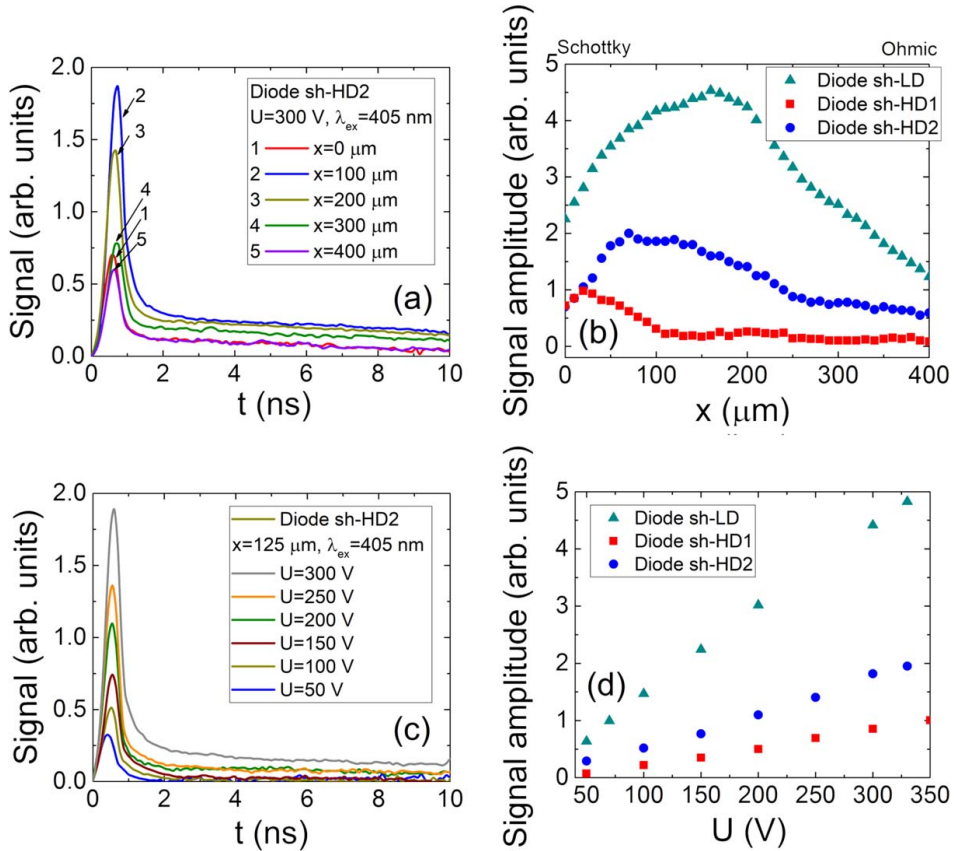


**Figure 8.** Current transients recorded on diode sh-HD2 (a and c) at different charge injection (by a strip-focused light spot) positions  $x$  within sample thickness (a) and bias voltages (c). Peak values of current transients as a function of both charge injection position within thickness of a diode (a) and (b) and the bias voltage (c) and (d) for diodes sh-HD1, sh-HD2 (a)–(d) and sh-LD (b) and (d).

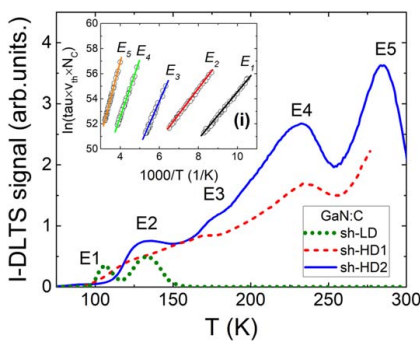


**Figure 9.** The O-I-DLTS spectra recorded on diodes sh-HD1 and sh-HD2. In the inset (i), the Arrhenius plots for the O-I-DLTS peaks are depicted.

voltages, indicating the impact of charge drift. The profiles of the ICDC peak-current values, obtained by scanning carrier injection position within inter-electrode gap, are found to be

asymmetric for sh-HD2 diodes, while the largest ICDC current in sh-LD diode appears for injection location nearby the middle of diode thickness, figure 7(b).

The largest current appears for the injection positions at the high-field electrode, figure 8(b), for sh-HD1 and sh-HD2 diodes. Also, the Schottky contacts for diodes sh-HD1 and sh-HD2 were intentionally deposited on the surface of the smallest surface recombination velocity revealed by profiling of the MW-PC transients [36]. Thereby, the ICDC peak-current profiles reproduce well the asymmetry of surface recombination in the same samples containing contacts. On the other hand, the sample HD1 had shown [36] the shorter recombination lifetime in comparison with HD2 when MW-PC transients were examined. Thus, the ICDC peak current profiles again reproduce the charge decay velocity distribution within the depth of diode structure. For the LD sample, the symmetry of surface recombination velocities had been found [36], however, with elevated values of surface recombination velocity, relative to HD GaN:C samples. Appearance of the largest ICDC response near the half-depth of a diode,



**Table 2.** Thermal activation energy and cross-section values deduced from fitting of the Arrhenius plots of the O-I-DLT spectra and association of traps.

sh-LD		sh-HD1		sh- HD2		Defect identification according to referenced literature
$E$ (eV)	$\sigma$ (cm <sup>2</sup> )	$E$ (eV)	$\sigma$ (cm <sup>2</sup> )	$E$ (eV)	$\sigma$ (cm <sup>2</sup> )	
$E_1 = 0.16$	$4 \times 10^{-16}$	$E_1 = 0.16$	n/a	$E_1 = 0.16$	$7 \times 10^{-17}$	$V_N$ [59, 60]
$E_2 = 0.20$	$5 \times 10^{-17}$	$E_2 = 0.20$	n/a	$E_2 = 0.20$	$2 \times 10^{-16}$	$V_N$ [59–61]
		$E_3 = 0.26$	n/a	$E_3 = 0.28$	$4 \times 10^{-16}$	$V_N$ - $V_{Ga}$ [60, 62]
		$E_4 = 0.45$	$1 \times 10^{-15}$	$E_4 = 0.44$	$6 \times 10^{-16}$	$C_{Ga}$ [63, 64]
		$E_5 = 0.57$	n/a	$E_5 = 0.56$	$8 \times 10^{-15}$	$N_{Ga}$ [62, 65]

for the sh-LD diode, reproduces a profile of initial injection, where the surface recombination reduces the injection efficiency, lowered at contacts. Also, bulk recombination lifetime had been found [36] to be longest for the LD sample. This is in agreement with the largest ICDC current, obtained for the sh-LD diode, when comparing with that for sh-HD ones, figure 7(b).

### 3.4. DLTS spectra

The deep level spectra recorded using the O-I-DLTS regime are illustrated in figure 9. The diodes were continuously illuminated with an LED emitting 380 nm wavelength. The current transients were recorded by varying parameters of the lock-in amplifier. The parameters (activation energy and capture cross-section) of thermal emission centres were then extracted by fitting Arrhenius plots using different correlation functions [45] (inset for figure 9).

Up to five DLTS peaks have been revealed for both sh-HD1 and sh-HD2 diodes (figure 9), however, only two shallow centres have been revealed for the sh-LD diode. Moreover, a concentration of these thermal emission centres, which is proportional to the amplitudes of DLT spectral peaks has been found to be larger for sh-HD2 samples relative to that for sh-HD1. For the latter sh-HD1 diode material, the considerably shorter carrier lifetimes had been deduced [36], and smaller TCT current values obtained (figure 7(b)). This implies that different concentrations of the non-radiative recombination centres are contained in the sh-HD1 and sh-HD2 materials, despite the same density of carbon dopants. The difference in deep recombination centres determine a level of filling of the thermal emission centres. As a consequence, the difference in DLTS peak amplitudes appears when comparing spectra recorded on the sh-HD1 and sh-HD2 diodes.

An origin of each DLTS peak has been identified by matching the thermal activation energy parameters with literature data. These parameters are listed in table 2. Most of the thermal emission centres, being rather shallow for GaN materials, have been ascribed to the nitrogen vacancies and their complexes (peaked at  $E_1$ – $E_3$ ) as well as to the anti-site defect ( $E_5$ ).

The carbon attributed thermal emission centre, peaked at  $E_4 \cong 0.45$  eV within DLT spectra, has only been identified. This defect had been referenced [63, 64] as a carbon atom on the Ga site within a GaN lattice. The spectral peaks related to

the carbon impurities are commonly observable in the temperature range from 320 K to 500 K [63, 64]. These thermal-emission centres have not been detected in our experiments due to the I-DLTS regime and limited temperature range. Comparison of the DLTS data (table 2) and photo-ionization spectra [36] has shown that carbon impurities mainly manifest as deep photo-active centres active in radiative recombination.

## 4. Discussion

Spectroscopy of photo-ionization [36] and thermal emission (section 3.4) has shown that carbon doped GaN:C HVPE grown on Ammono substrate materials contain a rather rich spectrum of point defects (tables 1 and 2). The deep centres are related to carbon impurities and mainly responsible for radiative recombination processes. The thermal emission centres are mainly associated with imperfections of the GaN crystalline lattice. Additional defects, not identified within PPIS (table 1) and O-DLTS spectra (table 2), can be implied from MW-PC and TR-PL transients where fast initial decay has been revealed. These defects seem to be responsible for the non-radiative recombination.

Despite a large variety of defects, rather qualitative diodes can be fabricated using the HVPE GaN grown on Ammono substrate material. The exceptionally good quality of this HVPE GaN material, relative to MOCVD GaN epilayers, is also corroborated by elevated values of carrier mobility relative to those reported on MOCVD GaN. The carrier mobility has been evaluated by examining variations of the serial resistance as a function of the excitation power and excess carrier density in sh-LD and sh-HD diodes (figure 10). The serial resistance has been evaluated by using delay times  $\tau_{RsCb0}$  (figure 10(a)) within BELIV transients (inset for figure 10(b)). To get barrier capacitance  $C_{b0}$ , the descending component within the BELIV transient (inset for figure 10(b)) is extrapolated to the idealized capacitance value at the initial ( $t = 0$ ) instant. These  $C_{b0}$  values linearly increase with excitation power (figure 10(b)), as the initial depletion width shrinks with increase of carrier density within electrically neutral region (ENR). Consequently, a delay time (figure 10(a)) of the BELIV peak appearance (inset for figure 10(b)) is shortened with increase of the excitation power or excess carrier density within ENR. Variations of the serial resistance as a function of the excess carrier density can then be extracted by using the  $\tau_{delay} = \tau_{RsCb0}$  and  $C_{b0}$

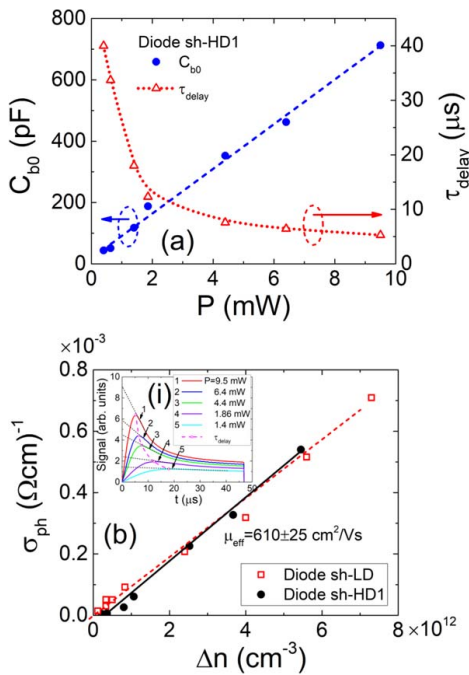


**Figure 10.** (a)—Variations of the barrier capacitance and of delay times in formation of the peaks within BELIV transients as a function of the power of the steady-state 405 nm wavelength illumination. (b)- Photo-conductivity in the ENR of the sh-HD1 diode as a function of the excess carrier concentration. In the inset, the procedures of the extrapolation to the  $C_{b0}$  instants within BELIV transients and evolution of the delay time in BELIV peak formation, dependent on the excitation power, are sketched.

characteristics. The photo-conductivity  $\sigma_{ph}$  variations related to  $R_s$  (through geometrical parameters of the contact area and diode thickness  $d$ ) as a function of excess carrier density can then be obtained by considering the  $\tau_{delay}$  changes (figure 10(a) and inset for figure 10(b)). The slope of the  $\sigma_{ph}$ - $n_{ex}$  characteristic (figure 10(b)) sets the mobility of carriers. Nearly the same slope for the  $\sigma_{ph}$ - $n_{ex}$  characteristics measured on sh-LD and sh-HD diodes has been obtained. The evaluated rather large effective mobility  $\mu_{eff} = 610 \pm 25$  cm $^2$ /Vs indicates the high quality of materials relative to the carrier scattering processes.

Carbon dopants seem to modify compensation of the technological defects that determine n-type conductivity of the pristine HVPE GaN material. The latter shallow defects revealed by DLT spectroscopy are associated with vacancies and anti-site defects in the HVPE GaN material. The enhanced densities of carbon dopants, as obtained for sh-HD1 and sh-HD2 diodes (figure 6(b)), lead to the equilibrium carrier densities of  $2 \times 10^{10}$  cm $^{-3}$ , while the value of  $10^{11}$  cm $^{-3}$  has been obtained for the sh-LD diode. The ratio of these concentrations agrees well with that estimated from SIMS data. Such a highly resistive material is suitable for fabrication of

particle sensors. Moreover, the Schottky junctions made of this material are capable of withstanding rather high voltages of  $\geq 300$  V (figure 8(d)). However, the too short initial decay lifetimes ( $< 5$  ns) hide a carrier drift component in formation of the response of detectors. Also, carrier capture and recombination determines a fast fall down of the detector signals. Nevertheless, short carrier decay lifetimes in the high resistivity HVPE GaN materials might be beneficial in the fabrication of fast response and ionising-radiation-sensitive, but solar-blind, detectors. Complementarily, HVPE growth of the non-polar GaN [66] is promising to avoid complications in formation of the reliable contacts and junctions where piezo- and spontaneous polarization effects can be negligible.

## 5. Summary

A comprehensive study of the electrical characteristics in Schottky diodes made of GaN:C grown by HVPE technology on AT-GaN substrates has been reported. The Schottky junctions were made of Ni/Au (25/200 nm) metal stack and ohmic contacts were fabricated by Ti/Al/Ni/Au (30/90/20/100 nm) e-beam deposition of the metal thin-films followed by rapid thermal annealing. The routine measurements in dark of the C-V's and I-V's have shown a capacitor-like behaviour in C-V's and a slight asymmetry in I-V's for the fabricated devices. A good quality of fabricated Schottky diodes has been proven by considering the transient shape using pulsed technique of barrier evaluation under linearly increasing voltage (BELIV). The concentrations of equilibrium carriers of  $2 \times 10^{10}$  cm $^{-3}$  and of  $10^{11}$  cm $^{-3}$  have been evaluated for heavy carbon doped samples using photo-capacitance characteristics dependent on excitation intensity. The effective mobility of carriers of  $\mu_{eff} = 610 \pm 25$  cm $^2$ /Vs has been estimated by considering serial resistance variations through analysis of the delay times that appeared in the formation of peaks within BELIV transients, dependent on excitation density. This value of carrier effective mobility indicates a rather low density of dislocations [67] in HVPE GaN materials grown on Ammono substrates. The injected charge drift current transients with durations of a few nanoseconds indicated the recombination dominant diode response, when the excess carriers are injected by a slit-focused 30 ps pulse laser beam which impinges through a diode edge boundary. The optical deep level transient spectroscopy has shown that thermal emission from the rather shallow centres (with activation energies of  $< 0.45$  eV) prevails. However, the origin of these centres, ascribed to vacancy and anti-site defects as well as to carbon on Ga site, differs from those, carbon associated, dominating in the photo-ionization processes. It has been demonstrated that Schottky junctions made of heavy carbon doped ( $N_C \geq 10^{18}$  cm $^{-3}$ ) HVPE GaN material are capable of withstanding voltages of  $\geq 300$  V. It can be inferred that short carrier decay lifetimes in the high resistivity HVPE GaN materials might be beneficial in the fabrication of fast response and ionising-radiation sensitive GaN detectors.

## Acknowledgments

This research was partially funded by Lithuanian Research Council grant No. LAT-01/2016. The fabrication of materials for this research was supported by the Department of the Navy, Office of Naval Research (ONRG - NICOP -N62909-17-1-2004) and by the Polish National Science Centre through project No. 2017/25/B/ST5/02897.

## ORCID iDs

E Gaubas  <https://orcid.org/0000-0003-3079-8140>

## References

- Saitoh Y, Sumiyoshi K, Okada M, Horii T, Miyazaki T, Shiomi H, Ueno M, Katayama K, Kiyama M and Nakamura T 2010 Extremely low on-resistance and high breakdown voltage observed in vertical GaN Schottky barrier diodes with high-mobility drift layers on low-dislocation-density GaN substrates *Appl. Phys. Express* **3** 081001
- Everts J *et al* 2011 A 96% efficient high-frequency DC–DC converter using e-mode GaN DHFETs on Si *IEEE Electron Device Lett.* **32** 1370
- Ha M W *et al* 2011 High-voltage Schottky barrier diode on silicon substrate *Jpn. J. Appl. Phys.* **50** 06GF17
- Mishra U K, Parikh P and Wu Y F 2002 AlGaIn/GaN HEMTs —an overview of device operation and applications *Proc. IEEE* **90** 1022
- Gaubas E *et al* 2017 Study of neutron irradiated structures of ammonothermal GaN *J. Phys. D: Appl. Phys.* **50** 135102
- Sellin P J and Vaitkus J 2006 New materials for radiation hard semiconductor detectors *Nucl. Instrum. Methods A* **557** 479–89
- Pearnton S J, Kang B S, Kim S, Ren F, Gila B P, Abernathy C R, Lin J and Chu S N G 2004 GaN-based diodes and transistors for chemical, gas, biological and pressure sensing *J. Phys. Condens. Matter* **16** R961–94
- Sugiura M, Kushimoto M, Mitsunari T, Yamashita K, Honda Y, Amano H, Inoue Y, Mimura H, Aoki T and Nakano T 2016 Study of radiation detection properties of GaN pn diode *Jpn. J. Appl. Phys.* **55** 05FJ02
- Vaitkus J, Gaubas E, Kazukauskas V, Blue A, Cunningham W, Rahman M, Smith K and Sakai S 2005 A new radiation hard semiconductor—semi-insulating GaN: photoelectric properties *AIP Conf. Proc.* **CP772** 207–8
- Moll M 2006 Radiation tolerant semiconductor sensors for tracking detectors *Nucl. Instrum. Methods A* **565** 202–11
- Gaubas E, Ceponis T, Jasunas A, Kovalevskij V, Meskauskaitė D, Pavlov J, Remeikis V, Tekorius A and Vaitkus J 2014 Correlative analysis of the *in situ* changes of carrier decay and proton induced photoluminescence characteristics in chemical vapor deposition grown GaN *Appl. Phys. Lett.* **104** 62104
- Pittet P, Guo N L, Jean M G, Jean M B, Anas I, Jean Y G and Balosso J 2009 PL characterization of GaN scintillator for radioluminescence-based dosimetry *Opt. Mater.* **31** 1421–4
- Pittet P, Lu G N, Galvan J M, Loisy J Y, Ismail A, Giraud J Y and Balosso J 2009 Implantable real-time dosimetric probe using GaN as scintillation material *Sensors Actuators A Phys.* **151** 29–34
- Wang R, Pittet P, Ribouton J, Lu G-N, Chaikh A and Ahnesjö A 2013 Implementation and validation of a fluence pencil kernels model for GaN-based dosimetry in photon beam radiotherapy *Phys. Med. Biol.* **58** 6701–12
- Polyakov A Y and Lee I H 2015 Deep traps in GaN-based structures as affecting the performance of GaN devices *Mater. Sci. Eng. R Reports* **94** 1–56
- Jain S C, Willander M, Narayan J and Overstraeten R V 2000 III–nitrides: growth, characterization, and properties *J. Appl. Phys.* **87** 965
- Reshchikov M A and Morkoç H 2005 Luminescence properties of defects in GaN *J. Appl. Phys.* **97** 61301
- Oishi T *et al* 2003 Highly resistive GaN layers formed by ion implantation of Zn along the *c* axis *J. Appl. Phys.* **94** 1662
- Cho Y S *et al* 2006 Effect of carrier gas on GaN epilayer characteristics *Phys. Status Solidi* **3** 1408
- Hardtdegen H *et al* 2007 New approaches for growth control of GaN-based HEMT structures *Appl. Phys. A* **87** 491
- Heikman S, Keller S, DenBaars S P and Mishra U K 2002 Growth of Fe doped semi-insulating GaN by metalorganic chemical vapor deposition *Appl. Phys. Lett.* **81** 439
- Ogino T and Aoki M 1980 Mechanism of yellow luminescence in GaN *Jpn. J. Appl. Phys.* **19** 2395
- Poblenz C, Waltereit P, Rajan S, Heikman S, Mishra U K and Speck J S 2004 Effect of carbon doping on buffer leakage in AlGaIn/GaN high electron mobility transistors *J. Vac. Sci. Technol. B* **22** 1145
- Armstrong A, Arehart A R, Moran B, DenBaars S P, Mishra U K, Speck J S and Ringel S A 2004 Impact of carbon on trap states in n-type GaN grown by metalorganic chemical vapor deposition *Appl. Phys. Lett.* **84** 374
- Erickson R W and Maksimovic D 2001 *Fundamentals of Power Electronics* 2nd edn (New York: Springer)
- Reshchikov M A, Demchenko D O, Usikov A, Helava H and Makarov Y 2014 Carbon defects as sources of the green and yellow luminescence bands in undoped GaN *Phys. Rev. B* **90** 235203
- Demchenko D O, Diallo I C and Reshchikov M A 2013 Yellow luminescence of gallium nitride generated by carbon defect complexes *Phys. Rev. Lett.* **110** 087404
- Matsubara M and Bellotti M 2017 A first-principles study of carbon-related energy levels in GaN. I. Complexes formed by substitutional/interstitial carbons and gallium/nitrogen vacancies *J. Appl. Phys.* **121** 195701
- Matsubara M and Bellotti E 2017 A first-principles study of carbon-related energy levels in GaN. II. Complexes formed by carbon and hydrogen, silicon or oxygen *J. Appl. Phys.* **121** 195702
- D'Evelyn M P *et al* 2007 Bulk GaN crystal growth by the high-pressure ammonothermal method *J. Cryst. Growth* **300** 11
- Dwiliński R *et al* 2008 Excellent crystallinity of truly bulk ammonothermal GaN *J. Cryst. Growth* **310** 3911
- Hashimoto T, Wu F, Speck J S and Nakamura S 2008 Ammonothermal growth of bulk GaN *J. Cryst. Growth* **310** 3907
- Bockowski M, Iwinska M, Amilusk M, Fijałkowski M, Lucznik B and Sochacki T 2016 Challenges and future perspectives in HVPE-GaN growth on ammonothermal GaN seeds *Semicond. Sci. Technol.* **31** 93002
- Bergsten J, Thorsell M, Adolph D, Chen J-T, Kordina O, Sveinbjörnsson E Ö and Rorsman N 2018 Electron trapping in extended defects in microwave AlGaIn/GaN HEMTs with carbon-doped buffers *IEEE Trans. Electron Devices* **65** 2446
- Mikulics M *et al* 2005 Ultrafast metal-semiconductor-metal photodetectors on low-temperature-grown GaN *Appl. Phys. Lett.* **86** 211110
- Gaubas E *et al* Study of spectral and recombination characteristics of HVPE GaN grown on Ammono substrates will be published elsewhere



- [37] Pearson S J, Zolper J C, Shul R J and Ren F 1999 GaN: processing, defects, and devices *J. Appl. Phys.* **86** 1
- [38] Wickenden A E, Koleske D D, Henry R L, Twigg M E and Fatemi M 2004 Resistivity control in unintentionally doped GaN films grown by MOCVD *J. Cryst. Growth* **260** 54
- [39] Koller C, Pobegen G, Ostermaier C, Huber and Pogany D 2017 The interplay of blocking properties with charge and potential redistribution in thin carbon-doped GaN on n-doped GaN layers *Appl. Phys. Lett.* **111** 032106
- [40] Jakštas V, Jorudas J, Janonis V, Minkevičius L, Kašalynas I, Prystawko P and Leszczynski M 2018 Development of AlGaIn/GaN/SiC high-electron-mobility transistors for THz detection *Lith. J. Phys.* **58** 135–40
- [41] Gaubas E, Čeponis T, Sakalauskas S, Uleckas A and Velička A 2011 Fluence dependent variations of barrier and generation currents in neutron and proton irradiated Si particle detectors *Lith. J. Phys.* **51** 227–33
- [42] Gaubas E, Ceponis T, Uleckas A and Grigonis R 2012 Room temperature spectroscopy of deep levels in junction structures using barrier capacitance charging current transients *J. Instrum.* **7** P01003
- [43] Gaubas E, Čeponis T, Kalendra V, Kusakovskij J and Uleckas A 2012 Barrier evaluation by linearly increasing voltage technique applied to Si solar cells and irradiated pin diodes *ISRN Materials Science* **2012** 543790
- [44] Gaubas E, Čeponis T and Vaitkus J V 2013 *Pulsed Capacitance Technique for Evaluation of Barrier Structures* (Saarbrücken-Berlin: LAMBERT Academic Publishing)
- [45] FT 1030 Deep-Level Transient Spectroscopy System. (<http://phys.tech.de/products/dlts/dlts.htm>) (accessed 11 June 2018)
- [46] Spieler H 2005 *Semiconductor Detector Systems* (Oxford: Oxford University Press)
- [47] Kramberger G 2014 Edge-TCT studies of irradiated HVCMSO sensor *Presentation at 25th rd50 Workshop (Geneva)* ([www.cern.ch/rd50](http://www.cern.ch/rd50))
- [48] Eremin V, Strokan N, Verbitskaya E and Li Z 1996 Development of transient current and charge techniques for the measurement of effective net concentration of ionized charges ( $N_{\text{eff}}$ ) in the space charge region of p-n junction detectors *Nucl. Instrum. Methods A* **372** 388–98
- [49] Eremin V, Verbitskaya E and Li Z 2002 The origin of double peak electric field distribution in heavily irradiated silicon detectors *Nucl. Instrum. Methods A* **476** 556–64
- [50] Gaubas E, Ceponis T and Pavlov J 2015 Pulsed current signals in capacitor type particle detectors *J. Instrum.* **10** C01006
- [51] Gaubas E, Ceponis T, Kalesinskas V, Pavlov J and Vysniauskas J 2015 Simulations of operation dynamics of different type GaN particle sensors *Sensors* **15** 5429–73
- [52] Gaubas E, Ceponis T, Jasunias A, Kalendra V, Pavlov J, Kazuchits N, Naumchik E and Rusetsky M 2014 Lateral scan profiles of the recombination parameters correlated with distribution of grown-in impurities in HPHT diamond *Diam. Relat. Mater.* **47** 15–26
- [53] Gaubas E, Ceponis T and Kalesinskas V 2013 Currents induced by injected charge in junction detectors *Sensors* **13** 12295–328
- [54] Gaubas E, Ceponis T, Meskauskaitė D and N Kazuchits N 2015 Profiling of current transients in capacitor type diamond sensors *Sensors* **15** 13424–58
- [55] Ramo S 1939 Currents induced by electron motion *Proc. IRE* **27** 584–5
- [56] Shockley W 1938 Currents to conductors induced by a moving point charge *J. Appl. Phys.* **9** 635–6
- [57] Lampert M A and Mark P 1970 *Current Injection in Solids* (New York: Academic)
- [58] Ryvkin S M 1963 *Photoelectric Effects in Semiconductors* (New York: Consultants Bureau)
- [59] Fang Z-Q, Look D C, Wang X L, Han J, Khan F A and Adesida I 2003 Plasma-etching-enhanced deep centers in n-GaN grown by metalorganic chemical-vapor deposition *Appl. Phys. Lett.* **82** 1562–4
- [60] Gotz W, Johnson N M, Amano H and Akasaki I 1994 Deep level defects in n-type GaN *Appl. Phys. Lett.* **65** 463–5
- [61] Placzek-Popko E, Trzmiel J, Zielony E, Grzanka S, Czernecki R and Suski T 2009 Deep level transient spectroscopy signatures of majority traps in GaN p-n diodes grown by metal-organic vapour-phase epitaxy techniques on GaN substrates *Physica B* **404** 4889–91
- [62] Tokuda Y, Matsuoka Y, Ueda H, Ishiguro O, Soejima N and Kachi T 2006 DLTS study of n-type GaN grown by MOCVD on GaN substrates *Superlattice. Microst.* **40** 268–73
- [63] Honda U, Yamada Y, Tokuda Y and Shiojima K 2012 Deep level defects in n-GaN doped with carbon studied by deep level and minority carrier transient spectroscopies *Jpn. J. Appl. Phys.* **51** 04DF04
- [64] Shah P B, Dedhia R H, Tompkins R P, Viveiros E A and Jones K A 2012 DLTS and MCTS analysis of the influence of growth pressure on trap generation in MOCVD GaN *Solid. State. Electronic.* **78** 121–6
- [65] Hacke P, Detchprohm T, Hiramatsu K, Sawaki N, Tadamoto K and Miyake K 1994 Analysis of deep levels in n-type GaN by transient capacitance methods *J. Appl. Phys.* **76** 304–9
- [66] Lee M, Vu T K O, Lee K S, Kim E K and Park S 2018 Electronic states of deep trap levels in a-plane GaN templates grown on r-plane sapphire by HVPE *Sci. Rep.* **8** 7841
- [67] Abdel-Motaleb I M and Korotkov R Y 2005 Modeling of electron mobility in GaN materials *J. Appl. Phys.* **97** 093715

A2

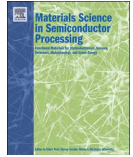
Study of spectral and recombination  
characteristics of HVPE GaN grown on  
ammono substrates

E. Gaubas, P. Baronas, T. Čeponis, **L. Deveikis**, D. Dobrovolskas, E.  
Kuokštis, J. Mickevičius, V. Rumbauskas, M. Bockowski, M. Iwinska, T.  
Sochacki

Mater. Sci. Semicond. Process **91** (2019) 341-355.

DOI:10.1016/j.mssp.2018.12.010

(Open access)



## Study of spectral and recombination characteristics of HVPE GaN grown on ammono substrates



E. Gaubas<sup>a,\*</sup>, P. Baronas<sup>a</sup>, T. Čeponis<sup>a</sup>, L. Deveikis<sup>a</sup>, D. Dobrovolskas<sup>a</sup>, E. Kuokstis<sup>a</sup>, J. Mickevičius<sup>a</sup>, V. Rumbauskas<sup>a</sup>, M. Bockowski<sup>b</sup>, M. Iwinska<sup>b</sup>, T. Sochacki<sup>b</sup>

<sup>a</sup> Institute of Photonics and Nanotechnology, Vilnius University, Sauletekio av. 3, LT-10257 Vilnius, Lithuania

<sup>b</sup> Institute of High Pressure Physics, Sokolowska 29/37, 01-142 Warsaw, Poland

### ARTICLE INFO

#### Keywords:

Carbon doped HVPE GaN  
Photo-ionization spectroscopy  
Photoluminescence spectroscopy  
Microwave probed photoconductivity transients  
Surface recombination

### ABSTRACT

A comprehensive study of the bulk ~400 μm thick GaN samples, grown by HVPE technology on AT-GaN seeds, and containing different carbon doping is reported. Spectroscopy of point centres has been implemented by combining several contactless/optical techniques: time resolved photoluminescence (TR-PL), microwave probed photoconductivity (MW-PC) transient and pulsed-photo-ionization spectroscopy (PPIS) techniques, together with steady-state PL (SS-PL) and transmission spectral measurements. The dynamics of the non-radiative and radiative recombination dependent on the excess carrier density and incorporated carbon concentration has been revealed. The cross-section of the photon-electron interaction and broadening factors due to electron-phonon coupling have been evaluated for various centres. Profiling of the excess carrier decay transients by scanning a wafer-edge boundary has been employed for estimation of surface recombination velocity. The asymmetry of surface recombination in heavily carbon doped samples has been corroborated by SS-PL intensity changes when comparing spectra recorded by exciting the opposite wafer surfaces using UV light. It has been inferred that the surface and bulk non-radiative recombination with 70 ns carrier lifetime is efficient only within initial stages of MW-PC and TR-PL transients. Several traps, tentatively attributed to  $C_N O_N$ ,  $C_N$ ,  $C_D$ ,  $V_{Ga}$  point defects, have been deduced from pulsed photo-ionization spectroscopy. The  $C_N^-$  defect appeared to be the most efficient in redistribution of the radiative recombination. For these centres, the parameters such as the photon-electron interaction cross-section, broadening factor due to electron-phonon coupling, and concentration have been evaluated for GaN samples, carbon doped with different levels. The  $C_N V_{Ga}$ ,  $G_C G_{Ga}$ ,  $C_{Ga} V_N$  complexes have also been implied by considering TR-PL and SS-PL spectra. The conversion from absorption to emission spectra has been revealed and explained based on van Roosbroeck-Shockley approach. The long-tail photoluminescence decay with durations up to tens of ms has been explained by nearly resonant photo-ionization and photoluminescence transitions in sequence of self-sustaining processes when local excitation travels by hopping over the re-absorption lengths.

### 1. Introduction

Development of bulk GaN growth technologies with crystal quality approaching to parameters inherent for the electronic-grade materials is important for fabrication of high-power high-frequency devices capable operate at elevated temperatures. The technology of the hydride vapour phase epitaxy (HVPE) [1] using high-quality ammonothermally synthesized (AT) [1–4] seeds/substrates with low density ( $< 5 \times 10^4 \text{ cm}^{-2}$ ) of structural defects (such as dislocations) is beneficial in rapid production of bulk GaN material. In low structural defect containing HVPE-AT GaN crystals, the inevitable impurity ascribed

defects mainly determine the optical and electrical properties of these materials. Therefore, spectroscopy and search for governing means of the activity of these point defects becomes an important item in the routes of the HVPE-AT GaN technology [1]. The oxygen (O), hydrogen (H), and metal (Mn, Mg) impurities are routine defects [5] inevitable in the HVPE-AT GaN technology. Mg is also the most widely used dopant in growth of p-conductivity type GaN material. However, the rather large thermal activation energy (160 meV) is a limiting factor to get elevated concentrations of equilibrium holes in p-GaN:Mg material. As usually, the as-grown GaN materials show an n-type conductivity due to Si impurities, intrinsic vacancies and interstitials, and other

\* Corresponding author.

E-mail address: [eugenijus.gaubas@ff.vu.lt](mailto:eugenijus.gaubas@ff.vu.lt) (E. Gaubas).

<https://doi.org/10.1016/j.mssp.2018.12.010>

Received 12 October 2018; Received in revised form 28 November 2018; Accepted 6 December 2018

Available online 12 December 2018

1369-8001/ © 2018 Elsevier Ltd. All rights reserved.

**Table 1**  
Concentration of dopants and impurities evaluated by SIMS technique. DL and asterisks denote values of concentrations extracted at detection limit.

Sample	Thickness d (μm)	Concentration of dopants and impurities (cm <sup>-3</sup> )						
		C	H	O	Si	Mg	Mn	Fe
LD	400	<sup>*</sup> 2 × 10 <sup>17</sup>	4.5 × 10 <sup>17</sup>	3 × 10 <sup>17</sup>	4 × 10 <sup>17</sup>	7 × 10 <sup>15</sup>	3 × 10 <sup>14</sup>	1.5 × 10 <sup>15</sup>
HD1	390	1 × 10 <sup>18</sup>	<sup>*</sup> 2.8 × 10 <sup>17</sup>	<sup>*</sup> 1 × 10 <sup>17</sup>	7 × 10 <sup>17</sup>	< DL	< DL	< DL
HD2	407	1 × 10 <sup>18</sup>	<sup>*</sup> 2.8 × 10 <sup>17</sup>	<sup>*</sup> 1 × 10 <sup>17</sup>	7 × 10 <sup>17</sup>	< DL	< DL	< DL

shallow traps. To compensate these donors (electron emission centres), the Mn, Mg and carbon (C) dopants are usually incorporated during crystal growth [5–7]. These dopants are commonly exploited to get the semi-insulating (SI) GaN materials, important in fabrication of fast-response, high voltage devices, optical spectrum-blind particle and radiation sensors. Actually, compensation with Mn, Mg dopants leads to the short carrier lifetime in GaN which often is a drawback of such SI materials. Carbon is an alternative (to Mg) dopant in formation of p-GaN and semi-insulating materials [6–9]. However, it appeared that electrical/optical activity and charged-state of C impurities considerably depends on co-doping with Si [6,7], on background concentrations of such impurities as H, O and Si [5–8], on growth conditions (either Ga or N rich [6,7,10], with additional illumination [11,12]). This leads to the enhanced probability for formation of various impurity complexes. It had been shown [12–15] from theoretical considerations that formation energy of different C-attributed centres depends on Fermi-level position/pinning, and it varies with Fermi-level shifts, making preferential carbon on nitrogen site (C<sub>N</sub>), on gallium site (C<sub>Ga</sub>) or interstitial (C<sub>i</sub>) state, with respective charging polarity and deep-level energy. These changes are diversely related to spectral variations of photoluminescence (PL) [12,16]. Therefore, investigations of the role of carbon in different technology and doping GaN:C materials remain to be significant. A serious issue is also the formation of the ohmic and Schottky contacts of acceptable quality on p-type and SI GaN materials. Thereby, the contactless and optical measurement techniques are more reliable for monitoring of the carbon containing/doped GaN materials.

In this article, a comprehensive study of the GaN: C bulk samples grown by HVPE technology on AT-GaN seeds is reported. Spectroscopy of point centres was performed by combining time resolved photoluminescence (TR-PL), microwave probed photoconductivity (MW-PC) transient and pulsed-photo-ionization spectroscopy (PPIS) techniques, together with spectral steady-state PL (SS-PL) and transmission measurements. All the measurements were performed at room temperature. The dynamics of the non-radiative and radiative recombination dependent on the excess carrier density and carbon concentration has been revealed. The cross-section of the photon-electron interaction and broadening factors due to electron-phonon coupling have been evaluated for various defect centres. The conversion from the photo-ionization to emission spectra have been considered based on van Roosbroeck-Shockley model. The long-tail photoluminescence decay with durations up to tens of ns has been explained by the decrease of capture cross-section and self-sustaining processes of the photo-ionization and photoluminescence transitions.

## 2. Samples and experimental techniques

The ~400 μm thick samples, grown by hydride vapour phase epitaxy (HVPE) GaN on ammonothermal (AT) GaN substrates, have been studied. The free-standing wafer-samples were prepared by removing of AT GaN seeds by mechanical polishing.

The growth conditions were the same as those described in [17]: 800 mbar pressure, 1143 K temperature of synthesis using GaCl, 1318 K GaN growth temperature, 48 ml min<sup>-1</sup> HCl flow. The carbon (C) precursor was CH<sub>4</sub>, which was transported to the growth zone with GaCl. Two different CH<sub>4</sub> flow regimes were applied: of 0.4 and 0.6 ml min<sup>-1</sup>.

Hillocks were observed on the growing surfaces (for details see [17,18]). For further characterization the crystals were sliced from the seeds. Then, they were diced into a few smaller square-like samples (~3 × 3 mm<sup>2</sup>). Sample surfaces with (0001) and (000 $\bar{1}$ ) crystal orientations were mechanically polished to the optical smoothness. All the samples were highly resistive at room temperature showing the n-type conductivity, as it was determined from electrical characterization of Schottky diodes made of the same samples and reported elsewhere [19].

Two sets of samples, containing different (low-LD and high-HD) density of the intentionally introduced carbon (GaN:C), were investigated (Table 1). Concentrations  $N_C$  of the C dopants and other unintentionally introduced impurities were estimated by the secondary ion mass spectroscopy (SIMS), as listed in Table 1. A few values, denoted by asterisks in Table 1, were estimated at the level of SIMS detection limit (DL). It is known [6] that activation of carbon dopants depends on concentration  $N_{Si}$  of simultaneously introduced Si. Thereby, LD samples satisfy relation  $N_{Si} > N_C$  while an opposite inequality  $N_C > N_{Si}$  is hold for HD samples. Rather high densities of O and H impurities, relative to C dopants, were also detected in LD samples.

The XRD measurements were performed to estimate density of dislocations by using X-ray diffractometer (HRXRD, Rigaku, SmartLab). The  $\omega/2\theta$  configuration [20,21] was employed, and the rocking curves ( $\omega$ -scans) were measured at (0002) and (30–32) reflections. The broadening (FWHM) of the (0002) peak within an  $\omega$ -scan was determined to be 64°, while broadening of the (30–32) reflection response was 106°.

Several contactless techniques were applied to evaluate the spectral and excess carrier recombination parameters at room temperature.

The microwave probed photoconductivity (MW-PC) transients [22] have been examined to trace variations of the excess carrier lifetime in various stages of carrier decay process. The 21 GHz MWs probe the UV (at 351 nm wavelength) 400 ps pulse duration laser induced PC using a slit antenna. The transients of the MW-PC response are recorded on 50 Ω load resistor connected in series with MW detector by using a 2 GHz oscilloscope LeCroy Wave Runner 620Zi. Wafer depth profiling of the MW-PC response (proportional to the excess carrier concentration,  $n_{ex}$ ) and of carrier lifetime has been implemented using a needle-tip coaxial MW probe [22] combined with parallel and perpendicular excitation-probing experimental geometries.

Variations of absorption spectra dependent on concentration of carbon dopants have been deduced from transmittance characteristics measured by using a Perkin-Elmer LAMBDA-1050 spectrophotometer.

The steady-state photoluminescence (SS-PL) spectra at low excitation level (where  $n_{ex} < 10^{15}$  cm<sup>-3</sup>) have been recorded by using an arrangement composed of a 325 nm He-Cd laser, a Jobin-Yvon monochromator and an UV-enhanced Hamamatsu photomultiplier, to detect the spectrally dispersed luminescence signals.

At high excitation level (with  $n_{ex} \geq 10^{18}$  cm<sup>-3</sup>), the time-resolved photoluminescence (TR-PL) spectra were examined using the Streak-Camera (SC) and Time-Gated PL Detection (TG-PLD) techniques. The SC technique provides the temporal and spectral evolution of the PL intensity measured at high-level excitation by using the  $\tau_p \sim 200$  fs duration PHAROS laser pulses at  $\lambda = 315$  nm wavelength (generated by optical parametric oscillator ORPHEUS at  $f = 100$  Hz repetition rate)

and the Hamamatsu C10627 streak-camera along with an Acton 2300 spectrometer. Excitation energy density was set to  $0.5 \mu\text{J}/\text{cm}^2$  at beam diameter of  $440 \mu\text{m}$ , in SC experiments. To cover wide scales (up to 5 orders of magnitude) of time and PL intensity variations, the TG-PLD spectroscopy was performed by the nanosecond gated luminescence measurements (in time scale from  $1 \mu\text{s}$  to  $100 \text{ms}$ ) using a nanosecond YAG:Nd<sup>3+</sup> laser NT-242 (Ekspla,  $\lambda = 350 \text{nm}$ ,  $\tau_p = 7 \text{ns}$ ,  $f = 10 \text{Hz}$ ), as an excitation source, and ICCD camera New iStar DH340T (Andor), as the time-gated detector with exponentially increasing delay and integration time. In TG-PLD experiments, the excitation energy density was kept at  $100 \mu\text{J}/\text{cm}^2$  with a beam diameter of  $400 \mu\text{m}$ .

The pulsed photo-ionization spectroscopy [22] (PPIS) was implemented in contactless mode at room temperature, by recording the MW-PC signals at tuneable excitation wavelength and excluding contact related effects. The dark current is rejected in PPIS by a capacitive filter and the changes of the recombination and trapping lifetimes of the photo-excited carriers, correlated with definite photo-ionization spectral steps, are simultaneously controlled. In this work, the PPI spectroscopy was performed using a ns laser equipped with an optical parametric oscillator (OPO) and by recording the microwave probed photoconductivity (MW-PC) transients. The nanosecond OPO instrument Ekspla NT342B with pulse duration of  $4 \text{ns}$  as well as wavelength tuning range from  $210$  to  $2300 \text{nm}$  was employed. The MW-PC signal  $U_{MW-PC}$  is proportional to a density of the photo-excited carriers, while their relaxation rate within a transient represents the carrier lifetime ascribed to later stages of trap filling/emptying. The PPI spectrum was recorded starting from long wavelength wing to avoid simultaneous filling of several traps. Variations of the MW-PC response peaks ( $U_{MW-PC,0}$ ) represent the step-like photo-ionization spectra, while the changes of the excess carrier decay lifetime are obtained by measuring a time interval needed for  $U_{MW-PC}$  reduction to a  $U_{MW-PC,0} \times e^{-1}$  value. The MW-PC transient shape also provides an additional information concerning the dominant and competing carrier decay processes.

### 3. Variations of carbon concentration dependent characteristics

#### 3.1. Absorption spectra

Spectral variations of the absorption coefficient ( $\alpha$ ) were extracted from the recorded spectra of optical transmission in samples, containing a relatively low (LD sample) and high (HD samples) concentration of carbon dopants. It has been obtained that the main spectral changes of  $\alpha$  appear in the  $370\text{--}430 \text{nm}$  spectral range of wavelengths when comparing data for the HD materials relative to LD one (Fig. 1a). To highlight these differences, the spectra of the differential absorption coefficient  $\Delta\alpha = \alpha_{HD} - \alpha_{LD}$  are composed for HD1 and HD2 samples, illustrated in Fig. 1b. The transmission of the rather thick samples is drastically decreased with reduction of wavelength of the incident light, when approaching to an UV spectral range, and the steep increase of absorption coefficient determines large errors in estimation of  $\Delta\alpha$  for wavelengths shorter than  $370 \text{nm}$ , and therefore it is omitted from consideration. These differential ( $\Delta\alpha$ ) absorption spectra exhibit a peak at  $h\nu = 3.30 \text{eV}$  photon energy (upper scale in Fig. 1). The  $\Delta\alpha(h\nu)$  spectral peak at  $h\nu \approx 3.30 \text{eV}$  is also reported for AT GaN:Mn sample [23]. This indicates that the spectral change of  $\Delta\alpha(h\nu)$  is caused by carbon impurities, while low carbon concentration  $< 10^{17} \text{cm}^{-3}$  [23] is inherent for LD sample. Seems, the sample HD1 contains the larger density of absorption active carbon centres relative to HD2.

The absolute value of the capture cross-section at the peak of the differential absorption ( $h\nu = 3.3 \text{eV}$ ) of  $\sigma_{|h\nu=3.30 \text{eV}} = 1.6 \times 10^{-13} \text{cm}^2$  was evaluated by calibrating the spectral irradiance of the Perkin-Elmer LAMBDA-1050 light source (halogen lamp). Here, the relations of  $\alpha_{|h\nu=3.30 \text{eV}} = \sigma_{|h\nu=3.30 \text{eV}} \times n_{\text{ex}}|_{h\nu=3.30 \text{eV}}$  with  $n_{\text{ex}}|_{h\nu=3.30 \text{eV}} = \alpha F|_{h\nu=3.30 \text{eV}}$  and  $F|_{h\nu=3.30 \text{eV}}$  surface density of incident photons were exploited. This value of  $\sigma_{|h\nu=3.30 \text{eV}}$  was employed as a benchmark for making of the absolute scale of values of the cross-sections for the photon-electron coupling.

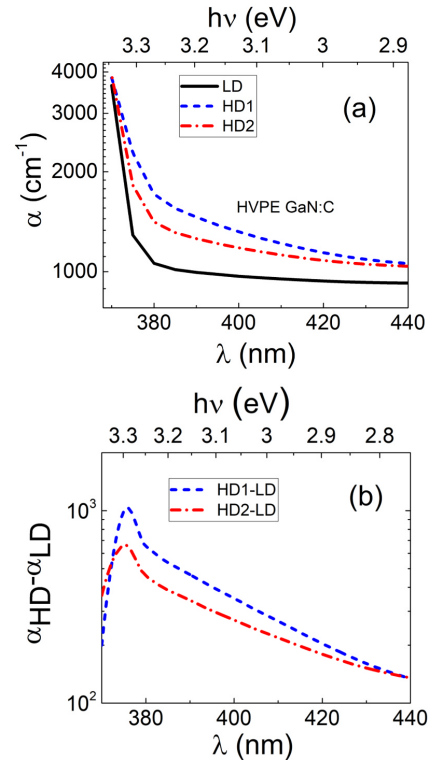


Fig. 1. (a) - Absorption coefficient as a function of wavelength obtained for HVPE GaN:C samples. (b) - Differential ( $\alpha_{HD} - \alpha_{LD}$ ) spectra of the absorption coefficient composed for the heavily C doped samples relative to the LD sample.

The efficiency  $\varepsilon = N_{C_A}/N_D$  of carbon impurities as the compensation centres introduced with large concentrations of  $N_C$  was evaluated from the differential absorption as,  $\Delta\alpha_{|h\nu=3.30 \text{eV}} = \varepsilon \times \sigma_{|h\nu=3.30 \text{eV}} \times (N_{HD} - N_{LD})$ . The estimated values of  $\varepsilon \sim 10^{-2}$  show a reduction of compensation efficiency at large concentrations of introduced carbon. This can be caused by clustering of the carbon impurities introduced with high densities.

#### 3.2. Photoluminescence spectra and transients

The photoluminescence spectra recorded using the steady-state UV excitation mode (SS-PL) are illustrated in Fig. 2. These spectra exhibit the prevailing of yellow (Y) PL spectral band, peaked at  $\sim 2.2 \text{eV}$ . The PL intensity is obtained to be larger for the LD sample than that for HD samples in both the Y and ultraviolet (UV), exhibiting the small intensity spectral shoulders at  $3.3 \text{eV}$ ,  $3.35 \text{eV}$  and a peak at  $3.4 \text{eV}$ , Fig. 2a) spectral bands. However, it has been obtained that the absolute values of PL intensity depend on the wafer side (surface) which is excited by the steady-state laser beam, when comparing Fig. 2a and b. This difference can be caused by carbon doping profile, gradients of other impurity concentration, and asymmetry of surface recombination velocity.

In any case, the PL light re-absorption, peaked at  $3.3 \text{eV}$  (Fig. 2b), could be a reason for the observed reduction of PL intensity within blue (B)-ultraviolet (UV) PL spectral range. The clear variations of the intensity of B-UV PL, dependent on carbon doping, can be deduced from Fig. 2a, where the lowest B-UV PL intensity is obtained for the HD1 sample. The excitation geometry, sketched in Fig. 2a, might be ascribed to a surface of the lowest C doping, where Y luminescence intensity has

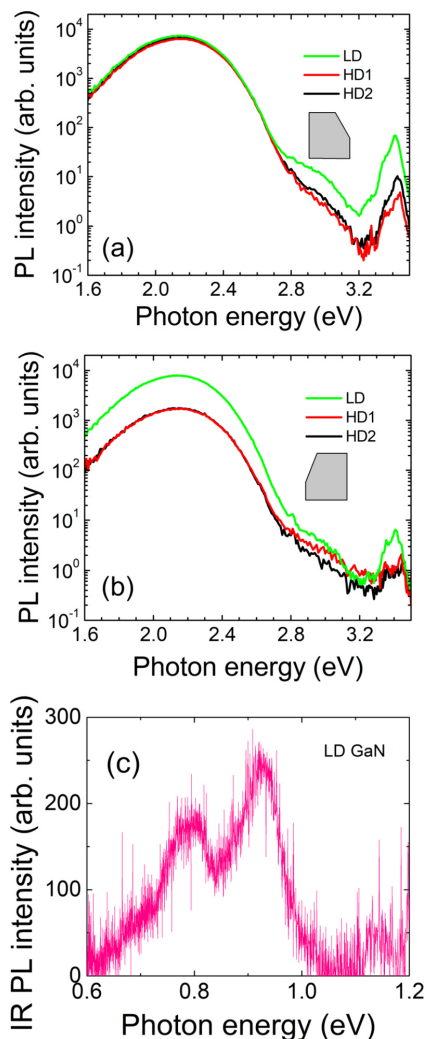


Fig. 2. SS-PL spectra obtained for HVPE GaN:C samples by exciting the opposite (Fig. a and Fig. b, which can be resolved using wafer off-cut orientation in figure legends) surfaces of wafers. (c) – SS-PL in the infrared spectral range.

been obtained nearly the same for all the examined samples. On the opposite surface containing the largest C concentration, the PL intensity difference between LD and HD samples becomes clear. These spectra variations are ascribed to the elevated level of the photo-injection (where  $n_{ex} \leq 10^{15} \text{ cm}^{-3}$  with equilibrium carrier (electron) concentration  $n_0 < 10^{13} \text{ cm}^{-3}$  [19]). The low intensity SS-PL spectrum (Fig. 2c) within infrared (IR) range was also recorded to verify the predicted conversion of the PPI spectrum into PL.

An intention to record temporal evolution of PL signals by employing the Streak-Camera (SC) technique leads to a necessity of elevated excitation intensities (with  $n_{ex} \geq 10^{18} \text{ cm}^{-3}$ ) when using pulsed UV light. The SC recordable PL signals were only obtained within green-yellow-red (G-Y-R) PL spectral range (Fig. 3). These PL spectra, obtained at fixed UV energy density per 200 fs pulse, are illustrated in Fig. 3. The asymmetric PL band in the range of 450–700 nm

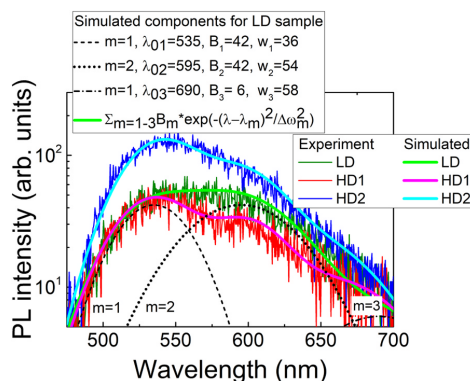


Fig. 3. The Streak-Camera recorded spectra on the HVPE GaN:C samples: as-recorded (noisy curves) and fitted (solid lines) using an approach of three Gaussian spectral bands. The simulated components of a PL spectrum (obtained for the LD sample) are illustrated by dot curves:  $m = 1, 2, 3$ .

wavelengths is observed. The nearly monotonous single-peak (at 530 nm) band is inherent for a SC spectrum recorded on LD sample, while two-peaks (at 535 and 595 nm) can be resolved for HD samples. Actually, the asymmetric PL spectral band can be composed of several spectral components. These components, employed in fitting of the experimental (noisy curve) spectrum, are illustrated by thin dot lines in Fig. 3 for LD sample. There, the Gaussian-shape components, peaked at different wavelengths and having different relative peak-amplitudes ( $B$ ) as well as band widths ( $w$ ), have been employed to fit the recorded spectrum. The Gaussian line-shape is a rather good approximation, and this shape coincides with that real component of the line-shape approximation function (for  $S > 5$ ), derived using a configuration diagram approach [24,25]. To reproduce the asymmetry in simulated spectrum, three Gaussian components were needed. The simulated spectra (Fig. 3) are represented by thick solid lines. It can be deduced from Fig. 3, that the amplitude  $B_2$  of the  $m = 2$  spectral component is decreased for HD1 sample relative to that for HD2 and LD samples, while the spectral components peaked at  $\lambda_{01} = 535 \text{ nm}$  ( $\sim 2.3 \text{ eV}$ ) and  $\lambda_{02} = 595 \text{ nm}$  ( $\sim 2.1 \text{ eV}$ ) are of nearly the same intensity in LD sample. The band-width ( $w_1$ ) of the first simulated component  $m = 1$  is always narrower than that for  $m = 2$ , while band-widths of  $m = 2$  and  $m = 3$  components are close.

The TR-PL transients, obtained for all the investigated samples by integrating two spectral fragments, are illustrated in Fig. 4. These TR-PL transients cover a rather wide time domain, up to ten milliseconds (ms). It can be noticed in Fig. 4 that all the TR-PL transients are two-componential, with the shortest initial PL decay time in LD samples when comparing with that for HD samples. This can be explained by the impact of surface recombination when a profile of the carrier depth distribution changes with time.

There (Fig. 4a), the TR-PL transients, integrated over spectral components  $m = 1$  and  $m = 2$  (peaked at  $\lambda_{01}$  and  $\lambda_{02}$ ), were examined. The transients for these  $\lambda_{01}$  and  $\lambda_{02}$  spectral segments show nearly exponential decays for HD samples. For the LD sample, two decay components can be clearly resolved (Fig. 4a): namely, the initial decay component with  $\tau_{1-in-ef} \approx 220 \mu\text{s}$  and asymptotic one with  $\tau_2, \text{eff} \approx 780 \mu\text{s}$ .

Unfortunately, the SC measurements, even using the least repetition rate ( $f \sim 100 \text{ Hz}$ ) of excitation pulses, did not enable getting of the complete decrease of PL intensity to the background level. Therefore, the time-gated-PL detection (TG-PLD) technique and spectroscopy instrumentation were additionally involved. There, the PL intensity background level was reached for about 90 ms delay times. It was



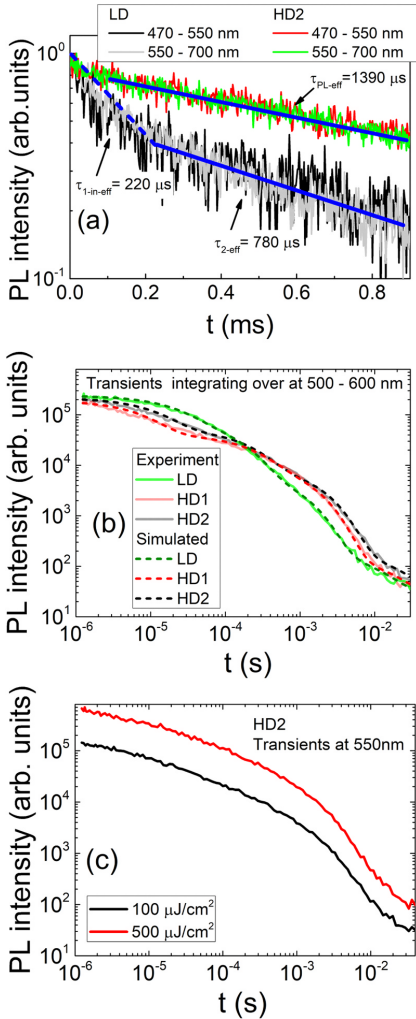


**Fig. 4.** (a) TRPL transients recorded by SC technique for LD and HD2 samples by integrating different spectral fragments, denoted in the legend. (b) Comparison of TRPL transients recorded by the TG-PLD technique on samples of both sets by integrating 500–600 nm spectral range. (c) TG-PLD transients recorded by integrating 550 nm spectral range on HD2 sample at different excitation pulse energy values.

deduced from the TG-PLD spectra evolution that the longest recordable decay is attributed to the spectral band peaked at 560 nm of the Y-PL band, while in the initial decay stages up to 100 μs, the component peaked at ~600–680 nm (R-PL) is also essential, and its peak shifts to the long wavelength spectral wing with reduction of the gate delay time. Another advantage of the TG-PLD technique is an exceptionally wide dynamic range of the delay time and PL intensity changes (Fig. 4b). However, the short decay components in the range of < 100 ns are not resolvable by this TG-PLD technique when using rather long (10 ns) excitation pulses of elevated energy density per pulse (~100 μJ/cm<sup>2</sup>). The log-log plots (Fig. b and c) of the PL signals, integrated over definite TG-PLD spectral range, enable an estimation of the characteristic PL decay time components.

The transients illustrated in Fig. 4 imply the multi-exponential (Fig. 4b) and slightly non-linear decay in the range of the asymptotic components (Fig. 4c). Also, the number of the decay components depends on the TR-PL spectral range of PL signal integration.

The registered signal  $RS(t)$  containing the multi-exponential decay components can be approximated by introducing the partial coefficients  $b_i$  and lifetimes  $\tau_i$ . The generalized signal relaxation model can then be expressed as [22]:

$$RS(t) = RS(t=0) \sum_{m=1}^{M \rightarrow \infty} b_m \exp\left[-\frac{t}{\tau_m}\right]. \quad (1)$$

Such a signal relaxation is often inherent for the simultaneously running linear (exponential in the integral characteristics) and independent decay processes. The partial coefficients  $b_m$  can be related either i) to a portion  $n_m$  of the total density of carriers  $n$ , decaying through  $m$ -type process ( $n_m/n$ ), or ii) to the different spatial frequencies of the surface recombination process, when a depth-distribution  $n(x)$  of carriers appears due to diffusion to surfaces with further recombination via surface states, or iii) to the PL signal collected ( $v_i/v$ ) from different partial volumes  $v_i$  relative to the whole volume  $v$ , when PL signal of the different energy photon bands is integrated, or iv) to the relative density of the radiative recombination centres of a definite species ( $N_{D-A,i}$ ) to the total density of recombination active defects ( $N$ ), etc. A variational principle suggests minimization of  $M$  in the sum of Eq. (1) to a limit when a proper fitting of experimental relaxation curve is reached. Here, the  $b_m$  coefficients should satisfy a normalization condition:  $\sum_{m=1}^M b_m = 1$ . Usually, the interplaying decay processes, for instance, when two systems of levels compete in redistribution of recombination flows, may also determine a two-componental transients [22], leading either to the carrier trapping or to the PL and photoconductivity quenching effects [26,27], etc. For the registered PL signals and linear processes, the transients can be fitted by using Eq.(1) and the PL decay lifetimes  $\tau_{PL}$  ascribed to different components of the decay integration and  $\Delta(h\nu)$  spectral ranges.

The Eq. (1) with  $RS(t) = I_{PL}(t)$ ,  $RS(t=0) = I_{PL}(t=0)$ , and  $\tau_{PL}$  was applied to fit a full shape of the PL decay transients. A fit of the experimental (solid curves) and the simulated (dash curves) transients is illustrated in Fig. 4b. The extracted decay parameters are listed in Table 2. There, the  $m = 0$  component was also used to incorporate the background level.

**Table 2**  
Parameters obtained by fitting a full transient curve.

LD		HD1		HD2	
$b_m$	$\tau_{PL,m}$ (s)	$b_m$	$\tau_{PL,m}$ (s)	$b_m$	$\tau_{PL,m}$ (s)
$b_0 = 1.2 \times 10^{-4}$	$\infty$ , Noise level	$b_0 = 1.3 \times 10^{-4}$	$\infty$ , Noise level	$b_0 = 1.0 \times 10^{-4}$	$\infty$ , Noise level
$b_1 = 0.68$	$\tau_1 = 23 \times 10^6$	$b_1 = 0.78$	$\tau_1 = 8 \times 10^6$	$b_1 = 0.75$	$\tau_1 = 12 \times 10^6$
$b_2 = 0.29$	$\tau_2 = 140 \times 10^6$	$b_2 = 0.16$	$\tau_2 = 230 \times 10^6$	$b_2 = 0.2$	$\tau_2 = 200 \times 10^6$
$b_3 = 0.028$	$\tau_3 = 1 \times 10^{-3}$	$b_3 = 0.05$	$\tau_3 = 1.4 \times 10^{-3}$	$b_3 = 0.04$	$\tau_3 = 1.8 \times 10^{-3}$
$b_4 = 0.0007$	$\tau_4 = 10 \times 10^{-3}$	$b_4 = 0.0007$	$\tau_4 = 15 \times 10^{-3}$	$b_4 = 0.0008$	$\tau_4 = 20 \times 10^{-3}$

It appeared that four components are sufficient to reproduce completely the shape of the TR-PL transient. This set ( $m$ ) of components is either close to the number ( $m=3$ ) of Gaussian spectral components involved into simulation of TR-PL band (Fig. 3) or even coincides when neglecting the small  $b_4$ . Actually, the partial amplitude  $b_4$  is too small to be resolvable within integrated spectrum, -  $b_4$  comprises less than 0.1% of the  $I_{pl}(t=0)$ . Nevertheless, these  $b_3$  and  $b_4$  components might be useful in understanding of the asymptotic decay curve. The  $b_1$  and  $b_2$  components prevail in this set, and they dominate when integration of the PL signals is implemented over all the examined range or various spectral ranges (Fig. 4). The  $b_2$  component with  $\tau_{PL,2} \sim 200 \mu\text{s}$  is resolvable in TR-PL transients recorded using both the SC (Fig. 4a) and TG-PLD (Fig. 4b and c) techniques. The close values of the  $\tau_{PL,2}$  and  $\tau_{PL,3}$ , deduced for all the LD and HD samples, indicate the reliable manifestation of defects, ascribed to the  $b_2$  and  $b_3$  decay components, residing in all the samples. The impact of the  $b_3$  component is nearly twice larger for HD samples relative to that for LD one. Also, the  $\tau_{PL,2}$  is the longer for HD samples relative to that for LD sample. Certainly, the shortest  $b_1$  decay component with  $\tau_{PL,1} \sim 10\text{--}20 \mu\text{s}$  also prevails in all the examined samples, however,  $\tau_{PL,1}$  appears to be shorter for the HD samples when comparing with that value obtained for LD sample. It is worth notice that the manifestation of different decay components might considerably depend on the recording and integration mode. Both TR-PL spectral components (peaked at 550 and 650 nm) with decay lifetime of 20  $\mu\text{s}$  have been recorded for all the samples (Fig. 4b). The two species of defects seem to dominate in different time-scale stages. The linear increase of filling of the first ( $b_1$ ) species defects might also be implied from Fig. 4c. Thereby, the decay shapes can also be understood keeping in mind that PL intensity ( $\sim B_1$ ) of the  $\lambda_{01}$  spectral band (shown in Fig. 3) significantly prevails relative to that ( $B_2$ ) of the  $\lambda_{02}$ . This leads to the rather monotonous changes of Y-R luminescence intensity within spectral band contour.

### 3.3. Carrier recombination transients recorded by MW-PC technique

The MW-PC transients represent the time-dependent changes of free excess carrier concentration (within bands), determined by both the radiative and non-radiative carrier transitions. Really, concentrations of the excess  $p_{ex}$  holes and electrons  $n_{ex}$  ( $n_{ex} = p_{ex}$ ) are nearly the same in the initial decay stages, as  $n_{ex}$  exceeds an equilibrium  $n_0$  one in the examined samples. The short (400 ps) UV pulse excitation of excess carriers enables observations of the short time-scale decay stages (Fig. 5a). To have reasonable resolution, these MW-PC transients were recorded by using short (Fig. 5a) and long (Fig. 5b) display scales.

The short initial-stage decay can be attributed to fast capture rates ( $dn_{ex}/dt = -\sum_i N_{Di}^+ v_{Ti} \gamma_{CD} n_{ex} = -\sum_i n_{ex} / \tau_{CDi}$  and  $dp_{ex}/dt = -\sum_i N_{Ai}^- v_{Ti} \gamma_{CAP} p_{ex} = -\sum_i p_{ex} / \tau_{CDi}$ ) of excess carriers to the ionized donors  $N_{Di}^+$  and acceptors  $N_{Ai}^-$  of different species. Alternatively, this short decay stage can be caused by the surface (s) and bulk (b) non-radiative recombination with  $n_{ex}(t) = -\sum_i A_i \exp[-(D\eta_j^2 + \tau_{bR})t]$  with  $\tau_s = 1/D\eta_j^2$  and  $\tau_{bR}$  lifetimes, respectively. Here,  $v_T$  is the thermal velocity,  $\gamma_C$  is the capture cross-section,  $\tau_C$  is the capture (trapping) lifetime of the respective carriers,  $\eta_j$  are the spatial frequencies and  $D$  the coefficient of the ambipolar diffusion involved in description of the surface recombination process. Depending on the symmetry of capture cross-section values to trap the single or both type carriers, some traps act as the thermal emission centres (interacting only with one of the continuum state bands) or the recombination centres. The radiative band-to-band or exciton radiative recombination of the initially captured carriers can result the simultaneous appearance of the UV-PL, resolved within SS-PL spectra. Due to a small UV-PL collection volume, the UV-PL intensity can be relatively low. Also, during short initial decay stages, the excess carriers are mainly located nearly the sample surface when UV pulsed or even SS excitation is applied. Then, the impact of the surface recombination is enlarged. It can be deduced from

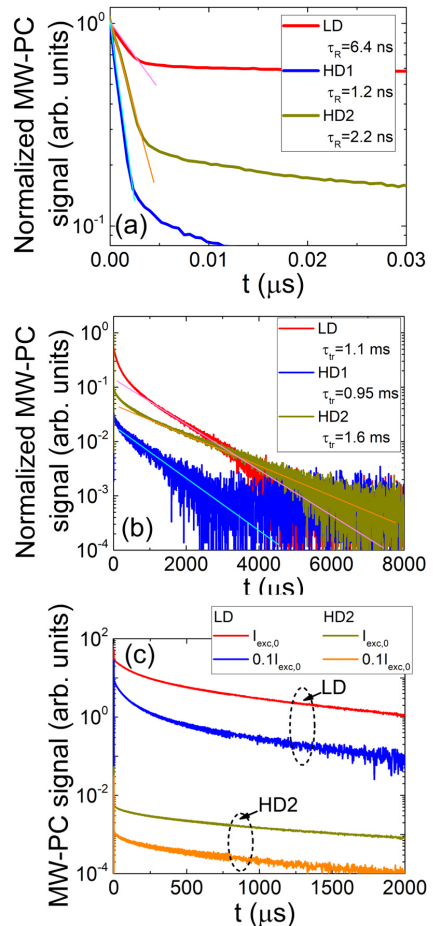


Fig. 5. The MW-PC transients recorded on both sets of samples using short (a) and long (b) display scales. (c) - The MW-PC transients recorded on LD and HD2 samples, varying excitation intensity.

Fig. 5a that the characteristic decay lifetime (with values denoted in the legend for Fig. 5a), ascribed to the initial decay component, decreases with enhancement of carbon dopant concentration when comparing decays recorded for LD and HD samples.

The time-scale of the long asymptotic decay component ( $t_r$ ) correlates well with that obtained within TR-PL and TG-PLD transients. The values of characteristic decay lifetime  $\tau_{tr}$  (see a legend for Fig. 5b) are close to a millisecond. These values are slightly dependent on UV excitation intensity and carbon concentration (Fig. 5c). The characteristic decay lifetime  $\tau_{tr}$  seems to be also attributed to carrier de-trapping (thermal emission) from PL centres. The thermally emitted carriers are then rapidly re-captured to the PL centres. The persistent recovery of free excess carrier density by thermal emission ( $\tau_{tr}$ ) and PL light excited carriers should be assumed to explain the long tail MW-PC signals in microsecond and millisecond time domains after short (200 fs and 500 ps) initial excitation pulse. The correlation between MW-PC and TR-PL decay shapes and PL as well as PC long-tail time-scales indicate the rather efficient conversion from PL light emission to absorption and vice versa, after fast initial filling of the defect states.



The SS-PL (Fig. 2) indicated the asymmetry of surfaces. The asymmetry of surfaces has also been examined by profiling of the MW-PC transients within initial decay component. The wafer surface was excited either by UV (354 nm) or green (532 nm) light pulse, which induces the initial excess carrier distribution with either in-homogeneous (using near-surface excitation wavelength) or rather homogeneous (at bulk excitation) profile. Variations of this profile within wafer thickness  $d \sim 400 \mu\text{m}$  are traced by a needle-tip MW antenna, translated by a few  $\mu\text{m}$  steps within wafer edge boundary. This profile evolves due to excess carrier surface as well as bulk recombination and diffusion [22]. A position of the peak concentration within these profiles becomes fixed when the flows of excess carriers to wafer opposite surfaces reach a balance. This happens for the main decay mode [22], characterized by its amplitude  $A_{i=1}$ . The characteristic decay lifetime ( $\tau_{\text{eff-Sb}}$ ) ascribed to the main decay mode ( $A_{i=1}$ ) depends on the layer thickness  $d_i$  (where a single-directional ( $i$ ) diffusion can be analysed), bulk recombination lifetime ( $\tau_b$ ) and velocity ( $s_i$ ) of recombination on wafer surface ( $i$ ) to which a diffusion flow is directed. To get the MW-PC transient component which would be related to surface recombination process, the PL attributed long-tail component is there subtracted. Thereby, the two-compartmental MW-PC transient fragment is composed (with excluded PL term). The initial stage of the two-compartmental MW-PC is related to a transitional process within surface recombination transient [22], while the longer asymptotic decay is ascribed to the main decay mode. The profiles of  $A_1$  and of  $\tau_{\text{eff-Sb}}$  are plotted in Fig. 6 for LD (a) and HD (b) samples, respectively. The asymmetry of the peak position of  $A_{i=1}$  values within wafer thickness  $d$  can be noticed in Fig. 6 for LD samples. This confirms the SS-PL results assuming that surface recombination velocities  $s_1$  and  $s_2$  differ in LD sample. The  $\tau_{\text{eff-Sb}}$  profiles also imply slight variations of bulk recombination lifetime  $\tau_b$ .

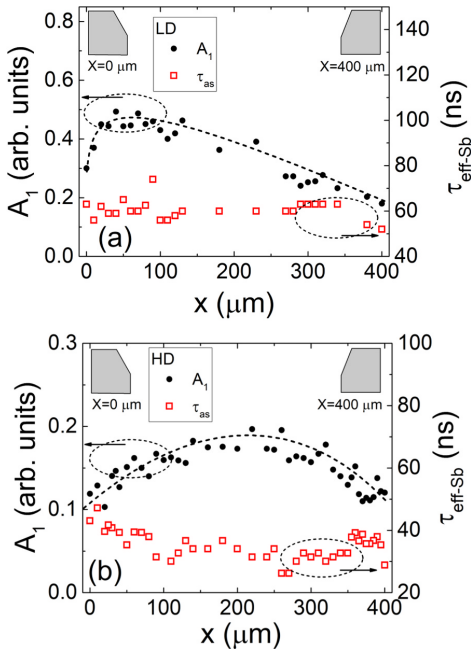


Fig. 6. Distribution of  $\tau_{\text{eff-Sb}}$  and MW-PC signal amplitude  $A_{i=1}$  (ascribed to the main decay mode ( $i = 1$ ) when surface recombination takes place) values obtained by cross-sectional scans of the sample edge boundary for wafers LD (a) and HD (b), respectively.

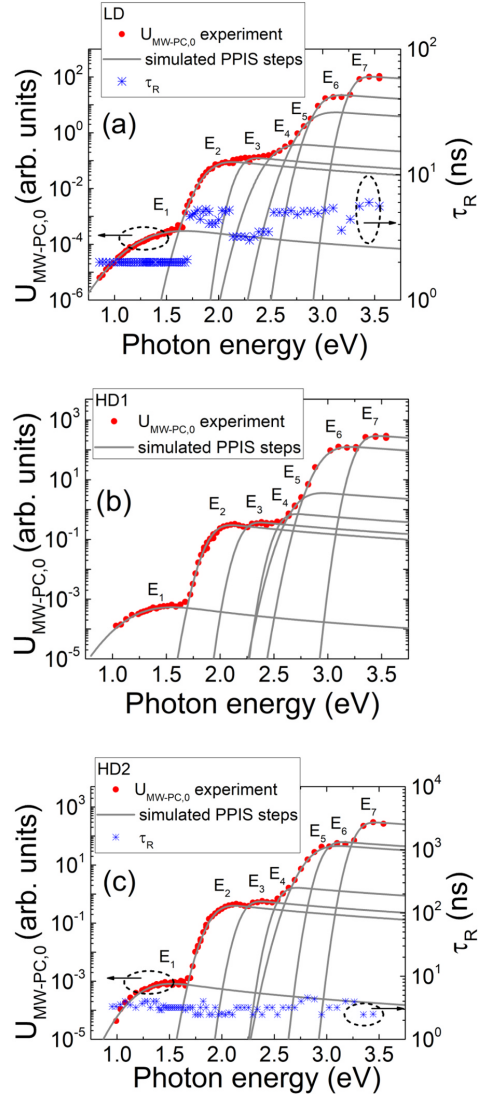


Fig. 7. Photo-ionization spectra recorded for different samples: LD (a), HD1 (b) and HD2 (c), respectively. Solid lines represent spectral steps simulated using Kopylov- Pikhtin [28] model.

### 3.4. Carrier trap spectra obtained using PPIS technique

Variations of the pulsed photo-ionization (PPI) spectra recorded for all the examined samples are illustrated in Fig. 7. The photon-electron coupling for carriers  $n_{i0}$  residing on a definite energy  $E_i$  level determines the values of an absorption coefficient  $\alpha(h\nu) = \sigma(h\nu)n_{i0}$  related to this level. The strength of the coupling is characterized by a spectrally varied cross-section  $\sigma_i(h\nu)$ . The density of photo-emitted carriers  $n_i^+ = \alpha(h\nu)F(h\nu)$  determines the peak value ( $U_{\text{MW-PC},0} \sim n_i^+ \sim \sigma_i(h\nu)$  at  $t = 0$ ) of the  $U_{\text{MW-PC}}$  response for a fixed surface density  $F(h\nu) = \text{const}$  of the incident photons. The surface density of the incident photons  $F(h\nu)$  is evaluated by calibration of the energy/per pulse measurements

within incident laser beam. The PPIS steps, recorded as  $U_{MW-PC,o}(h\nu)$ , represent the spectral distribution of  $\sigma_f(h\nu)$ . The shape  $\sigma_f(h\nu)$  of the spectral steps and spectral position ( $E_f$ ), ascribed to several  $f$  centres, serve for evaluation of the photo-activation energy  $E_f$  and identification of the definite ( $f$ ) defects. As usually, PPI spectrum contains a few spectral steps. The relative concentrations  $N_f$  of different defects  $f$  can be roughly estimated by using a spectrum of an absorption coefficient  $\alpha(h\nu)$ , Fig. 1a, independently measured on the same sample, and its correlation with  $\sigma(h\nu) \sim U_{MW-PC,o}$ , as  $N_f(h\nu) = \alpha(h\nu)/\sigma_f(h\nu)$ . Actually, the density  $N_f$  of the  $f$  species centres coincides with a partial density of the equilibrium carriers  $n_{f0}$  if  $f$  traps are completely filled.

The electron-phonon coupling can also play the important role in formation of the PPIS steps, determined by a photon-electron coupling. The phonon-assisted changes of the cross-section  $\sigma_f(h\nu)$  for a definite defect can be approximated by the Kopylov- Pikhhtin [28] approach

$$\sigma(h\nu) \propto \int_0^\infty \frac{e^{-(E+E_f-h\nu)^2/l^2} \sqrt{E} dE}{h\nu(E+E_f)^2}, \quad (2)$$

where electron-phonon coupling is determined by the broadening parameter  $\Gamma_f$ . The broadening of the absorption onset is also related to the Huang-Rhys [29] factor  $S$  and, consequently, to the Franck-Condon shift and the energy of the vibrational mode [30]. The expression (Eq. (2)) of the Kopylov- Pikhhtin [28] model is similar to that derived by Chantre-Vincent-Bois (CVB) [31].

The Kopylov-Pikhhtin [28] approach (Eq. (2)) has been applied for simulating of the  $U_{MW-PC,o}(h\nu)$  steps in the experimental spectra implemented by varying  $E_f$  and  $\Gamma_f$  as free parameters, to get the best fit estimated by a non-linear least square method. The activation energies (with fitting uncertainties of about 5%) and  $\Gamma_f$  parameters of the predominant centres have been identified and listed in Table 3. The defects (Table 3) have tentatively been identified using the activation energy values taken from literature referenced. Up to seven centres ( $f=1-7$ ) have been resolved in the examined samples.

Separation of the PPI spectral steps has been made by controlling whether the same step appears in different samples of nearly the same technology material. For instance, the  $E_4$  PPIS step is doubtful for the HD1 sample while it is more clear for samples LD and HD2. Additionally, the presence of PPIS step has been corroborated by the consequent change of the MW-PC lifetime (Fig. 7a). The same motivation was to involve into consideration the  $E_4$  PPIS step. Separation of the  $E_5$  and  $E_6$  PPIS steps has also been made by comparing the PPI spectra and MW-PC lifetime profiles (as a function of  $h\nu$ ) recorded for all the samples. However, values of the photo-activation energy of  $E_5$  and  $E_6$  PPIS steps are rather close, while this energy differs considerably when comparing simulation parameters for  $E_3$  and  $E_4$  PPIS steps.

#### 4. Discussion

The XRD inspection showed rather narrow X-ray rocking curves with (FWHM) of  $64''$  of the (0002) peak and of  $106''$  of the (30–32) reflection, respectively. This indicates a low density of structural

**Table 3**

Activation energy and broadening factor values estimated by fitting PPI spectral steps associated with different defects.

LD		HD1		HD2		Defect type
$E_f$ (eV)	$\Gamma_f$	$E_f$ (eV)	$\Gamma_f$	$E_f$ (eV)	$\Gamma_f$	
$E_1 = 1.4$	0.32	$E_1 = 1.3$	0.3	$E_1 = 1.3$	0.24	$C_i$ [32,33]
$E_2 = 1.9$	0.16	$E_2 = 1.9$	0.12	$E_2 = 1.9$	0.13	C related [32]
$E_3 = 2.2$	0.1	$E_3 = 2.2$	0.1	$E_3 = 2.2$	0.1	Vacancy $V_{Ga}$ [34]
$E_4 = 2.6$	0.17	$E_4 = 2.6$	0.1	$E_4 = 2.6$	0.1	Vacancy $V_{Ga}$ [35]
$E_5 = 2.9$	0.17	$E_5 = 2.8$	0.15	$E_5 = 2.9$	0.17	$C_N^-$ [9]
$E_6 = 3.0$	0.13	$E_6 = 3.0$	0.15	$E_6 = 3.0$	0.1	C related [32,33]
$E_7 = 3.3$	0.1	$E_7 = 3.3$	0.1	$E_7 = 3.3$	0.1	$C_N O_N$ [9] or $C_N$ [32]

defects (below XRD detection limit [20,21] for the estimation of the dislocation surface density) in all the investigated samples.

Differential analysis of absorption spectra (Fig. 1b) also hints on rather low density ( $< 10^{17} \text{ cm}^{-3}$ , close or below the detection limit for SIMS) of carbon impurities in LD sample relative to that in HD samples.

We did not find any electron spin resonance (ESR) signals in the examined samples till liquid nitrogen temperatures. The recently published EPR data [36] recorded at 3.5 K temperature on illuminated samples of the same GaN material showed only an indirect relation of the EPR spectra to carbon impurities. This indicates that introduction of carbon does not produce the recordable at room temperatures densities of the ESR active centres irrespective of C doping concentration. Nevertheless, the positron annihilation spectroscopy (PAS) made on carbon doped MOCVD GaN epi-layers [37] hints on the enhanced production of vacancy defects related to incorporation of carbon.

The deep level transient spectra (DLTS) recorded on the same samples (published elsewhere [19]) showed a rather rich spectrum of shallow traps with thermal activation energies in the range of  $< 0.56$  eV. This additionally implies that carrier traps with significantly asymmetric cross-sections (relative to coupling with either conduction or valence bands) might play the important role in carrier trapping and thermal emission. However, these shallow traps testified no affinity to carbon impurities. An impact of the trapping centres is different in steady-state and transient depth-distributions of the excess carriers. For the steady-state situations, the role of such the trapping centres is balanced and it is negligible. However, the trapping effect [22] is important and its role increases with carrier concentration decay in time, within MW-PC and TR-PL transients.

The rich spectrum of deep photo-active centres, reported above, together with shallow traps complicate significantly an analysis of the conversion of the excitation to carrier distribution and later their decay through radiation and radiation-less transitions. The most of experiments reported in literature on photoconductivity and photoluminescence spectroscopy had been performed at surface excitation, using UV illumination. Our experiments using bulk excitation wavelengths showed a non-efficient injection of carriers, while intensities necessary to have the recordable PC/PL signals are close to that where the non-linear two-photon/two-step absorption becomes important. This additionally complicates analysis of spectra. On the other hand, generation of excess carriers with either later their binding into excitons or capture to donors and acceptors (leading to phenomena of photoluminescence and photoconductivity) determines different excess carrier depth-distribution profiles.

In the simple case of carrier decay through several independent competing recombination channels, the fastest of them would dominate and determine the excess carrier lifetime. For instance, a spectral band with characteristic  $\tau_{PL} \sim 8 \mu\text{s}$  (Table 2) should completely hide the PL band with  $\tau_{PL} \sim 230 \mu\text{s}$ . However, the MW-PC transients indicate a long-living ( $> 1$  ms) continuum of free carriers together with  $\tau_{PL} \sim 8 \mu\text{s}$ . Additionally, the experiments on heavily hadron irradiated GaN materials [23,38] testify the simultaneous decrease of intensity of all the observed PL bands, due to radiation defects acting as the non-radiative recombination centres. Moreover, this PL intensity reduction directly depends on irradiation fluence. However, for the non-irradiated materials, the PL bands with different  $\tau_{PL}$  co-exist. This hints that the internal carrier generation sources appear, which compensate a carrier density loss due to radiative and radiation-less recombination. In the SS-PL regime, the UV excitation should keep the sharply decreasing concentration profile. In the case of TR-PL, the initial profile is smoothed by the in-depth diffusion. Therefore, the excess carrier depth distribution profiles at steady-state and pulsed excitation should be discussed. These profiles can manifest different aspects of the processes of energy conversion from carrier injection to light emission. Adjustment of these characteristics might be a key for the more reliable estimation of the parameters of various trap concentration and cross-sections of photon-electron and electron-phonon coupling.

4.1. Impact of carrier generation, diffusion and surface recombination

The SS-PL intensity (when comparing Fig. 2a and b) is independent of wafer excitation face (orientation), for HD samples. However, the asymmetry of PL intensity has been observed in the SS-PL spectra measured on LD samples, and this asymmetry is corroborated by MW-PC profiling experiments (Fig. 6). The impact of the surface recombination is inevitable, when UV excitation is employed, due to both effects: the enhanced non-radiative recombination rate within initial decay stages as well as shrinkage of the effective volume from which the short wavelength PL is collected. This is caused by a formation of the excess carrier density depth-profile which in TR-PL experiments additionally varies in time. In-depth diffusion of carriers and excitons (which are often responsible for the UV wing of PL spectrum) determines an increase of a volume from which Y-G-R luminescence is collected. However, the radiation of UV-B spectral range is re-absorbed in rather thick samples. Nevertheless, the UV-B PL photons are capable to inject carriers of multiple generations within material thickness for the rather thick samples.

A description of the steady-state carrier depth ( $0 \leq x \leq d$ ) distribution at sharp near-surface excitation with  $ad > 1$  can be found in text books (e.g. [39]), and this distribution is determined by the ambipolar diffusion length  $L = (D_a \tau_{R,eff})^{1/2}$  and by surface recombination velocity  $s$  as well as bulk recombination lifetime  $\tau_R$ . The excess carrier distribution is then expressed as

$$n(x) = \frac{g(0, h\nu) \exp(-\alpha(h\nu)x) \tau_{R,eff}}{h\nu} \left[ \frac{s \tau_{R,eff} \operatorname{sh}\left(\frac{d-x}{L}\right) + L \operatorname{ch}\left(\frac{d-x}{L}\right)}{(L^2 + s^2 \tau_{R,eff}^2) \operatorname{sh}\left(\frac{d}{L}\right) + 2Ls \tau_{R,eff} \operatorname{ch}\left(\frac{d}{L}\right)} \right]. \quad (3)$$

Here, the assumptions of equality  $n(0) = p(0)$  of the initially injected carriers by the band-to-band generation rate  $g(0, h\nu)$  and of the  $s_1 = s_2$  are accepted for simplicity. Also, the effective excess carrier recombination lifetime  $\tau_{R,eff}$  is implied, as an averaged impact of different carrier capture centres. The simulated profile of the steady-state distribution of the excess carriers is illustrated in Fig. 8a. This profile has been simulated using  $s$  as well as  $D_a$  values, inherent for GaN material, and  $\tau_{R,eff}$ , obtained for the recorded MW-PC transients.

The re-absorption effects can be a reason for the slightly outspread profile of carrier and exciton density distribution, which generates SS-PL of the long wavelength wing. Further outspread of the excited volume can be achieved by secondary PL photons propagating towards the rear surface of a sample and involved into absorption of the shallower photo-active centres. This would mean that additional light source with different absorption coefficient occurs behind the initial distribution profile by increasing an effective carrier diffusion length  $L$ . Thereby, the initial carrier distribution profile can be significantly modified (Fig. 8a) if sufficient set of different photo-ionization centres exist in the material. The latter can be implied when considering the schemes of possible transitions on the basis of literature data [13,14,40–42] and results of this study. The rather rich spectrum of deep traps and vast combinations of possible electronic transitions can be deduced by considering the concerted variations of PL and PPIS, based on rather exhaustive comparisons of the theoretical and experimental findings (published in Refs. [9,13,14,40–42]), addressed to interpretation and estimation of probable concentrations of point defects in Ga and N rich GaN materials containing different carbon doping levels.

In transient experiments, such as MW-PC or TR-PL, the excess carrier injection is usually implemented by a short pulse of the strongly absorbed light. Then, the excess carrier profile changes in time and stabilizes when the travelling in-depth carriers reach the rear surface of the sample. The impact of the surface and bulk recombination as well as the re-absorption of the secondary PL photons there appears in a slightly different mode.

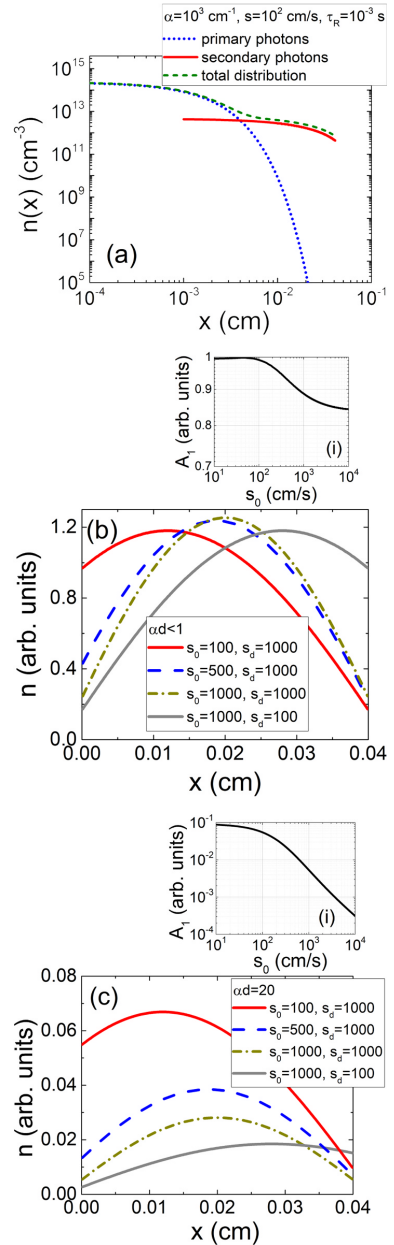


Fig. 8. (a) – The simulated distribution of excess carriers injected by the incident (primary photon flux) and by PL (secondary photons generated due to PL) photons. The simulated profiles of the excess carrier concentration depth-distribution within wafer of thickness  $d = 400 \mu\text{m}$  for bulk (homogeneous with  $ad < 1$ ) excitation (b) and near-surface excitation (c) (at  $ad = 20$ ). Values of surface recombination velocity of  $s_0$  and  $s_d$  are denoted in the legends for figures. In the insets, the functions  $A_1(s_0)$  are illustrated for bulk (b) and near-surface excitation (c) (where a laser beam impinges at  $x = 0$ ).

For transients, the excess carrier density variation in time  $t$  and over wafer depth-coordinate  $x$  can be expressed [22] as

$$n(x, t) = n_{ex,0} \sum_{l=1}^{\infty} A_l \exp \left[ - \left( D\eta_l^2 + \frac{1}{\tau_b} \right) t \right] \left[ \cos(\eta_l x) + \frac{s_0}{D\eta_l} \sin(\eta_l x) \right]. \quad (4)$$

Here,  $n_{ex,0}$  is the concentration of the light injected excess carrier pairs,  $A_l$  is a decay amplitude ascribed to the spatial frequency  $\eta_l$  of a decay mode  $l$ ,  $\tau_b$  is the bulk recombination lifetime,  $D$  is the coefficient of the ambipolar diffusion of carriers,  $s_i$  is the velocity of surface recombination on face ( $i = 0$ ) and back ( $i = d$ ) surfaces. This profile has been scanned in our experiments by the microwave needle-tip antenna, located at the wafer edge boundary and oriented perpendicularly to the excitation beam, impinging on wafer face surface, when sample is stepper moved relative to a MW probe. The MW needle-tip antenna of a radius  $\delta$  integrates the PC response over the wafer width  $w \approx 3$  mm perpendicularly to wafer thickness coordinate at  $x \pm \delta$  location. A peak of the  $w$  averaged amplitude [22] of the main decay mode ( $A_{l=1}$ ) in HD samples (Fig. 6b) has been obtained for the half of wafer thickness ( $d/2$ ). It can be inferred that the velocity of the surface recombination and density of surface traps on the opposite surfaces of HD wafer is nearly the same. Then, the surface recombination velocity can be evaluated either by the graph technique [22] using simulated  $A_l$  dependencies on  $sd/D$  for different values of  $ad$  or by solving the transcendental equations

$$\tan \eta d = \frac{\frac{s_0}{D\eta} + \frac{s_d}{D\eta}}{1 - \frac{s_0 s_d}{D\eta D\eta}}, \quad \tan \eta d_1 = \frac{s_0}{D\eta}, \quad \tan \eta(d-d_1) = \frac{s_d}{D\eta} \quad (5)$$

together with equations for  $A_l(\eta_1 d_1)$ ,  $A_l(\eta_1(d-d_1))$ . These  $A_l$  decay amplitudes are obtained as Fourier coefficients for the discrete  $m$  modes:

$$A_l = \frac{\int_0^d f(x, t=0) \left[ \cos(\eta_l x) + \frac{s_0}{D\eta_l} \sin(\eta_l x) \right] dx}{\int_0^d \left[ \cos(\eta_l x) + \frac{s_0}{D\eta_l} \sin(\eta_l x) \right]^2 dx} \quad (6)$$

when using an initial condition

$$f(x, t=0) = \exp(-\alpha x). \quad (7)$$

Integrals in Eq. (6) can be obtained analytically, however, this leads to the cumbersome expressions.

For a symmetry of surface recombination  $s_0 = s_d$  at opposite surfaces, corresponding to  $x = 0$  and  $x = d$ , expressions of Eq. (5) are shrunk to a single transcendental equation. For the asymmetric conditions  $s_0 \neq s_d$ , an inherent distance  $d_1$  (or  $d-d_1$ ) can be evaluated by solving Eq. (5). There, a maximum of concentration ( $A_l$  for the amplitude of the main decay mode) appears at  $x_c = d_1$  within its ( $n(x) \sim A_l$ ) depth profile, attributed to the asymptotic decay component with effective decay lifetime  $\tau_{eff-sb} = [(D\eta_1^2)^{-1} + \tau_b^{-1}]^{-1}$ . This extremum ( $x_c$ ) point (Fig. 8b) depends on values of  $s_0$ ,  $s_d$ , and it is shifted either to a surface of small recombination velocity (in the case of asymmetry) or appears at half-width  $d/2$  for  $s_0 = s_d$ . The profiling of  $n(x) \sim A_l$  is preferable at negligible absorption with  $ad < 1$ , when initial depth-inhomogeneity (Eq. (7)) of excitation can be ignored. This regime can be implemented using bulk excitation with photons of energy below bandgap,  $h\nu < E_G$ . There values of  $A_l$  are sufficiently large (inset for Fig. 8b) for the reliable registering of the PC responses. A steep (exp  $(-\alpha x)$ ) initial excitation at  $ad > 1$  with  $h\nu \sim E_G$  might crucially change the asymptotic distribution of  $n(x) \sim A_l(x)$ , Fig. 8c. However, the dynamic range of variations of the  $A_l(s_0, s_d)$  function is significantly wider for  $ad > 1$  (inset for Fig. 8c) than that for  $ad < 1$ . Therefore, combining of both bulk and surface excitation regimes is needed to reliably separate values of surface recombination velocity.

The transients governed by surface recombination were obtained by subtracting the long-tail PL component (Fig. 6). Then decay amplitudes,

ascribed to wafer surfaces within depth profiles, have been considered. For rough estimation, values  $D$  of the coefficient of the ambipolar diffusion can be assumed as  $D = 2D_n D_p / (D_n + D_p) \sim 1.5\text{--}2.8$  cm<sup>2</sup>/s with  $D_n \sim 25$  cm<sup>2</sup>/s electron and  $D_p \sim 0.8\text{--}1.5$  cm<sup>2</sup>/s hole diffusion coefficients, calculated using mobility values referenced in [5], respectively. This estimated  $D$  value is close to that  $D = 2.4$  cm<sup>2</sup>/s measured at high excitation level in bulk GaN materials [43]. The velocity of surface recombination  $s_0 = s_d \approx 2 \times 10^3$  cm/s has thereby been estimated for HD samples. For the LD sample (with wafer orientations sketched on Fig. 2), the asymmetric  $n(x)$  profile was obtained (Fig. 8b) (in agreement with the asymmetry of the SS-PL intensity in Fig. 2). The  $A_l$  peak appears to be located closer to the surface (with  $s_0$ ) with reduced value of velocity of the surface recombination. This peak location serves for estimation of the effective depth  $d_1$  overwhelming the single-directional carrier diffusion ( $s_0 d_1 / D$ ) due to a gradient created by the surface recombination of  $s_0$ . The amplitude  $A_l$  of the main decay mode depends only on the decay space frequency  $\eta_1$  [22] with  $d_1$  being either  $d_1$  or  $d-d_1$ . Values of  $s_0 \approx 400$  cm/s and  $s_d \approx 3 \times 10^3$  cm/s have been estimated using the above mentioned procedures. This hints on possible passivation of the near-surface layer by making the semi-insulating material layer. The enhanced concentration at dopant-rich surface is as usually confirmed by SIMS profiling. It has been deduced from Fig. 8b and c that the bulk lifetime shows nearly homogeneous depth-distribution with values of  $\tau_b \approx 70$  ns. The  $\tau_{eff-sb}$  values obtained from the profiling of the excess carrier decay components properly agree with carrier lifetime values directly measured by MW-PC (using a slit-antenna and parallel excitation-MW probe geometry). Thus, the instantaneous lifetimes of the MW-PC within the very initial decays stages (Fig. 5a) can be partially linked to the transitional phase of surface recombination transients.

Variations of the PL signals can also be significantly modified by a volume from which PL light is collected and where PL is generated. The latter volumes should correlate with the excess carrier depth-distribution profiles. Also, the volumes, from which PL light is collected, depend on sample thickness and photon energy. As it can be deduced from comparison of SS-PL spectra recorded in samples of different thickness, the ratio of the effective volumes, from which different spectral components are collected, comprises several orders of magnitude when comparing G-Y-R PL and UV-PL components (absorbed within a few  $\mu$ m depth). Contrary, in homogeneously excited thin ( $\sim 1$   $\mu$ m thick epi-layer) samples, UV PL intensity even exceeds that of G-Y-R PL.

The TR-PL spectra (Fig. 3) indicate that G-Y-R PL band contains a structure of a few peaks of different intensity when evolution of these peaks varies in time (Fig. 4). It can be inferred that the time variations are related to steps of conversion from absorption to emission through generation of excess carriers. There, the role of the radiation-less centres might be essential in the delay processes. Carrier capture into shallow trapping centres might lead to significant asymmetry between capture ( $\tau_c$ ) and thermal emission ( $\tau_e$ ) times to keep slowly varying density of free carriers (detected by MW-PC). Carrier concentration variations  $n_{ex}(t)$  in time  $t$  is a non-linear process with trapping coefficient  $K_{tr}(n_{ex})$ , [22,27]:

$$n_{ex}(t) = n_{ex}(0) \exp \left( - \frac{t}{\tau_R K_{tr}} \right), \quad (8)$$

$$K_{tr}(n_{ex}(t)) = 1 + \frac{M_{tr} N_{CM}}{[N_{CM} + n_{ex}(t)]^2}. \quad (9)$$

Here,  $\tau_c = [v_{th} \gamma_{CM} (M_{tr} - m)]^{-1}$  is the carrier lifetime related to capture into traps  $M_{tr}$ ,  $\tau_R$  is carrier lifetime relative to radiation-less recombination,  $v_{th}$  is the thermal velocity of carriers,  $\gamma_{CM}$  is carrier capture cross-section relative trapping centres of species  $M$  and concentration  $M_{tr}$ , initially filled by density of carriers  $m$ ,  $N_{CM} = N_{cc} \exp(-\Delta E_M / k_B T)$  is the effective density of continuum states  $N_{cc}$  relative to thermally ( $k_B T$ ) induced emission from traps  $M$  with activation energy  $\Delta E_M$ . The trapping centres maintain the slowly

varying excess carrier density when  $\tau_c$  is shorter than  $\tau_{PL}$ , associated with different radiative centres. Variations of the excess carrier concentration described by Eqs. (8) and (9) lead also to a two-compartmental transient, similar to that illustrated in Fig. 4 for the TR-PL and in Fig. 5 for the MW-PC transients. The trapping becomes essential ( $K_{tr} > 1$ ) within the asymptotic decay component when  $n_{ex}(t)$  approaches to  $N_{CM}$ . Moreover,  $K_{tr}$  exponentially depends on temperature when  $K_{tr} > 1$  and may form the broaden peaks as a temperature dependent function. Actually,  $K_{tr} \rightarrow 1$  when excess carrier density exceeds that of trap concentration,  $n_{ex}^2 > M_p N_{CM}$ . Trapping might be the crucial reason for the excess carrier density saturation and photoconductivity quenching effects.

#### 4.2. Conversion from photo-ionization to emission spectra

It has been found that the as-recorded MW-PC transients one-to-one reproduce qualitatively the TR-PL transients when comparing MW-PC (Fig. 5) and TR-PL (Fig. 4) decays. The structure of the SS-PL spectrum with the highest peak at 2.15 eV in heavily carbon doped GaN can be well approximated by configuration diagram model [e.g. 25, 30] of the  $C_N^-$  centre. A width of the SS-PL band peaked at 2.1–2.2 eV (Y-PL), covering the R-Y-G PL wavelength range, can be fitted by decreasing a value of the Huang-Rhys factor  $S$ . Such an adjustment of  $S$  value also leads to the asymmetric shape of a wide Y-PL band. However, an inclusion of re-absorption always determines a reduction of the PL intensity in the short wavelength wing of the PL band even for the rather symmetric PL bands. Certainly, a rather good fit of the SS-PL Y-PL band (using the configuration diagram) is facilitated when the excess carrier concentrations and their variations with excitation intensity are extracted from the same PL data, without independent control of carrier distributions and decay rates. The configuration model would be doubtless if a single deep centre, attributed to carbon, is an exceptional reason for the Y-PL band formation. Nevertheless, the PL band peaked nearby 2.2 eV is observable in most of samples grown using different technologies, differing in thickness, doping densities and species of introduced impurities.

In the SS-PL spectra (Fig. 2), a few UV-B PL peaks in photon energy range of 3.2 – 3.5 can be implied. These peaks are routinely attributed to exciton and band-to-band (b-b) radiative recombination. Based on the van Roosbroeck-Shockley (vR-S) approach [44,45], the coefficient  $B$  of the band-to-band radiative recombination for GaN materials is evaluated [46] to be  $B = 2.2 \times 10^{-10} \text{ cm}^3 \text{ s}^{-1}$ . There [46], the radiative recombination rate is also estimated as  $R_0 = 8.9 \times 10^{-30} \text{ cm}^{-3} \text{ s}^{-1}$ , which leads to the spontaneous PL lifetime of  $\tau_{b-b, PL} = 4.5 \text{ ns}$ . The latter  $\tau_{b-b, PL}$  value is in-line (by order of magnitude) with an initial MW-PC decay lifetime (Fig. 5a). Actually, the initial MW-PC decay component (Fig. 5a) is slightly shorter, keeping in mind that the MW-PC transients were recorded in our experiments at the lower densities ( $< 10^{15} \text{ cm}^{-3}$ ) of excess carriers than that ( $\sim 10^{18} \text{ cm}^{-3}$ ) used in [46] for  $\tau_{b-b, PL}$  estimation. Short initial MW-PC decay lifetimes can then be explained by simultaneous capture of the excess carriers by the b-b radiative and radiation-less channels. Nevertheless, the intensity of these UV-B PL peaks (the detail origin of which is omitted from further consideration in our analysis) can serve as a benchmark for estimation of the radiative recombination rate related to the PL peaks, ascribed to deep centres.

Up to seven deep photo-active centres with activation energies in the range of 1.3–3.3 eV (PPIS, Table 3) and up to five shallower trapping centres with activation energies in the range of 0.16 – 0.56 eV (by recording DLTS [19]) have been separated for the examined samples. This result is in-line with a generally accepted opinion that AT and HVPE GaN materials contain a big nomenclature of point defects regardless of their perfect crystalline structure relative to extended defects. The big amount of different species defects complicates the detail analysis of a definite centre. Therefore, the more general approach is necessary to fit spectra of conversion from absorption to light emission and vice versa. Such an approach can be based on van Roosbroeck -

Shockley relation [44,45] between absorption and emission, derived using the condition of detail balance. This approach enables simulation of the Stokes shifts between the outspread photo-ionization (PPIS) steps and the respective PL band peaks.

At thermal equilibrium, the rate of radiation  $R_f(h\nu)$  for the photons of energy  $h\nu$  is related to the cross-sections  $\sigma_f(h\nu)$  [47] of the photon-electron coupling, and, for the  $f$ -species deep charged centres filled with electrons of density  $n_f$  equal to concentration  $N_f$  of the respective traps, can be expressed as:

$$R_f(h\nu) = 8\pi \left( \frac{k_B T}{h} \right)^3 \left( \frac{\kappa}{c} \right)^2 \frac{\left( \frac{h\nu}{k_B T} \right)^2}{\exp\left(\frac{h\nu}{k_B T}\right) - 1} \sigma_f(h\nu) N_f \\ = \rho_0 \left( \frac{h\nu}{k_B T} \right) \sigma_f(h\nu/k_B T) N_f. \quad (10)$$

Here,  $\kappa$  denotes the refraction index of material,  $h$  is Planck constant,  $c$  is velocity of light in vacuum,  $\rho_0$  is the surface density of photons ascribed to a unit frequency  $\nu$  within absorption spectrum. An attribution of the initial and final states (either localized or continuum) is adjusted to  $\sigma_f$  for the photo-ionization or photo-neutralization processes, respectively. For situations far from the thermal equilibrium, the change of radiation rate is expressed as [45]:

$$\Delta R_f(h\nu) = R_{f,PL}(h\nu) \left[ \frac{(n_0 + n_{ex})(p_0 + p_{ex})}{n_i^2} - 1 \right]. \quad (11)$$

Here,  $n_i = 2 \times 10^{-10} \text{ cm}^{-3}$  is the intrinsic concentration for GaN [46],  $n_0$  and  $p_0$  represent the equilibrium densities of filled initial states and empty final states, respectively, for radiative transitions, while  $n_{ex}$  and  $p_{ex}$  denote filling of the non-equilibrium states. In the case of band-to-band radiative transitions,  $n_{ex,0}$  and  $p_{ex,0}$  denote the concentrations of electrons and holes, respectively. The carrier lifetime relative to radiative transitions for the case of  $n_{ex} = p_{ex}$  i.e. PL lifetime  $\tau_{PL}$  is related to the photo-ionization  $\sigma_{f,PL}$  cross-section and to the density of photons at the peak of the PL band [45] as

$$\Delta R_f(h\nu) = \frac{n_{ex,\Delta h\nu}}{\tau_{PL,\Delta h\nu}} = \rho_{f,PL} \left( \frac{h\nu}{k_B T} \right) \sigma_{f,PL}(h\nu/k_B T) N_f \frac{n_{ex,\Delta(h\nu)} N_f}{n_i^2}. \quad (12)$$

As noted in [47],  $n_{ex}$  and  $p_{ex}$  are evaluated using the quasi-Fermi level statistics, while  $n_{ex,\Delta(h\nu)}$  should be determined as a partial concentration decaying through a definite radiative channel. It is relevant to assume that  $n_{ex,f,\Delta h\nu} \sim \Delta R_{\Delta h\nu,PL}$ ,  $\tau_{PL,\Delta h\nu} \sim \sigma_{f,PL}(h\nu)$  within the PL spectral range. For situations of the short pulse excitation, the  $n_{ex,\Delta(h\nu)}(t, K_{tr})$  and  $\Delta R_{\Delta(h\nu)}(t)$  become the functions of time and of parameters of the non-radiative transitions.

The correlation between the photo-ionization and photoluminescence spectra can be simulated by using Eqs. (2, 9–12). To have the equality in relation of Eq. (2), the latter expression should be multiplied by the value of square of the matrix element ( $|M_{fk}|^2$ ) for the transition from level  $f$  to continuum ( $k$ ) [31].

The comparison of the simulated photo-ionization and photoluminescence spectra is illustrated in Fig. 9. The photo-ionization spectrum (Fig. 9a) has been simulated taking (from Table 2) the extracted values of the cross-section of photo-electron coupling  $\sigma_f(h\nu)$  and of the photo-ionization energy  $E_f$  as well as broadening factors  $\Gamma_f$  for all ( $f = 1-7$ ) the separated photo-active centres. The absolute values of  $\sigma_f(h\nu)$  have been determined using a benchmark  $\sigma_{|h\nu=3.30 \text{ eV}}$  independently estimated from the transmission spectroscopy measurements. Also, the  $\sigma_f(h\nu)$  corrections have been made including the impact of shallower traps on deep ones for  $f > 1$ . The simulated spectrum (Fig. 9a) of the photo-ionization cross-sections resembles the experimental PIS curves (Fig. 7). The PL spectrum (Fig. 9b) has been simulated using the determined  $\sigma_f(h\nu, \Gamma_f)$  and Eq. (10) to fit Stokes shifts of the definite PL spectrum bands, ascribed to the specific ( $f = 1-7$ ) centres. The  $\sigma_f(h\nu, \Gamma_f)$  curve has been simulated to fit the experimental SS-PL



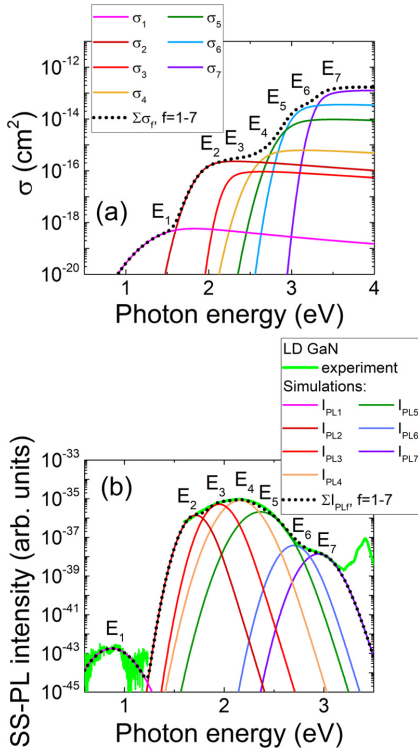


**Fig. 9.** (a) - Comparison of the simulated photo-ionization (a) and photo-luminescence (b) spectra using PPIS experimental data (listed in Table 2), extracted for the HVPE LD GaN:C material. In Fig. (b), the quantitative comparison of the recorded and simulated SS-PL spectra is also depicted.

spectral component with a PL peak at  $\sigma_{f,PI}(\nu_{f,PI}, I_f)$ . The modified values of the  $\sigma_{f,PI}(\nu_{f,PI}, I_f)$  and the  $\rho_f(\nu_{f,PI})$  parameters have thereby been obtained. The simulated PL peak intensity has been additionally adjusted by varying the parameter  $\varphi_f = (\alpha^1/d)\Delta\rho_{f,PL} = (\alpha^1/d)N_f n_{f,ex}$  which includes corrections due to PL collection volume and concentrations of the excess carrier as well as radiative centre. Simulation of the whole SS-PL spectrum, related to deep centres, was performed in order to fit the experimental SS-PL recorded for the definite (LD, HD) sample. Here, PL peaks ascribed to the exciton annihilation and band-to-band radiative transitions have not been considered.

As illustrated in Fig. 9 (for LD sample), a rather good quantitative fit of the simulated (using vR-S approach) and experimental SS-PL spectra has been obtained. Simulations of the PPI in a PL spectra showed that the additional PL peak within infrared (IR) spectral range (peaked within 0.8–1.3 eV) is probable. Based on this prediction, the additional search of IR PL has been performed, and detail results will be discussed elsewhere. Indeed, such an IR PL spectral band was revealed (Fig. 2c). It is also sketched in Fig. 9.

#### 4.3. Estimation of concentration of different deep centres

The concentrations and photon-electron coupling cross-sections were estimated, based on correlations between PPIS, PL and absorption spectroscopy data. The concentration  $N_f$  of different species  $f$  centres have been estimated from the fitting parameters  $\varphi_f$  adjusted when relating PPI and SS-PL spectra on the basis vR-S equation for the non-equilibrium situations (Eqs. 10, 11). Here, it has been accepted  $n_{ex} = p_{ex}$ ,

as UV excitation is employed. The  $n_{ex,f}$  has there been included within radiative recombination rate expressed through PL lifetime. On the other hand, the radiative recombination rates  $\Delta R_f$  are fitted (Fig. 9) by simulating of the vR-S conversion characteristics. Certainly, the steady-state is kept under balance of the permanent generation  $g$  and carrier capture rates ascribed to trapping centres ( $\tau_{c,tr}$ ), to band-to-band PL ( $\tau_{b-b,PL}$ ) and to PL ( $\tau_{PL,f}$ ) through deep centres of species  $f$  associated with point defects, as

$$g(x) = n_{ex}(x)(\tau_{c,tr}^{-1} + \sum \tau_{PL,f}^{-1} + \tau_{b-b,PL}^{-1}) = (n_{ex}(x)/\tau_{c,tr}) + \Delta R_f + Bn_{ex}^2(x). \quad (13)$$

Here, the neutrality condition of  $n_{ex} + \sum(N_{A,f}N_{D,f}^+) = p_{ex}$  should also be preserved. The parameters  $\tau_{c,tr}$ ,  $\Delta R_f$ ,  $\tau_{PL,f}$ ,  $\tau_{b-b,PL}$  and  $B$  are estimated by using data extracted from MW-PC and TR-PL transients, measured independently. Clearly, the shortest lifetimes and the largest radiative recombination rates govern the intensity of processes. The photon emission rates  $\Delta R_f$  have been calculated based on vR-S model using the photon-electron coupling cross-section parameters, extracted from PPI and transmission spectroscopy, and the Plank relation for  $\rho_f(\nu_{f,PI})$ , to fit the SS-PL spectral bands. The TR-PL spectra measured at extremely high excitation intensities ensure a complete filling of the most of  $N_f$  deep centres. Then, either  $n_{ex,f} = N_A \approx N_f$  or  $p_{ex,f} = N_{D,f}^+$  is valid for estimation of trap density using the  $\varphi_f$  values estimated by fitting the  $\Delta R_f$  conversion relations. For the linear processes, assuming that full filling of the deep centres of concentration  $N_f$  is reached, and  $\Delta R_{f,PL} = n_f/\tau_{PL,f} = R_{f,PI}/(n_f N_f / n_i^2)$ , the concentration  $N_f$  of the definite type traps can then be obtained using Eq. (12) as

$$N_f = n_i / \sqrt{\varphi_f \rho_{f,PI} \sigma_{f,PI} \tau_{PL,f}}. \quad (14)$$

The intensity of the band-to-band (or exciton) PL (though is taken out of consideration) spectral peaks can also be simulated using the vR-S approach [45]. A scale of  $\sigma_f$  is set by the highest PPIS step. Therefore, the PPIS  $E_7 = 3.3$  eV level (Table 3) has been chosen as a benchmark level within simulations of the conversion between PPIS and PL spectra, for which values of  $\sigma_f$ ,  $\alpha_f$ ,  $\Delta\rho_{f,PI} \approx \tau_{MW-PC}$  can be verified by independent measurements. The  $\tau_{TR-PL,f}$  values for deep centres  $E_1 - E_7$  (Table 3) have been deduced using  $\tau_{TR-PL,f}$  data (listed in Table 2 and depicted in Figs. 4–7) as well as MW-PC characteristic decay lifetimes for the respective TR-PL and SS-PL bands, ascribed to different species deep centres. Fitting of the SS-PL spectrum was performed by keeping fixed  $E_f$ ,  $\sigma_f$  and  $\Gamma_f$  parameters while varying (as free parameters)  $\varphi_f$ ,  $h\nu_{f,PI}$  quantities which include the differences in effective volume ( $V \sim \alpha_f^{-1}$ , from which light of the definite spectral band is collected), difference in theoretical and fitted  $\rho_{f,PI}(h\nu)$  (which changes as an  $\exp(-h\nu/kT)$  function respective to the photon energy according to vR-S approach) and smoothing of the excess carrier depth-distribution profiles due to carrier diffusion-recombination and inner re-emission of UV band light through band-to-band and excitonic transitions. Fitted SS-PL spectrum clearly shows Stokes' shifts for all the PL bands, where quantitative shifts depend on  $h\nu_f$  for a peak of  $f$ -th PL band and  $\Gamma_f$  as well as on  $\sigma_{f,PI}$  and  $\rho_{f,PI}$  parameters. Trap concentrations and corrected values of  $\sigma_f$  estimated by the above discussed procedures, are listed within Table 4.

In analysis of transients, the PL decay partial lifetimes  $\tau_{PL,f}$  depend not only on  $\Delta R_{\Delta h\nu,f}$  but also on emission times  $\tau_e$  from the shallow trapping centres. The latter parameter  $\tau_{e,i} = [v_{th} \sigma_{C,M} N_C \times \exp(-\Delta E_{M,i}/k_B T)]^{-1}$  is estimated to be in the range from 1 ns to 10 ns assuming inherent values of  $v_{th} \sim 1.3 \times 10^7$  cm/s,  $\sigma_{C,M} \sim 10^{-14}$  cm<sup>2</sup>,  $N_C \sim 1.3 \times 10^{18}$  cm<sup>-3</sup> at room temperature for  $\Delta E_{M,i} \sim 0.16 - 0.56$  eV extracted using DLTS for the same samples. Assuming independent PL and radiation-less capture processes, the effective PL decay lifetime  $\tau_{PL,eff}$  can be estimated [45] as  $\tau_{PL,eff} = (\tau_{PL,f}^{-1} + \tau_{e,i}^{-1})^{-1}$ . The estimated values of  $\tau_{PL,eff}$  are in agreement with the experimental data listed in Table 2 and MW-PC transients (Fig. 5). Several PL decay components (Table 2) obtained by fitting experimental TR-PL transients indicate an interplay

**Table 4**

Concentration and photon-electron coupling cross-section values deduced by fitting conversion between PPI spectral steps and SS-PL spectral bands as well as by using TR-PL data on PL lifetimes for the resolved TR-PL spectral bands, attributed to different species defects.

Trap E (eV)	LD			HD		
	$\sigma$ (cm <sup>2</sup> )	$\tau_{PL}$ (s)	N (cm <sup>-3</sup> )	$\sigma$ (cm <sup>2</sup> )	$\tau_{PL}$ (s)	N (cm <sup>-3</sup> )
$E_1 = 1.4$	$5.7 \times 10^{-19}$	$1 \times 10^{-3}$	$5 \times 10^{14}$	$4.5 \times 10^{-19}$	$1.4 \times 10^{-3}$	$4 \times 10^{14}$
$E_2 = 1.9$	$1.6 \times 10^{-16}$	$2.3 \times 10^{-5}$	$4 \times 10^{10}$	$2.5 \times 10^{-16}$	$8 \times 10^{-6}$	$3 \times 10^{10}$
$E_3 = 2.2$	$9.1 \times 10^{-17}$	$1 \times 10^{-5}$	$3 \times 10^{10}$	$1.1 \times 10^{-16}$	$8 \times 10^{-6}$	$2 \times 10^{10}$
$E_4 = 2.6$	$6.3 \times 10^{-16}$	$1 \times 10^{-6}$	$8 \times 10^{10}$	$5.0 \times 10^{-16}$	$1 \times 10^{-6}$	$3 \times 10^{10}$
$E_5 = 2.9$	$9.1 \times 10^{-15}$	$1 \times 10^{-6}$	$1 \times 10^{12}$	$2.5 \times 10^{-15}$	$1 \times 10^{-6}$	$1 \times 10^{12}$
$E_6 = 3.0$	$3.1 \times 10^{-14}$	$1 \times 10^{-6}$	$4 \times 10^{13}$	$1.0 \times 10^{-13}$	$1 \times 10^{16}$	$3 \times 10^{13}$
$E_7 = 3.3$	$1.6 \times 10^{-13}$	$7 \times 10^{-8}$	$2 \times 10^{16}$	$1.6 \times 10^{-13}$	$7 \times 10^{-8}$	$3 \times 10^{16}$

of different traps. Thus,  $\tau_{PL,eff}$  actually measured values and employed for  $N_f$  evaluations (instead of  $\tau_{PL,f}$ ) introduce some errors for estimated  $N_f$  data. Furthermore, the  $\tau_{PL,eff}$  should be included into evaluations of quantum efficiency of PL ascribed to different PL bands. The radiationless rather shallow traps seem to be the mediators which keep rather slow decay of free carriers irrespective of fast radiative channels such as exciton annihilation. Complementarily, exciton and carrier in-depth diffusion and radiative spread of excitation determine a smoothing of free carrier distribution profile, while PL of various spectral ranges might be collected from different volumes. Moreover, the reduced values of interaction cross-section appear (according to Kopylov-Pikhtin model (Eq. (2))) within long-wavelength wing at Stokes' shifted PL peaks (relative to the photo-ionization cross-section values (Table 4) and according to vR-S model (Eq. (12))). The decreased cross-section values at Stokes' shifted PL peaks can also be a reason for the slow carrier capture within radiative recombination and long PL relaxation lifetimes.

The evaluated concentrations of deep traps cover the range of  $\sim 10^{10}$ – $3 \times 10^{16}$  cm<sup>-3</sup> being rather lower than that on sample surface estimated from SIMS. It seems that the introduced impurities might compose clusters (when their densities are sufficiently large,  $> 10^{18}$  cm<sup>-3</sup>) which actually represent the extended defects. Using these values, the PL decay lifetimes  $\tau_{PL}$  can then be estimated as capture (to the photo-active centres) lifetime  $\tau_{PL,c,f} = (v_T \sigma_f N_f)^{-1}$  by assuming the peak capture cross-section  $\sigma_f$  and trap density values, listed in Table 4, and thermal velocity value of  $v_T = 1.3 \times 10^7$  cm/s. These calculated  $\tau_{PL,c,f}$  lifetimes cover the range starting from 0.25 to 64 ns for ( $E_7$  and  $E_6$  centres, respectively) going through 9–27  $\mu$ s (for  $E_5$  and  $E_1$  centres, respectively) and the reaching millisecond scale: 1.6, 12 and 28 ms (for  $E_4$ ,  $E_2$  and  $E_3$  centres, respectively). The estimated  $\tau_{PL,c,f}$  is in rather acceptable agreement with that values obtained in TR-PL experiments, although which appear at different spectral ( $h\nu$ ) positions for  $\tau_{PL,c,f}$  and  $\tau_{PL,f}$ .

The type of the deep centres, resolved by combining the PPI, SS-PL and TR-PL spectroscopy, is tentatively denoted in Table 3 based on reported literature data. The PPIS traps with photo-ionization energy of  $E_7 = 3.30$  eV agree well with absorption peak (Fig. 1b) related to the carbon dopant concentration increase and originated from formation  $C_N$  neutral centres, according to literature data [9]. Although, the acceptor type centres, empty from electrons, would be inefficient for electron photo-emission to a conduction band, indicating an incorrect density of these centres. The PPIS trap with  $E_2 = 1.9$  eV, which is also related to carbon dopants, can be associated with Y PL of  $h\nu_2 = 2.0$  eV or R PL  $h\nu_3 = 1.8$  eV transitions. However, a type of the  $E_2$  defect is not clear in detail. The trap with activation energy of  $h\nu = 2.3$  eV is associated with Ga vacancies, according to literature data [34]. Additionally, the dominant traps can tentatively be estimated by using an algebra of the obtained photo-activation energy values relative to a band-gap ( $E_G = 3.45$  eV [48]) as well as valence/conduction band edges and to the identified PPIS traps as well as G-Y-R range PL (SS-PL and

TR-PL) transitions. Thereby,  $E_1 - ppis = 1.4$  eV can be resulted from  $E_G - h\nu_2 \approx 1.3 \pm 0.1$  eV.

The exceptionally long PL decay transients, inherent for carbon doped GaN materials, can be commonly interpreted [40,49] by Thomas-Hopfield-Augustyniak model [50], based on donor-acceptor (DA) PL (DAP), dependent on the length of the spatial separation between A–D pairs. Such DAP processes usually determine the non-exponential TR-PL decays. However, in our SC and TG-PLD experiments, the long-tail PL decays nearly exponentially. Such the TR-PL transients imply a feature of the self-sustaining processes. This can be explained by the photo-ionization processes (on the specific carbon associated traps) induced by the PL light generated from other centres (also attributed to C impurities) in the system of C impurity-rich material. For instance, photons, generated by PL due to  $C_N O_N$  centres, are sufficient to photo-ionize the  $C_N$  or  $C_I$  centres. There, excitation travels by hopping and it retains within a re-absorption length, while necessary type of trap-filling is supported by a capture/thermal-emission of free-carriers, observable within MW-PC transients. The similar combinatorics of the photoluminescence and photo-ionization photons can be implied for the sub-systems of  $C_N O_N - C_N - C_I - C_N V_{Ga}$  centres as well as for the  $C_{Ga} - C_I$  and  $C_{Ga} - V_N$  traps. Certainly, the SS-PL and TR-PL spectral bands are rather wide and composed of several overlapping spectral sub-bands. The decreased cross-section values can also be a reason for the slow carrier capture within radiative recombination processes and long PL relaxation lifetimes. Nevertheless, a state of identification of different point defects in GaN is far from completion, and origin of various spectral peaks is debated [9] in literature. The main reason is a crystal quality and unavoidable impurities in nowadays GaN materials. The most of crystal imperfections and impurities are not researched by techniques sensitive to defect microscopic configuration, such as NMR, EPR. As to carbon dopants, usage of <sup>13</sup>C isotope within doping precursors might be promising for the detail analysis of the carbon associated centres and their complexes.

## 5. Summary

A comprehensive study of the GaN:C bulk samples grown by HVPE technology on AT-GaN seeds has been reported. Spectroscopy of point centres has been implemented by combining several contactless/optical techniques: the time resolved (TR-PL) photoluminescence (PL), microwave probed photoconductivity (MW-PC) transients and pulsed-photoionization spectroscopy (PPIS) techniques, together with steady-state PL (SS-PL) and transmission spectral measurements. The dynamics of the non-radiative and radiative recombination dependent on the excess carrier and carbon density has been revealed. The cross-section of the photon-electron interaction and broadening factors due to electron-phonon coupling have been evaluated for various defect centres. Profiling of excess carrier decay transients by scanning the wafer-edge boundary showed that the role of surface recombination depends on carbon doping, - namely, in heavily-C doped GaN samples, a symmetry

of surface recombination velocity of  $s_0 = s_d \approx 2 \times 10^3$  cm/s has been deduced, while for low-doped samples velocities of  $s_0 = 400$  cm/s and  $s_d \approx 3 \times 10^3$  cm/s have been estimated from the MW-PC scans. This asymmetry is also corroborated by SS-PL intensity changes when comparing spectra recorded by exciting the opposite wafer surfaces by UV light. It appears that surface and bulk non-radiative recombination with bulk carrier lifetime of 70 ns is efficient only within initial stages of MW-PC and TR-PL transients. Several carbon ascribed traps, identified as  $C_N O_N$ ,  $C_N$ ,  $C_i$ , and  $V_{Ga}$  point defects, have been implied from the pulsed photo-ionization spectroscopy. The  $C_N^-$  defect seems to be the most efficient in redistribution of the radiative recombination. For these centres, the parameters such as the photon-electron interaction cross-section, broadening factor due to electron-phonon coupling have been estimated in GaN samples. The  $C_N V_{Ga}$ ,  $C_i C_{Ga}$ ,  $C_{Ga} V_N$  complexes have also been implied by considering TR-PL and SS-PL spectra. The long-tail photoluminescence decay with durations up to tens of milliseconds might alternatively be explained by the nearly resonant photo-ionization and photoluminescence transitions. These events happen in sequence of self-sustaining processes together with trap-filling supported by capture/thermal-emission of free-carriers which determine the long-lasting and efficient PL when local excitation travels by hopping and it retains within an efficient re-absorption length. The concentration of different species centres has been estimated by using the joint fitting of the photo-ionization and photo-luminescence spectra on the basis van Roosbroeck-Shockley equation and employing the excess carrier decay parameters deduced from the recorded MW-PC and TR-PL characteristics. The evaluated concentrations of deep traps cover the range of  $10^{10} - 3 \times 10^{16}$  cm<sup>-3</sup>.

## Acknowledgements

This research was partially funded by the European Regional Development Fund, Lithuania according to the supported activity 'Research Projects Implemented by World-class Researcher Groups' under Measure No. 01.2.2-LMT-K - 718 - 1-0013. Fabrication of materials and samples for this research was supported by the Department of the Navy, Office of Naval Research, Poland (ONRG - NICOP -N62909 - 17 -1-2004) and by Polish National Science Centre, Poland through project No. 2017/25/B/ST5/02897. Authors are indebted to T.Malinauskas for XRD inspection of the samples, to J.Vaitkus and A.Alkauskas for fruitful discussions on deep trap spectroscopy.

## References

- [1] M. Bockowski, M. Iwinska, M. Amilusik, M. Fijalkowski, B. Lucznik, T. Sochacki, Challenges and future perspectives in HVPE-GaN growth on ammonothermal GaN seeds, *Semicond. Sci. Technol.* 31 (2016) 93002.
- [2] M.P. D'Evelyn, et al., Bulk GaN crystal growth by the high-pressure ammonothermal method, *J. Cryst. Growth* 300 (2007) 11.
- [3] R. Dzwiliński, et al., Excellent crystallinity of truly bulk ammonothermal GaN, *J. Cryst. Growth* 310 (2008) 3911.
- [4] T. Hashimoto, F. Wu, J.S. Speck, S. Nakamura, Ammonothermal growth of bulk GaN, *J. Cryst. Growth* 310 (2008) 3907.
- [5] S.J. Pearton, J.C. Zolper, R.J. Shul, F. Ren, GaN: processing, defects, and devices, *J. Appl. Phys.* 86 (1999) 1-78.
- [6] C.H. Seager, A.F. Wright, J. Yu, W. Gotz, Role of carbon in GaN, *J. Appl. Phys.* 92 (2002) 6553.
- [7] H. Tang, J.B. Webb, J.A. Bardwell, S. Raymond, J. Salzman, C. Uzan-Saguy, Properties of carbon-doped GaN, *Appl. Phys. Lett.* 78 (2001) 757.
- [8] A.F. Wright, Substitutional and interstitial carbon in wurtzite GaN, *J. Appl. Phys.* 92 (2002) 2575.
- [9] M.A. Reshchikov, D.O. Demchenko, A. Usikov, H. Helava, Y. Makarov, Carbon defects as sources of the green and yellow luminescence bands in undoped GaN, *Phys. Rev. B* 90 (2014) 235203.
- [10] P. Reddy, F. Kaess, J. Tweedie, R. Kirste, S. Mita, R. Collazo, Z. Sitar, Defect quasi Fermi level control-based  $C_N$  reduction in GaN: evidence for the role of minority carriers, *Appl. Phys. Lett.* 111 (2017) 152101.
- [11] M. Leroux, N. Grandjean, B. Beaumont, G. Nataf, F. Semond, J. Massies, P. Gibart, Temperature quenching of photoluminescence intensities in undoped and doped GaN, *J. Appl. Phys.* 86 (1999) 3721.
- [12] F. Kaess, P. Reddy, D. Alden, A. Klump, L.H. Hernandez-Balderrama, A. Franke, R. Kirste, A. Hoffmann, R. Collazo, Z. Sitar, The effect of illumination power density on carbon defect configuration in silicon doped GaN, *J. Appl. Phys.* 120 (2016) 235705.
- [13] J.L. Lyons, A. Janotti, C.G. Van de Walle, Carbon impurities and the yellow luminescence in GaN, *Appl. Phys. Lett.* 97 (2010) 152108.
- [14] C.G. Van de Walle, J. Neugebauer, First-principles calculations for defects and impurities: applications to III-nitrides, *J. Appl. Phys.* 95 (2004) 3851.
- [15] P. Kempisty, Y. Kangawa, A. Kusaba, K. Shiraishi, S. Krukowski, M. Bockowski, K. Kakimoto, H. Amano, DFT modeling of carbon incorporation in GaN(0001) and GaN(000-1) metalorganic vapor phase epitaxy, *Appl. Phys. Lett.* 111 (2017) 141602.
- [16] P. Reddy, M.P. Hoffmann, F. Kaess, Z. Bryan, I. Bryan, M. Bobea, A. Klump, J. Tweedie, R. Kirste, S. Mita, M. Gerhold, R. Collazo, Z. Sitar, Point defect reduction in wide bandgap semiconductors by defect quasi Fermi level control, *J. Appl. Phys.* 120 (2016) 185704.
- [17] M. Iwinska, R. Piotrkowski, E. Litwin-Staszewska, T. Sochacki, M. Amilusik, M. Fijalkowski, B. Lucznik, M. Bockowski, Highly resistive C-doped hydride vapor phase epitaxy-GaN grown on ammonothermally crystallized GaN seeds, *Appl. Phys. Express* 10 (2017) 011003.
- [18] M. Bockowski, M. Iwinska, M. Amilusik, M. Fijalkowski, B. Lucznik, T. Sochacki, Challenges and future perspectives in HVPE-GaN growth on ammonothermal GaN seeds, *Semicond. Sci. Technol.* 31 (2016) 93002.
- [19] E. Gaubas, et al., Electrical characterization of HVPE GaN containing different concentrations of carbon dopants, *Semicond. Sci. Technol.* 33 (2018) 125024.
- [20] M.A. Moram, M.E. Vickers, X-ray diffraction of III-nitrides, *Rep. Prog. Phys.* 72 (2009) 036502.
- [21] H. Heinke, V. Kirchner, S. Einfeldt, D. Hommel, X-ray diffraction analysis of the defect structure in epitaxial GaN, *Appl. Phys. Lett.* 77 (2000) 2145.
- [22] E. Gaubas, E. Simoen, J. Vanhellemont, Review-Carrier lifetime spectroscopy for defect characterization in semiconductor materials and devices, *ECS J. Solid State Sci. Technol.* 5 (2016) P3108.
- [23] E. Gaubas, et al., Study of neutron irradiated structures of ammonothermal GaN, *J. Phys. D: Appl. Phys.* 50 (2017) 135102.
- [24] M.A. Reshchikov, J.D.O. McNamara, M. Toporov, V. Avrutin, H. Morkoc, A. Usikov, H. Helava, Y. Makarov, Determination of the electron-capture coefficients and the concentration of free electrons in GaN from time-resolved photoluminescence, *Sci. Rep.* 6 (2016) 37511.
- [25] M.A. Reshchikov, D.O. Demchenko, J.D. McNamara, S. Fernandez-Garrido, R. Calarco, Green luminescence in Mg-doped GaN, *Phys. Rev. B* 90 (2014) 035207.
- [26] A. Rose, Concepts in Photoconductivity and Allied Problems, Interscience Publishers John Wiley & Sons, New York, 1963.
- [27] S.M. Ryvkin, Photoelectric Effects in Semiconductors, Consultants Bureau, New York, 1963.
- [28] A.A. Kopylov, A.N. Pikhtin, Influence of temperature on spectra of optical absorption by deep levels in semiconductors, *Sov. Phys. Solid State* 16 (1975) 1200.
- [29] K. Huang, A. Rhy, Theory of light absorption and non-radiative transitions in F-centre, *Proc. R. Soc. Lond. A: Math. Phys. Eng. Sci.* 204 (1950) 406.
- [30] A. Alkauskas, D.M. McCluskey, C.G. Van de Walle, Tutorial: defects in semiconductors—combining experiment and theory, *J. Appl. Phys.* 119 (2016) 181101.
- [31] A. Chantre, G. Vincent, D. Bois, Deep-level optical spectroscopy in GaAs, *Phys. Rev. B* 23 (1981) 5335.
- [32] A. Armstrong, A.R. Arehart, D. Green, U.K. Mishra, J.S. Speck, S.A. Ringel, Impact of deep levels on the electrical conductivity and luminescence of gallium nitride codoped with carbon and silicon, *J. Appl. Phys.* 98 (2005) 053704.
- [33] A.Y. Polyakov, N.B. Smirnov, E.A. Kozhukhova, A.V. Osinsky, S.J. Pearton, Temperature stability of high-resistivity GaN buffer layers grown by metalorganic chemical vapor deposition, *J. Vac. Sc. Technol. B* 31 (2013) 051208.
- [34] C.H. Qiu, J.I. Pankove, Deep levels and persistent photoconductivity in GaN thin films, *Appl. Phys. Lett.* 70 (1997) 1983.
- [35] Z. Zhang, C.A. Hurni, A.R. Arehart, J. Yang, R.C. Myers, J.S. Speck, S.A. Ringel, Deep traps in nonpolar m-plane GaN grown by ammonia-based molecular beam epitaxy, *Appl. Phys. Lett.* 100 (2012) 52114.
- [36] W.R. Willoughby, et al., A compensating point defect in carbon-doped GaN substrates studied with electron paramagnetic resonance spectroscopy, *J. Appl. Phys.* 123 (2018) 161547.
- [37] A. Uedono, M. Zhao, E. Simoen, Probing the effect of point defects on the leakage blocking capability of  $Al_{0.1}Ga_{0.9}N/Si$  structures using a monoenergetic positron beam, *J. Appl. Phys.* 120 (2016) 215702.
- [38] E. Gaubas, et al., *In situ* characterization of radiation sensors based on GaN LED structure by pulsed capacitance technique and luminescence spectroscopy, *Sens. Actuators A* 267 (2017) 194.
- [39] R.A. Smith, *Semiconductors*, 2nd ed., Cambridge University Press, London, 1978.
- [40] M.A. Reshchikov, M. Zafar Iqbal, H. Morkoc, S.S. Park, K.Y. Lee, Long-lasting photoluminescence in freestanding GaN templates, *Appl. Phys. Lett.* 83 (2003) 266.
- [41] M. Matsubara, M. Bellotti, A first-principles study of carbon-related energy levels in GaN. I. Complexes formed by substitutional/interstitial carbons and gallium/nitrogen vacancies, *J. Appl. Phys.* 121 (2017) 195701.
- [42] M. Matsubara, E. Bellotti, A first-principles study of carbon-related energy levels in GaN. II. complexes formed by carbon and hydrogen, silicon or oxygen, *J. Appl. Phys.* 121 (2017) 195702.
- [43] R. Aleksiejunas, P. Scajvas, Z. Nargelas, T. Malinauskas, A. Kadys, K. Jarasiunas, Impact of diffusivity to carrier recombination rate in nitride semiconductors: from bulk GaN to  $(In,Ga)N$  quantum wells, *Jpn. J. Appl. Phys.* 52 (2013) 08JK01.
- [44] W. van Roosbroeck, W. Shockley, Photon-radiative recombination of electrons and holes in germanium, *Phys. Rev.* 94 (1954) 1558.
- [45] J.I. Pankove, *Optical Processes in Semiconductors*, Prentice-Hall, New Jersey, 1971.



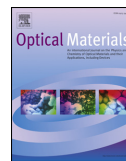
- [46] E.F. Schubert, *Light-Emitting Diodes*, 3rd ed., Cambridge University Press, London, 2018.
- [47] R. Bhattacharya, B. Pal, B. Bansal, On conversion of luminescence into absorption and the van Roosbroeck-Shockley relation, *Appl. Phys. Lett.* 100 (2012) 222103.
- [48] J.F. Muth, J.H. Lee, I.K. Shmagin, R.M. Kolbas, H.C. Casey, B.P. Keller Jr., U.K. Mishra, S.P. DenBaars, Absorption coefficient, energy gap, exciton binding energy, and recombination lifetime of GaN obtained from transmission measurements, *Appl. Phys. Lett.* 101 (2012) 254102.
- [49] M.A. Reshchikov, H. Morkoç, Luminescence properties of defects in GaN, *J. Appl. Phys.* 97 (2005) 061301.
- [50] D.G. Thomas, J.J. Hopfield, W.M. Augustyniak, Kinetics of radiative recombination at randomly distributed donors and acceptors, *Phys. Rev.* 140 (1965) A202.

A3

Room-temperature infrared  
photoluminescence in GaN doped with  
various impurities

E. Gaubas, T. Čeponis, **L. Deveikis**, D. Dobrovolskas, V. Rumbauskas, M.  
Viliunas

Opt. Mater. **94** (2019) 266-271.  
DOI:10.1016/j.optmat.2019.05.054  
(Open access)



# Room-temperature infrared photoluminescence in GaN doped with various impurities



E. Gaubas<sup>\*</sup>, T. Čeponis, L. Deveikis, D. Dobrovolskas, V. Rumbauskas, M. Viliunas

*Institute of Photonics and Nanotechnology, Vilnius University, Sauletekio av. 3, LT-10257, Vilnius, Lithuania*

## ARTICLE INFO

### Keywords:

Carbon  
Magnesium  
Manganese and iron doped GaN  
Photo-ionization spectroscopy  
Photoluminescence spectroscopy  
Room-temperature infrared-luminescence  
Free-standing ammono-thermal and hydride vapour-phase epitaxy grown GaN

## ABSTRACT

The steady-state infrared-photoluminescence spectra (IR-PL) emitted from about 400  $\mu\text{m}$  thick, free-standing GaN wafers, grown by the ammono-thermal and hydride vapour-phase epitaxy GaN, and containing carbon, magnesium, manganese and iron doping have been examined. The room-temperature IR-PL spectra are correlated with pulsed-photo-ionization spectra using van Roosbroeck-Schockley approach for spectrum conversion. It has been revealed that iron and carbon dopants appear as the most efficient impurities for the room temperature of infra-red emission from GaN grown using different technologies.

## 1. Introduction

The room temperature (RT) infrared photoluminescence (IR-PL) in GaN, covering spectral range from the  $\sim 1.0$ – $1.54 \mu\text{m}$ , is promising for applications in optical communications [1–13]. Also, GaN materials doped with dedicated impurities (for instance, Mg) might serve as IR single photon emitters (SPE) for applications in quantum computing [1]. It had been demonstrated that the rear-earth dopants such as Pr [2], Er [3,6,7,9,10] and other, introduced into GaN host, can be efficient IR (Pr at  $1.3 \mu\text{m}$ , Er at  $1.54 \mu\text{m}$ ) emitters at room temperature. It had been shown [7] that IR photons in such GaN:Er materials are emitted due to 4f the intra-shell transitions, and this luminescence is thermally quenched due to energy back-transfer to the semiconductor host. Nevertheless, the inhomogeneous broadening of IR spectral lines due to the existence of multiple Er sites appears to be dependent on excitation mode [9]. However, IR luminescence efficiency determined by incorporation of the rare-earth ions seem to strongly depend on the preparation method of GaN material [7] due to existence of additional defects. It had been predicted [4] that among the transition metals, only three candidates offer an electronic 3d configuration in III-V semiconductors, as Ti<sup>+</sup>, V<sup>+</sup>, and Cr<sup>+</sup>. Complementarily, the room temperature IR-PL peaked at  $1.047 \mu\text{m}$ ,  $1.19 \mu\text{m}$  and  $1.30 \mu\text{m}$  had been revealed and ascribed to Co [5] or V [11], to Ti [5] or Cr [8,11] and to Fe [5,8,11], respectively. These IR spectral components were explained by the d-d intra-shell transitions. However, some aspects within interpretation of the IR-PL in transition metal doped GaN and the origin of

the zero-phonon-lines (ZPL) are unclear and deserve further investigations. The origin of the room-temperature IR PL (within the spectral range of  $0.9$ – $1 \mu\text{m}$ ) in Mg doped GaN had been comprehensively studied by optically detected magnetic resonance (OMDR) means [12], where the role of vacancy-Mg and Mg–O complexes in formation of IR-PL had been clarified. However, the understanding of the microscopic structure of the PL centres is very limited. The room temperature IR emission had also been revealed in GaN irradiated by high energy particles [14]. Spectroscopy of the ultra-violet (UV) light excited PL of GaN has mostly been addressed to the visible (VIS) and UV-PL spectral range, stimulated by applications of GaN hetero-structures in light-emitting-diode fabrication. Nevertheless, the RT IR emitters arranged through conversion of the UV excitation in GaN are desirable for the optical communication systems and other applications. Therefore, the IR range PL spectroscopy of GaN materials needs further developments.

In this article, the steady-state IR-PL (SS-PL) spectra measured on GaN samples doped with various dopants and grown by different technologies are reported. The ammono-thermal and hydride vapour phase epitaxy materials, grown on the single-crystal seeds and containing rather small density of dislocations, have been chosen to avoid complications due to the extended defects in formation of IR-PL spectral bands. GaN materials doped with most promising elements for emission of IR light, such as Mn, Mg, Fe have been researched. Nevertheless, some inevitable technological impurities such as carbon and oxygen are present even in high quality AT and HVPE GaN materials, which might also be efficient in formation of the IR-PL. Therefore, the intentionally

<sup>\*</sup> Corresponding author.

E-mail address: [eugenijus.gaubas@ff.vu.lt](mailto:eugenijus.gaubas@ff.vu.lt) (E. Gaubas).

<https://doi.org/10.1016/j.optmat.2019.05.054>

Received 18 January 2019; Received in revised form 29 May 2019; Accepted 30 May 2019

Available online 07 June 2019

0925-3467/© 2019 Elsevier B.V. All rights reserved.

carbon doped HVPE GaN and Fe, Mn, Mg doped, however, carbon containing materials, have been studied for comparison. This is important in choosing of the technologies and dopants for fabrication of GaN based RT IR emitters. The efficiency and spectrum of the IR emission from GaN have been examined by correlating the steady-state IR-PL spectra with photon-electron coupling cross-section data extracted from pulsed photo-ionization measurements. The cross-section of the photon-electron interaction and broadening factors due to electron-phonon coupling have also been evaluated for various defect centers. The conversion from the photo-ionization to IR emission spectra have been considered based on van Roosbroeck-Shockley model. Thereby, the room temperature (RT) IR-PL spectrum, excited by UV laser light and Stokes' shifted relatively to the pulsed photo-ionization steps, can be predicted and associated with impurities and point defects, efficient for RT IR-PL.

## 2. Samples and spectroscopy techniques

The free-standing, ~400  $\mu\text{m}$  thick GaN wafer-samples, grown by the ammonothermal (AT) and hydride vapour phase epitaxy (HVPE) methods have been studied. The HVPE GaN samples were doped with carbon (C), magnesium (Mg) and iron (Fe), while AT GaN materials were doped with Mg and manganese (Mn). Regardless of high crystalline quality of the AT and HVPE grown materials relative to the extended defects, existence of different additional impurities (C, O, H) within these AT and HVPE GaN samples is inevitable. The HVPE and AT GaN samples, doped with C, Fe, Mg and Mn, were obtained from various vendors: UNIPRESS, MTL, KYMA, and AMMONO, respectively. The dopant concentrations varied in the range of  $10^{17}$ – $2 \times 10^{19} \text{ cm}^{-3}$ . The growth methods, dopant concentrations and vendors of the studied samples are summarized in Table 1.

A set of AT GaN samples were irradiated by reactor neutrons using fluences in a wide range from  $10^{12}$  to  $5 \times 10^{16} \text{ n/cm}^2$  at Jožef Stefan Institute (Ljubljana) TRIGA reactor. Sample surfaces with (0001) and (000 $\bar{1}$ ) crystal orientations were mechanically polished to the optical smoothness. All the samples were highly resistive at room temperature showing the n-type conductivity, which was determined from electrical characterization of Schottky diodes made of the same samples, as reported elsewhere [15]. Concentrations of the dopants and other unintentionally introduced impurities were estimated by the secondary ion mass spectroscopy (SIMS) and verified (for Mn, Fe) by electron spin resonance (ESR) [16] measurements.

The pulsed photo-ionization spectroscopy [17,18] (PPIS) is performed in contactless mode at room temperature, by recording the microwave probed (MW)-photoconductivity (PC) transient signals induced by the tuneable excitation wavelength. The recombination and trapping lifetimes of the photo-excited carriers, correlated with definite photo-ionization spectral steps, are simultaneously controlled to prove existence of the definite photo-active centers. The 22 GHz MW probing is arranged by using a slit antenna. The transients of the MW-PC response are recorded on 50 Ohm load resistor connected in series with MW detector by using a 2 GHz oscilloscope LeCroy Wave Runner 620Zi. The PPIS measurements were implemented using nanosecond (4 ns) laser equipped with an optical parametric oscillator (OPO) and by

**Table 1**  
Growth method, dopant concentration and vendor of studied samples.

Sample	Growth method	Dopants	Concentration of dopants ( $\text{cm}^{-3}$ )	Vendor
HVPE GaN:C	HVPE on AT	C	$10^{18}$	UNIPRESS
HVPE GaN:Fe	HVPE	Fe	$2 \times 10^{18}$	MTI Corporation
HVPE GaN:Mg	HVPE	Mg	$1.7 \times 10^{17}$	KYMA
AT GaN:Mg	AT	Mg	$10^{18}$	AMMONO
AT GaN:Mn	AT	Mn	$2 \times 10^{19}$	AMMONO

recording the MW-PC transients. The nanosecond OPO instrument Ekspla NT342B with pulse duration of 4 ns covers a wavelength tuning range from 210 to 2300 nm. The MW-PC signal  $U_{MW-PC}$  is proportional to a density of the photo-excited carriers, while their relaxation rate within a transient is linked to the carrier lifetime within later stages of trap filling/emptying. The PPI spectrum was recorded starting from long wavelength wing to avoid simultaneous filling of several traps. Variations of the MW-PC response peaks ( $U_{MW-PC,0}$ ) represent the step-like photo-ionization spectra, while the changes of the excess carrier decay lifetime are obtained by measuring a time interval needed for  $U_{MW-PC}$  reduction to a  $U_{MW-PC,0} \times e^{-1}$  value.

The steady-state photo-luminescence (SS-PL) spectra in the infrared range are recorded using a He–Cd laser (KIMMON) ultraviolet (UV) 325 nm wavelength excitation. The RT IR-PL spectra are recorded in the back-emission geometry using an ANDOR monochromator and an InGaAs detector. Routine corrections of the PL signals and UV-VIS blocking spectral filters are involved to properly reproduce a spectrum of IR PL.

## 3. Photo-ionization and infrared photo-luminescence spectra

The UV excited SS IR-PL spectra, peaked in the spectral range of 0.75–1.2 eV (Fig. 1a) have been revealed for all the examined samples. The recorded IR-PL spectral bands showed an asymmetric shape, which commonly required to account for an overlap of two spectral lines ( $I_{PL1}$ ,  $I_{PL2}$  depicted in Fig. 1b by dash and dot curves) in simulations, to reproduce the experimental IR-PL spectrum. It also appeared for neutron irradiated samples that PL intensity of the spectral band, peaked at

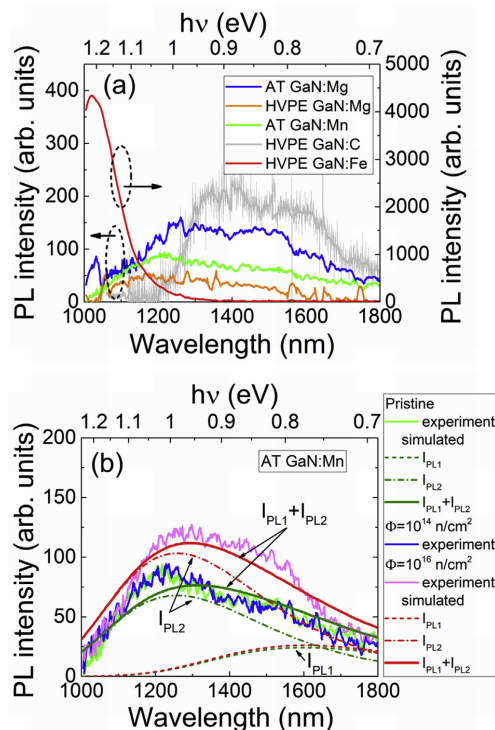


**Fig. 1.** (a) SS-PL spectra recorded on different GaN materials (supplied by AMMONO, KYMA, UNIPRESS and MTI) in the IR range. (b) Evolution of the IR-PL in AT GaN:Mn dependent on reactor neutron irradiation fluence.

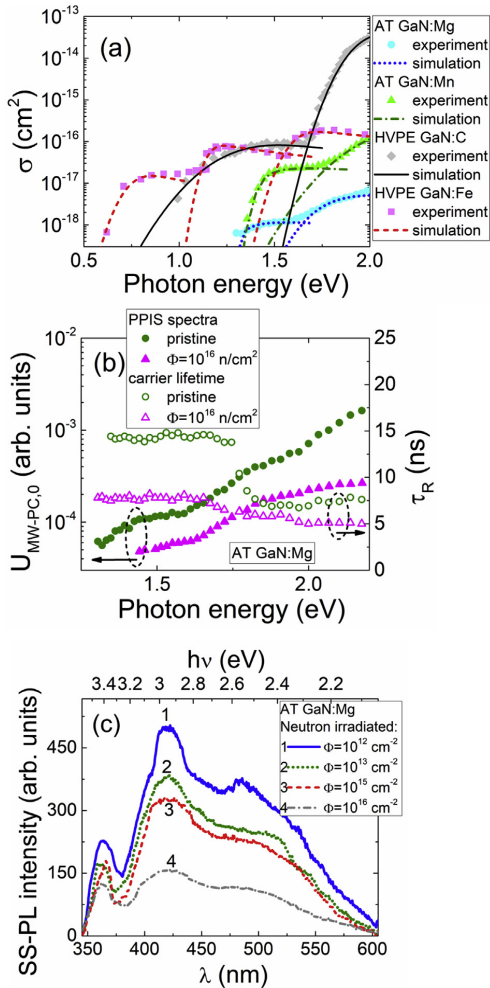


Fig. 2. (a) PPI spectra recorded at room temperature in carbon as well as iron doped HVPE GaN and magnesium as well as manganese doped AT GaN samples. (b) The PPI signals and carrier lifetime probed by microwaves as a function of photon energy in magnesium doped AT GaN before and after heavy irradiation with reactor neutrons by varying fluence  $\Phi$ . (c) – Variations of the PL spectra in AT GaN dependent on neutron fluence.

1 eV, increases with neutron irradiation fluence.

Several PPIS peaks have as usually been obtained within PPI spectra recorded for GaN materials, as reported in Refs. [16–18]. Most of these peaks are related to deep traps, ascribed to different dopants as well as other point defects, which are responsible for absorption in the UV-VIS spectral range. The PL peaks originated from different defects can be predicted [19] by analyzing the PPI spectral steps at assumption of Stokes shifts appeared through van Roosbroeck-Shockley (vRS) process [20,21] of photon energy conversion from absorption to emission. This methodology has also been applied in this study for analysis of IR-PL band appearance. Therefore, the PPI spectra recorded within a long wavelength wing are only considered to reveal the dominant defects responsible for the RT IR-PL spectral bands. Such a consideration is important in choosing of the technologies and dopants for fabrication of

GaN based RT IR emitters. The PPI spectra, recorded for different materials examined, are illustrated in Fig. 2a and b.

The density of photo-emitted carriers  $n_d^+ = \alpha(h\nu)F(h\nu)$  determines the peak value ( $U_{MW-PC,0} - n_d^+ - \sigma_d(h\nu)$  at  $t = 0$ ) of the  $U_{MW-PC}$  response for a fixed surface density  $F(h\nu) = \text{const}$  of the incident photons. The surface density of the incident photons  $F(h\nu)$  is evaluated by calibration of the energy/per pulse measurements within incident laser beam. The PPIS steps, recorded as  $U_{MW-PC,0}(h\nu)$ , represent spectral distribution of  $\sigma_d(h\nu)$ . The shape  $\sigma_d(h\nu)$  of the spectral steps and spectral position ( $E_d$ ), ascribed to several  $d$  centers, serve for evaluation of the photo-activation energy  $E_d$  and identification of the definite ( $d$ ) defects. As usually, PPI spectrum contains a few spectral steps.

The PPIS step, attributed to a definite trap with photo-activation energy  $E_d$ , is determined by a photon-electron coupling (with a matrix element  $M_{ik}$  of a dipole transition from an initial ( $i$ ) trap level to the continuum ( $k$ ) state), and spectral (dependent on the incident photon energy  $h\nu$ ) variation of the photon-electron interaction cross-section  $\sigma(h\nu)$  determines the shape and position of PPI spectral steps. Such the transitions also include the electron-phonon coupling. The phonon-assisted changes of the cross-section  $\sigma(h\nu)$  for a definite defect ( $d$ ) can be approximated by the Kopylov- Pikhtin [22] approach

$$\sigma(h\nu) = M_{ik}^2 \int_0^\infty \frac{e^{-(E+E_d-h\nu)^2/\Gamma^2} \sqrt{E} dE}{h\nu(E+E_d)^2} \quad (1)$$

where electron-phonon coupling is determined by the broadening parameter  $\Gamma$ . The broadening of the absorption onset is also related to the Huang-Rhys [23] factor and, consequently, to the Franck-Condon shift and the energy of the vibrational mode [24]. It can be deduced from simulations using Eq. (1) that the value of the photon-electron coupling cross-section increases with shallowing ( $E_d$ ) of levels. The cross-section of the photon-electron coupling directly determines the efficiency of the conversion of absorption into emission [25].

The parameters of rather shallow traps, that can determine the IR-PL due to Stokes shift and by conversion of the absorption into emission, have been extracted by fitting (depicted by thin solid lines) the recorded (represented by curves plotted using symbols) PPI spectral peaks, shown in Fig. 2a. These  $E_d$  and  $\Gamma_d$  parameters are listed in Table 2, where a tentative identification of defects performed using literature data is also presented. It can be deduced from Table 2 that together with the specific dopant attributed traps ( $C_i$  and  $C$  related PPIS steps in GaN:C,  $Fe^{3+}$ , Mg and Mn related PPIS steps within GaN:Fe, GaN:Mg and GaN:Mn, respectively), the impact of the unintentionally introduced impurities (e.g., of carbon in GaN:Mg and GaN:Mn) and crystal imperfections (such as vacancy,  $V_{Ga}$  and anti-site,  $N_{Ga}$ ) might be significant. Moreover, the oxygen associated complexes of  $V_{Ga}O_N$  are responsible for a formation of the PPIS steps within long wavelength spectral wing (Fig. 2a), recorded on the pristine and neutron irradiated GaN:Mg.

Values of capture cross-sections, attributed to different defects, have there been estimated by fitting the experimentally revealed PPIS steps (Fig. 2a and b). The PPI spectra are considerably richer in amount of PPIS steps [16,18,19] than that shown in Fig. 2, where the PPIS steps related to IR-PL are only considered. It appeared (Fig. 2a) that a few PPIS steps recorded for the GaN:Fe (Figs. 2a and 3a) are also ascribed to IR absorption transitions by traps with photo-ionization energies in the range of 0.6–1.4 eV (Table 2), attributed to iron dopants and carbon impurities. The shallowest traps (with  $E_d \sim 0.6$  eV) are close to that identified by DLTS [15], and hardly can originate the RT IR-PL. Therefore, such the traps (with  $E_d \leq 0.6$  eV) cannot be efficient in IR PL emission.

The irradiation induced defects commonly lead to a decrease of the PL intensity [36] over all the observed visible (VIS)-ultraviolet (UV) SS-PL spectral bands, as illustrated for the GaN:Mg in Fig. 2c, while shallow photo-active centers with  $E_d < 1.5$  eV, attributed to the crystal defects (such as interstitial carbon- $C_i$ ), show also a reduced effective

**Table 2**  
Parameters of the rather shallow photo-active traps in HVPE and AT GaN processed by different technologies and evaluated by PPI spectroscopy.

HVPE GaN:C			HVPE GaN:Fe		
$E_d(\text{eV})$	$\Gamma_d$	Defect type [reference]	$E_d(\text{eV})$	$\Gamma_d$	Defect type [reference]
$E_{1C} = 1.4 \pm 0.05$	0.20	$C_i$ [26,27]	$E_{1Fe} = 0.6 \pm 0.1$	0.10	$V_{Ga}^-$ [14]
$E_{2C} = 1.9 \pm 0.05$	0.13	C related [26]	$E_{2Fe} = 1.1 \pm 0.1$	0.06	$N_{Ga}$ [32]
$E_{3C} = 2.2 \pm 0.1$	0.10	$V_{Ga}O_N$ [28,29]	$E_{3Fe} = 1.6 \pm 0.1$	0.13	$Fe^{3+}$ [30]
AT GaN:Mg			AT GaN:Mg neutron irradiated $\phi = 10^{16}n/cm^2$		
$E_d(\text{eV})$	$\Gamma_d$	Defect type [reference]	$E_d(\text{eV})$	$\Gamma_d$	Defect type [reference]
$E_{Mg-1} = 1.3 \pm 0.05$	0.12	$C_i$ [26,27]			
$E_{Mg-2} = 1.75 \pm 0.05$	0.18	Mg related [33,35]	$E_{Mg-2} = 1.75 \pm 0.05$	0.23	Mg related [33,35]
$E_{Mg-3} = 2.07 \pm 0.05$	0.23	$V_{Ga}O_N$ [28,29]	$E_{Mg-3} = 2.05 \pm 0.05$	0.27	$V_{Ga}O_N$ [28,29]
AT GaN:Mn			AT GaN:Mn neutron irradiated $\phi = 10^{16}n/cm^2$		
$E_d(\text{eV})$	$\Gamma_d$	Defect type [reference]	$E_d(\text{eV})$	$\Gamma_d$	Defect type [reference]
$E_{Mn-1} = 1.40 \pm 0.05$	0.15	$C_i$ [26,27] or Mn related [34]	$E_{Mn-1} = 1.42 \pm 0.02$	0.15	$C_i$ [26,27] or Mn related [34]
$E_{Mn-2} = 1.98 \pm 0.05$	0.23	Mn related [31]	$E_{Mn-2} = 1.98 \pm 0.02$	0.23	Mn related [31]

concentration. This is in agreement with fluence dependent variations of the long-wavelength component  $I_{PL1}$  (Fig. 1b), however, these changes are rather small. This phenomenon is usually explained by an enhancement of density of the radiation defects, acting as the radiationless recombination centers. It can also be deduced from Table 2 that the electron-phonon coupling, characterized by the factor  $\Gamma$ , retains (within errors of measurements and fitting) for the most of the resolved PPIS peaks when comparing the pristine and irradiated material samples. Nonetheless, an increase of density of the radiation induced vacancies with neutron irradiation fluence can be beneficial for the enhanced formation of the  $V_{Ga}O_N$  complexes in the neutron irradiated GaN:Mg.

The deep levels resolved within PPIS (Figs. 2a and 3a) normally originate the Stokes shifted IR-PL bands which in our RT experiments actually emerge with peaks in the range of 0.8–1.3 eV for all the examined GaN materials. These IR-PL peaks have been fitted (Fig. 3) by using the van Roosbroeck-Shockley (vRS) approach [20,21] in relating the conversion from the PPI to IR-PL spectra, to specify more precisely the parameters of  $\sigma(h\nu)$ ,  $E_d$  and  $\Gamma$  and to identify the traps responsible for IR PL. The rate  $\Delta R(h\nu)$  of the SS emission via trap of photo-activation energy  $E_d$  is then linked to the photon-electron interaction cross-section  $\sigma(h\nu)$ , which value is shifted to the IR-PL peak photon energy (assigned to PL as  $\sigma_{d,PL}(h\nu)$ ) and expressed as follows:

$$\Delta R_d(h\nu) = \frac{n_{ex,\Delta}(h\nu)}{\tau_{PL,\Delta}(h\nu)} = \rho_{d,PL} \left( \frac{h\nu}{k_B T} \right) \sigma_{d,PL}(h\nu/k_B T) N_d \frac{n_{ex,\Delta}(h\nu) N_d}{n_i^2} \quad (2)$$

Here,  $n_i = 2 \times 10^{-10} \text{ cm}^{-3}$  is the intrinsic carrier concentration for GaN materials [37],  $k_B$  is the Boltzmann constant,  $h$  is Planck constant,  $\rho_d$  is the surface density of photons ascribed to a unit frequency  $\nu$  within absorption spectrum for the spectral range  $\Delta(h\nu)$ , inherent to dedicated trap of concentration  $N_d$ , and  $n_{ex,\Delta}(h\nu)$  is the excess carrier density generated through photo-ionization in the definite spectral range  $\Delta(h\nu)$ ,  $\tau_{PL,\Delta}(h\nu)$  is the PL relaxation time.

The correlation between the photo-ionization and photoluminescence spectra (Fig. 3) can be simulated by using Eqns. (1) and (2). The comparison of the simulated photo-ionization and IR photoluminescence spectra for all the pristine material samples is illustrated in Fig. 3. The photo-ionization spectrum (Fig. 3a) has been simulated taking (from Table 2) the extracted values of the cross-section of photon-electron coupling  $\sigma_d(h\nu)$  and of the photo-ionization energy  $E_d$  (as well as broadening factors  $\Gamma_d$ ) and by adjusting the  $\sigma_{d,PL}(h\nu)$  function to fit  $I_{PL}(h\nu)$  spectral band. Actually,  $\sigma_d(h\nu)$  and  $\Gamma_d$  are the adjustable parameters in the latter simulations. An association of the PPIS steps to the IR PL peaks is also sketched in Fig. 3a by denoting the respective deep traps ( $E_i$ ,  $i=1..3$  according to notifications in Table 2) responsible for IR-PL. The simulated spectrum (Fig. 3a) of the photo-ionization (PI) cross-sections resembles the experimental PIS curves (Fig. 1). The IR-PL spectra (Fig. 3b–f) have been simulated using the

determined  $\sigma_d(h\nu, \Gamma_d)$  (Table 2) and Eqn. (2) to fit Stokes shifts of the definite IR-PL spectrum bands, ascribed to specific centers.

As illustrated in Fig. 3, a rather good quantitative fit of the simulated (using vR-S approach) and experimental IR SS-PL spectra has been obtained. It appeared that two PPIS deep traps act as emission centers for the AT and HVPE GaN doped with Mg (Fig. 3b and c) as well as for AT GaN doped with Mn (Fig. 3d) and for neutron irradiated GaN samples (Fig. 1b). Thereby asymmetric IR-PL bands can satisfactorily be reproduced by simulations using two PPIS levels (with different  $E_d$  values) which generate the overlapping IR-PL bands. While, the impact of a single (PPIS) trap is sufficient to reproduce the experimental RT IR-PL bands recorded on carbon and iron doped HVPE GaN. However, the spectral width at HWHM of all the IR-PL bands is rather large for the bulk self-standing GaN samples, and narrowing of IR bands seems to be possible in nanometer crystallites [1] acting as narrow-band spectral filters. According to Table 2, the long wavelength IR-PL component is related to the un-intentionally introduced carbon impurities in magnesium and manganese doped GaN, while the short wavelength IR-PL component can be ascribed to dopants (Mg and Mn, respectively) or  $V_{Ga}O_N$  complexes [38] in the pristine and neutron irradiated GaN:Mg. In iron and carbon doped GaN samples the single-peak IR-PL band can be attributed to dopant related centers (Fe and C, respectively). The long wavelength IR-PL component in the reactor neutron irradiated samples seems to be related to carbon impurities, and intensity of this IR-PL peak is nearly insensitive to appearance of radiation defects. However, the short-wavelength component can be ascribed to  $V_{Ga}O_N$  complexes, which density increases due to the enhanced formation of vacancies related to the irradiation fluence.

#### 4. Summary

In summary, the combined study of pulsed photo-ionization and the steady-state infrared-photoluminescence spectra (IR-PL), emitted from about 400  $\mu\text{m}$  thick, free-standing GaN wafers, grown by the ammonothermal and hydride vapour-phase epitaxy GaN, and containing various dopants have been performed. The room temperature IR-PL spectra have been correlated with pulsed-photo-ionization spectra using van Roosbroeck-Schockley approach for spectrum conversion. Thereby, the extracted PPIS parameters can be employed for prediction of the efficiency and spectrum of RT IR-PL for the UV excited GaN materials. It has been revealed that iron and carbon dopants appear to be the most efficient impurities for the room temperature of infra-red emission from GaN grown using different technologies. The increase of the RT IR-PL intensity with neutron irradiation fluence is determined by the enhanced vacancy generation linked to fluence, and the short wavelength IR-PL component can be attributed to  $V_{Ga}O_N$  complexes, as oxygen impurities of rather large concentration are inevitable for most of the

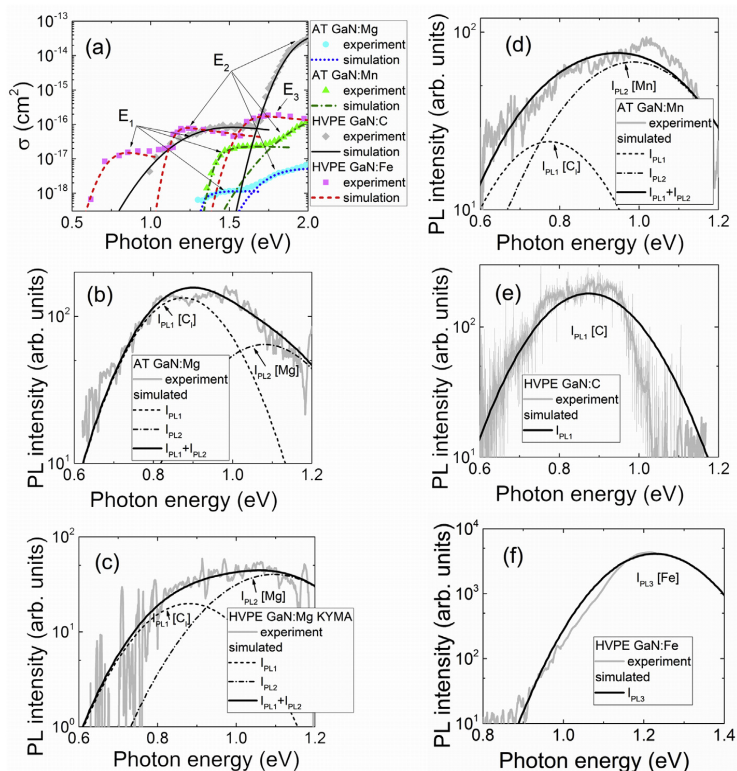


**Fig. 3.** (a) – The recorded and fitted PPI spectral steps, representing spectral variations of the photon-electron coupling cross-sections responsible for IR-PL in GaN grown using AT and HVPE technologies containing different dopants. (b) The Stokes-shifted IR photo-luminescence spectral bands relative to the PPI spectral steps (listed in Table 2 and depicted in Fig. (a)) simulated using either double component (originated from two PPI steps), - for GaN:Fe, GaN:Mg, GaN:Mn materials, or a single component, (for GaN:C and GaN:Fe) IR-PL bands.

AT and HVPE GaN materials.

#### Declaration of interests

The authors declare that they have no known competing financial interests or personal relationships that could have appeared to influence the work reported in this paper.

#### Author declaration

We wish to confirm that there are no known conflicts of interest associated with this publication and there has been no significant financial support for this work that could have influenced its outcome. We confirm that the manuscript has been read and approved by all named authors and that there are no other persons who satisfied the criteria for authorship but are not listed. We further confirm that the order of authors listed in the manuscript has been approved by all of us. We confirm that we have given due consideration to the protection of intellectual property associated with this work and that there are no impediments to publication, including the timing of publication, with respect to intellectual property. In so doing we confirm that we have followed the regulations of our institutions concerning intellectual property.

We understand that the Corresponding Author is the sole contact for the Editorial process (including Editorial Manager and direct communications with the office). He is responsible for communicating with the

other authors about progress, submissions of revisions and final approval of proofs. We confirm that we have provided a current, correct email address.

#### Acknowledgements

This study was partially supported by Lithuanian Academy of Sciences, grant LMA-CERN-2019 and performed in the framework of the CERN RD50 collaboration. This work was also partially supported by the European Union's Horizon Research and Innovation program under AIDA- 2020 grant agreement no. 654168.

#### References

- [1] Y. Zhou, Z. Wang, A. Rasmita, S. Kim, A. Berhane, Z. Bodrog, G. Adamo, A. Gali, I. Aharonovich, W. Gao, Room temperature solid-state quantum emitters in the telecom range, *Sci. Adv.* 4 (2018) eaar3580.
- [2] S.F. Song, W.D. Chen, F. Su, J. Zhu, K. Ding, C.C. Hsu, Structure and photoluminescence studies of Pr-implanted GaN, *J. Cryst. Growth* 267 (2004) 400–404.
- [3] R. Birkhahn, M. Garter, A.J. Steckl, Red light emission by photoluminescence and electroluminescence from Pr-doped GaN on Si substrates, *Appl. Phys. Lett.* 74 (1999) 2161–2163.
- [4] R. Heitz, P. Thurián, I. Loa, L. Eckey, A. Hoffmann, I. Broser, K. Pressel, B.K. Meyer, E.N. Mokhov, Identification of the 1.19-eV luminescence in hexagonal GaN, *Phys. Rev. B* 52 (1995) 16508–16515.
- [5] K. Pressel, S. Nilsson, R. Heitz, A. Hoffmann, B.K. Meyer, Photoluminescence study of the 1.047 eV emission in GaN, *J. Appl. Phys.* 79 (1996) 3214–3218.
- [6] N.A. Sobolev, A.M. Emel'yanov, V.I. Sakharov, I.T. Serenkov, E.I. Shek, A.I. Besyul'kin, W.V. Lundin, N.M. Shmidt, A.S. Usikov, E.E. Zavarin,



- Photoluminescence in Er-implanted AlGaIn/GaN superlattices and GaN epilayers, *Physica B* 340–342 (2003) 1108–1112.
- [7] J.T. Seo, U. Hommerich, J.D. MacKenzie, C.R. Abernathy, J.M. Zavada, Near Infrared luminescent device and optical spectroscopy of Er-doped gallium nitride prepared by metalorganic molecular beam epitaxy, *J. Korean Phys. Soc.* 36 (2000) 311–315.
  - [8] J. Baur, K. Maier, M. Kunzer, U. Kaufmann, J. Schneider, H. Amano, I. Akasaki, T. Detchprohm, K. Hiramoto, Infrared luminescence of residual iron deep level acceptors in gallium nitride (GaN) epitaxial layers, *Appl. Phys. Lett.* 64 (1994) 857–859.
  - [9] U. Hommerich, J.T. Seo, C.R. Abernathy, A.J. Steckl, J.M. Zavada, Spectroscopic studies of the visible and infrared luminescence from Er doped GaN, *Math. Sci. Eng.* B81 (2001) 116–120.
  - [10] S.F. Song, W.D. Chen, J. Zhu, C.C. Hsu, Dependence of implantation-induced damage with photoluminescence intensity in GaN:Er, *J. Cryst. Growth* 265 (2004) 78–82.
  - [11] C. Wetzel, D. Volm, B.K. Meyer, K. Pressel, S. Nilsson, E.N. Mokhov, P.G. Baranov, GaN epitaxial layers grown on 6H-SiC by the sublimation sandwich technique, *Appl. Phys. Lett.* 65 (1994) 1033–1035.
  - [12] M.W. Bayerl, M.S. Brandt, O. Ambacher, M. Stutzmann, E.R. Glaser, R.L. Henry, A.E. Wickenden, D.D. Koleske, T. Suski, I. Grzegory, S. Porowski, Optically detected magnetic resonance of the red and near-infrared luminescence in Mg-doped GaN, *Phys. Rev. B* 63 (2001) 125203.
  - [13] X. He, N.F. Hartmann, X. Ma, Y. Kim, R. Ihly, J.L. Blackburn, W. Gao, J. Kono, Y. Yomogida, A. Hirano, T. Tanaka, H. Kataura, H. Htoon, S.K. Doorn, Tunable room-temperature single-photon emission at telecom wavelengths from sp<sup>3</sup> defects in carbon nanotubes, *Nat. Photon.* 11 (2017) 577–582.
  - [14] M.A. Reshchikov, H. Morkoc, Luminescence properties of defects in GaN, *J. Appl. Phys.* 97 (2005) 061301.
  - [15] E. Gaubas, T. Ceponis, L. Deveikis, D. Meskauskaitė, J. Pavlov, V. Rumbauskas, M. Bockowski, B. Lucznik, Electrical characterization of HVPE GaN containing different concentrations of carbon dopants, *Semicond. Sci. Technol.* 33 (2018) 125024.
  - [16] E. Gaubas, T. Ceponis, L. Deveikis, D. Meskauskaitė, S. Miasojedovas, J. Mickevičius, J. Pavlov, K. Pukas, J. Vaitkus, M. Velicka, M. Zajac, R. Kucharski, Study of neutron irradiated structures of ammonothermal GaN, *J. Phys. D Appl. Phys.* 50 (2017) 135102.
  - [17] E. Gaubas, E. Simoen, J. Vanhellefont, Review-Carrier lifetime spectroscopy for defect characterization in semiconductor materials and devices, *ECS J. Solid State Sci. Technol.* 5 (2016) P3108–P3137.
  - [18] E. Gaubas, T. Ceponis, J. Mickevičius, J. Pavlov, V. Rumbauskas, M. Velicka, E. Simoen, M. Zhao, Pulsed photo-ionization spectroscopy in carbon doped MOCVD GaN epi-layers on Si, *Semicond. Sci. Technol.* 33 (2018) 075015.
  - [19] E. Gaubas, P. Baronas, T. Ceponis, L. Deveikis, D. Dobrovolskas, E. Kuokstis, J. Mickevičius, V. Rumbauskas, M. Bockowski, M. Iwinska, T. Sochacki, Study of spectral and recombination characteristics of HVPE GaN grown on Ammono substrates, *Mater. Sci. Semicond. Process.* 91 (2019) 341–355.
  - [20] J.I. Pankove, *Optical Processes in Semiconductors*, Prentice-Hall, New Jersey, 1971.
  - [21] W. van Roosbroeck, W. Shockley, Photon-radiative recombination of electrons and holes in germanium, *Phys. Rev.* 94 (1954) 1558–1560.
  - [22] A.A. Kopylov, A.N. Pikhtin, Influence of temperature on spectra of optical absorption by deep levels in semiconductors, *Sov. Phys. Solid State* 16 (1975) 1200.
  - [23] K. Huang, A. Rhy, Theory of light absorption and non-radiative transitions in F-centre, *Proc. R. Soc. London A: Math. Phys. Eng. Sci.* 204 (1950) 406–423.
  - [24] A. Alkauskas, D.M. McCluskey, C.G. Van de Walle, Tutorial: defects in semiconductors—combining experiment and theory, *J. Appl. Phys.* 119 (2016) 181101.
  - [25] R. Bhattacharya, B. Pal, B. Bansal, On conversion of luminescence into absorption and the van Roosbroeck-Shockley relation, *Appl. Phys. Lett.* 100 (2012) 222103.
  - [26] A. Armstrong, A.R. Arehart, D. Green, U.K. Mishra, J.S. Speck, S.A. Ringel, Impact of deep levels on the electrical conductivity and luminescence of gallium nitride codoped with carbon and silicon, *J. Appl. Phys.* 98 (2005) 053704.
  - [27] A.Y. Polyakov, N.B. Smirnov, E.A. Kozhukhova, A.V. Osinsky, S.J. Pearton, Temperature stability of high-resistivity GaN buffer layers grown by metalorganic chemical vapor deposition, *J. Vac. Sci. Technol. B* 31 (2013) 051208.
  - [28] I.-H. Lee, A.Y. Polyakov, N.B. Smirnov, A.V. Govorkov, A.S. Usikov, H. Helava, Y.N. Makarov, S.J. Pearton, Deep hole traps in undoped n-GaN films grown by hydride vapor phase epitaxy, *J. Appl. Phys.* 115 (2014) 223702.
  - [29] M.A. Reshchikov, Point defects in GaN, defects in semiconductors, *Book Series: Semiconduct. Semimet.* 91 (2015) 315–367.
  - [30] P. Thurian, A. Hoffmann, L. Eecke, P. Maxim, R. Heitz, I. Broser, K. Pressel, B.K. Meyer, J. Schneider, J. Baur, M. Kunzer, Photoluminescence of Fe-complexes in GaN, *MRS Proc* 449 (1996) 707–712.
  - [31] A. Wolos, M. Palczewska, M. Zajac, J. Gosk, M. Kaminska, A. Twardowski, M. Bockowski, I. Grzegory, S. Porowski, Optical and magnetic properties of Mn in bulk GaN, *Phys. Rev. B* 69 (2004) 115210.
  - [32] H. Tang, Z.Q. Fang, S. Rolfe, J.A. Bardwell, S. Raymon, Growth kinetics and electronic properties of unintentionally doped semi-insulating GaN on SiC and high-resistivity GaN on sapphire grown by ammonia molecular-beam epitaxy, *J. Appl. Phys.* 107 (2010) 103701.
  - [33] S.J. Chung, O.H. Cha, H.K. Cho, M.S. Jeong, C.-H. Hong, E.-K. Suh, H.J. Lee, Photocurrent spectroscopy investigations of Mg-related defects levels in p-type GaN, *MRS Proc* 595 (1999) F99W11.83.
  - [34] R.Y. Korotkov, J.M. Gregie, B.W. Wessels, Optical properties of the deep Mn acceptor in GaN:Mn, *Appl. Phys. Lett.* 80 (2002) 1731–1733.
  - [35] G.C. Yi, B.W. Wessels, Deep level defects in Mg-doped GaN, *MRS Proc* 423 (1996) 525–530.
  - [36] E. Gaubas, T. Ceponis, A. Jasiunas, V. Kovalevskij, D. Meskauskaitė, J. Pavlov, V. Remeikis, A. Tekorius, J. Vaitkus, Correlative analysis of the in situ changes of carrier decay and proton induced photoluminescence characteristics in chemical vapor deposition grown GaN, *Appl. Phys. Lett.* 104 (2014) 062104.
  - [37] E.F. Schubert, *Light-Emitting Diodes*, third ed., Cambridge University Press, London, 2018.
  - [38] M.A. Reshchikov, D.O. Demchenko, A. Usikov, H. Helava, Yu Makarov, Carbon defects as sources of the green and yellow luminescence bands in undoped GaN, *Phys. Rev. B* 90 (2014) 235203.



A4

Spectroscopy of defects in neutron  
irradiated ammono-thermal GaN by  
combining photo-ionization,  
photoluminescence and positron  
annihilation techniques

J. Pavlov, T. Čeponis, **L. Deveikis**, T. Heikkinen, J. Raisanen, V.  
Rumbauskas, G. Tamulaitis, F. Tuomisto, E. Gaubas

Lith. J. Phys. **59** (4) (2019) 211-223.

DOI:10.3952/physics.v59i4.4137

(Open access)

# SPECTROSCOPY OF DEFECTS IN NEUTRON IRRADIATED AMMONO-THERMAL GaN BY COMBINING PHOTOIONIZATION, PHOTOLUMINESCENCE AND POSITRON ANNIHILATION TECHNIQUES

J. Pavlov<sup>a</sup>, T. Čeponis<sup>a</sup>, L. Deveikis<sup>a</sup>, T. Heikkinen<sup>b,c</sup>, J. Raisanen<sup>c</sup>, V. Rumbauskas<sup>a</sup>,

G. Tamulaitis<sup>a</sup>, F. Tuomisto<sup>b,c,d</sup>, and E. Gaubas<sup>a</sup>

<sup>a</sup> *Institute of Photonics and Nanotechnology, Vilnius University, Saulėtekio 3, 10257 Vilnius, Lithuania*

<sup>b</sup> *Department of Applied Physics, Aalto University, 00076 Aalto Espoo, Finland*

<sup>c</sup> *Department of Physics, University of Helsinki, 00014 Helsinki, Finland*

<sup>d</sup> *Helsinki Institute of Physics, University of Helsinki, 00014 Helsinki, Finland*

Email: jevgenij.pavlov@tmi.vu.lt

Received 11 September 2019; accepted 30 September 2019

In this work, pulsed photoionization as well as photoluminescence and positron annihilation spectroscopy were combined to detect different species of defects. The GaN crystals, grown by the ammono-thermal method, doped with Mn as well as Mg impurities and irradiated with different fluences of reactor neutrons, were examined to clarify the role of the technological and radiation defects. The evolution of the prevailing photoactive centres was examined by pulsed photoionization spectroscopy. Positron annihilation spectroscopy was applied to reveal vacancy-type defects.

**Keywords:** pulsed photoionization spectroscopy, photoluminescence, positron annihilation spectroscopy, GaN, defects

## 1. Introduction

GaN material and its alloys with aluminium have become widely used in fabrication of devices for biological, chemical and radiation sensing [1, 2]. Modern technology grown GaN is particularly interesting for production of radiation tolerant detectors capable of operating in extremely harsh radiation environments. The high luminosity large hadron collider (HL-LHC) will reach fluxes from 5 to 7 of the nominal LHC luminosity [3] and the future circular collider (FCC) is anticipated to reach particle energy up to 100 TeV [4, 5]. Therefore, the HL-LHC and FCC detectors should withstand the extremely high fluences up to  $10^{17}$  cm<sup>-2</sup>. Therefore, much effort has been made in search of modern materials for detectors to be used in such conditions for a long time [6]. GaN-based detectors are beneficial due to their capability to

generate both the electrical and optical signals. The GaN-based detectors raise technical interest in development of the double-purpose devices capable to operate both as scintillating and charge collecting detectors for tracking of high-energy particles [7–10]. The depth and lateral homogeneity of the sensor structures are therefore necessary to get the linear response of the detector [11]. Moreover, thick sensor structures which satisfy the requirement of bulk uniformity are required to detect events of the relatively small interaction cross-sections. This situation appears in the detection of strongly penetrating radiations. As a result of irradiation, the displacement damage occurs. Then, the lattice atoms are knocked out of their sites creating thereby vacancies and interstitials [12]. Clusters of radiation defects acting as carrier traps affect the opto-electronic characteristics of the devices, reducing the luminescence intensity and efficiency

of charge collection, increasing the leakage current and thereby changing the detector response [13, 14].

The GaN single-crystals (even grown by advanced technologies) contain a lot of technological defects yet. Therefore, a trade-off should be found in choice of the GaN growth technology to have a cheap, fast way to devise rather thick radiation sensors, capable of generating double responses. MOCVD GaN epilayers usually have large densities of dislocations, which lead to a fairly high leakage current. The lattice mismatch between the substrate (sapphire, Si or SiC) and GaN causes stress wafer bowing. This determines the dislocation density not less than  $10^9 \text{ cm}^{-2}$  [15]. Especially, screw dislocations strongly affect the electrical properties of the electronic devices [16]. There exists the epitaxial-lateral-overgrowth (ELO) technology, which allows making of GaN layers relatively clean from dislocations. However, this technology excludes growth of thick single crystals [17]. The most promising GaN growth technologies are hydride vapour phase epitaxy (HVPE) and ammono-thermal (AT) method in production of the double-response detectors [18, 49]. The dislocation density less than  $10^6 \text{ cm}^{-2}$  can be reached by the HVPE method. Even lower dislocation densities  $\leq 10^5 \text{ cm}^{-2}$  are achievable by employing the AT technology.

In this study, the AT GaN crystals doped with various impurities and irradiated with different fluences of neutrons were examined to clarify the role of the technological and radiation defects. Mg impurities are widely exploited in formation of modern devices having specific electrical characteristics [20, 21]. Moreover, Mg impurities serve as the main dopants in formation of the p-type conductivity GaN. Other dopants, namely Mn, may act as the compensating centres for unintentionally induced donor-type defects and fast carrier traps, and that can also be used to obtain semi-insulating or highly resistive material. By manipulating the ratio between the dopant density and the concentration of radiation defects, it is possible to increase the radiation resistance of the sensors. In this work, the evolution of the pulsed photoionization (PPIS), scintillation (pulsed photoluminescence – PPL) and positron annihilation (PAS) [22–25] spectroscopy means have been combined to reveal the prevailing defects of different species and scintillation efficiency with neutron irradiation fluence. The contactless PPIS is beneficial in discovery of

photoactive centres. PAS is a powerful method for detecting vacancy-type defects [23].

## 2. Samples

The bulk GaN crystals were grown by the ammono-thermal method [26] at *Ammono Company* (Poland) [27]. The GaN samples were doped with Mg and Mn of concentrations  $1 \times 10^{18} \text{ cm}^{-3}$  and  $10^{19} \text{ cm}^{-3}$ , respectively. The thickness of free-standing AT GaN samples was 400–450  $\mu\text{m}$ . The AT GaN crystals contained the dislocation density less than  $10^5 \text{ cm}^{-2}$  [28, 29]. In order to emulate the evolution of particle detector functionality during experiments at the LHC, it is preferable to use the reactor neutron irradiation, since homogeneous damage thereby can easily be achieved. The 1 MeV neutron equivalent of radiation damage, caused by the non-ionizing energy loss (NIEL), is widely used for the estimation of the effective fluence, because the NIEL damage becomes then similar under irradiations with different type particles [30]. The AT GaN samples were irradiated by a nuclear reactor at the Jožef Stefan Institute (Ljubljana) TRIGA reactor [31]. Fast neutrons with the energy peak at 1 MeV and of  $7.5 \times 10^{12} \text{ n}/(\text{cm}^2\text{s})$  flux act as the main generator in defect formation.

## 3. Spectroscopy techniques

### 3.1. Pulsed photoionization spectroscopy

A few results on neutron-irradiated AT GaN materials and the spectral data of the prevailing defects have been reported in our previous publications [32, 33]. In this work, the evolution of the PPI [34] spectra with neutron fluence in a range of  $10^{12}$ – $5 \times 10^{16} \text{ n}/\text{cm}^2$  has been studied in more detail. The pulsed response is recorded using microwave probed photoconductivity transients (MW-PC). The peak MW-PC values were determined within the MW-PC transients to estimate the excess carrier density generated by photoionization processes. These values represent a step-like photoionization spectrum. The relaxation shape and duration of the MW-PC transients represent the carrier lifetime and trap filling/emptying processes within later carrier decay stages. The definite steps of photoionization spectra commonly

correlate with the changes of the carrier recombination lifetimes, and this allows one to additionally control the filling state of the photoactive centres. The PPIS is preferable for recording of the PC signals, as it is operational in a contactless mode at room temperature and excludes contact-related effects. In this work tuneable wavelength (in a range of 210 to 2300 nm) nanosecond (4 ns) light pulses are generated by an OPO instrument *Ekspla* NT342B. The sample was placed on the slit-antenna of 21 GHz microwave (MW) system and excited by a laser beam. The MW-PC transients were recorded by a 2 GHz oscilloscope *LeCroy* Wave Runner 620 Zi on a 50  $\Omega$  load resistor connected in series with an MW detector.

Photoionization or photo-neutralization of deep levels is characterized by photoionization cross-sections. Spectral changes of the photoionization cross-section  $\sigma(h\nu)$  can be described by the Kopylov–Pikhtin model [35]:

$$\sigma(h\nu) = M_{ik}^2 \int_0^\infty \frac{\exp[-(E + E_d - h\nu)^2 / \Gamma^2] \sqrt{E} dE}{h\nu(E + E_d)^2}. \quad (1)$$

Here  $E_d$  is the photo-activation energy,  $\Gamma$  is the broadening factor, which determines electron–phonon coupling, and  $M_{ik}$  is the matrix element of a dipole transition from the initial ( $i$ ) (trap level) to the final ( $k$ ) (continuum) state. The broadening factor depends on the ground and excited state vibrational frequencies and Franck–Condon shift [36]. In PPI spectra fitting, the  $E_d$  and  $\Gamma$  were varied as the free parameters to get the best fit estimated by the nonlinear least squares method for experimental spectra. Changes of the absorption coefficient  $\alpha(h\nu)$  for  $h\nu$  energy photons due to photoionization of trapped carriers can then be described by

$$\alpha(h\nu) = \sigma(h\nu)n_{d0}. \quad (2)$$

Here  $n_{d0}$  is the concentration of the trapped carriers. The density of the photoemitted carriers, registered by an MW probe, comes from illumination by a light pulse of the surface density of the incident photons

$$n_d^* = \sigma(n\nu)n_{d0}F(h\nu), \quad (3)$$

where  $n_d^*$  is the density of the photoemitted carriers and  $F(h\nu)$  is the fixed surface density of the incident photons of varied energy  $h\nu$ .

### 3.2. Pulsed scintillation spectroscopy

The scintillation characteristics have been examined by recording of the UV laser-induced pulsed photoluminescence spectra (PPL) under the experimental conditions close to those of the PPIS measurements. An ultraviolet (UV) laser STA-3H emitting 351 nm light pulses of 400 ps was employed for the excitation of photoluminescence (PL). A PL response was filtered from a laser beam (using an interference 100% mirror at laser wavelength), collected into a UV adjusted fiberscope and transmitted to a spectrophotometer. An AvaSpec-2018L grating spectrophotometer was exploited to integrate the spectrally dispersed PL response. Over  $10^3$  PL transients were integrated and averaged to get the scintillation spectrum in the samples irradiated with the fixed reactor neutron fluence. The PL spectra recorded on pristine and irradiated AT GaN samples provided evolution of scintillation efficiency within various spectral bands.

### 3.3. Positron annihilation spectroscopy

For PAS experiments, the pristine and  $1 \times 10^{16}$  cm $^{-2}$  as well as  $5 \times 10^{16}$  cm $^{-2}$  neutron fluence irradiated samples were employed. As the pristine samples contain significant concentrations of vacancy complexes, usage of rather low fluences is insufficient to produce detectable densities of radiation defects [24, 25]. Positrons implanted into the sample are captured and localized at neutral and negative vacancies. It is possible to determine the concentration of vacancies as well as to distinguish between different types of vacancies ( $V_{Ga}$ ,  $V_{Ga}-O_N$ ,  $V_{Ga}-H_n$ ) [24, 25]. The Mg-doped ( $1 \times 10^{20}$  cm $^{-3}$ ) pristine non-annealed AT GaN sample was used as a reference – possible extraction of the annihilation parameters of the GaN lattice has been shown [24]. The pristine and neutron-irradiated AT GaN samples were examined at room temperature (RT), using a digital positron lifetime spectrometer with a Gaussian time resolution of 250 ps. Two identical pristine samples were sandwiched together with the  $^{22}Na$   $\mu Ci$  positron source foiled in 1.5  $\mu m$  thick aluminium. To have the PAS spectrum, the positron lifetime records of  $10^6$  positron annihilation (PA) events were collected. The PAS measurements for irradiated samples were made using the same source, but with a different sandwich-structure (the source between the pristine and the irradiated samples). In the latter case,

the  $2 \times 10^6$  events were accumulated to record a PA spectrum and the spectrum of the pristine sample was subtracted in the analysis. The spectrum of the positron decay  $P(t)$  (after subtracting the constant background) due to annihilations in the source material (Al foil 210–215 ns, NaCl 400 ns and positronium 1500 ns [23]) was analysed assuming the sum of the exponential components

$$P(t) = \sum_i I_i e^{-t/\tau_i}, \quad (4)$$

where positrons in the state  $i$  annihilate with the lifetime  $\tau_i$  and the intensity  $I_i$ . The increase of the average lifetime  $\tau_{\text{ave}}$  [23] above the bulk lattice lifetime  $\tau_b$  indicates that positrons annihilate as trapped at vacancy defects. Moreover, this parameter is insensitive to the fitting procedures, and even a change of 1 ps in its value can be resolved [23]. The  $\tau_b$  parameter is the positron lifetime in the delocalized state in the lattice, and  $\tau_v$  ( $\tau_2$  in a two-component spectrum) is the lifetime component that gives directly the vacancy-specific lifetime. Because the electron density at a vacancy is lower than that within the bulk, the lifetime  $\tau_v$  is always longer than the bulk lifetime  $\tau_b$ . The first lifetime component is  $\tau_1 = (\tau_b^{-1} + \kappa_v)^{-1} < \tau_b$ , where  $\kappa_v$  is the positron trapping rate at one species of vacancy defects:

$$\kappa_v = c_v \mu_v. \quad (5)$$

Here  $c_v$  denotes the vacancy concentration and  $\mu_v$  is the positron trapping coefficient, which strongly depends on the charge-state of the vacancy defect. The bulk lifetime  $\tau_b$  of GaN is approximately  $\tau_b = 160$  ps, as measured in the reference sample. The parameter  $\tau_v$  depends on defect species, it varies in the range 220–240 ps for  $V_{\text{Ga}}$  and  $V_{\text{Ga}}$  complexes with a single O or H atom. This is clearly less than 200 ps for  $V_{\text{Ga}}$ -multi-hydrogen complexes [25]. It is likely that  $V_{\text{Ga}}$  complexed with 3 or more hydrogen atoms do not trap positrons [23, 25]. Typical positron trapping coefficients are  $\mu_v = 1 \times 10^{15} \text{ s}^{-1}$  for neutral vacancies and  $\mu_v = 2\text{--}3 \times 10^{15} \text{ s}^{-1}$  for negatively charged vacancies at RT, respectively.

#### 4. Evolution of the PPI spectra

The PPI spectra have been recorded at room temperature on AT GaN:Mg and AT GaN:Mn. The photoionization spectrum is obtained as the MW-PC

peak-signal amplitude, proportional to the excess carrier density generated by photoionization, which depends on photon energy. The evolution of the PPI spectra with neutron fluence are illustrated in Fig. 1 for AT GaN:Mn (a) and AT GaN:Mg (b), respectively.

The step-like photoionization spectra contained four spectral peaks for AT GaN:Mn (Fig. 1(a)) and seven peaks for AT GaN:Mg samples (Fig. v(b)), obtained by fitting the recorded PPI spectra.

The PPI spectral steps  $E_{\text{Mn},1}$  and  $E_{\text{Mn},2}$  are nearly independent of neutron irradiation (Fig. 1(a)). With fluence enhancement, a few times reduction (relative to that obtained for the pristine sample) of the PPI spectral step of  $E_{\text{Mn},4}$  can be deduced

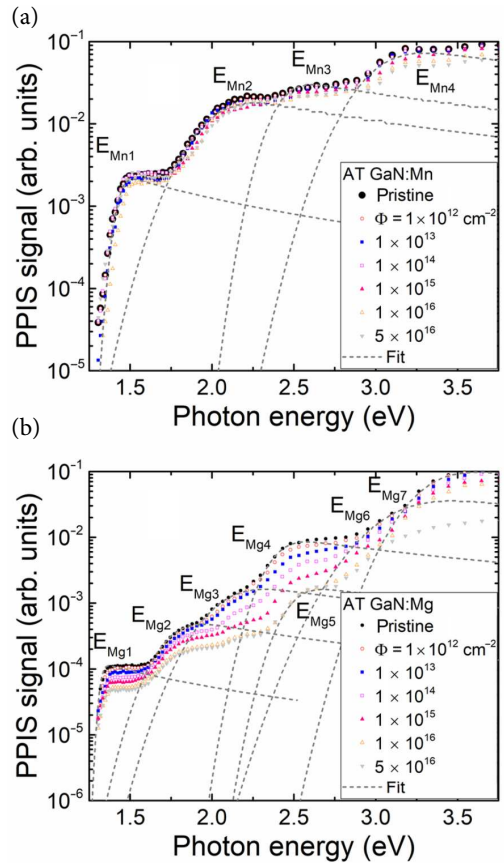


Fig. 1. (Coloured online.) Fitting of the PPI spectra, recorded on the pristine and neutron-irradiated samples (AT GaN:Mn (a) and AT GaN:Mg (b)). Thin dash lines show the PPI steps simulated using Eqs. (1) and (2).

from Fig. 1(a). This implies the decrease of concentration (proportional to the height of the PPIS step) of this  $E_{Mn,4}$  definite trap of the same origin (with an invariable cross-section). The insignificant variation of the  $E_{Mn,3}$  trap density can also be implied from the fluence-dependent evolution of Mn-doped AT GaN (in Fig. 1(a)). The decrease of concentration of the initially existing defects formed by crystal growth can be explained by defect transformations. Really, such a transformation of Mn ascribed defects has been revealed by ESR spectroscopy in our previous study [33]. On the other hand, the carrier lifetime reduction (observed on these samples [33]) with enhancement of neutron fluence seems to be the main reason for the reduced initial filling of  $E_{Mn,4}$  traps.

In Table 1, the identified activation energies and values of the broadening factor are listed for the predominant centres in Mn-doped AT GaN samples. The threshold photoionization energy values, taken from literature, were compared with those, extracted from fitting of the PPIS peaks, and these values have been employed for identifying of the defects. The density of the Mn associated traps  $E_{Mn,1}$  and  $E_{Mn,2}$  seems to be independent of neutron irradiation fluence, despite this the impact of the carrier lifetime decrease is the same for all the resolved traps  $E_{Mn,1}$ – $E_{Mn,4}$ . This hints that the PPIS step height highlights the initial filling state of the definite photoactive trap. Thereby, radiation defects seem to make the biggest impact on the initial filling of the  $E_{Mn,4}$  centres, however, of unknown origin.

A rather different evolution (relative to Mn-doped AT GaN material) of the PPIS steps was obtained in Mg-doped AT GaN samples (Fig. 1(b)). The most resolvable changes of the height of PPI

$E_{Mg,3}$ – $E_{Mg,5}$  spectral steps were obtained. The ESR spectroscopy, performed on these Mg-doped AT GaN samples [33], showed prevailing of the gallium vacancy and substitutional oxygen ( $V_{Ga}$ – $O_N$ ) [33, 39, 40] defects in the pristine material and hinted on the appearance of the nitrogen split interstitial [33, 41, 42] defects under irradiation. However, longer carrier lifetimes (relative to the Mn-doped material) and existence of a small density of Mn impurities in the pristine Mg-doped AT GaN samples were evidenced [33]. A significant decrease (up to an order of magnitude) of the height of the  $E_{Mg,3}$ – $E_{Mg,4}$  spectral steps has been obtained in this study, while less changes of the PPIS signals have been revealed for  $E_{Mg,1}$  and  $E_{Mg,2}$  spectral steps. Moreover, nearly invariable height has been observed for the  $E_{Mg,7}$  spectral step with enhancement of the neutron fluence. For the Mg-doped samples, appearance of the additional PPIS centre  $E_{Mg,5}$  in the range of elevated fluences ( $>10^{14}$  n/cm<sup>2</sup>) can be deduced from Fig. 1(b). The capture cross-section values for all the mentioned traps are nearly the same. This implies that neutron irradiation governs only the initial filling (density of carriers on the definite type centres) of the technologically induced defects.

Values of the estimated activation energy and the broadening factor for different traps are listed in Table 1 for the predominant centres in the Mg-doped AT GaN samples. There, the traps associated with vacancies, interstitials, impurities and dopants are tentatively identified. The amplitudes of different components, which are proportional to the initial filling of the photoactive centres, are plotted in Fig. 2. It can be inferred that neutron irradiations do not change considerably the structure of the photoactive technological defects. In

Table 1. The PPIS parameters in the pristine and neutron-irradiated samples extracted by fitting the PPIS steps.

	AT GaN:Mn				AT GaN:Mg						
	$E_{Mn1}$	$E_{Mn2}$	$E_{Mn3}$	$E_{Mn4}$	$E_{Mg1}$	$E_{Mg2}$	$E_{Mg3}$	$E_{Mg4}$	$E_{Mg5}$	$E_{Mg6}$	$E_{Mg7}$
$E_d \pm 0.04$ (eV)	1.43	1.99	2.41	2.99	1.32	1.74	2.06	2.38	2.48	3.10	3.31
$\Gamma_d$	0.06	0.25	0.15	0.26	0.03	0.18	0.24	0.15	0.15	0.32	0.25
Defect type	Mn [43]	Mn [44]	Ga <sub>i</sub> [45]	N/A	Donor [46]	Mg related [47]	$V_{Ga}$ related [48]	Ga <sub>i</sub> [45]	$V_{Ga}$ related [49]	Mg related [47]	$V_N$ [45]

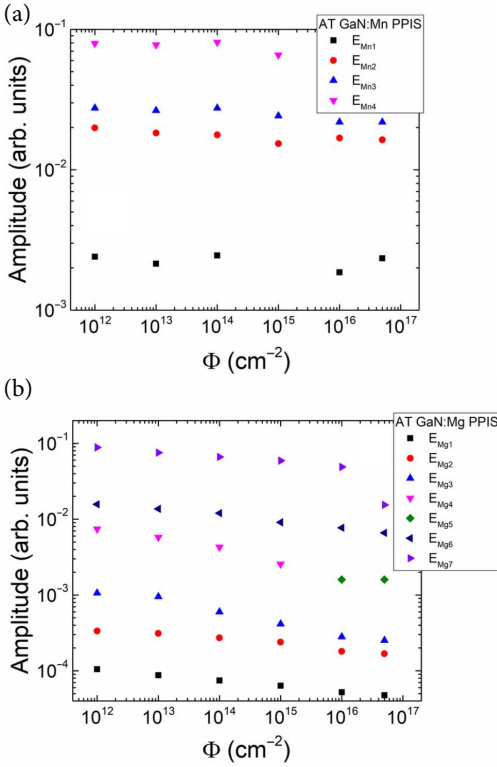


Fig. 2. (Coloured online.) Amplitudes of the PPI spectrum components, proportional to the initial filling of different traps, estimated from fitted PPI spectra for the pristine and neutron-irradiated samples (AT GaN:Mn (a) and AT GaN:Mg (b)), as functions of neutron irradiation fluence.

the Mg-doped sample, the radiation-induced defect  $E_{Mg5}$  is only observable for the samples irradiated with elevated fluences of  $>10^{14}$  n/cm<sup>2</sup>. The latter defect can play the role of a fast recombination centre. Its impact appears only when the carrier lifetime, linked to this radiation defect, becomes shorter than that inherent for the pristine material.

## 5. Evolution of the photoluminescence spectra

The neutron fluence  $\Phi$  dependent evolution of the UV pulse excited photoluminescence (PL) spectra *ex situ* recorded in Mn (a) and Mg (b) doped AT GaN is illustrated in Fig. 3.

In Mn-doped AT GaN (Fig. 3(a)), a rather wide spectral band peaked at 2.5 eV appears in the yellow–green (YG) PL range. The low intensity blue (B) PL

peaked at 3 eV can also be deduced from these (Fig. 3(a)) spectra. A clear decrease of the intensity of the YG-PL band with the enhancement of fluence is clearly observed only for large fluences  $>10^{16}$  n/cm<sup>2</sup>. The intensity of B-PL decreases nearly monotonically with the increase of irradiation fluence.

In the PL spectra recorded for Mg-doped AT samples (Fig. 3(c)), the same PL bands appear. However, the intensity of the B-PL wing is larger in this material relative to that in Mn-doped AT GaN. Moreover, the intensity of both YG-PL and B-PL is nearly invariable up to irradiations with moderate fluences  $<10^{15}$  n/cm<sup>2</sup>. A clear reduction of the PL intensity appears only for  $\Phi \geq 10^{15}$  n/cm<sup>2</sup>. This intensity reduction is most expressed for the B-PL spectral wing.

It is very probable that wide PL bands (especially YG-PL) are composed of several overlapping PL peaks. These peaks can be predicted by correlating PPI and PL spectra in consideration of the conversion from absorption to emission.

The absorption centres resolved within PPIS (Fig. 1) may originate the Stokes shifted PL bands. These YG-PL and B-PL peaks were fitted (Fig. 3) by using the van Roosbroeck–Shockley (vR–S) approach [50, 51] in relating the conversion from the PPI to PL spectra. The rate  $\Delta R_d(h\nu)$  of the emission via the trap of photo-activation energy  $E_d$  is linked to the photon–electron interaction cross-section  $\sigma(h\nu)$ , whose value also covers the B- and YG-PL peak photon energy (assigned to PL as  $\sigma_{d,PL}(h\nu)$ ) and is expressed as follows:

$$\Delta R_d(h\nu) = \frac{n_{\text{ex},\Delta(h\nu)}}{\tau_{\text{PL},\Delta(h\nu)}} = \quad (6)$$

$$\rho_{d,PL} \left( \frac{h\nu}{k_B T} \right) \sigma_{d,PL}(h\nu / k_B T) N_d \frac{n_{\text{ex},\Delta(h\nu)} N_d}{n_i^2}.$$

Here  $n_i = 2 \times 10^{-10}$  cm<sup>-3</sup> is the intrinsic carrier concentration for GaN materials [52],  $k_B$  is the Boltzmann constant,  $h$  is the Planck constant,  $\rho_d$  is the surface density of photons ascribed to the unit frequency  $\nu$  within the absorption spectrum for the spectral range  $\Delta(h\nu)$ , inherent to the dedicated trap of the concentration  $N_d$ , and  $n_{\text{ex},\Delta(h\nu)}$  is the excess carrier density generated through photoionization in the definite spectral range  $\Delta(h\nu)$ ,  $\tau_{\text{PL},\Delta(h\nu)}$  is the PL relaxation time.

The relations between the photoionization and photoluminescence spectra (Fig. 3) were simulated

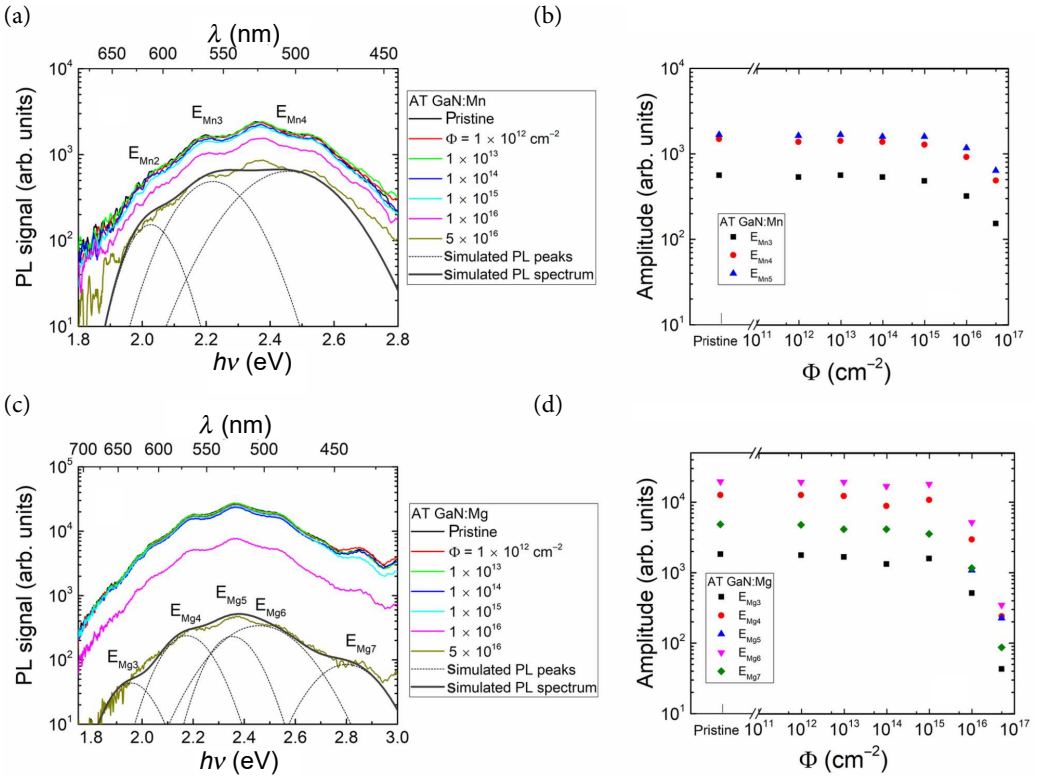


Fig. 3. (Coloured online.) Recorded and fitted evolution of photoluminescence spectra (a, c), using PPIS experimental data (listed in Table 1), and the amplitudes of the fitted PL spectral components (b, d), extracted for AT GaN:Mn (a, b) and AT GaN:Mg (c, d) materials, respectively. Thin dash lines represent PL peaks simulated using Eqs. (1) and (6), a thick grey line shows a resultant PL spectrum composed of the simulated PL peaks.

using Eqs. (1, 2, 3). The comparison of the simulated photoionization and photoluminescence spectra ascribed to several PPIS steps is illustrated in Fig. 3. For neutron-irradiated materials, the structure of B- and YG-PL was reproduced by varying the  $N_d$  value with irradiation fluence which means variation of the filling level of definite centres. Simulations were performed using the extracted values of the cross-section of the photon–electron coupling  $\sigma_d(h\nu)$  and of the photoionization energy  $E_d$  (as well as broadening factors  $\Gamma_d$ ) and by adjusting the  $\sigma_{d,PL}(h\nu)$  function to fit  $I_{PL}(h\nu)$  spectral peaks comprising a rather broad PL band. An association of the PPIS steps to the definite PL peaks is also sketched in Fig. 3 by denoting the respective deep traps ( $E_i$ ,  $i = 2-7$  according to notifications in Table 1).

A rather good reconstruction of the PL components, necessary for composing of wide PL spectral

bands, was obtained by simulating (using vR–S approach) the experimental PL (Fig. 3(a, c)). The evolution of the amplitudes of different PL spectral components with neutron irradiation fluence is illustrated in Fig. 3(b, d) for GaN:Mn and GaN:Mg materials, respectively. The simulations of PIS and PL spectra show that the additional radiation-induced trap  $E_{Mg,5}$  PPIS peak is very probable. Based on these fits it can be inferred that existence of technological defects in AT GaN:Mn is the main reason for the appearance of YG-PL. The richer PPI and PL spectra, recorded on AT GaN:Mg, and their modifications with neutron irradiation are determined by a variety of technological defects, the filling level of which changes with the appearance of fast non-radiative recombination centres, and radiation-induced additional photoactive traps. There, the faster reduction of the amplitudes of different PL spectral components



(Fig. 3(b, d)) in comparison with the PPIS component amplitudes (Fig. 2(a, b)) can be explained by the additional (relative to the initial filling of definite traps) decrease of excess carrier concentration (the term  $n_{\text{exd}(hv)}$  in Eq. 2) through non-radiative decay channels. The B and YG bands are assigned to Mg impurities and Ga-vacancy complexes in Mg-doped AT GaN material [53]. Vacancy complexes are plausible centres responsible for luminescence variations with neutron fluence when generation of radiation vacancies is very probable. Vacancy complexes with oxygen ( $V_{\text{Ga}}\text{-O}_{\text{N}}$ ) or silicon ( $V_{\text{Ga}}\text{-Si}_{\text{Ga}}$ ) might be responsible for YG luminescence. Additionally,  $C_{\text{N}}\text{-O}_{\text{N}}$  technological defects may also be a reason for YG luminescence [54]. It seems that Ga vacancies are most probable non-radiative recombination centres. By generalizing the PL data, a significant reduction of the overall PL intensity is quite evident (Fig. 3(b, d)). Also the overall PL intensity appears lower in the Mn-doped material from the very beginning. The dominant traps can tentatively be estimated by using the algebra of the obtained photo-activation energy values relative to a band gap ( $E_{\text{G}} = 3.45$  eV [50]) as well as valence/conduction band edges and to the identified PPIS traps as well as B and YG range PL transitions. Thereby,  $E_{1\text{-ppis}} = 1.4$  eV can be resulted from  $E_{\text{G}} - hv_2 \approx 1.3 \pm 0.1$  eV.

## 6. Irradiation-induced vacancy defects observed by positron annihilation spectroscopy

Figure 4 shows the average positron lifetime measured at RT in the pristine and neutron-irradiated AT GaN:Mn and AT GaN:Mg samples. The positron lifetime spectra consisted of only one resolvable component, suggesting saturation trapping at  $V_{\text{Ga}}$ -hydrogen complexes and also a contribution from negative ions (Mn and Mg), as discussed for the case of AT GaN in detail in Refs. [23–25]. Nevertheless, important conclusions can be drawn from the average positron lifetime. First, the average positron lifetime in the pristine AT GaN:Mn and AT GaN:Mg is clearly longer than the bulk lifetime of 160 ps, indicating that positrons are trapped at vacancy defects in these samples. Moreover, the average positron lifetime is longer in pristine AT GaN:Mn than that in AT GaN:Mg, indicating that the total amount of the open volume is larger in AT GaN:Mn, suggesting that the concentration of the Ga vacancy related

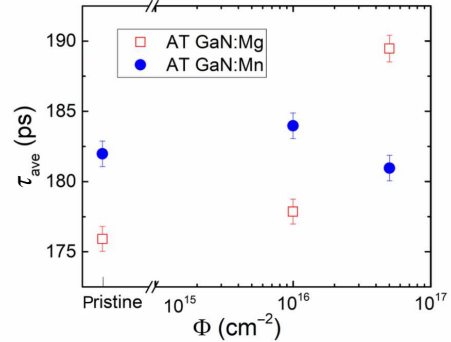


Fig. 4. (Coloured online.) Average positron lifetime in pristine and neutron-irradiated AT GaN:Mn and AT GaN:Mg.

defects is higher. Other possible explanations, namely that the vacancy defects would be larger (that is, contain less hydrogen) in AT GaN:Mn or that AT GaN:Mg would contain more negative ions (that in GaN affect the data also at RT to some extent), are considered unlikely. Also, the hydrogen content in the samples is similar, and the Mn doping is higher (by a factor of two) than the Mg doping.

The average positron lifetime increases significantly after neutron irradiation in AT GaN:Mg, in particular at a higher fluence of  $5 \times 10^{16} \text{ cm}^{-2}$ . This indicates the introduction of Ga vacancy defects in the irradiation process, similarly as observed after, e.g. electron irradiation and hydrogen implantation [37, 38]. As the vacancy defect concentrations in the pristine AT GaN samples are likely to be of the order of  $10^{18} \text{ cm}^{-3}$  (or more due to the saturation phenomenon discussed in Ref. [25]), at least similar concentrations of vacancy defects are introduced in the neutron-irradiated samples with the higher fluence. Interestingly, the average positron lifetime is hardly affected by the neutron irradiation in the AT GaN:Mn samples, although the concentrations of the irradiation-induced vacancy defects are necessarily the same as in AT GaN:Mg. This supports the interpretation that the vacancy defect concentrations are significantly higher in AT GaN:Mn than those in the AT GaN:Mg samples in the pristine material.

## 7. Discussion

The positron annihilation spectroscopy (PAS) data show that the pristine AT GaN:Mn material

contains a higher concentration of vacancy defects than AT GaN:Mg. This is seen both as a higher average lifetime of positrons in the pristine material, and also by the neutron irradiation having very little effect on the average lifetime in AT GaN:Mn. In contrast, in AT GaN:Mg, the irradiation (in particular with the highest fluence) causes a strong increase in the vacancy defect concentrations observed by the increase of the positron average lifetime. This is equivalent to an increase in the average size of the open volume in the vacancies. The increase of the positron average lifetime is related (as we have shown earlier [24, 25]) to the fact that the ingrown Ga vacancies in AT GaN are present in hydrogen complexes that produce a shorter lifetime than ‘pure’  $V_{\text{Ga}}$  produced by the irradiation. It means that the concentration of irradiation-induced vacancies is significant compared to the concentration of the ingrown vacancies (Mg-doped) if the average open volume at the vacancies observed with positrons increases. Also, it means that the concentrations of the ingrown vacancies in Mn-doped AT GaN are significantly higher than those created by irradiation, even at the highest fluence, when no changes of the positron lifetime are observed.

The comparison of the PAS and PL data shows that the Ga vacancies produced by irradiation are non-radiative recombination centres. The significant reduction of the overall PL intensity with the enhancement of neutron fluence nicely correlates with the positron annihilation data. This effect is stronger in the Mg-doped material; as the ingrown Ga vacancy-hydrogen complexes are probably also detrimental for the PL intensity in general, the Mn-doped material appears to luminesce less than the pristine Mg-doped material. Also, the stronger irradiation effect in the Mg-doped materials supports this hypothesis. Moreover, this comparison between the Mg- and Mn-doped materials evidences the smaller effect in the Mn-doped samples, where the pristine vacancy concentrations seem to be higher, as the irradiation-induced vacancies affect the positron lifetime data so little.

## 8. Conclusions

The decrease of concentration of the initially existing defects formed by crystal growth has been observed after neutron irradiation and it can be

explained by defect transformations. This defect transformation effect of Mn-ascribed defects was revealed by ESR spectroscopy. The carrier lifetime reduction (observed for these samples) with the enhancement of neutron fluence seems to be the main reason for the reduced initial filling of  $E_{\text{Mn},4}$  traps. The density of the Mn associated traps  $E_{\text{Mn},1}$  and  $E_{\text{Mn},2}$  seems to be independent of neutron irradiation fluence; despite this the impact of the carrier lifetime decrease is the same for all the resolved traps  $E_{\text{Mn},1}-E_{\text{Mn},4}$ . This hints that the PPIS step height highlights the initial filling state of the definite photoactive trap. Thereby, radiation defects seem to make the biggest impact on the initial filling of the  $E_{\text{Mn},4}$  centres of unknown origin. The most resolvable changes of the height of PPI  $E_{\text{Mn},3}-E_{\text{Mn},4}$  spectral steps have been obtained.

A rather different evolution (relative to the Mn-doped AT GaN material) of the PPIS steps has been obtained in the Mg-doped AT GaN samples. The longer carrier lifetimes (relative to the Mn-doped material) and existence of a small density of Mn impurities in the pristine Mg-doped AT GaN samples have been evidenced by EPR. The significant decrease (up to an order of magnitude) of the height of the  $E_{\text{Mg},3}-E_{\text{Mg},4}$  spectral steps has been obtained with the enhancement of neutron irradiation fluence. Meanwhile, less changes of the PPIS signals have been revealed for  $E_{\text{Mg},1}$  and  $E_{\text{Mg},2}$  spectral steps and nearly invariable height has been observed for the  $E_{\text{Mg},7}$  spectral step with the enhancement of neutron fluence. For the Mg-doped samples, the appearance of the additional PPIS centre  $E_{\text{Mg},5}$  in the range of elevated fluences ( $>10^{14}$  n/cm<sup>2</sup>) has been deduced. It has been concluded that neutron irradiation governs only the initial filling (density of carriers on the definite type centres) of the technologically ingrown defects.

The traps associated with vacancies, interstitials, impurities and dopants have been tentatively identified. It has been inferred that neutron irradiations do not change considerably the structure of the photoactive technological defects. The radiation induced defect  $E_{\text{Mg},5}$  is only observable for the samples irradiated with the elevated fluence of  $>10^{14}$  n/cm<sup>2</sup>. The latter defect can play the role of a fast recombination centre whose impact appears only when the carrier lifetime, linked to this radiation defect, becomes shorter than that inherent for the pristine material.

The relations between the photoionization and photoluminescence spectra have been simulated using the van Roosbroeck–Shockley approach. For neutron-irradiated materials, the structure of B- and YG-PL has been reproduced by varying the  $N_d^+$  value with irradiation fluence which means variation of the filling level of definite centres. An association of the PPIS steps to the definite components of the PL bands has been performed. A rather good reconstruction of the PL components, necessary for composing of the wide PL spectral bands, has been obtained by simulating the experimental PL spectra. The evolution of the amplitudes of different PL spectral components with neutron irradiation fluence has been obtained. The richer PPI and PL spectra, recorded on AT GaN:Mg, and their modifications with neutron irradiation are determined by the wider variety of technological defects, the filling level of which changes with the appearance of fast non-radiative recombination centres, and radiation-induced additional photoactive traps. The faster reduction of the amplitudes of different PL spectral components in comparison with the PPIS component amplitudes can be explained by the additional decrease of the excess carrier concentration  $n_{ex\Delta(h\nu)}$  through the non-radiative decay channels. Vacancy complexes with oxygen ( $V_{Ga}-O_N$ ) or silicon ( $V_{Ga}-Si_{Ga}$ ) might be responsible for YG luminescence. Ga vacancies are most likely non-radiative recombination centres. This is supported by the PL data. Additionally,  $C_N-O_N$  technological defects may also be a reason for YG luminescence. The positron annihilation data support the hypothesis that Ga vacancies are non-radiative recombination centres and show that the Mn-doped material has more vacancies than the Mg-doped material.

### Acknowledgements

This research is funded by the European Social Fund under Measure No. 09.3.3- LMT-K-712 -02-0012 ‘Development of Competences of Scientists, other Researchers and Students through Practical Research Activities’. The authors are indebted to Dr. M. Zajac for providing the AT GaN materials. The neutron irradiations at the TRIGA Facility were supported by the AIDA-2020 Transnational Access Project funded by the EU Horizon 2020 R&D Programme under Grant Agreement No. 654168.

### References

- [1] P. Pittet, P. Jalade, G. Gindraux, P. Guiral, R. Wanga, J.M. Galvan, and G.N. Lua, DoRGaN: Development of quality assurance and quality control systems for high dose rate brachytherapy based on GaN dosimetry probes, *IRBM* **39**, 279–290 (2018), <https://doi.org/10.1016/j.irbm.2018.04.005>
- [2] S.J. Pearton, B.S. Kang, S. Kim, F. Ren, B.P. Gila, C.R. Abernathy, J. Lin, and S.N.G. Chu, GaN-based diodes and transistors for chemical, gas, biological and pressure sensing, *J. Phys. Condens. Matter* **16**, R961–R994 (2004), <https://doi.org/10.1088/0953-8984/16/29/R02>
- [3] <https://home.cern/science/accelerators/high-luminosity-lhc>
- [4] <https://home.cern/science/accelerators/future-circular-collider>
- [5] O. Kortner, S. Kortner, H. Kroha, S. Podkladkin, and R. Richter, Design of the FCC-hh muon detector and trigger system, *Nucl. Instrum. Methods Phys. Res. A* **936**, 447–448 (2019), <https://doi.org/10.1016/j.nima.2018.10.013>
- [6] P.J. Sellin and J. Vaitkus, New materials for radiation hard semiconductor detectors, *Nucl. Instrum. Methods Phys. Res. A* **557**, 479–489 (2006), <https://doi.org/10.1016/j.nima.2005.10.128>
- [7] T. Yanagida and Y. Fujimo, Evaluation of scintillation properties of GaN, *e-J. Surf. Sci. Nanotech.* **12**, 396–399 (2014), <https://doi.org/10.1380/ejssnt.2014.396>
- [8] P. Pittet, G.N. Lu, J.M. Galvan, J.Y. Loisy, A. Ismail, J.Y. Giraud, and J. Balosso, Implantable real-time dosimetric probe using GaN as scintillation material, *Sens. Actuators A Phys.* **151**, 29–34 (2009), <https://doi.org/10.1016/j.sna.2009.02.018>
- [9] P. Pittet, N.L. Guo, M.G. Jean, M.B. Jean, I. Anas, Y.G. Jean, and J. Balosso, PL characterization of GaN scintillator for radioluminescence-based dosimetry, *Opt. Mater.* **31**, 1421–1424 (2019), <https://doi.org/10.1016/j.optmat.2008.09.012>
- [10] E. Gaubas, T. Ceponis, A. Jasiunas, V. Kovalevskij, D. Meskauskaitė, J. Pavlov, V. Remeikis, A. Tekorius, and J. Vaitkus, Correlative analysis of the *in situ* changes of carrier decay and proton induced photoluminescence characteristics

- in chemical vapor deposition grown GaN, *Appl. Phys. Lett.* **104**, 62104 (2014), <https://doi.org/10.1063/1.4865499>
- [11] H. Spieler, *Semiconductor Detector Systems* (Oxford University Press, New York, 2005).
- [12] M. Huhtinen, Simulation of non-ionising energy loss and defect formation in silicon, *Nucl. Instrum. Methods Phys. Res. A* **491**, 194–215 (2002), [https://doi.org/10.1016/S0168-9002\(02\)01227-5](https://doi.org/10.1016/S0168-9002(02)01227-5)
- [13] E. Gaubas, T. Ceponis, and J. Vaitkus, Impact of generation current on evaluation of the depletion width in heavily irradiated Si detectors, *J. Appl. Phys.* **110**, 033719 (2011), <https://doi.org/10.1063/1.3619802>
- [14] E. Gaubas, T. Ceponis, A. Jasiunas, A. Uleckas, J. Vaitkus, E. Cortina, and O. Militaru, Correlated evolution of barrier capacitance charging, generation and drift currents and of carrier lifetime in Si structures during 25 MeV neutrons irradiation, *Appl. Phys. Lett.* **101**, 232104-1–3 (2012), <https://doi.org/10.1063/1.4769370>
- [15] H.M. Foronda, A.E. Romanov, E.C. Young, C.A. Robertson, G.E. Beltz, and J.S. Speck, Curvature and bow of bulk GaN substrates, *J. Appl. Phys.* **120**, 035104 (2002), <https://doi.org/10.1063/1.4959073>
- [16] S.W. Lee, D.C. Oh, H. Goto, J.S. Ha, H.J. Lee, T. Hanada, M.W. Cho, S.K. Hong, H.Y. Lee, S.R. Cho, et al., Analysis of the relation between leakage current and dislocations in GaN-based light-emitting devices, *Phys. Status Solidi* **4**, 37–40 (2007), <https://doi.org/10.1002/pssc.200673552>
- [17] Z. Yu, M.A.L. Jhonsan, N.A. El-Masry, J.W. Cook Jr, and J.F. Schetzina, Study of the epitaxial-lateral-overgrowth (ELO) process for GaN on sapphire, *J. Cryst. Growth* **195**, 333–339 (1998), [https://doi.org/10.1016/S0022-0248\(98\)00638-1](https://doi.org/10.1016/S0022-0248(98)00638-1)
- [18] M. Bockowski, M. Iwinska, M. Amilusik, M. Fijalkowski, B. Lucznik, and T. Sochacki, Challenges and future perspectives in HVPE-GaN growth on ammonothermal GaN seeds, *Semicond. Sci. Technol.* **31**, 93002 (2016), <https://doi.org/10.1088/0268-1242/31/9/093002>
- [19] M.P. D'Evelyn, H.C. Hong, D.S. Park, H. Lu, E. Kaminsky, R.R. Melkote, P. Perlin, M. Lesczynski, S. Porowski, and R.J. Molnal, Bulk GaN crystal growth by the high-pressure ammonothermal method, *J. Cryst. Growth* **300**, 11–16 (2007), <https://doi.org/10.1016/j.jcrysgro.2006.10.232>
- [20] J. Simon, V. Protasenko, C. Lian, H. Xing, and D. Jena, Polarization-induced hole doping in wide-band-gap uniaxial semiconductor heterostructures, *Science* **327**, 60–64 (2010), <https://doi.org/10.1126/science.1183226>
- [21] P. Kozodoy, M. Hansen, S.P. DenBaars, and U.K. Mishra, Enhanced Mg doping efficiency in  $\text{Al}_{0.2}\text{Ga}_{0.8}\text{N}/\text{GaN}$  superlattices, *Appl. Phys. Lett.* **74**, 3681–3683 (1999), <https://doi.org/10.1063/1.123220>
- [22] S. Suihkonen, S. Pimputkar, S. Sintonen, and F. Tuomisto, Defects in single crystalline ammonothermal gallium nitride, *Adv. Electron. Mater.* **3**, 1600496 (2017), <https://doi.org/10.1002/aelm.201600496>
- [23] F. Tuomisto and I. Makkonen, Defect identification in semiconductors with positron annihilation: Experiment and theory, *Rev. Mod. Phys.* **85**, 1583–1631 (2013), <https://doi.org/10.1103/RevModPhys.85.1583>
- [24] F. Tuomisto, J.M. Maki, and M. Zajac, Vacancy defects in bulk ammonothermal GaN crystal, *J. Cryst. Growth* **312**, 2620–2623 (2010), <https://doi.org/10.1016/j.jcrysgro.2010.04.023>
- [25] F. Tuomisto, T. Kuittinen, M. Zajac, R. Doradzinski, and D. Wasik, Vacancy–hydrogen complexes in ammonothermal GaN, *J. Cryst. Growth* **403**, 114–118 (2014), <https://doi.org/10.1016/j.jcrysgro.2014.06.005>
- [26] R. Dwilinski, R. Doradzinski, J. Garczynski, L.P. Sierzputowski, A. Puchalski, Y. Kanbara, K. Yagi, H. Minakuchi, and H. Hayashi, Bulk ammonothermal GaN, *J. Cryst. Growth* **311**, 3015–3018 (2009), <https://doi.org/10.1016/j.jcrysgro.2009.01.052>
- [27] <https://www.unipress.waw.pl/growth/index.php/ammono-gan-wafers-sales>
- [28] R. Kucharski, M. Zajac, A. Puchalski, T. Sochacki, M. Bockowski, J.L. Weyher, M. Iwinska, J. Serafinczuk, R. Kudrawiec, and Z. Siemiątkowski, Ammonothermal growth of GaN crystals on HVPE-GaN seeds prepared with the use of ammonothermal substrates, *J. Cryst. Growth*

- 427, 1–6 (2015), <https://doi.org/10.1016/j.jcrysgro.2015.06.019>
- [29] M. Imanishi, Y. Todoroki, K. Murakami, D. Matsuo, H. Imabayashi, H. Takazawa, M. Maruyama, M. Imade, M. Yoshimura, and Y. Mori, Dramatic reduction of dislocations on a GaN point seed crystal by coalescence of bunched steps during Na-flux growth, *J. Cryst. Growth* **427**, 87–93 (2015), <https://doi.org/10.1016/j.jcrysgro.2015.07.001>
- [30] M. Moll, Radiation tolerant semiconductor sensors for tracking detectors, *Nucl. Instrum. Methods Phys. Res. A* **565**, 202–211 (2006), <https://doi.org/10.1016/j.nima.2006.05.001>
- [31] L. Snoj, G. Zerovnik, and A. Trkov, Computational analysis of irradiation facilities at the JSI TRIGA reactor, *Appl. Radiat. Isot.* **70**, 483–488 (2012), <https://doi.org/10.1016/j.apradiso.2017.09.022>
- [32] E. Gaubas, T. Čeponis, L. Deveikis, D. Meskauskaitė, S. Miasojedovas, J. Mickevičius, J. Pavlov, K. Pukas, J. Vaitkus, M. Velicka, M. Zajac, and R. Kucharski, Study of neutron-irradiated structures of ammonothermal GaN, *J. Phys. D* **50**, 135102 (2017), <https://doi.org/10.1088/1361-6463/aa5c6c>
- [33] E. Gaubas, T. Čeponis, D. Meškauskaitė, J. Mickevičius, J. Pavlov, V. Rumbauskas, R. Grigonis, M. Zajac, and R. Kucharski, Pulsed photoionization spectroscopy of traps in as-grown and neutron-irradiated ammonothermally synthesized GaN, *Sci. Rep.* **9**, 1473 (2019), <https://doi.org/10.1038/s41598-018-38138-6>
- [34] E. Gaubas, E. Simoen, and J. Vanhellefont, Review-carrier lifetime spectroscopy for defect characterization in semiconductor materials and devices, *ECS J. Solid State Sci. Technol.* **5**, P3108–P3137 (2016), <https://doi.org/10.1149/2.0201604jss>
- [35] A.A. Kopylov and A.N. Pikhtin, Influence of temperature on spectra of optical absorption by deep levels in semiconductors, *Sov. Phys. Solid State* **16**, 1200–1203 (1975).
- [36] A. Alkauskas, M.D. McCluskey, and C.G. Van de Walle, Tutorial: Defects in semiconductors – Combining experiment and theory, *J. Appl. Phys.* **119**, 181101 (2016), <https://doi.org/10.1063/1.4948245>
- [37] F. Tuomisto, V. Ranki, D.C. Look, and G.C. Farlow, Introduction and recovery of Ga and N sublattice defects in electron-irradiated GaN, *Phys. Rev. B* **76**, 165207 (2007), <https://doi.org/10.1103/PhysRevB.76.165207>
- [38] F. Tuomisto, Vacancy profiles and clustering in light-ion-implanted GaN and ZnO, *Appl. Surf. Sci.* **255**, 54 (2008), <https://doi.org/10.1016/j.apusc.2008.05.172>
- [39] N.T. Son, C.G. Hemmingsson, T. Paskova, K.R. Evans, A. Usui, N. Morishita, T. Ohshima, J. Isoya, B. Monemar, and E. Janzén, Identification of the gallium vacancy-oxygen pair defect in GaN, *Phys. Rev. B* **80**, 153202 (2009), <https://doi.org/10.1103/PhysRevB.80.153202>
- [40] N.T. Son, C.G. Hemmingsson, N. Morishita, T. Ohshima, T. Paskova, K.R. Evans, A. Usui, J. Isoya, B. Monemar, and E. Janzén, Radiation-induced defects in GaN, *Phys. Scr.* **T141**, 14015 (2010), <https://doi.org/10.1088/0031-8949/2010/T141/014015>
- [41] H.J. Von Bardeleben, J.L. Cantin, U. Gerstmann, A. Scholle, S. Greulich-Weber, E. Rauls, M. Landmann, W.G. Schmidt, A. Gentils, J. Botsoa, and M.F. Barthe, Identification of the nitrogen split interstitial (N–N)N in GaN, *Phys. Rev. Lett.* **109**, 206402 (2012), <https://doi.org/10.1103/PhysRevLett.109.206402>
- [42] H.J. von Bardeleben, J.L. Cantin, H. Vrielinck, F. Callens, L. Binet, E. Rauls, and U. Gerstmann, Nitrogen split interstitial center (N–N)N in GaN: High frequency EPR and ENDOR study, *Phys. Rev. B* **90**, 85203 (2014), <https://doi.org/10.1103/PhysRevB.90.085203>
- [43] R.Y. Korotkov, J.M. Gregie, and B.W. Wessels, Optical properties of the deep Mn acceptor in GaN:Mn, *Appl. Phys. Lett.* **80**, 1731–1733 (2002), <https://doi.org/10.1063/1.1456544>
- [44] A. Wolos, M. Palczewska, M. Zajac, J. Gosk, M. Kaminska, A. Twardowski, M. Bockowski, I. Grzegory, and S. Porowski, Optical and magnetic properties of Mn in bulk GaN, *Phys. Rev. B* **69**, 115210 (2004), <https://doi.org/10.1103/PhysRevB.69.115210>
- [45] Z. Zhang, A.R. Arehart, E.C.H. Kyle, J. Chen, E.X. Zhang, D.M. Fleetwood, R.D. Schrimpf,

- J.S. Speck, and S.A. Ringel, Proton irradiation effects on deep level states in Mg-doped p-type GaN grown by ammonia-based molecular beam epitaxy, *Appl. Phys. Lett.* **106**, 022104 (2015), <https://doi.org/10.1063/1.4905783>
- [46] S.J. Chung, O.H. Cha, H.K. Cho, M.S. Jeong, C.-H. Hong, E.-K. Suh, and H.J. Lee, Photocurrent spectroscopy investigations of Mg-related defects levels in p-type GaN, *MRS Proc.* **595**, F99W11.83 (1999), <https://doi.org/10.1557/PROC-595-F99W11.83>
- [47] G.C. Yi and B.W. Wessels, Deep level defects in Mg-doped GaN, *MRS Proc.* **423**, 525–530 (1996), <https://doi.org/10.1063/1.116075>
- [48] C.H. Qiu and J.I. Pankove, Deep levels and persistent photoconductivity in GaN thin films, *Appl. Phys. Lett.* **70**, 1983–1985 (1997), <https://doi.org/10.1063/1.118799>
- [49] Z. Zhang, C.A. Hurni, A.R. Arehart, J. Yang, R.C. Myers, J.S. Speck, and S.A. Ringel, Deep traps in nonpolar m-plane GaN grown by ammonia-based molecular beam epitaxy, *Appl. Phys. Lett.* **100**, 52114 (2012), <https://doi.org/10.1063/1.3682528>
- [50] J.I. Pankove, *Optical Processes in Semiconductors* (Prentice-Hall, New Jersey, USA, 1971).
- [51] R. Bhattacharya, B. Pal, and B. Bansal, On conversion of luminescence into absorption and the van Roosbroeck–Shockley relation, *Appl. Phys. Lett.* **100**, 222103 (2012), <https://doi.org/10.1063/1.4721495>
- [52] E. Gaubas, T. Ceponis, L. Deveikis, D. Dobrovolskas, V. Rumbauskas, and M. Viliunas, Room-temperature infrared photoluminescence in GaN doped with various impurities, *Opt. Mater.* **94**, 266–271 (2019), <https://doi.org/10.1016/j.optmat.2019.05.054>
- [53] S. Sintonen, S. Kivisaari, S. Pimputkar, S. Suihkonen, T. Schulz, J.S. Speck, and S. Nakamura, Incorporation and effects of impurities in different growth zones within basic ammonothermal GaN, *J. Cryst. Growth* **456**, 43–50 (2016), <https://doi.org/10.1016/j.jcrysgro.2016.08.040>
- [54] M. Julkarnain, N. Kamata, T. Fukuda, and Y. Arakawa, Yellow luminescence band in undoped GaN revealed by two-wavelength excited photoluminescence, *Opt. Mater.* **60**, 481–486 (2016), <https://doi.org/10.1016/j.optmat.2016.09.003>

## NEUTRONAIS APŠVITINTO AMONOTERMINĖS TECHNOLOGIJOS GaN SPEKTROSKOPIJA FOTOJONIZACIJOS, FOTOLIUMINESCENCIJOS IR POZITRONŲ ANIHILIACIJOS METODAIS

J. Pavlov<sup>a</sup>, T. Čeponis<sup>a</sup>, L. Deveikis<sup>a</sup>, T. Heikkinen<sup>b,c</sup>, J. Raisanen<sup>c</sup>, V. Rumbauskas<sup>a</sup>, G. Tamulaitis<sup>a</sup>, F. Tuomisto<sup>b,c,d</sup>, E. Gaubas<sup>a</sup>

<sup>a</sup> Vilniaus universiteto Fotonikos ir nanotechnologijų institutas, Vilnius, Lietuva

<sup>b</sup> Aalto universiteto Taikomosios fizikos fakultetas, Espas, Suomija

<sup>c</sup> Helsinkio universiteto Fizikos fakultetas, Helsinkis, Suomija

<sup>d</sup> Helsinkio universiteto Fizikos institutas, Helsinkis, Suomija

### Santrauka

Impulsinės fotojonizacijos, fotoluminescencijos ir pozitronų anihilacijos spektroskopinių tyrimų rezultatai buvo derinami siekiant identifikuoti savituosius ir radiacinius defektus reaktoriaus neutronais apšvitintose amonoterminės technologijos GaN (AT GaN) medžiagoje, priemaišintose Mn ir Mg. Įvertintos defektų evoliucijos charakteristikos keičiant neutronų apšvitos įtėkį plačiame  $10^{12} - 5 \times 10^{16}$  n/cm<sup>2</sup> intervale. Atskleista, kad nespindulinę rekombinaciją nulemia galio vakansijos,

kurių koncentracija yra didesnė Mn priemaišintame AT GaN. Vakansijų kompleksai su deguonies ir kitomis priemaišomis nulemia fotoluminescencijos spektrų evoliuciją ir visų aptiktų liuminescencijos smailių intensyvumo mažėjimą didėjant apšvitos įtėkiui. Fotojonizacijos ir fotoluminescencijos spektrų sąsajos paaiškintos Kopylovo-Pikhtino ir van Roosbroecko-Shockley modelių artinyje. Vakansiniai defektai identifikuoti matuojant pozitronų gyvavimo trukmę.

A5

Evolution of scintillation and electrical characteristics of AlGaN double-response sensors during proton irradiation

T. Čeponis, K. Badokas, **L. Deveikis**, J. Pavlov, V. Rumbauskas, V. Kovalevskij, S. Stanionytė, G. Tamulaitis, E. Gaubas

Sensors **19** (15) (2019) 3388.

DOI:10.3390/s19153388

(Open access)



Article

# Evolution of Scintillation and Electrical Characteristics of AlGa<sub>N</sub> Double-Response Sensors During Proton Irradiation

Tomas Ceponis <sup>1,\*</sup>, Kazimieras Badokas <sup>1</sup> , Laimonas Deveikis <sup>1</sup>, Jevgenij Pavlov <sup>1</sup>, Vytautas Rumbauskas <sup>1</sup>, Vitalij Kovalevskij <sup>1,2</sup>, Sandra Stanionyte <sup>1,2</sup>, Gintautas Tamulaitis <sup>1</sup> and Eugenijus Gaubas <sup>1</sup>

<sup>1</sup> Institute of Photonics and Nanotechnology, Vilnius University, Sauletekio ave. 3, LT-10257 Vilnius, Lithuania

<sup>2</sup> Centre for Physical Sciences and Technology, Sauletekio ave. 3, LT-10257 Vilnius, Lithuania

\* Correspondence: tomas.ceponis@ff.vu.lt; Tel.: +370-5-223-4486

Received: 4 July 2019; Accepted: 31 July 2019; Published: 1 August 2019



**Abstract:** Wide bandgap AlGa<sub>N</sub> is one of the most promising materials for the fabrication of radiation hard, double-response particle detectors for future collider facilities. However, the formation of defects during growth and fabrication of AlGa<sub>N</sub>-based devices is unavoidable. Furthermore, radiation defects are formed in detector structures during operation at extreme conditions. In this work, study of evolution of the proton-induced luminescence spectra and short-circuit current has been simultaneously performed during 1.6 MeV proton irradiation. GaN and AlGa<sub>N</sub> (with various Al concentrations) epi-layers grown by metalorganic chemical vapour deposition technique and Schottky diode structures have been examined. Variations of spectral and electrical parameters could be applied for the remote dosimetry of large hadron fluences.

**Keywords:** GaN; AlGa<sub>N</sub>; proton induced luminescence; radiation defects; dosimetry; scintillation characteristics; electrical characteristics

## 1. Introduction

The wide bandgap AlGa<sub>N</sub> with varied Al content is one of the most promising materials for fabrication of radiation hard [1,2], double-response particle detectors [3] in particle accelerator facilities. However, the formation of extended and point defects during growth and fabrication of AlGa<sub>N</sub> based devices is unavoidable. This leads to the appearance of ultraviolet (UV) photo-luminescence peaks which are shifted to the short-wavelength range with increase of Al content within this ternary material [4]. The radiation defects are formed in detector structures during operation at extreme fluence conditions which can modify optical and electrical characteristics. Modifications of these characteristics can be applied for dosimetry of high energy radiations. Discovery of the most efficient structures for fabrication of the solar-blind, high sensitivity and wide dynamic range double-response particle detectors and dosimeters is important for design of the advanced devices, capable of operating in harsh environments of high-luminosity particle accelerators.

Study of the evolution of the proton-induced luminescence spectra and diode short-circuit current during 1.6 MeV proton irradiation has been simultaneously performed in this work. GaN and AlGa<sub>N</sub> (with various Al content) epi-layers grown by metalorganic chemical vapour deposition technique have been examined. Thin epi-layers ensured the penetrative conditions for 1.6 MeV protons. To evaluate a correlation of the parameters of emission and cross-sections of the photon–electron coupling, ascribed to technological and radiation defects in the GaN/AlGa<sub>N</sub> crystals, the complementary *ex situ* measurements were performed by pulsed photo-ionization spectroscopy on several GaN/AlGa<sub>N</sub>



samples and by UV pulsed laser-induced photo-luminescence in pristine and the largest proton fluence irradiated samples.

It has been shown in this work that these combined methods of the in situ and ex situ measurements enable ones to trace evolution of the electrical and scintillation characteristics of AlGa<sub>N</sub> layers with proton fluence up to  $4 \times 10^{15} \text{ cm}^{-2}$ . Variations of spectral and electrical parameters could be applied for the remote dosimetry of large hadron fluences.

## 2. Sample Preparation

Several sets of samples were examined. The first set consists of the commercial photo-detectors GUYA-T216D-U, GUVB-T216D-U and GUV C-T206D-U (supplied by Roithner Laser Technik GmbH, Vienna, Austria), adapted for registration of different spectral range radiation. Therefore, these planar Schottky diodes were made of AlGa<sub>N</sub> materials with different Al content. For spectral measurements during irradiation, the mount of the detector was removed. The microscopy image of the commercial photo-detectors with indicated Schottky and ohmic contacts is shown in Figure 1a.

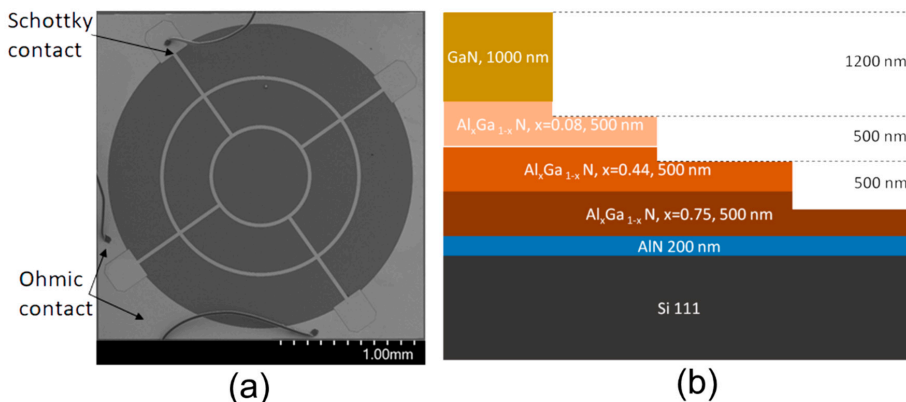


**Figure 1.** (a) The microscopy image of the commercial photo-detectors GUYA–GUV C. Schottky and ohmic contacts are indicated by arrows. (b) The diagram of the mesa structure of GaN–AlGa<sub>N</sub> layers uncovered by reactive ion etching technique.

This bare diode structure was examined by X-ray diffraction (XRD) and scanning electron microscopy (SEM) together with energy dispersed X-ray spectroscopy (EDXS) techniques. A SEM instrument Hitachi SU8230 (obtained from Hitachi High-Technologies Corporation, Tokyo, Japan) equipped with an EDX Bruker spectrometer (supplied by Bruker Nano GmbH, Berlin, Germany) was then employed. Samples were XRD characterized using a high resolution (HRXRD) Rigaku SmartLab instrument equipped with Ge(400) double monochromator and scintillation detector SC-70 (all components obtained from Rigaku, Tokyo, Japan). The XRD 2-theta spectra obtained for these GUYA–GUV C samples are illustrated in Figure 2. Sample GUYA contained only GaN layer, while GUV B and GUV C samples showed the AlGa<sub>N</sub> layers of different Al concentration. Al content has been calculated from difference in 2-theta values using Vegard’s law. Values of the percentage aluminium content of 32% and 50% were thereby determined for the GUV B and GUV C samples, respectively.

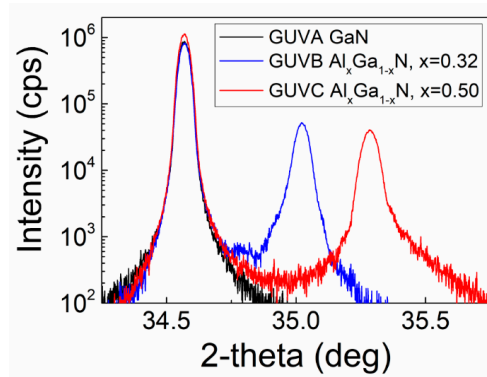


Figure 2. The XRD spectra recorded on GUYA–GUYC samples.

The elemental content determined by EDXS for these GUYA–GUYC samples is listed in Table 1.

Table 1. Elemental content in GUYA–GUYC samples determined by EDXS.

Diode	C	N	O	Al	Si	Ga
GUYA	9.08	24.39	23.04	0.15	5.53	37.10
GUYB	7.75	23.81	31.32	6.90	6.72	22.87
GUYC	6.05	19.79	33.70	11.01	8.10	20.84

It can be deduced from Table 1 that samples also contain carbon (C), oxygen (O) and silicon (Si) impurities.

The second set of samples was prepared as mesa structures made of top 1  $\mu\text{m}$  thick GaN layer and several AlGaN layers underneath grown on Si substrates (Figure 1b). The AlGaN material have a 500 nm thick epi-layers of different Al content. These definite AlGaN layers were layer-by-layer uncovered by reactive ion etching (RIE) technique. The samples were placed within a vacuumed chamber of OXFORD Instruments Plasmalab System 100 RIE equipment. The special masks were made to shield etching plasma to form dedicated mesa steps. Chlorine and argon inductively coupled plasma (ICP) was used for etching. The layer thickness and content were verified by the structure profiling and XRD means. The percentage of Al as 8%, 44% and 75% have been determined by XRD for the underneath AlGaN uncovered three mesa steps.

The latter mesa steps were covered by metal mask, impermeable for proton beam, during irradiation, successively leaving only single mesa-step uncovered to have a response only from the single layer. The 1.6 MeV irradiations were performed by a Tandetron 4110A accelerator with proton currents in the range of 20–40 nA. The GUYA–GUYC diode structures also were electrically connected to Keithley pico-ammeter for simultaneous control of the short-circuit current ( $I_{SC}$ ) induced by a proton beam.

### 3. Evolution of Scintillation and Short-Circuit Current in GaN/AlGaN Structures

#### 3.1. The Mesa Structure Samples

The fluence ( $\Phi$ )-dependent evolution of the proton-induced luminescence (PIL) spectra in different layers of the mesa structure samples with various content of aluminium is illustrated in Figure 3.

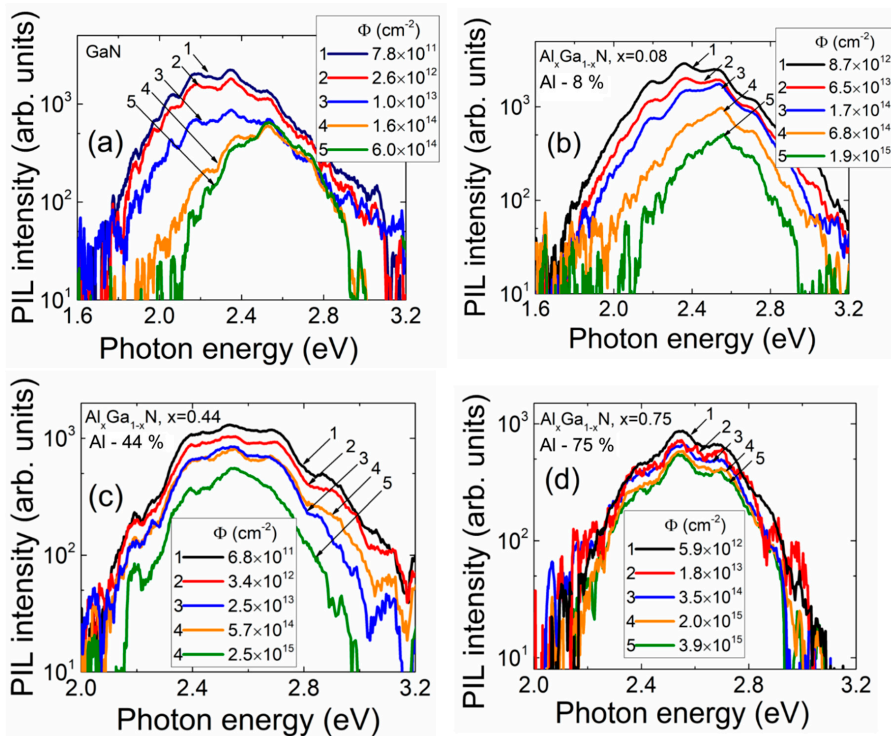


**Figure 3.** Fluence-dependent evolution of proton-induced scintillation spectra recorded on different Al content (0% (a); 8% (b); 44% (c); 75% (d)) mesa structure layers, respectively.

The main feature of this evolution in the set of mesa structure samples is a decrease of the intensity of the long-wavelength component with enhancement of proton irradiation fluence. The decrease of all the spectral components is only observed in GaN and AlGaN epi-layers with the increase of Al content and irradiation fluence (Figure 3a–d). The PIL spectra have been spread into three spectral components for quantitative evaluation of fluence-dependent changes of PIL intensity. The fluence-dependent variation of peak intensity of the separated PIL bands with irradiation fluence are presented in Figure 4 for the mesa structure samples. These dependences imply that the fluence value calibrated PIL intensity reduction can be applied for dosimetry of penetrative particle irradiation with different sensitivity attributed to various PIL spectral bands and content of Al. The steepest decrease appears for the long wavelength components; however, the dynamic range of dosimetry is the narrowest using the latter characteristics. Moreover, for the samples with the largest (75%) content of Al (Figure 3d), the PIL spectrum becomes narrow with small dynamic range of intensity variations in the spectral band peaked at 2.3–2.6 eV.

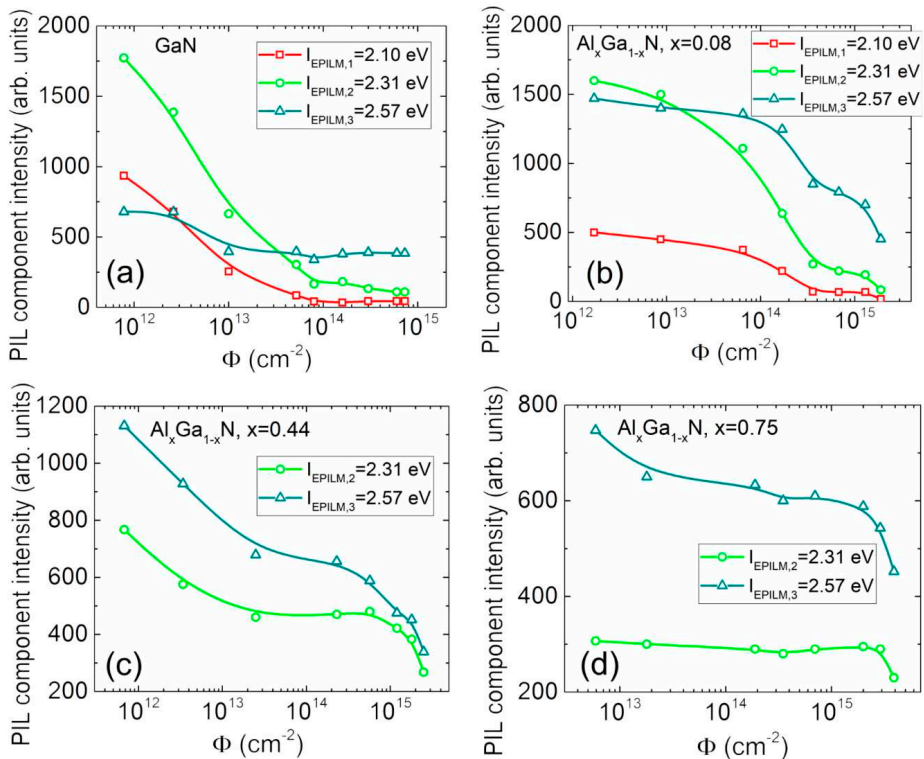


**Figure 4.** Fluence-dependent variations of the intensity of different spectral components within proton-induced luminescence (PIL) on different Al content (0% (a); 8% (b); 44% (c); 75% (d)) mesa structure layers, respectively.

To identify the origin of different PIL components, the predominant spectral components have been correlated with pulsed photo-ionization spectra (PPIS), measured on satellite mesa structures of the same material. The PPIS technique and its application for defect spectroscopy in GaN materials is described in recent our articles [5–8]. The recorded and simulated PPIS spectral steps, ascribed to the definite defects responsible for the PIL spectral components, are illustrated within inset 1 for Figure 5. Based on these PPIS components, the luminescence bands (inset 2 for Figure 5) were consequently simulated [5,6] by using the van Roosbroeck–Shockley (vRS) approach [9,10] to correlate the conversion from absorption (PPIS) to Stokes shifted emission (PIL). The latter fitted luminescence components, which peaked at 2.57 eV, 2.31 eV and 2.10 eV, were chosen to deduce an evolution of the PIL spectral components. These PIL spectral components have been ascribed to  $(\text{C}_\text{N}\text{O}_\text{N})^0$  [11] (peaked at  $\sim 3.35$  eV in PPIS and  $\sim 2.57$  in PIL),  $\text{C}_\text{N}^-$  [11] (peaked at 2.92 eV in PPIS and 2.31 eV in PIL) and  $\text{V}_\text{Ga}$  [11] (peaked at 2.57 eV [12] in PPIS and 2.10 eV in PIL) defects.

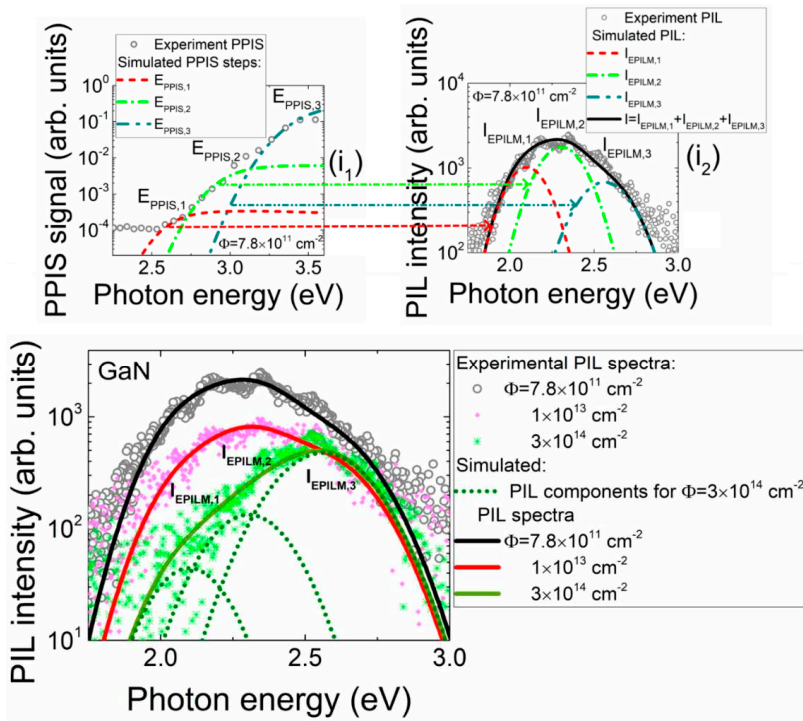


**Figure 5.** Sketch of association of defects to the predominant spectral peaks within fluence-dependent variations of the intensity of different spectral components within PIL. In the insets: the recorded and simulated PPIS steps (i1) and PIL spectral components obtained through simulations of conversion from absorption to emission (i2) made for respective PPIS steps.

The fluence-dependent PIL evolution has been consequently fitted by varying the amplitude only of the chosen (deduced from PPIS and vRS PL analysis as sketched in the insets 1 and 2 for Figure 5) luminescence peaks. The fits of this fluence-dependent PIL evolution are sketched in Figure 5. The fluence-dependent variations of the intensity of different spectral components within PIL were thereby composed from the fits illustrated in Figure 5. The evolution of the intensity of these PIL spectral components can be explained by varied initial filling of the predominant defects due to irradiation. The filling level of various traps is modified by non-radiative recombination centres introduced by proton irradiation.

### 3.2. Schottky Diode Structures

Evolution of PIL spectra recorded on the set of GUV diodes during proton irradiation is illustrated in Figure 6a–c. The general feature of spectra variations is a decrease of intensity of the long wavelength PIL band with further enhancement of the short wavelength band under increase of proton irradiation fluence. However, the rate of fluence-dependent intensity variations is specific for diodes made of different Al content containing materials. The long wavelength band split can be hinted for GaN and  $\text{Al}_{0.32}\text{Ga}_{0.68}\text{N}$  material diodes.

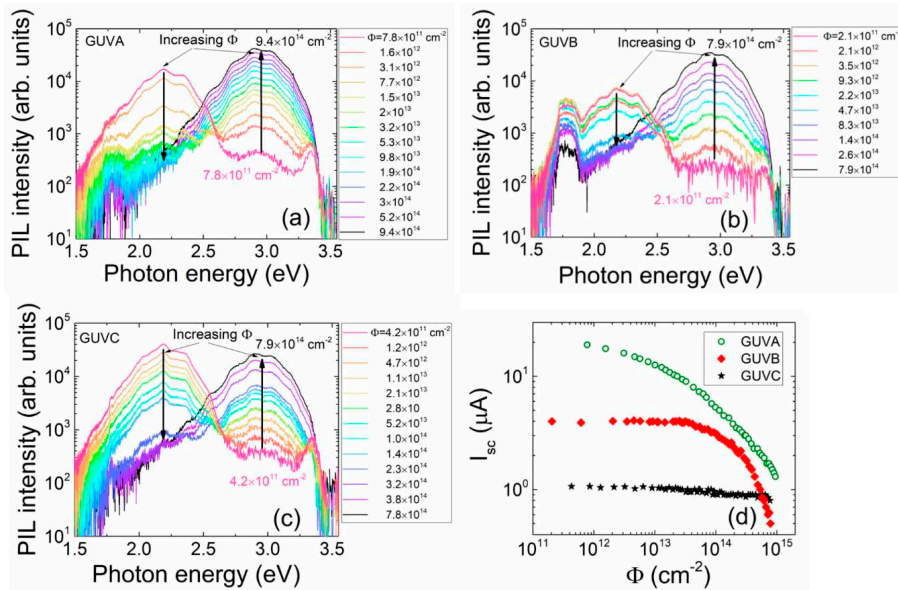


**Figure 6.** Fluence-dependent evolution of proton-induced scintillation spectra recorded on different Al content (0% (a); 32% (b); 50% (c)) containing diodes GUA–GUV, respectively. (d) Evolution of SC current in different GUA–GUV diodes.

The fluence-dependent short-circuit current ( $I_{sc}$ ) variations (Figure 6d), measured simultaneously with PIL spectra, differ significantly for diodes made of different Al content materials. The largest  $I_{sc}$  values have been observed for pure GaN material (GUA) diodes. Consequently, the dynamic range of  $I_{sc}$  variations is the widest using these GUA diodes. Thereby, sensitivity to fluence changes is also the highest for the GUA diodes. An increase of bandgap with Al content leads to reduction of the  $I_{sc}$  current. Therefore, a recordable change of  $I_{sc}$  as a function of fluence is obtained in 32% Al containing material only for the moderate fluences of  $\Phi > 3 \times 10^{13}$  p/cm<sup>2</sup>. Even the less values and changes of  $I_{sc}$  (for  $\Phi > 10^{14}$  p/cm<sup>2</sup>) were obtained in diodes (GUV) of 50% Al content (Figure 6d).

As can be deduced from Figure 6, the spectral and intensity variations of PIL provide the more reliable characteristics in dosimetry detection.

It appeared that the PIL spectra should be spread into five spectral components for GUV diode structures to quantitatively reproduce the fluence-dependent changes of PIL spectrum and intensity. The Gaussian approximation of the spectral component shape  $S(h\nu, \sigma) = A_f \exp[-(h\nu - E_f)^2/\sigma^2]$  with  $A_f$  as the peak intensity of the  $f$ -th component with peak energy  $E_f$  and  $\sigma$  the band width has been accepted in fitting of PIL spectra. A sketch of the deconvolution of the predominant spectral peaks and the fluence-dependent evolution of the intensity of different spectral components within PIL in the diode GUA is presented in Figure 7. There, symbols denote the experimental data, thick solid lines represent a total (sum) of intensities of the separate components shown by thin dotted lines, simulated for spectrum obtained at fixed irradiation fluence. In simulations of the total PIL intensity as a function of the photon energy  $h\nu$ , only the peak intensity  $A_f$  of definite spectral components was modified as a free variable. In addition to PIL spectral bands peaked at 2.10 eV, 2.31 eV as well as 2.57 eV in mesa structures, the PIL peaks at 1.8 eV, 2.52 eV, 2.95 eV and 3.35 eV appear in GUV diodes. This implies that point defect structure slightly differs for mesa and diode samples. The 2.52 eV and 2.95 eV peak intensities increase with fluence indicating the main difference of AlGaN structures grown on Si and commercially manufactured materials. It seems that RIE etching does not produce additional defects, as GUV diodes PIL spectra are richer than that of mesa structures.



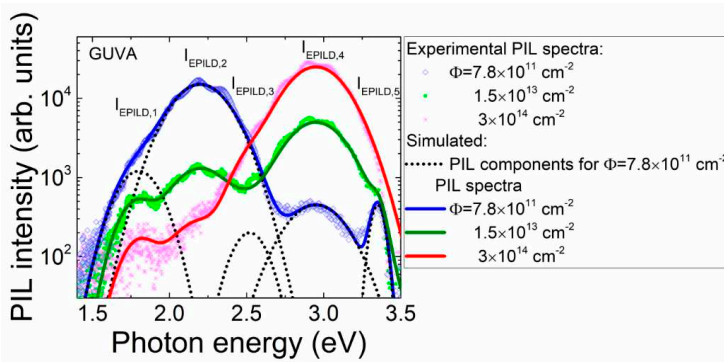


**Figure 7.** Sketch of deconvolution of the predominant spectral peaks and the fluence-dependent evolution of the intensity of different spectral components within PIL in the GUVa diode.

The fluence-dependent peak intensities, extracted from simulations performed according to the method sketched in Figure 7, and attributed to different spectral components, are plotted in Figure 8. It can be deduced from Figure 8 that the largest intensities and the widest dynamic range are obtained for the  $E_{PILD,2}$  and  $E_{PILD,4}$  spectral components in all the examined diodes. Thereby, these components can be employed for dosimetry based on PIL spectral variations, as the largest intensity determines the highest sensitivity and reliability of spectrum recording.

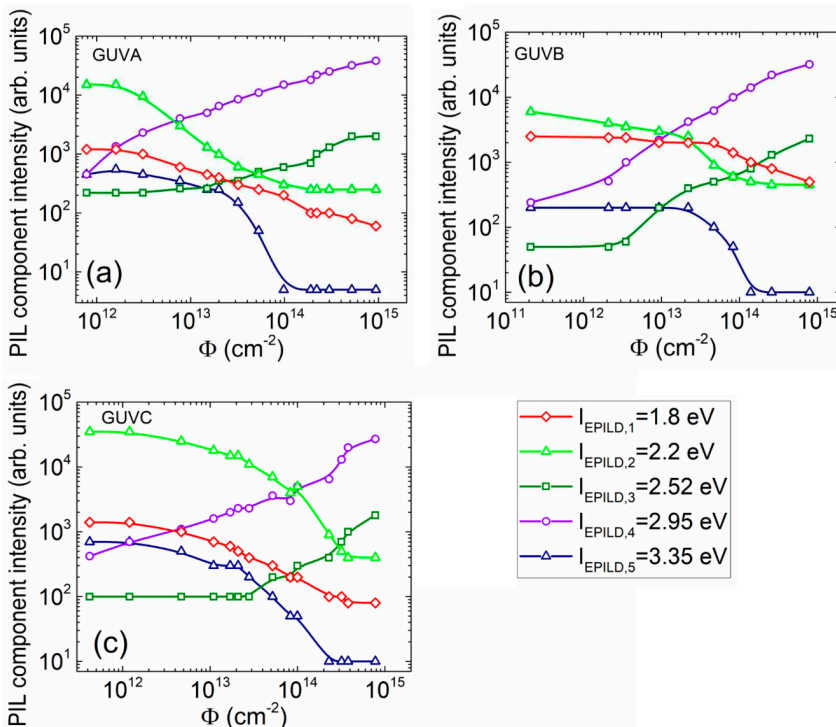


**Figure 8.** Fluence-dependent variations of the intensity of different spectral components within PIL obtained for different Al content (0% (a); 32% (b); 50 % (c)) GUV diodes, respectively.

The spectral components have been tentatively associated with defects in ternary AlGa<sub>x</sub>N materials identified in literature referenced. These components are listed in Table 2. The peak energy values ascribed to definite spectral components (inherent for the full range of Al content ( $x$ ) possible changes) are there denoted and ascribed to the specific defects in Table 2.

**Table 2.** Association of the luminescence spectral peaks to different point defects in GaN-AlGa<sub>x</sub>N materials according to literature data.

Al <sub>x</sub> Ga <sub>1-x</sub> N		
PIL Peak Quantum Energy (eV)	Defect Type	Reference
$E_{\text{PILD},1} = 1.27$ for $x = 0$ ; $1.89$ for $x = 1$ ; $1.8$ for $x = 0$ ; $1.9$ for $x = 0$	$(V_{\text{III}}\text{-O}_N)^{2-1-}$ ; $V_{\text{Ga}}$ related complex; shallow donor and a deep acceptor pair	[13] [14] [15]
$E_{\text{PILD},2} = 2.15$ for $x = 0$ ; $3.9$ for $x = 1$	$V_{\text{Ga}}$ or $V_{\text{Ga}}$ related complex	[16]
$E_{\text{PILD},3} = 2.20$ for $x = 0$ ; $3.9$ for $x \sim 1$	$V_{\text{Ga}}\text{-O}_N$ ; shallow donor and a deep acceptor pair; $V_{\text{III}}\text{-O}_N$	[17,18] [19] [13]
$E_{\text{PILD},4} = 2.80$ for $x = 0$ ; $3.0$	$V_{\text{III}}\text{-O}_N$ related	[20]
$E_{\text{PILD},5} = 2.80$ for $x = 0$ ; $3.17$	$V_{\text{III}}$ related	[21]

Thereby, the Ga vacancies or DAP centres and V-O complexes prevail in both sets of AlGa<sub>x</sub>N sample sets, keeping in mind the blue-shift of PIL peak position with enhancement of  $x$  ascribed to definite defects.

#### 4. Discussion

The stability of the fluence-dependent modifications of the spectral and electrical characteristics has been verified by comparing the UV pulsed laser-excited photo-luminescence (PL) spectra and electrical signals measured ex situ before and after proton irradiations. The coincidence of spectrum structures and  $I_{\text{SC}}$  values have been obtained. Also, the concentration of the proton generated secondary electron-hole pairs have been estimated by comparing the intensity of spectral PL components and  $I_{\text{SC}}$ . These measurements are inevitable in calibration of the double-response dosimeters.

It can be deduced from Figures 4, 6d and 8 that the most acceptable structures in design of the double-response dosimeters are GaN/Al<sub>0.08</sub>Ga<sub>0.92</sub>N structures. Concerning the aspect of linearity of the PIL dose-dependent characteristic, control of the PIL spectral component  $E_{\text{PILD},4}$  peaked at 2.95 eV would be preferable (Figure 8). The AlGa<sub>x</sub>N epi-layers of enhanced thickness  $\geq 1$   $\mu\text{m}$  (when comparing GUV diodes and mesa structures) are preferable to have the relevant interaction depth for the penetrative particle irradiations. To simultaneously record the most reliable optical and electrical responses, the Ga vacancy and oxygen-rich AlGa<sub>x</sub>N materials with small content of Al and doped with carbon would be desirable in fabrication of the solar-blind and wide dynamic range dosimeters. The point defects prevail in formation and dose-dependent modification of PIL spectra regardless of high density of dislocations, inherent for the MOCVD-grown AlGa<sub>x</sub>N materials. The junction structures are preferable to get the electrical signals. The different type electrical signals as  $I_{\text{SC}}$ , barrier capacitance [3], etc. can then be employed for the in situ control of the particle beam induced changes of recorded characteristics.

The AlGa<sub>x</sub>N structures can be applied for the remote sensing of particle beams and of accumulated their fluences. The solar-blind and small leakage current AlGa<sub>x</sub>N detectors are insensitive to the visible (VIS)-near infrared (NIR) spectrum background emissions and thereby preferable in comparison with Si-based sensors. A tentative scheme (employed in this work) for remote dosimetry of particle beams is sketched in Figure 9, which allows to perform measurements in vacuum chamber and harsh environment of irradiations. The vacuum-proof electrical and fiber connections have been



there exploited for output of the electrical and PIL signals. The multi-string UV clear (up to 240 nm) fiberscopes (BF20HSMA01—Round Fiber Bundle, V2H6S—Fiber Feedthrough as well as M93L02—Fiber Patch Cable (supplied by Thorlabs, Inc., Newton, New Jersey, United States)) and an AvaSpec-2048L spectrophotometer (obtained from Avantes BV, Apeldoorn, Netherlands) were employed to transfer and record the PIL signals. The  $I_{SC}$  current was measured by using a Keithley pico-ammeter. Collection and primary processing of the  $I_{SC}$  and PIL signals as well as proton beam current were performed by personal computer (PC). Control of regimes of the measurement devices and data display was implemented via LAN connection on the remote PC.

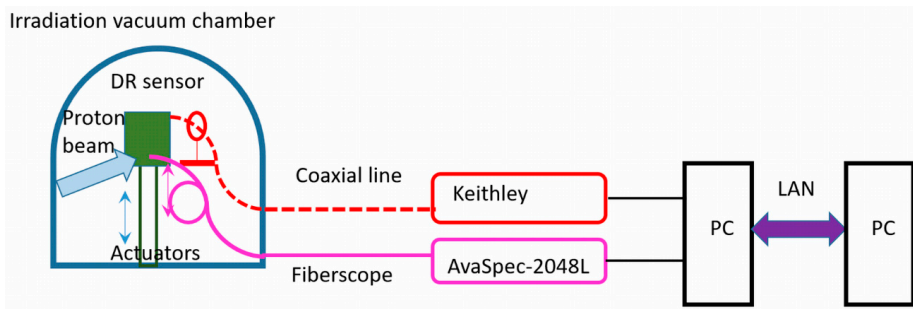


**Figure 9.** A scheme of remote dosimetry using double-response (DR) AlGaIn sensor.

## 5. Summary

The AlGaIn structures of different Al content have been examined in order to fabricate the efficient double-response particle sensors and dosimeters. The double-response sensors are preferable when it is important to simultaneously control the instantaneous particle flux and the accumulated fluence at the fixed location of the sensor or to increase sensitivity and reliability of the dosimeter in the range of large fluences. It has been shown that the most acceptable structures in design of the double-response dosimeters are GaN/Al<sub>0.08</sub>Ga<sub>0.92</sub>N structures. The linearity of the PIL dose-dependent characteristic can be achieved for the PIL spectral component peaked at 2.95 eV. The defects prevailing in modifications of PIL spectra have been tentatively identified. The point defects are predominant in formation and dose-dependent modification of PIL spectra regardless of the high density of dislocations inherent for the MOCVD-grown AlGaIn materials. The Ga vacancy and oxygen-rich AlGaIn materials with small content of Al and doped with carbon would be desirable in the fabrication of wide dynamic range dosimeters. The junction structures are preferable to record the different types of electrical signals. A possible scheme for remote dosimetry of particle beams has been approved in this work for measurements in a vacuum chamber and harsh environment of irradiations.

**Author Contributions:** E.G. conceived the main ideas, made the main interpretations of results and wrote the main text. T.C. performed the main experiments, wrote and edited the main text. K.B. performed RIE etching in preparation of mesa structures. L.D. performed initial experiments and prepared initial illustrations. J.P. planned experiments, made analysis of results, wrote preliminary text. V.R. prepared samples and technical instruments for experiments, analyzed results and prepared preliminary illustrations. V.K. managed accelerator and irradiation regimes. S.S. performed XRD measurements and analysis. G.T. supervised research and article writing.

**Funding:** This research is funded by the European Social Fund under the No 09.3.3- LMT-K-712 -02-0012 “Development of Competences of Scientists, other Researchers and Students through Practical Research Activities” measure.

**Conflicts of Interest:** The authors declare no conflict of interest.

## References

1. Sellin, P.J.; Vaitkus, J. New materials for radiation hard semiconductor detectors. *Nucl. Instrum. Methods A* **2006**, *557*, 479–489. [[CrossRef](#)]
2. Moll, M. Radiation tolerant semiconductor sensors for tracking detectors. *Nucl. Instrum. Methods A* **2006**, *565*, 202–211. [[CrossRef](#)]
3. Gaubas, E.; Ceponis, T.; Meskauskas, D.; Pavlov, J.; Zukauskas, A.; Kovalevskij, V.; Remeikis, V. In situ characterization of radiation sensors based on GaN LED structure by pulsed capacitance technique and luminescence spectroscopy. *Sens. Actuators A Phys.* **2017**, *267*, 194–199. [[CrossRef](#)]
4. Podlipskas, Z.; Aleksiejunas, R.; Kadys, A.; Mickevicius, J.; Jurkevicius, J.; Tamulaitis, G.; Shur, M.; Jang, J.; Gaska, R. Dependence of radiative and nonradiative recombination on carrier density and Al content in thick AlGaIn epilayers. *J. Phys. D Appl. Phys.* **2016**, *49*, 145110. [[CrossRef](#)]
5. Gaubas, E.; Ceponis, T.; Deveikis, L.; Dobrovolskas, D.; Rumbauskas, V.; Viliunas, M. Room-temperature infrared photoluminescence in GaN doped with various impurities. *Opt. Mater.* **2019**, *94*, 266–271. [[CrossRef](#)]
6. Gaubas, E.; Ceponis, T.; Mickevicius, J.; Pavlov, J.; Rumbauskas, V.; Velicka, M.; Simoen, E.; Zhao, M. Pulsed photo-ionization spectroscopy in carbon doped MOCVD GaN epi-layers on Si. *Semicond. Sci. Technol.* **2018**, *33*, 075015. [[CrossRef](#)]
7. Gaubas, E.; Ceponis, T.; Meskauskaitė, D.; Mickevicius, J.; Pavlov, J.; Rumbauskas, V.; Grigonis, R.; Zajac, M.; Kucharski, R. Pulsed photo-ionization spectroscopy of traps in as-grown and neutron irradiated ammonothermally synthesized GaN. *Sci. Rep.* **2019**, *9*, 1473. [[CrossRef](#)] [[PubMed](#)]
8. Gaubas, E.; Baronas, P.; Ceponis, T.; Deveikis, L.; Dobrovolskas, D.; Kuokstis, E.; Mickevicius, J.; Rumbauskas, V.; Bockowski, M.; Iwinska, M.; et al. Study of spectral and recombination characteristics of HVPE GaN grown on ammono substrates. *Mater. Sci. Semicond. Process.* **2019**, *91*, 341–355. [[CrossRef](#)]
9. Pankove, J.I. *Optical Processes in Semiconductors*; Prentice Hall: Englewood Cliffs, NJ, USA, 1971.
10. Bhattacharya, R.; Pal, B.; Bansal, B. On conversion of luminescence into absorption and the van Roosbroeck-Shockley relation. *Appl. Phys. Lett.* **2012**, *100*, 222103. [[CrossRef](#)]
11. Reshchikov, M.A.; Demchenko, D.O.; Usikov, A.; Helava, H.; Makarov, Y. Carbon defects as sources of the green and yellow luminescence bands in undoped GaN. *Phys. Rev. B* **2014**, *90*, 235203. [[CrossRef](#)]
12. Zhang, Z.; Humn, C.A.; Arehart, A.R.; Yang, J.; Myers, R.C.; Speck, J.S.; Ringel, S.A. Deep traps in nonpolar m-plane GaN grown by ammonia-based molecular beam epitaxy. *Appl. Phys. Lett.* **2012**, *100*, 52114. [[CrossRef](#)]
13. Sedhain, A.; Lin, J.Y.; Jiang, H.X. Nature of optical transitions involving cation vacancies and complexes in AlN and AlGaIn. *Appl. Phys. Lett.* **2012**, *100*, 221107. [[CrossRef](#)]
14. Reshchikov, M.A.; Morkoc, H. Luminescence properties of defects in GaN. *J. Appl. Phys.* **2005**, *97*, 061301. [[CrossRef](#)]
15. Goldys, E.M.; Godlewski, M.; Langer, R.; Barski, A.; Bergman, P.; Monemar, B. Analysis of the red optical emission in cubic GaN grown by molecular-beam epitaxy. *Phys. Rev. B* **1999**, *60*, 5464. [[CrossRef](#)]
16. Nam, K.B.; Nakarmi, M.L.; Lin, J.Y.; Jiang, H.X. Deep impurity transitions involving cation vacancies and complexes in AlGaIn alloys. *Appl. Phys. Lett.* **2005**, *86*, 222108. [[CrossRef](#)]
17. Lee, I.H.; Polyakov, A.Y.; Smirnov, N.B.; Govorkov, A.V.; Usikov, A.S.; Helava, H.; Makarov, Y.N.; Pearton, S.J. Deep hole traps in undoped n-GaN films grown by hydride vapor phase epitaxy. *J. Appl. Phys.* **2014**, *115*, 223702. [[CrossRef](#)]
18. Reshchikov, M.A. Point Defects in GaN. In *Semiconductors and Semimetals: Defects in Semiconductors*; Jagadish, C., Privitera, V., Romano, L., Eds.; Academic Press: Burlington, UK, 2015.
19. Polyakov, A.Y.; Smirnov, N.B.; Govorkov, A.V.; Redwing, J.M. Deep traps in high resistivity AlGaIn films. *Solid State Electron.* **1998**, *46*, 831–838. [[CrossRef](#)]

20. Nepal, N.; Nakarmi, M.L.; Lin, J.Y.; Jiang, H.X. Photoluminescence studies of impurity transitions in AlGaIn alloys. *Appl. Phys. Lett.* **2006**, *89*, 092107. [[CrossRef](#)]
21. Henry, T.A.; Armstrong, A.; Allerman, A.A.; Crawford, M.H. The influence of Al composition on point defect incorporation in AlGaIn. *Appl. Phys. Lett.* **2012**, *100*, 043509. [[CrossRef](#)]



© 2019 by the authors. Licensee MDPI, Basel, Switzerland. This article is an open access article distributed under the terms and conditions of the Creative Commons Attribution (CC BY) license (<http://creativecommons.org/licenses/by/4.0/>).

A6

Modification of characteristics of AlGaN  
photodiodes by 1.6 MeV proton  
irradiation

J. Pavlov, T. Čeponis, **L. Deveikis**, V. Rumbauskas, G. Tamulaitis, E.  
Gaubas

JINST **15** (2020) C01026.

DOI:10.1088/1748-0221/15/01/C01026

(Accepted manuscript reprinted with permission from IOP Publishing,  
Ltd and Sissa Medialab)

# Modification of characteristics of AlGaN photodiodes by 1.6 MeV proton irradiation

---

**J. Pavlov,\* T. Ceponis, L. Deveikis, V. Rumbauskas, G. Tamulaitis, and E. Gaubas**

*Institute of Photonics and Nanotechnology, Vilnius University,  
Sauletekio Ave. 3, LT-10257 Vilnius, Lithuania*

*\*E-mail: jevgenij.pavlov@tmi.vu.lt*

ABSTRACT: The wide direct-bandgap AlGaN is one of the most promising materials for fabrication of radiation hard, double response particle detectors for future collider facilities. However, formation of defects is unavoidable during growth and fabrication of AlGaN based devices. Furthermore, radiation defects are formed in detector structures during operation at extreme conditions. In this work, the study of electrical and optical characteristics after 1.6 MeV proton irradiation has been performed. Commercial photodiodes of GaN and AlGaN (with various Al concentrations) fabricated using epi-layers grown by metalorganic chemical vapor deposition technique on sapphire substrate have been examined. Electrical characteristics of the devices have been examined by combining pulsed technique of barrier evaluation by linearly increasing voltage, steady-state photo-ionization and deep level transient spectroscopy.

KEYWORDS: AlGaN detectors; Photo-diodes; Detection of defects; Radiation-hard detectors.

---

\* Corresponding author.

---

## Contents

<b>1. Introduction</b>	<b>1</b>
<b>2. Samples</b>	<b>2</b>
<b>3. Electrical and spectral parameters extracted by combining different techniques</b>	<b>2</b>
3.1. Carrier lifetime variations	2
3.2. DLT spectrum of carrier emission centres	3
3.3. Spectrum of photo-active centres	4
3.4. Impact of defects on electrical characteristics of detectors	5
<b>4. Summary</b>	<b>7</b>

---

## 1. Introduction

GaN and its AlGa<sub>N</sub> alloys are promising materials for modern and future electronic devices applied in medicine, telecommunication and radiation monitoring equipment [1-3]. Exceptional feature of the detectors made of these materials would be capability to generate double responses (electrical and optical). Moreover, AlGa<sub>N</sub> materials show high efficiency of luminescence and enhanced tolerance to radiation damage [2]. The important requirements in fabrication of particle detectors for high energy physics (HEP) experiments are the rather small amount of point as well as extended defects and the homogeneity of the crystals. However, the rather high density of technological defects is inherent even for advanced technology (such as ammonothermal and lateral-overgrowth [4, 5]) growth of GaN/AlGa<sub>N</sub> materials, limiting electro-optical characteristics of the formed devices [6]. Thereby, the spectroscopy of technological as well as radiation defects in GaN/AlGa<sub>N</sub> materials and the study of their impact on the electro-optical characteristics of devices is important to predict and modify the detector characteristics.

In this work, a comparative analysis of the electrical and optical characteristics in pristine and 1.6 MeV proton irradiated samples of Al<sub>x</sub>Ga<sub>1-x</sub>N photo-diodes varying content of Al in the range from  $x = 0$  to  $x = 0.5$  has been performed. The steady-state photo-ionization (SS-PIS) and deep level transient spectroscopy (DLTS) techniques [7] were combined to reveal spectra of deep traps. The I-V and barrier evaluation by linearly increasing voltage (BELIV) techniques have been applied for measurements of device electrical characteristics before and after proton irradiation. Carrier lifetime variations were examined by using microwave-probed [8] photo-conductivity (MW-PC) transients. A reduction of carrier lifetime and increase of leakage current as well as of resistance of the electrically neutral region (ENR) served as a measure of radiation hardness of Al<sub>x</sub>Ga<sub>1-x</sub>N materials. Three carrier emission centres have been resolved from DLT spectra. The light absorption associated traps of the photo-activation energy of  $E_{PIS1} = 0.55$  eV,  $E_{PIS2} = 1.35$  eV and  $E_{PIS3} = 1.6$  eV have been revealed by fitting the SS-PIS spectral steps using Kopylov-Pikhtin model. Carrier mobility parameters have been evaluated from analysis of bias illumination intensity dependent changes of ENR resistance and delay of BELIV transient peaks.

## 2. Samples

The commercial UV photodiodes fabricated using GaN (GUVA-T21GD-U),  $\text{Al}_{0.32}\text{Ga}_{0.68}\text{N}$  (GUVB-T21GD-U) and  $\text{Al}_{0.5}\text{Ga}_{0.5}\text{N}$  (GUVC-T20GD-U) were acquired from Roithner Laser Technik GmbH. The input window was removed from commercial photo-diodes for direct interaction of proton beam with diode material during *in situ* detection of 1.6 MeV proton flux. The detectors contained planar contacts. The content of Al within  $\text{Al}_x\text{Ga}_{1-x}\text{N}$  alloys has been determined [6] by using energy dispersed X-ray spectroscopy (EDXS) and X-ray diffraction (XRD) techniques. The electrical and optical characteristics were measured *ex situ* in the pristine and  $10^{15}$  p/cm<sup>2</sup> fluence irradiated samples. The irradiation with 1.6 MeV penetrating protons were performed by using Tandetron-4110 particle accelerator.

## 3. Electrical and spectral parameters extracted by combining different techniques

### 3.1. Carrier lifetime variations

Carrier lifetime is the most important parameter which determines the charge collection efficiency of the radiation detectors. Reduction of carrier lifetime with irradiation dose is a factor which indicates radiation damage due to induced radiation defects. On the other hand, the carrier lifetime also limits the speed of detector response when fast detectors are desirable. Moreover, the carrier lifetime parameter is inevitable in evaluating the excess carrier density within bias illumination experiments of pulsed photo-capacitance.

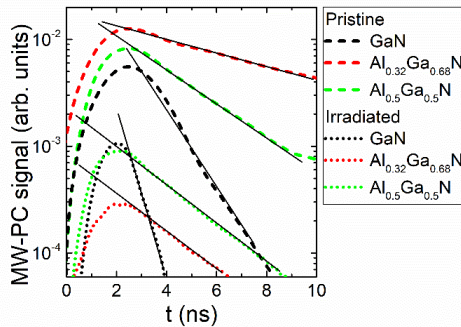


**Figure 1.** The initial stage of the MW-PC relaxation in diodes made of AlGaIn materials with different Al content before (dash curves) and after (dot curves) 1.6 MeV proton irradiation with a fluence of  $10^{15}$  p/cm<sup>2</sup>.

In this work, the carrier lifetime was extracted from transients of the microwave-probed photoconductivity [8]. The photo-conductivity transients were excited by 400 ps ultra-violet (UV, 354 nm) laser pulses. The excited area of the sample was probed by 22 GHz MW's using needle-tip coaxial antenna [8]. The transients were registered by a TDS-5104 oscilloscope using 50  $\Omega$  load resistor. Carrier lifetime was measured within the initial MW-PC decay stage (figure 1) at  $\exp(-1)$  level (for  $t=\tau$ , as  $\tau=n/(-\partial n/\partial t)$ ) relative a peak value of the MW-PC transient. Most transients were two-componential with a long asymptotic decay component, which is related to carrier random-walk within dislocation nets. This asymptotic decay component fits well a stretched-exponential relaxation [8]. However, this decay component is less sensitive to radiation damage [9], thus, analysis of this relaxation stage is omitted from further consideration.

The recombination lifetime values for different Al content samples before and after proton irradiation are listed in Table 1.

Table 1. Carrier lifetime in AlGaN materials of different Al content.

Material	GaN		Al <sub>0.32</sub> Ga <sub>68</sub> N		Al <sub>0.5</sub> Ga <sub>0.5</sub> N	
Sample	pristine	irradiated	pristine	irradiated	pristine	irradiated
$\tau_R$ (ns)	1.3	0.6	8	2.6	3	2.7

Values of carrier recombination lifetimes ( $\tau_R$ ) within a few ns scale imply a high density of native defects in the pristine samples. It can be inferred from Table 1 that the shortest carrier recombination lifetime was obtained for pure GaN material. A clear decrease of recombination lifetime has been determined in all the diodes after proton irradiation. This recombination lifetime reduction (more than twice in samples of rather low Al content) indicates an efficient introduction of radiation defects. On the other hand, the observed  $\tau_R$  decrease being less than an order of magnitude, testifies the rather good radiation-hardness of AlGaN materials.

### 3.2. DLTS spectrum of carrier emission centres

The large-resistivity of the examined samples required DLTS measurements in current (I-DLTS) regime. The I-DLTS spectra were recorded by using a commercial HERA-DLTS 1030 equipment in 30-475 K temperature range with parameters of the reverse biasing voltage of 5 V and 1 s duration injection pulses of 0.1 V amplitude.

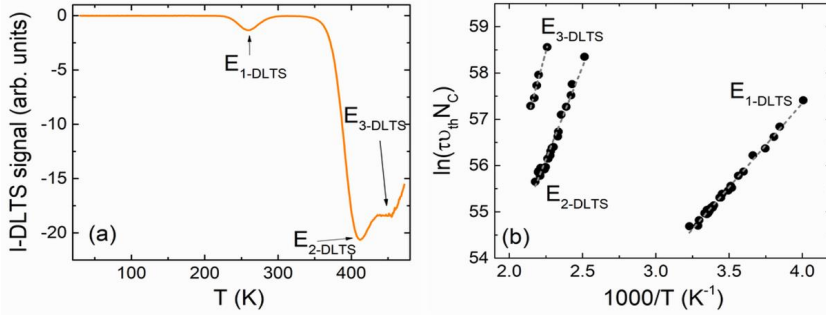


Figure 2. (a)- A typical I-DLT spectrum recorded in the proton irradiated AlGaN materials. (b)- Arrhenius plots ascribed to different I-DLTS peaks.

No peaks were found in the I-DLT spectra recorded on pristine diodes. Nevertheless, three I-DLTS spectral peaks were resolved in the devices irradiated by 1.6 MeV protons. The inherent I-DLT spectrum is illustrated in figure 2a. The activation energy of traps has been evaluated by using Arrhenius plots (figure 2b). The origin of the traps was tentatively identified by using activation energy values published in literature. The trap with activation energy of 0.316 eV (E<sub>1-DLTS</sub>) is associated with a complex of nitrogen and gallium vacancies ( $V_N-V_{Ga}$ ) [10,11], 0.792 eV (E<sub>2-DLTS</sub>) is the carbon-related (C-related) defect [12] and 1 eV (E<sub>3-DLTS</sub>) is associated with the nitrogen interstitials ( $N_i$ ) [12]. The latter peak may also be related to dislocation defects [13,14]. Appearance of the E<sub>1-DLTS</sub> and E<sub>3-DLTS</sub> I-DLTS peaks can be explained by efficient introduction of vacancy and interstitial type radiation defects. Highlighting of carbon associated traps under irradiation indicates the presence of carbon impurities in the pristine material where proton irradiation converts these impurities into emission-activate centres.

### 3.3. Spectrum of photo-active centres

The photo-active centres prevailing in carrier excitation processes were examined by using steady-state photo-ionisation spectroscopy (SS-PIS). The photon energy ( $h\nu$ ) varied photo-



excitation was implemented by using photometric 800W lamp which light was dispersed through a double-way monochromator DMR4. The photo-current induced by different excitation wavelengths was measured using a Keithley 6430 source-meter. The sample was mounted in the cryostat and cooled to liquid nitrogen temperature to diminish the impact of phonons and leakage current. The SS-PI spectrum was recorded starting from the long wavelength spectral wing to avoid the background filling of centres.

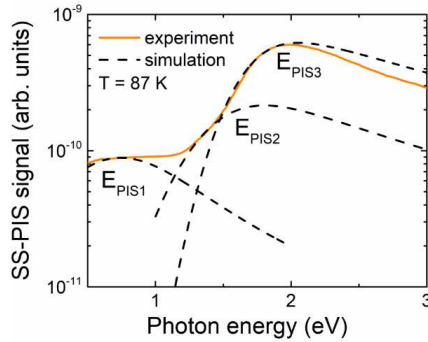


**Figure 3.** A typical SS-PI spectrum recorded in the proton irradiated AlGaIn materials.

The SS-PI spectrum comprises a step-like structure (figure 3) where each photo-ionization step is attributed to a particular photo-active centre. The step-like structure is caused by the spectrally ( $h\nu$ ) varied photo-ionization cross-section  $\sigma_{p-e}(h\nu)$ . The shape and spectral position of each SS-PI step can be approximated by the Kopylov-Pikhtin model [15]:

$$\sigma_{p-e} \propto \int_0^{\infty} \frac{\exp[-(E+E_{dl}-h\nu)^2/\Gamma^2] \sqrt{E} dE}{h\nu(E+E_{dl})^2}, \quad (1)$$

where  $E_{dl}$  is the photo-activation energy of a definite center and the electron-phonon coupling is defined by the broadening factor  $\Gamma$ . In the depleted detector, the photo-generated excess carriers of density  $n^*(h\nu)$  induce a photo-current  $i(h\nu) = q_e n^*(h\nu) S \mu U_R / d$ , where  $q_e$  is the elementary charge,  $S$  is the junction area,  $d$  is the base thickness,  $\mu$  is the carrier mobility and  $U_R$  is the reverse bias.

No spectral peaks were revealed in the pristine material diodes. Three SS-PI spectral steps were resolved in the sample irradiated by 1.6 MeV protons. These spectral steps have been fitted (figure 3) by using the Kopylov-Pikhtin model (equation 1). The photo-activation energy values of traps were extracted from these fits (figure 3). The origin of photo-ionization centres was tentatively identified on the basis of photo-activation energy values referenced in literature. Thereby, the trap with photo-activation energy of 0.55 eV ( $E_{PIS1}$ ) has been ascribed to gallium vacancy ( $V_{Ga}$ ) [16], the trap  $E_{PIS2}$  with photo-activation energy of 1.35 eV has been associated with anti-site defect ( $N_{Ga}$ ) [16] and the photo-ionization centre  $E_{PIS3}$  with photo-activation energy of 1.6 eV has been related to a complex of gallium and oxygen vacancies ( $V_{Ga}-V_O$ ) [17]. Such an identification of photo-ionization centres is in qualitative agreement with probable introduction of excess vacancy prevailed radiation defects.

### 3.4. Impact of defects on electrical characteristics of detectors

Electrical characteristics of the pristine and irradiated material detectors have been examined by measurements of dc current-voltage (I-V) reverse as well as forward biasing branches and pulsed capacitance transients. I-V characteristics were measured by using a Keithley 6430 electrometer. Reverse voltage was changed up to 5 V in reverse bias mode.

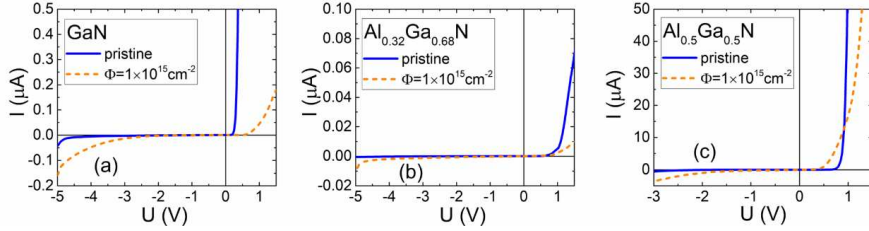


**Figure 4.** I-V characteristics measured in dark on GaN (a),  $\text{Al}_{0.32}\text{Ga}_{0.68}\text{N}$  (b) and  $\text{Al}_{0.5}\text{Ga}_{0.5}\text{N}$  (c) photo-detectors before and after proton irradiation.

The I-V characteristics obtained for the AlGaN photo-diodes of different Al content before and after proton irradiation are illustrated in figure 4. The  $\text{Al}_{0.32}\text{Ga}_{0.68}\text{N}$  material diodes appeared to be the most resistive sample (figure 4b). This can be related to the good quality of the crystal. The leakage current increases and the built-in barrier  $U_{bi}$  decreases after irradiation by protons in all the examined diodes due to occurrence of radiation defects.

The pulsed capacitance characteristics were examined by using a technique of barrier evaluation by linearly increasing voltage (BELIV) [19]. This technique is implemented by recording of the barrier charging transients. The BELIV circuitry contains an adjusted output of a generator of linearly increasing voltage (GLIV). A junction structure under test and a load resistor are connected in series with GLIV. The barrier capacitance charging current transients within load resistor have been recorded by a DSO6102A oscilloscope using  $50\ \Omega$  load input. The BELIV transients were recorded both in dark and under steady-state illumination of varied intensity. The bias illumination was performed by using a 380 nm wavelength light emitting diode (LED), and illumination intensity was varied by employing neutral optical filters. The illumination light energy density was calibrated using energy meter and beam cross-sectional width. To separate different current components, the BELIV transients were examined by using different GLIV pulse durations in the range from Hz to MHz.

The evolution of the BELIV transients measured varying illumination intensity and rather short (450 ns) GLIV pulses is illustrated in figure 5.

The BELIV technique for a reverse biased diode is based on the analysis of the changes in the barrier capacitance ( $C_b$ ) with linearly increasing voltage  $U_p(t) = At$  pulse with  $A = U_P/\tau_{PL}$  the ramp of GLIV pulse of the  $U_P$  peak amplitude and  $\tau_{PL}$  duration. The barrier capacitance of the diode under test (DUT) can be expressed as  $C_b = C_{b0}(1 + U/U_{bi})^{-1/2}$ , with  $C_{b0}$  barrier capacitance for a non-biased diode of an area  $S$  and  $U_{bi}$  built-in potential barrier. The time dependent changes of the charge  $q = C_b U$  within junction determine a current transient  $i_c(t)$  in the external circuit, expressed as:

$$i_c(t) = \frac{dq}{dt} = \begin{cases} \frac{\partial U}{\partial t} (C_b + U \frac{\partial C_b}{\partial U}) = \frac{\partial U}{\partial t} C_{b0} \frac{1 + \frac{U_c(t)}{2U_{bi}}}{(1 + \frac{U_c(t)}{U_{bi}})^{3/2}} \approx AC_{b0} \frac{1 + \frac{At}{2U_{bi}}}{(1 + \frac{At}{U_{bi}})^{3/2}}, & \text{at } U < U_{FD} \\ \frac{\partial U}{\partial t} (C_{geom} + U \frac{\partial C_{geom}}{\partial U}) = \frac{\partial U}{\partial t} C_{geom} \approx AC_{geom}, & \text{for } U \geq U_{FD} \end{cases} \quad (2)$$

The transient for a rather small peak voltage  $U_P$  below values  $U_P < U_{FD}$  of full depletion voltage ( $U_{FD}$ ) contains an initial ( $t=0$ ) step  $AC_{b0}$  due to a displacement current and a descending component governed by the charge extraction. For an insulating material and for  $U_P > U_{FD}$ , this transient contains only a displacement current, and it shows a capacitor-like response. The

capacitor-like BELIV transients (figures 5a and 5b) recorded in dark and after irradiation with  $10^{15}$  proton/cm<sup>2</sup> fluence indicate a full-depletion of the diodes. The BELIV transient contains a displacement current step and a descending charge extraction component for  $0 < U_F \leq U_{FD}$ , and it saturates at time instant  $t_{FD} = U_{FD}/A + C_{geom}R$ .

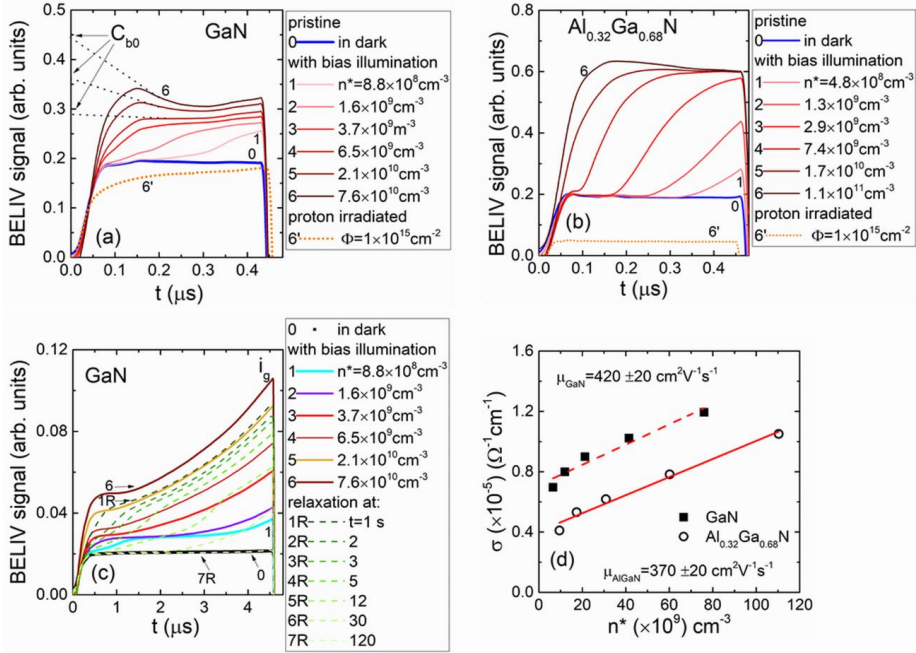


**Figure 5.** Evolution of BELIV transients recorded in dark and under illumination of varied intensity before and after proton irradiation of GaN (a), Al<sub>0.32</sub>Ga<sub>0.68</sub>N (b) photo-detectors using 450 ns GLIV pulses. Intensity of bias illumination is represented through the excess carrier density calculated using absorption coefficient values taken from Ref. [18] and carrier recombination lifetimes measured by MW-PC technique. The BELIV transients in the samples irradiated by protons of  $10^{15}$  p/cm<sup>2</sup> fluence were recorded using the largest illumination intensity. (c)- Evolution and relaxation of BELIV transients recorded in dark and under illumination of varied intensity of GaN photo-detectors using 4.5  $\mu$ s GLIV pulses. (d)-Evaluation of carrier mobility using independent measurements of ENR resistance (conductivity) and excess carrier density. For lateral diodes, the efficient  $S/d$  ratio can be estimated using values of geometrical capacitance  $C_g \cong C_{b0}$  of fully depleted diode.

A delay appears due to serial processes of dielectric relaxation within quasi-neutral range of the non-depleted layer, drift and diffusion of carriers to complete a circuit. The maximal barrier capacitance  $C_{b0}$  for DUT acts during the initial instants of GLIV pulse (when  $At < U_{bi}$ ), and it can be estimated by extrapolation to the initial instant of the transient (figure 5a). Thus, the fastest initial component of the BELIV current transient is determined by the transition time constant  $RC_{b0}$ , where  $R$  is the largest acting resistance (either  $R_{load}$  or  $R_{ENR}$ ). The  $RC_{b0}$  modifications of the initial step of barrier capacitance charging current  $i_c(t \approx 0)$  can be roughly emulated by a convolution integral

$$i_{RC}(t) = \frac{1}{\tau_{RC}} \int_0^t i_C(x) \exp\left[-\frac{(t-x)}{\tau_{RC}}\right] dx. \quad (3)$$

Thus, the peak is shifted from the initial instant within a current transient. The peak current within BELIV transient is then shifted proportionally to the resistivity dependent on excess carrier mobility and density (figures 5a and 5b), generated within electrically neutral region (ENR) of the large resistivity material under bias illumination. Also, the characteristic relaxation time of BELIV transients, after the illumination is switched off, enables the evaluation of  $RC_{b0}$  (figure 5c). This allows to evaluate the excess carrier mobility when excess carrier density is estimated from the calibration of the energy density of varied bias illumination (figure 5d).

For BELIV regime implemented using long GLIV pulses, the generation current term may appear due to carrier emission from traps and a time scale of carrier generation lifetime can be estimated. This generation current component is included in equation (2) by a simple increase of volume from which carriers are collected. The generation current  $i_g(t) = en_i S w_0 (1 + U_C(t)/U_{bi})^{1/2} / \tau_g$  increases with the voltage  $U_C(t)$  and can exceed the barrier charging current in the rearward phase of the transient (figure 5c). Here,  $N_D$  in expressions for  $w_0$  and  $C_{b0}$  should be replaced by its effective value  $N_{Def} = N_D \pm N_T^\pm$ , due to emission traps of density  $N_T$ . The descending component of the charge extraction and the ascending component of the generation current imply the existence of a current minimum within the current transient (figures 5a and 5c). Thereby values of generation lifetime and carrier mobility denoted in figures 5c and 5d, respectively, have been estimated. These values indicate a reduced carrier mobility in AlGaIn materials relative to pure GaN. A reduced amplitude of BELIV current and square-like shape (figures 5a and 5b) can be explained by the increase of carrier recombination and capture centres after proton irradiations.

#### 4. Summary

Moderate reduction of carrier recombination lifetime implies a rather good tolerance of AlGaIn materials to proton irradiation. Carrier emission centres with activation energy of  $E_{1-DLTS} = 0.316$  eV,  $E_{2-DLTS} = 0.792$  eV, and  $E_{3-DLTS} = 1$  eV have been resolved from DLT spectra recorded on AlGaIn materials after proton irradiation with fluence of  $10^{15}$  p/cm<sup>2</sup>. The radiation induced carrier recombination and capture centres caused an increase of leakage current observed within I-V's. Photo-active centers of activation energy of  $E_{PIS1} = 0.55$  eV,  $E_{PIS2} = 1.35$  eV and  $E_{PIS3} = 1.6$  eV have been revealed in the irradiated diodes by fitting the SS-PI spectral steps. These traps have been identified by comparing with literature data. The vacancy prevailing radiation defects have been identified. A carrier mobility of about 400 cm<sup>2</sup>/Vs has been evaluated from analysis of bias illumination intensity dependent changes of ENR resistance and delay of BELIV transient peaks.

#### Acknowledgment

This research is funded by the European Social Fund under the No 09.3.3- LMT-K-712 -02-0012 "Development of Competences of Scientists, other Researchers and Students through Practical Research Activities" measure.

#### References

- [1] H-Y. Kim et al., *Optical and electrical characterization of AlGaIn/GaN high electron mobility transistors irradiated with 5 MeV protons*, 2011 *J. Cryst. Growth* **326** 62-64 .

- [2] E. Gaubas et al., *Carrier decay and luminescence characteristics in hadron irradiated MOCVD GaN*, 2014 *JINST* **9** C12044.
- [3] S.J. Pearton et al., GaN-based diodes and transistors for chemical, gas, biological and pressure sensing, 2004 *J. Phys. Condens. Matter* **16** R961–94.
- [4] M.P. D'Evelyn et al., *Bulk GaN crystal growth by the high-pressure ammonothermal method*, 2007 *J. Cryst. Growth* **300** 11-16.
- [5] Z. Yu, *Study of the epitaxial-lateral-overgrowth (ELO) process for GaN on sapphire*, 1998 *J. Cryst. Growth* **195** 333-339.
- [6] T. Ceponis et al., *Evolution of scintillation and electrical characteristics of algan double-response sensors during proton irradiation*, 2019 *Sensors* **19** 3388.
- [7] P. Blood and J.W. Orton, *The electrical characterization of semiconductors: majority carriers and electron* (States Academic Press inc., Sandiego, 1992)
- [8] E. Gaubas, E. Simoen, and J. Vanhellemont, *Review - Carrier lifetime spectroscopy for defect characterisation in semiconductor materials and devices* 2016 *ECS J. Solid State Sci. Technol.* **5** P3108.
- [9] E. Gaubas et al., *Pulsed photo-ionization spectroscopy in carbon doped MOCVD GaN epi-layers on Si*, 2018 *Semicond. Sci. Technol.* **33** 075015.
- [10] U. Honda, Y. Yamada, Y. Tokuda, and K. Shiojima, *Deep levels in n-GaN doped with carbon studied by deep level and minority carrier transient spectroscopies*, 2012 *Jpn. J. Appl. Phys.* **51** 04DF04
- [11] W. Gotz, N.M. Johnson, H. Amano and I. Akasaki, *Deep level defects in n-type GaN*, 1994 *Appl. Phys. Lett.* **65** 463
- [12] Z-Q. Fang et al., *Plasma-etching-enhanced deep centers in n-GaN grown by metalorganic chemical-vapor deposition*, 2003 *Appl. Phys. Lett.* **82** 1562.
- [13] Z-Q. Fang, D.C. Look and L. Polenta, *Dislocation-related electron capture behaviour of traps in n-type GaN*, 2002 *J. Phys.: Condens. Matter* **14** 13061-13068
- [14] Y. Tokuda et al., *DLTS study of n-type GaN grown by MOCVD on GaN substrates*, 2006 *Superlattice Microst.* **40** 28-273
- [15] A.A. Kopylov, A.N. Pikhtin, *Effect of temperature on the optical-absorption spectra of deep centers in semiconductors*, 1975 *Sov. Phys. Solid State.* **16** 1200
- [16] M.A. Reshchikov and H. Morkoc, *Luminescence properties of defects in GaN*, 2005 *J. Appl. Phys.* **97** 061301
- [17] E.B. Yakimov, *Electron-beam-induced-current study of defects in GaN; experiments and simulation*, 2002 *J. Phys.: Condens. Matter* **14** 13069-13077
- [18] J.F. Muth et al., *Absorption coefficient and refractive index of GaN, AlN and AlGaIn alloys*, 1999 *Mat. Res. Soc. Symp. Proc.* **537**.
- [19] E. Gaubas, T. Ceponis and J-V. Vaitkus, *Pulsed capacitance technique for evaluation of barrier structures* (LAP Lambert Academic Publishing, Berlin, 2013)

A7

## Profiling of proton beams by fluence scanners

**L. Deveikis**, J. V. Vaitkus, T. Čeponis, M. Gaspariūnas, V. Kovalevskij, V.  
Rumbauskas, E. Gaubas

Lith. J. Phys. **61** (2) (2021) 75-83.

DOI:10.3952/physics.v61i2.4436

(Open access)

## PROFILING OF PROTON BEAMS BY FLUENCE SCANNERS

L. Deveikis <sup>a</sup>, J.V. Vaitkus <sup>a</sup>, T. Čeponis <sup>a</sup>, M. Gaspariūnas <sup>b</sup>, V. Kovalevskij <sup>a,b</sup>,

V. Rumbauskas <sup>a</sup>, and E. Gaubas <sup>a</sup>

<sup>a</sup> *Institute of Photonics and Nanotechnology, Vilnius University, Saulėtekio 3, 10257 Vilnius*

<sup>b</sup> *Centre for Physical Sciences and Technology, Saulėtekio 3, 10257 Vilnius*

Email: laimonas.deveikis@tmi.vu.lt

Received 6 April 2021; accepted 15 April 2021

Profiling of particle beams is one of the most important diagnostic procedures for operating any kind of accelerator. In this work, the proton beam profilers, based on fluence measurements performed by recording the changes of carrier lifetime in Si material and scintillation intensity of thin GaN layers, caused by radiation induced defects and emission centres, are presented. The beams of penetrative (26 GeV/c) and stopped (1.6 MeV) protons have been examined. It is shown that the penetrative particle regime should be employed to appropriately record 2D fluence distribution profiles. It is also illustrated that the presented profiling techniques can be applied for scanning of other charged (namely, pions) and neutral (neutrons) particle beams.

**Keywords:** particle beam profiling, carrier lifetime, microwave probed photoconductivity, luminescence, scintillators

**PACS:** 29.27.-a, 29.40.Mc, 72.40.+w, 78.60.-b

### 1. Introduction

Profiling of particle beams is one of the essential radiation diagnostic procedures for governing any kind of accelerator. The profile measurement principles are mainly based on either coupling to the particle electromagnetic field, which is freely propagating as radiation, or on the energy deposition due to the interaction of the particle electromagnetic field with matter [1–3]. As concerns the freely propagating fields, depending on the separation mechanism associated with coupling of the electromagnetic field and moving particles, different types of radiation such as synchrotron, transition, diffraction, parametric X ray, Cherenkov, and Smith–Purcell radiation are considered [1]. Radiation generation can be understood in terms of a separation of the virtual photon field associated with the charged particle. The most common of them are the meth-

ods based on transition radiation [4–8] and scintillation [1, 8, 9] of various materials. A broad band electromagnetic radiation, named transition radiation, is produced when a charged particle passes the boundary between two media with different dielectric constants [1, 7]. The wide frequency range radiation from THz to X rays is emitted on both sides of a conductive foil. This transition radiation originates from the currents induced on the foil by moving charged particles and by time-varying surface currents [7]. The visible spectrum of this radiation (optical transition radiation, OTR) is predominantly considered, and the recorded intensity profile is a measure of the particle beam spot. Thereby, the OTR recording is beneficial in that it allows fast single shot beam profile measurements, and the radiation output scales linearly with the particle beam bunch intensity [1]. The transition radiation measurement instrumentation is

usually implemented using a thin aluminium foil deposited on dielectrics. Alternatively, secondary electron emission (SEE) from a few nanometre layer next to the surface of the thin films can be employed for a beam profiling [4]. This ultra-thin layer is deposited on membrane and can afford high absorbed doses. The transverse beam profiles are controlled in monitoring of functioning of an accelerator and halo formation prevention [5]. The accelerated particles are typically distributed according to the Gaussian function within transverse beam profiles [3, 4]. The large energy deposition can lead to the destruction of profiler sensor materials. Therefore, usage of the traditional multi-wire chambers and wire scanners [3] is limited within inspection of the high repetition rates of pulsed beams and especially for continuous beam operation [5]. The recombination of the secondary carrier pairs produced by the passage of a charged particle leads to the generation of scintillation signals [3]. This material de-excitation process usually involves many metastable levels. Different types of phosphor materials have been developed to obtain large scintillation yields [3, 9, 10]. Generation of the laser-accelerated pulsed proton beams comprises the basis of the modern technologies in radiation biology and therapy [1, 10]. Profiling of these beams is inevitable due to the broad angular divergence of the laser-accelerated proton beams and stringent requirements on dose homogeneity and total flux at the irradiated body [10]. However, traditional beam profiling techniques are based on scanning of the flux lateral distribution due to the interaction of the particle electromagnetic field with matter [1–3], while local dose rates and accumulated fluence are the most important characteristics in radiation therapy.

In this work, the proton beam profilers, based on fluence measurements performed by recording the changes of carrier lifetime in Si material and scintillation intensity of thin GaN layers, caused by radiation induced defects and emission centres, are discussed. The measured beam parameters and scanned profiles are compared with those extracted using traditional beam profile monitors installed at CERN. The beams of penetrative (26 GeV/c) and stopped (1.6 MeV) protons have been examined. The prospects of the proposed techniques for direct profiling of doses within proton beams have been shown. It has been illus-

trated that these profiling techniques can be applied for scanning of other charged (namely, pions) and neutral (neutrons) particle beams.

## 2. Principles of techniques and instruments for fluence scanning

The deposited energy of irradiation may create defects in materials used for radiation detection. Probing of these radiation defects – either the centres of radiative recombination, modifying dose dependent scintillation intensity, or the induced non-radiative carrier decay processes, changing carrier lifetime – serves for measurement of irradiation fluence and its distribution within particle beams. In this work, both the scintillation and non-radiative response signals have been exploited for profiling of proton beams.

### 2.1. Scanning of carrier lifetime distribution within irradiated Si wafers

Rather universal dependence (Fig. 1) of the carrier recombination lifetime ( $\tau_R$ ) in high purity, large resistivity silicon materials as a function of hadron irradiation fluence ( $\Phi$ ) has been revealed [11]. Si materials grown either by the float zone (FZ) or Czochralski applying magnetic field (MCZ) technology are the most suitable for reliable detection of this characteristic. This dependence can be employed for detection of penetrative hadrons the stopping range  $L_p$  of which exceeds the sample thickness  $d$ .

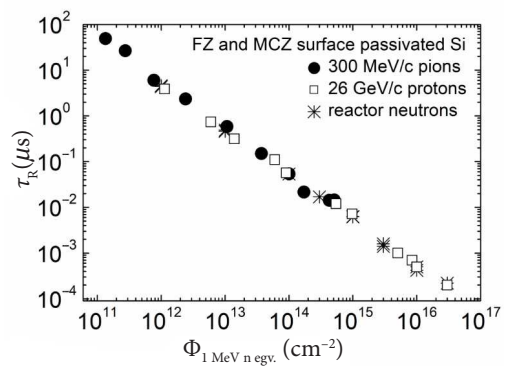


Fig. 1. Typical dependence of the recombination lifetime as a function of the penetrative hadron irradiation fluence obtained on high purity (FZ and MCZ) and surface passivated Si wafer fragments.



Rather thick ( $d \sim 300 \mu\text{m}$ ) Si wafers or wafer fragments are usually employed to integrate a response from the relevant density of recombination centres. The reciprocal characteristic of  $\tau_R - \Phi$  is obtained within a double logarithmic scale. This characteristic indicates the hyperbolic dependence and the prevalence of point radiation defects: for those the linear relation between the defect concentration ( $N_R$ ) and recombination rate  $R = 1/\tau_R = \sigma v_T N_R$  exists, where  $\sigma$  is the cross-section of interaction of the carriers with a definite type of recombination centres, and  $v_T$  is the thermal velocity of carriers. The linear  $\log \tau_R - \log \Phi$  characteristic (Fig. 1) covers about 6 orders of magnitude. Either the surface passivated large resistivity silicon material should be used or corrections due to surface recombination velocity ( $s$ ) are necessary when  $\tau_R \geq d/s$ . The corrections relatively to excess carrier injection rate also should be made in the range of the largest irradiation fluences if the excess carrier excitation pulses of moderate duration ( $\sim 1$  ns) are employed. The exponential decay is usually observed in the as-irradiated Si materials. Therefore, the carrier lifetime values are extracted using the photoconductivity decay transients, as  $\tau_R = n/(-\partial n/\partial t)|_{\text{exp}(-1)}$ . The contactless MW-PC technique of the microwave (MW) probed photoconductivity (PC) is commonly applied for carrier lifetime measurements [11].

The FZ Si wafer fragments of  $30 \times 30$  mm dimensions (Fig. 2(a)) irradiated with 26 GeV/c protons at CERN were scanned with  $2 \mu\text{m}$  step to reproduce the initial particle beam profile. The carrier lifetime profiling has been performed in dark using a Vilnius University proprietary made instrument VUTEG-4 (Fig. 2(b)). This instrument enables 2D scanning of Si wafers of dimensions up to 12 cm in diameter. The nitrogen gas and temperature stabilized environment is usually maintained during profiling measurements. Also, the scan regime of wafer edge is foreseen in this instrument, which is implemented using a needle-tip MW antenna probe intersecting with a single mode fibre tip. The slit MW antenna of  $10\text{--}100 \mu\text{m}$  width was employed for scanning of the laser beam excited area. The excess carrier excitation was implemented using 500 ps laser pulses. The IR ( $\lambda_{\text{ex}} = 1062$  nm) excitation was implemented through a MW slit. The laser light spot was transferred using a single-mode fibre mounted within the MW antenna. The simplified Vilnius University proprietary made carrier lifetime profiler VUTEG-

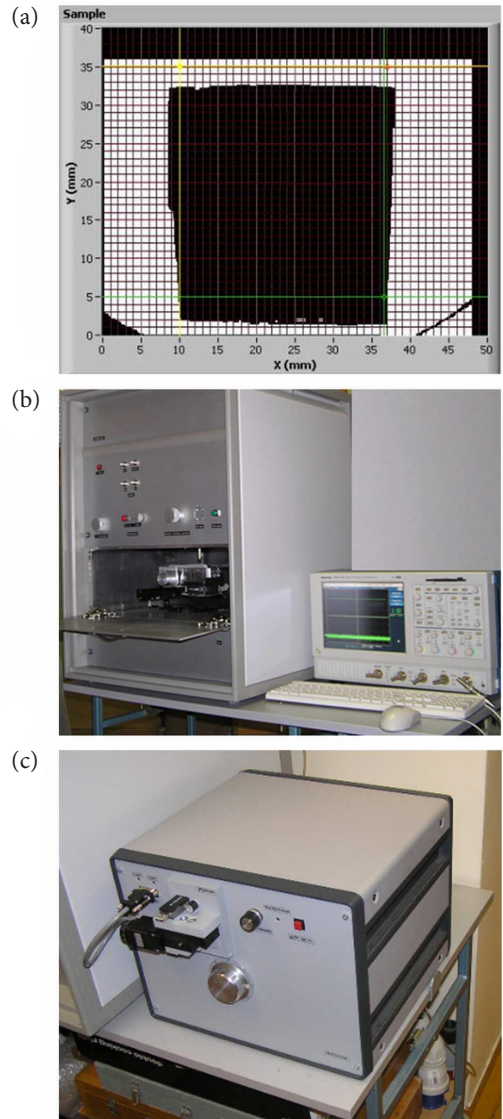


Fig. 2. Size and position coordinates (of wafer  $30 \times 30$  mm fragment) in lifetime scanning experiments are controlled using CCD imaging within an instrument VUTEG-4 (a). The Vilnius University proprietary made instruments VUTEG-4 (b) and VUTEG-5-AIDA (c).

5-AIDA (Fig. 2(c)) is installed at CERN. The latter instrument is devoted to rapid examination of the as-irradiated Si materials residing in harsh environment. There, the 1D lateral scanning is commonly performed, while the perpendicular rotation

of sample fragments of dimensions  $\sim 11$  mm enables one to have a cross-profile within sample diameter direction.

Lateral profiling of the irradiated areas using the Si and MW-PC carrier lifetime scanning technique is simply applicable in the diagnostics of penetrative particle beams. For rather low energy protons with short ranging ( $< 30 \mu\text{m}$ ), the depth inhomogeneity of radiation defect distribution complicates the reliable extraction of local fluence values. Sometimes the depth profiling by using the wafer edge scanning regime can be applied [12], however the high resolution lateral profiling of beams is then impossible.

## 2.2. Fluence scans using scintillation intensity variations in GaN wafer fragments

Scanning of the scintillation signals is a good alternative for profiling of the short-range particle beams. The rather thin GaN layers with  $L_p \sim 26 \mu\text{m}$  stopping range for  $\leq 2$  MeV protons have been employed for accumulation of the definite dose where the depth homogeneous distribution of radiation defects can be obtained. The consequent changes of the scintillation spectrum or single spectral peak intensity are commonly profiled. The calibrated fluence dependent variation of yellow-green (YG) luminescence intensity (Fig. 3) of the  $\sim 3 \mu\text{m}$  thick MOCVD grown

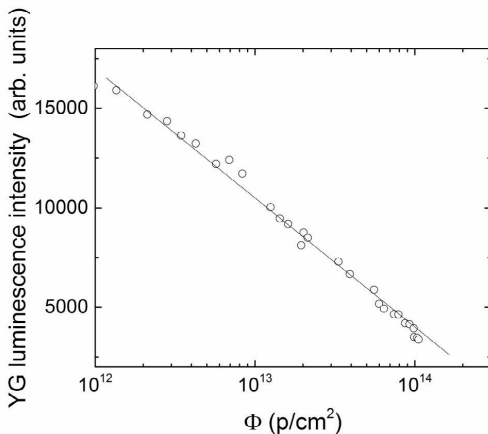


Fig. 3. The calibration characteristic for the short-range particle beam profiling based on YG luminescence intensity variations dependent on 1.6 MeV proton fluence.

GaN layer is initially measured to extract fluence values. The measurements of the calibration curve are performed by the *in situ* or stepped spectroscopy [13] of the GaN luminescence variations under successive accumulation of fluence within a laterally homogeneous irradiation spot. The proton beam of a diameter that exceeds the dimensions of the GaN wafer fragment is commonly applied to have a nearly homogeneously irradiated sensor area. It can be noticed in Fig. 3 that a rather narrow dynamic range of fluences, in comparison with Fig. 1, can be covered within the calibration curve when direct control of scintillation intensity is applied. The same GaN sensor material is then exploited for scanning of a rather narrow beam profile (Fig. 4). The latter procedure is implemented *ex situ* by using ultraviolet (UV) short pulse (400 ps) laser excitation.

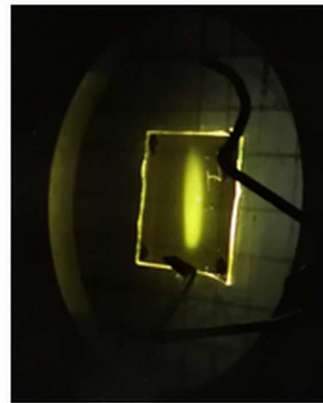


Fig. 4. The narrow beam of 1.6 MeV proton excited YG luminescence image. The GaN wafer fragment exceeds dimensions of the proton beam.

Profiling of the rather narrow beam trace within an irradiated GaN wafer fragment is commonly performed by lateral scans of YG scintillation in a GaN sensor using the optical arrangement sketched in Fig. 5(a). An ultraviolet laser STA-3H emitting the 351 nm light was employed for excitation of GaN YG photoluminescence. The PL response filtered from the laser beam is collected into a UV range fibrescope and transmitted to a spectrophotometer. An *Avantes* grating spectrophotometer was exploited to accumulate the spectrally dispersed PL response.

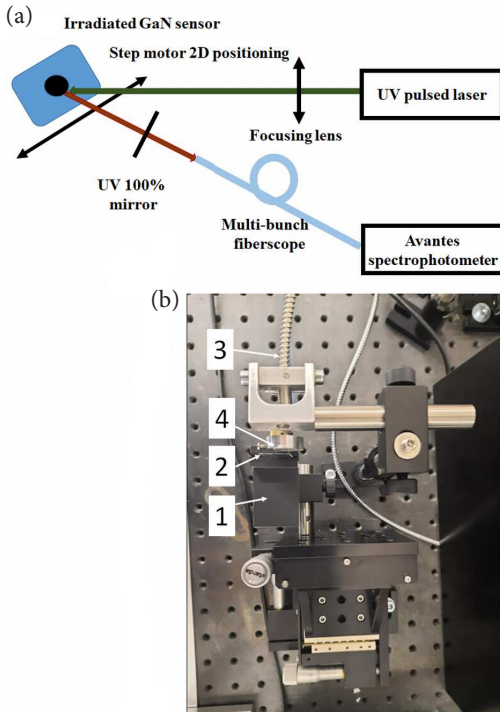


Fig. 5. (a) Sketch of the instrumentation for the profiling of YG photoluminescence (PL) in a proton beam irradiated GaN sensor. The local excitation with a laser light spot dimension of  $\sim 10 \mu\text{m}$  is implemented using a single-mode fibre. The YG scintillation light is collected by using a multi-bunch fibrescope and displayed by an *Avantes* spectrophotometer. Several elements are employed to reject the UV laser illumination of the spectrometer slit. The scans are performed by using  $2 \mu\text{m}$  precision steppers. (b) An image of the experimental arrangement of beam profiler using scintillation scans: sample holder (1), irradiated GaN sensor (2), multi-bunch fibrescope (3), UV 100% mirror (4).

### 3. Recorded profiles of hadron beams

The 2D profile of carrier recombination lifetime distribution within the FZ Si wafer fragment of  $30 \times 30 \text{ mm}$  dimensions, irradiated with relativistic of  $26 \text{ GeV}/c$  protons, is illustrated in Fig. 6(a). This lateral distribution has been scanned with spatial resolution of several microns using an instrument VUTEG-4. The fluence values were extracted using the recombination lifetime dependence on the penetrative hadron irradiation fluence illustrated in

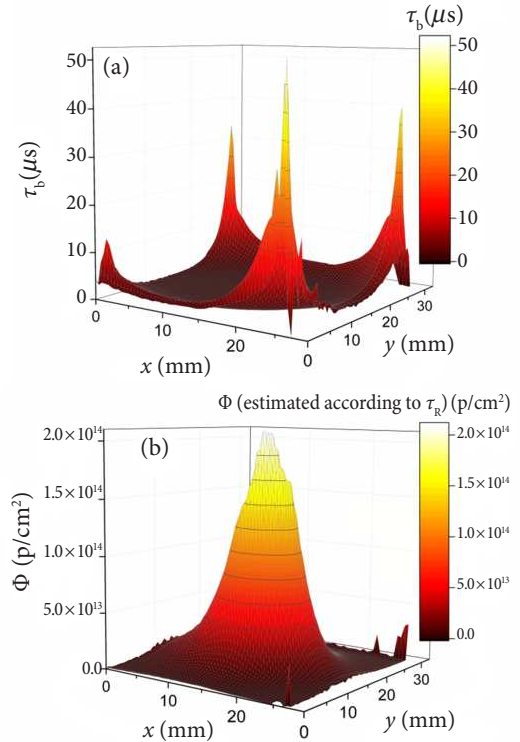


Fig. 6. The 2D profiles of carrier recombination lifetime (a) and fluence (b) in the  $26 \text{ GeV}/c$  proton beam irradiated Si wafer fragment of dimensions  $30 \times 30 \text{ mm}$ , scanned using a VUTEG-4 instrument.

Fig. 1. This profile is illustrated in Fig. 6(b). It shows the bell-shape curve. The particle beam profile is commonly approximated by the Gauss function [1, 3] due to the variation of accelerated particle velocities within a beam.

The profiles of fluence variations within  $X$  and  $Y$  sections crossing the beam centroid are illustrated in Fig. 7. There, the asymmetry within the shape of the  $X$  section can be noticed in Fig. 7(a), while the  $Y$  section is close to the Gaussian curve shape (Fig. 7(b)). The latter fluence distribution profile  $\Phi(Y)$  can be easily approximated by using the 1D Gauss function, read as [3]

$$\Phi(Y) = \frac{N}{\sqrt{2\eta\sigma_Y}} \exp\left[-\frac{(Y - Y_0)^2}{2\sigma_Y^2}\right]. \quad (1)$$

Here,  $N$  is the quantity of radiation defects accumulated within the centroid (close to the point  $X_0, Y_0$ )

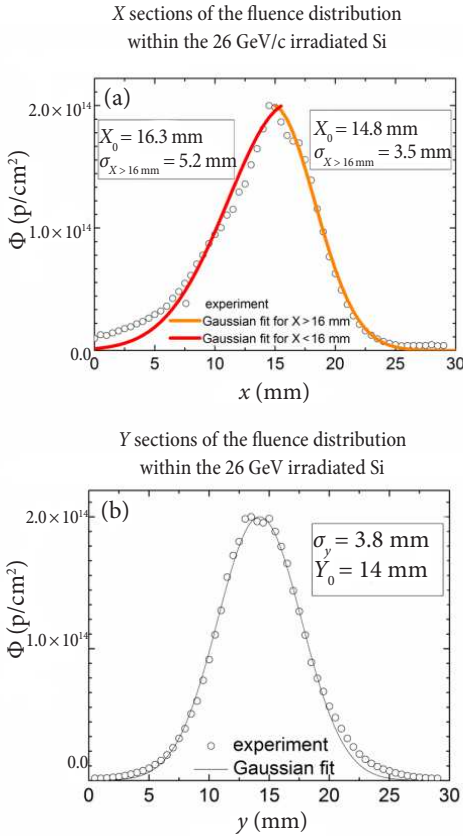


Fig. 7. X (a) and Y sections (b) of the fluence distribution within the 26 GeV/c proton beam irradiated Si wafer fragment.

of the irradiation beam, and  $\sigma_y$  is the effective cross-section of the Gaussian function. Consequently, the 2D profile is described by the function

$$\Phi(X, Y) = \frac{N}{2\eta\sigma_x\sigma_y} \exp\left\{-\left[\frac{(X-X_0)^2}{2\sigma_x^2} + \frac{(Y-Y_0)^2}{2\sigma_y^2}\right]\right\}. \quad (2)$$

A fit of the  $\Phi(Y)$  profile obtained for the 26 GeV/c proton beam is represented by a solid curve in Fig. 7(b). This fitting procedure enables one to get parameters of the beam, as  $N$  and  $\sigma_y$ . However, the beam profile within the  $X$  section cannot be approximated by a single parameter  $\sigma_x$ . The beam  $X$  direction movements during accumulation of irradiation damage led to a significant asymmetry of the  $\Phi(X)$  beam profile. Then, different values of the beam effective width should be assumed, as  $\sigma_x = 5.2$  mm for  $X < 16$  mm and  $\sigma_x = 3.5$  mm for

$X > 16$  mm. The latter value of  $\sigma_x = 3.5$  mm is close to that ( $\sigma_y = 3.8$  mm) determined from  $Y$  section fits. The  $\sigma_{x,y}$  parameters outline the beam full width ( $S_{x,y}$ ) at half maximum of its amplitude (FWHM), and for Gaussian beams it is the well-known relation  $S_{x,y} = 2.35\sigma_{x,y}$ , respectively [3].

The impact of beam stability is less important when an instantaneous particle flux is controlled by a beam profile monitor. The comparison of 2D beam profiles scanned by measurements of accumulated fluence and by the beam profile monitor, installed at CERN, is illustrated in Fig. 8. The fluence has been re-calculated using the flux data in Fig. 8(b), to be able to compare the beam profiles scanned by different techniques and instruments. Also, the beam profile monitor was significantly

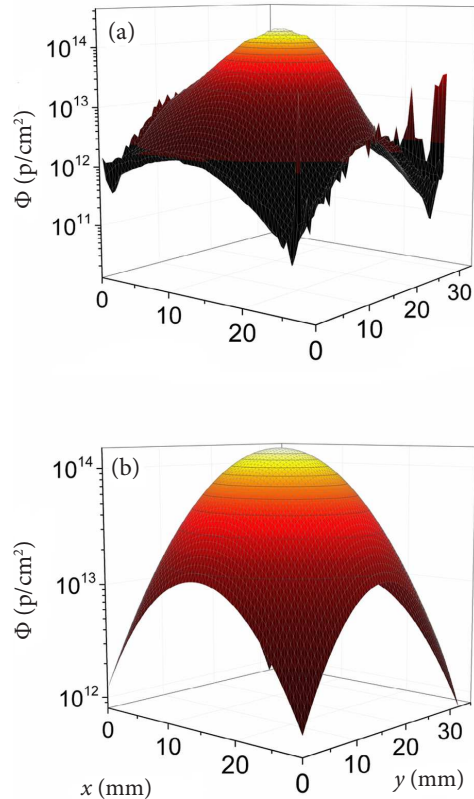


Fig. 8. Comparison of the 2D fluence distribution profiles measured within the 26 GeV/c proton beam irradiated Si wafer fragment by employing a VUTEG-4 instrument (a) and using a proton beam profiler (b) installed at CERN.

shifted (about 20 cm) from the location of Si wafer fragment within the impinging particle beam. It can be noticed in Fig. 8(b) that a rather symmetric and Gaussian shaped beam has been recorded by using the CERN beam profile monitor. Nevertheless, the difference in fitted beam parameters has been revealed as  $\sigma_x = 6.6$  mm,  $\sigma_y = 7.0$  mm,  $X_0 = 16.0$  mm and  $Y_0 = 15.4$  mm. These values are also close to that ( $\sigma_x = 5.2$  mm) obtained from the profile fitting in fluence distribution scans (Fig. 7(a)). The 2D beam shape in Fig. 8(a), recorded by fluence scans, seems to be spiked relative to the flattened one obtained using the beam profile monitor, in Fig. 8(b). Nonetheless,  $\Phi_0 \cong N$  values of  $2 \times 10^{14}$  cm $^{-2}$  fluence in the beam centre were obtained using both instruments, the VUTEG-4 (together with FZ Si sensors) and CERN beam profile monitor.

The 8 MeV protons remain the penetrative particles for  $\sim 300$   $\mu$ m thick Si wafers. Thereby, the VUTEG-4 instrument has been applied for 8 MeV irradiated MCZ Si wafer fragments. Such a proton beam was emitted by a *Tandem* accelerator at Helsinki University. The  $X$  section of the beam appeared to be close to the Gaussian shape (Fig. 9), shown by a solid curve.

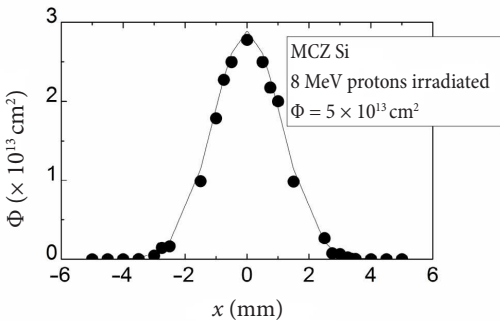


Fig. 9. The 1D fluence distribution profile measured by the VUTEG-4 instrument within the 8 MeV proton beam irradiated 300  $\mu$ m thick MCZ Si wafer fragment.

However, the shape of pion beams, recorded at CERN, appeared to be clearly non-Gaussian (Fig. 10(b)). There, the single-directional recombination lifetime scans (Fig. 10(a)) by VUTEG-5-AIDA instrument were performed using a narrow ( $\leq 1$  cm) FZ Si sensor (wafer fragment). Fitting of the lateral fluence distribution within the pion irra-

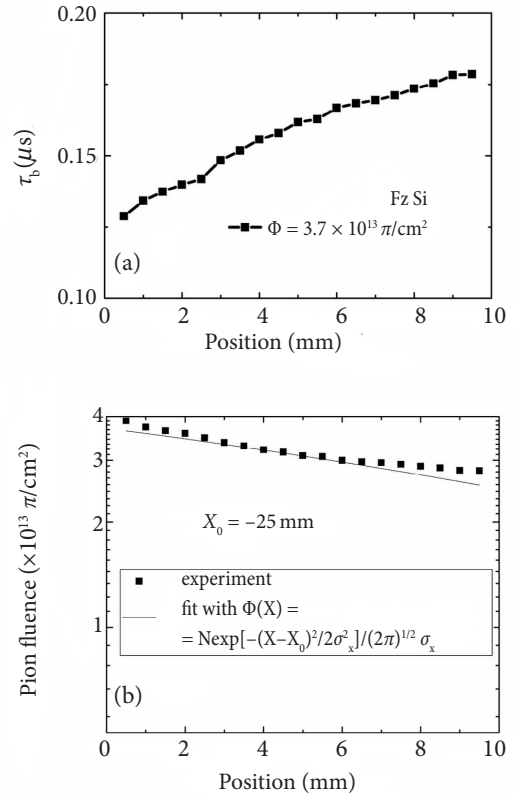


Fig. 10. The 1D profiles of carrier recombination lifetime (a) and fluence (b) in the 300 MeV/c pion irradiated Si wafer fragment of dimensions 10  $\times$  10 mm and scanned using the VUTEG-5-AIDA instrument. In Fig. 10(b) the fluence distribution profile (symbols) and the best fit (solid curve) using the Gauss function are shown.

diated Si wafer fragment sets the centroid position ( $X_0 = -25$  mm) outside the sensor area.

The luminescence intensity profile obtained in the 1.6 MeV proton irradiated 3  $\mu$ m thick GaN layer, MOCVD grown on sapphire, is illustrated in Fig. 11(a). The stopping range of  $L_p \sim 26$   $\mu$ m of 1.6 MeV protons, evaluated using transport of ions in matter (TRIM) simulations, significantly exceeds the GaN layer thickness  $d = 3$   $\mu$ m. Thereby, depth-homogeneous introduction of radiation defects can be assumed. The fluence distribution profile can then be restored (Fig. 11(b)) using the calibration curve (Fig. 3) which relates the YG scintillation intensity of the same GaN material



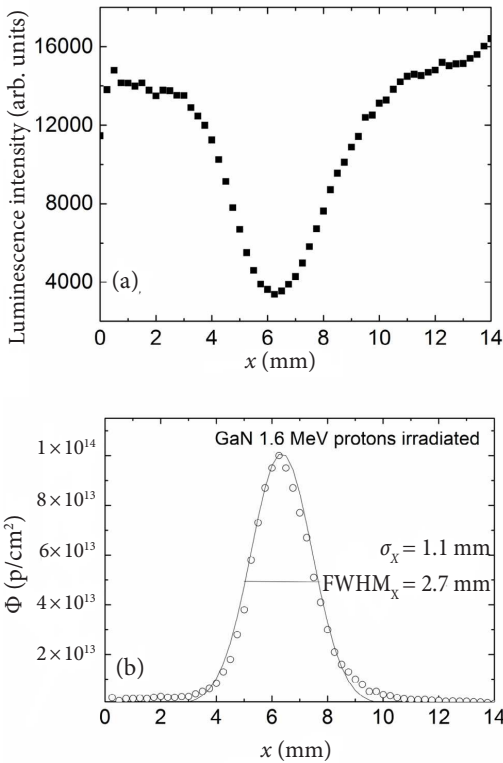


Fig. 11. The 1D profiles of YG luminescence distribution within a  $3 \mu\text{m}$  thick MOCVD GaN layer irradiated with 1.6 MeV protons (a) and of fluence (b) extracted using a calibration curve, illustrated in Fig. 3. In Fig. 11(b), the fluence distribution profile (symbols) fitted using the Gauss function (a solid curve) is represented.

and the accumulated fluence. The rather symmetric X-directional cross-section of the focused 1.6 MeV proton beam was examined. Whereas, the proton beam can be outstretched (as shown in Fig. 4) by the focusing system of a *Tandem* accelerator. It can be noticed in Fig. 11(b) that the UV laser recovered luminescence intensity reproduces well the fluence distribution of a Gaussian shape. Then, the beam parameter  $FWHM_x = 2.7 \text{ mm}$  has been extracted. The  $FWHM_x$  and  $\Phi$  parameters appeared to correlate well with the predicted characteristics, estimated using the beam current, exposure time and other irradiation data [14]. Thereby, such a scintillation technique is reliable for the *in situ* quantitative control of irradiation characteristics.

#### 4. Summary

The beam profiling techniques based on dosimetry of the hadron irradiated Si and GaN sensors have been demonstrated. It is shown that the penetrative particle regime, with  $L_p \gg d$ , should be employed to appropriately record 2D fluence distribution profiles. Therefore, for beams of rather low energy particles thin sensors are preferable. Then, the scintillation techniques are desirable to have recordable responses from thin sensors. The Gaussian shape beams are commonly recorded. However, the fluence measurement based techniques enable one to reveal the asymmetry of beams due to instability of beam position during prolonged exposures. These techniques also allow the profiling of neutral particles, such as neutrons [15], based on the universal recombination lifetime dependence on hadron irradiation fluence in high purity Si materials.

#### Acknowledgements

This research was partially funded by the European Regional Development Fund according to the supported activity ‘Research Projects Implemented by World-class Researcher Groups’ under Measure No. 01.2.2-LMT-K-718-1-0013. The authors are indebted to I. Mateu, M. Moll and S. Martens for proton irradiations and proton beam characterization at CERN. This research is devoted to the 80-year Anniversary of Professor J.V. Vaitkus.

#### References

- [1] G. Kube, in: *Proceedings of the 2018 CERN Accelerator School's Course on Beam Instrumentation* (CERN, Geneva) pp. 18–119, arXiv-2005.08389.
- [2] K. Wittenburg, in: *Proceedings of the CERN Accelerator School's Course on High Power Hadron Machines*, ed. R. Bailey (CERN, Geneva, 2013) pp. 251–308.
- [3] E. Bravin, in: *Proceedings of the 2018 CERN Accelerator School's Course on Beam Instrumentation* (CERN, Geneva) pp. 318–354.
- [4] B. Boyer, R. Cornat, E. Delagnes, Y. Geerebaert, O. Gevin, F. Haddad, C. Koumeir, F. Magniette, P. Manigot, F. Poirier, et al., Development of an ultra thin beam profiler for charged particle

- beams, Nucl. Instrum. Methods Phys. Res. A **936**, 29–30 (2019).
- [5] P. Ausset, S. Bousson, D. Gardès, A.C. Mueller, B. Pottin, R. Gobin, G. Belyaev, and I. Roudskoy, in: *Proceedings of 8th European Particle Acceleration Conference EPAC 2002* (European Physical Society, Geneva, 2002) pp. 1840–1842.
- [6] V.E. Scarpine, Transverse beam shape measurements of intense proton beams using optical transition radiation, Phys. Procedia **37**, 2123–2128 (2012).
- [7] A. Nause, E. Dyunin, R. Ianconescu, and A. Gover, Exact theory of optical transition radiation in the far and near zones, J. Opt. Soc. Am. B **31**(10), 2438–2445 (2014).
- [8] C. Belver-Aguilar, S. Braccini, T.S. Carzaniga, A. Gsponer, P.D. Häffner, P. Scampoli, and M. Schmid, A novel three-dimensional non-destructive beam-monitoring detector, Appl. Sci. **10**(22), 8217 (2020).
- [9] N.P. Dover, M. Nishiuchi, H. Sakaki, M.A. Alkhimova, A.Ya. Faenov, Y. Fukuda, H. Kiriya, A. Kon, K. Kondo, K. Nishitani, et al., Scintillator-based transverse proton beam profiler for laser-plasma ion sources, Rev. Sci. Instrum. **88**, 073304 (2017).
- [10] M. Cavallone, A. Flacco, and V. Malka, Shaping of a laser-accelerated proton beam for radiobiology applications via genetic algorithm, Phys. Med. **67**, 123–131 (2019).
- [11] E. Gaubas, E. Simoen, and J. Vanhellefont, Review–Carrier lifetime spectroscopy for defect characterization in semiconductor materials and devices, ECS J. Solid State Sci. Technol. **5**, P3108–P3137 (2016).
- [12] E. Gaubas, T. Ceponis, A. Uleckas, J. Vaitkus, K. Žilinskas, V. Kovalevskij, M. Gaspariunas, and V. Remeikis, *In situ* analysis of the carrier lifetime in silicon during implantation of 1.5 MeV protons, Lith. J. Phys. **50**(4), 427–433 (2010).
- [13] E. Gaubas, T. Ceponis, A. Jasiunas, V. Kovalevskij, D. Meskauskaitė, J. Pavlov, V. Remeikis, A. Teikorius, and J. Vaitkus, Correlative analysis of the *in situ* changes of carrier decay and proton induced photoluminescence characteristics in chemical vapour deposition grown GaN, Appl. Phys. Lett. **104**, 62104 (2014).
- [14] P.J. Sellin and J. Vaitkus, New materials for radiation hard semiconductor detectors, Nucl. Instrum. Methods Phys. Res. A **557**, 479–489 (2006).
- [15] E. Gaubas, T. Ceponis, A. Jasiunas, A. Uleckas, J. Vaitkus, E. Cortina, and O. Militaru, Correlated evolution of barrier capacitance charging, generation and drift currents and of carrier lifetime in Si structures during 25 MeV neutrons irradiation, Appl. Phys. Lett. **101**, 232104 (2012).

## PROTONŲ PLUOŠTELIŲ PROFILIAVIMAS ĮTĖKIO SKENERIAIS

L. Deveikis <sup>a</sup>, J.V. Vaitkus <sup>a</sup>, T. Čeponis <sup>a</sup>, M. Gaspariūnas <sup>b</sup>, V. Kovalevskij <sup>a,b</sup>, V. Rumbauskas <sup>a</sup>, E. Gaubas <sup>a</sup>

<sup>a</sup> Vilniaus universiteto Fotonikos ir nanotechnologijų institutas, Vilnius, Lietuva

<sup>b</sup> Fizinių ir technologinių mokslų centras, Vilnius, Lietuva

### Santrauka

Darbe aptartos protonų pluoštelių charakterizavimo technologijos pasitelkiant Si ir GaN sensorius bei apšvitos įtėkio skenavimo būdus. Šie būdai yra pagrįsti krūvininkų gyvavimo trukmės didžiavaržiamame Si ir žaliai geltonosios GaN liuminescencijos intensyvumo pasiskirstymo kontrole. Parodyta, kad egzistuoja gana universalios charakteristikos, nusakanti radiacinių defektų koncentracijos, krūvininkų gyvavimo trukmės

ir liuminescencijos intensyvumo ryšius su Si bei GaN medžiagų apšvitos hadronais įtėkiu. Šios charakteristikos yra pasitelktos įtėkio pasiskirstymo profiliams identifikuoti. Parodyta, kad daugeliu atveju įvairių dalelių greitintuvų formuojamų pluoštelių forma gali būti aproksimuojama Gauso funkcija. Aptartos šių metodų taikymo galimybės elektringiems ir neutraliems dalelių pluoštams kiekybiškai charakterizuoti.

P1

# Hybrid multi-layer sensor and method for large fluence dosimetry and fluximetry

E. Gaubas, T. Čeponis, **L. Deveikis**, J. Pavlov, V. Rumbauskas

Application No. 21 165 145.0

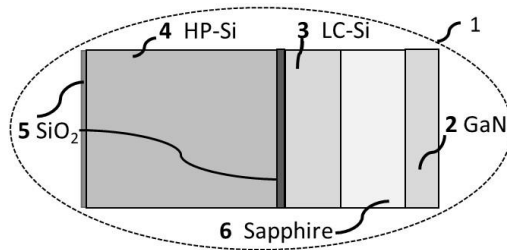
Submitted: 2021 03 26



## ABSTRACT

### Hybrid multi-layer sensor and method for large fluence dosimetry and fluxmetry

This invention discloses a hybrid multi-layer sensor and the methods for large fluence dosimetry and fluxmetry by using this sensor. The sensor which comprises the scintillator layer made of wide-bandgap semiconductor and a photoelectric-response layer made of high purity, large resistivity semiconductor, separated by the visible spectrum filtering, electric insulating and passivating layers, and which operates in pulsed as well as steady-state (dc) modes. The signals from scintillator and photoelectric response layers are scanned during dosimetry and fluxmetry procedures by using the external instruments - a fiber-coupled spectrophotometer and the microwave needle-tip antenna connected to a microwave detection system. The discrimination of particle species and particle energy values is performed by correlating signals of the scintillator spectrum structure and the microwave probed photoconductivity amplitude and decay lifetime profiles, where the multi-layered scintillator together with the photoelectrical response layer act as the complementary detectors. This multi-layer sensor is designed for contactless dosimetry and fluxmetry, and it is complemented with reading apparatuses for implementing of the methods intended for monitoring of harsh radiation facilities and control of mixed particle beams in nuclear reactors, in storages of nuclear fuel waste, in large particle accelerators and neutron spallators.



Hybrid sensor structure and its reading device.

**HIBRIDINIS DAUGIASLUOKSNIS JUTIKLIS IR DIDELIŲ ĮTĖKIŲ BEI SRAUTŲ  
MATAVIMO HIBRIDINIAIS JUTIKLIAIS METODAS**

(HYBRID MULTI-LAYER SENSOR AND METHOD FOR LARGE FLUENCE  
DOSIMETRY AND FLUXIMETRY)

Pareiškėjas:

Vilniaus universitetas (Vilnius University, Universiteto 3, LT -01513 Vilnius, Lithuania)

Išradėjai:

Eugenijus Gaubas, Pajautos 3-38, LT-06203 Vilnius, Lithuania; (30%)

Tomas Čeponis, Erfurto 14-65, LT-04116 Vilnius, Lithuania; (25%)

Laimonas Deveikis, Volungės 15-5, LT-10316 Vilnius, Lithuania; (15%)

Jevgenij Pavlov, I. Simonaitytės 9-21, LT-06294 Vilnius, Lithuania; (10%)

Vytautas Rumbauskas, Anapilė 26, LT-10230 Vilnius, Lithuania. (20%)



## Acknowledgement of receipt

We hereby acknowledge receipt of your request for grant of a European patent as follows:

Submission number	9640593	
Application number	EP21165145.0	
File No. to be used for priority declarations	EP21165145	
Date of receipt	28 March 2021	
Your reference	V83-78 EP	
Applicant	Vilnius University	
Country	LT	
Title	HYBRID MULTI-LAYER SENSOR AND METHOD FOR LARGE FLUENCE DOSIMETRY AND FLUXMETRY	
Documents submitted	package-data.xml application-body.xml SPECEPO-1.pdfFiled_Specification_L T83-78LT.pdf (27 p.)	ep-request.xml ep-request.pdf (4 p.) f1002-1.pdf (2 p.)
Submitted by	CN=secure.epoline.org	
Method of submission	Online	
Date and time receipt generated	28 March 2021, 11:08 (CET)	
Message Digest	43:22:E3:D6:9A:43:1A:B4:8A:D3:4D:0F:3F:5E:7C:62:E1:50:16:22	

/European Patent Office/

P2

Oriented triplex sensor and method of  
identification of the radiation source  
location and its dosimetry

E. Gaubas, T. Čeponis, **L. Deveikis**, J. Pavlov, V. Rumbauskas

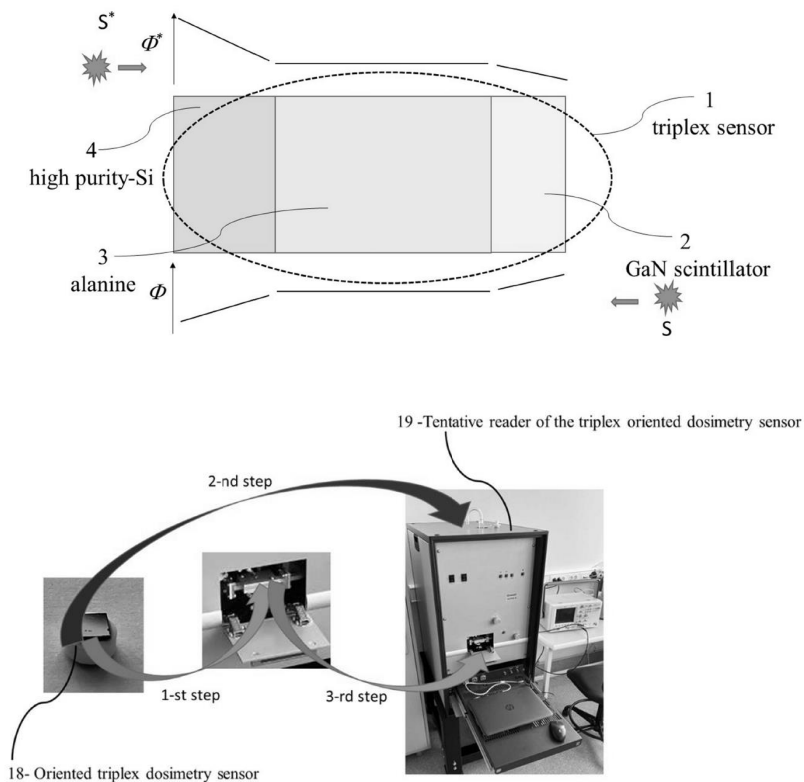
Application No. EP22171639.2

Submitted: 2022 05 04

## ABSTRACT

### ORIENTED TRIPLEX SENSOR AND METHOD FOR IDENTIFICATION OF THE RADIATION SOURCE LOCATION AND ITS DOSIMETRY

This invention discloses an oriented triplex dosimetry sensor composed of three layers, namely, the photo-sensor made of large-resistivity semiconductor bulk-plate pasted to the intermediate alanine layer, where radiation induced free radicals are detected by EPR technique, which is agglutinated further to a GaN scintillator (2) (Fig. 1), wherein (2), (3) and (4) layers of the triplex sensor (1) are sequentially scanned by the spectrophotometer, the EPR scanner and the microwave detection system, where particle discrimination and fluence measurements are performed by correlating signals of the scintillator spectrum structure, the EPR signal amplitude and the photoconductivity decay lifetime, while depth variations of the accumulated dose serve for estimation of the radiation streamline. These small dimension triplex sensors can be composed into 1D cells comprising several face-to-face and in line deployed triplex sensors, while triplex sensor structures oriented in perpendicular directions are applicable for estimation of location of the radiation source.



Triplex sensor structure and its reading device.

Form 1002 - 1: Public inventor(s)

Designation of inventor

User reference: EPP2022/48  
 Application No:

Public

	<p><b>Inventor</b></p> <p>Name: Gaubas Eugenijus                  Address: 01513 Vilnius                  Lithuania</p> <p>The applicant has acquired the right to the European patent:</p>	<p>As employer</p>
	<p><b>Inventor</b></p> <p>Name: Čeponis Tomas                  Address: 01513 Vilnius                  Lithuania</p> <p>The applicant has acquired the right to the European patent:</p>	<p>As employer</p>
	<p><b>Inventor</b></p> <p>Name: Rumbauskas Vytautas                  Address: 01513 Vilnius                  Lithuania</p> <p>The applicant has acquired the right to the European patent:</p>	<p>As employer</p>
	<p><b>Inventor</b></p> <p>Name: Deveikis Laimonas                  Address: 01513 Vilnius                  Lithuania</p> <p>The applicant has acquired the right to the European patent:</p>	<p>As employer</p>
	<p><b>Inventor</b></p> <p>Name: Pavlov Jevgenij                  Address: 01513 Vilnius                  Lithuania</p> <p>The applicant has acquired the right to the European patent:</p>	<p>As employer</p>

Signature(s)

Place:

Date: 04 May 2022

Signed by: /Reda Zaboliene/

Representative name: Reda Zaboliene

Capacity: Representative



## Acknowledgement of receipt

We hereby acknowledge receipt of your request for grant of a European patent as follows:

Submission number	10913680		
Application number	EP22171639.2		
File No. to be used for priority declarations	EP22171639		
Date of receipt	04 May 2022		
Your reference	EPP2022/48		
Applicant	Vilniaus Universitetas		
Country	LT		
Title	ORIENTED TRIPLEX SENSOR AND METHOD OF IDENTIFICATION OF THE RADIATION SOURCE LOCATION AND ITS DOSIMETR		
Documents submitted	<table><tr><td>package-data.xml application-body.xml SPECEPO-1.pdf Gaubas-Oriented dosimeter and reader - FINAL_JA_05_01-EGRED-05-02_final.pdf (35 p.)</td><td>ep-request.xml ep-request.pdf (4 p.) f1002-1.pdf (2 p.)</td></tr></table>	package-data.xml application-body.xml SPECEPO-1.pdf Gaubas-Oriented dosimeter and reader - FINAL_JA_05_01-EGRED-05-02_final.pdf (35 p.)	ep-request.xml ep-request.pdf (4 p.) f1002-1.pdf (2 p.)
package-data.xml application-body.xml SPECEPO-1.pdf Gaubas-Oriented dosimeter and reader - FINAL_JA_05_01-EGRED-05-02_final.pdf (35 p.)	ep-request.xml ep-request.pdf (4 p.) f1002-1.pdf (2 p.)		
Submitted by	CN=secure.epoline.org		
Method of submission	Online		
Date and time receipt generated	04 May 2022, 15:31 (CEST)		
Message Digest	92:C3:D8:AC:E1:C2:3D:DE:4F:7C:A5:18:0B:C1:28:99:3A:30:39:71		

/European Patent Office/

Vilniaus universiteto leidykla  
Saulėtekio al. 9, III rūmai, LT-10222 Vilnius  
El. p. [info@leidykla.vu.lt](mailto:info@leidykla.vu.lt), [www.leidykla.vu.lt](http://www.leidykla.vu.lt)  
[bookshop.vu.lt](http://bookshop.vu.lt), [journals.vu.lt](http://journals.vu.lt)  
Tiražas 20 egz.